Small Molecules Atomistic Simulations: From QCT to Machine Learned Models

Inauguraldissertation

zur

Erlangung der Würde eines Doktors der Philosophie

vorgelegt der

Philosophisch-Naturwissenschaftlichen Fakultät

der Universität Basel

von

Juan Carlos San Vicente Veliz

Basel, 2023

Genehmigt von der Philosophisch-Naturwissenschaftlichen Fakultät
auf Antrag von
Prof. Dr. Markus Meuwly, Prof. Dr. Stefan Willitsch und Prof. Dr. Thomas E. Schwartzentruber.

Basel, den 13. Dezember 2022

Prof. Dr. Marcel Mayor

Dekan

Abstract

The understanding of chemical processes and their underlying mechanism has been fundamental in chemical and physical sciences. From large-scale astronomical phenomena to the evolution of microscopic organisms. The characterization and study of such a system has given new insight to experiments, which presents its own difficulty for systems that are bordering the technical possibilities.

With the improvement of computer resources, simulations are being conducted at conditions and settings that are just not possible with current experimental techniques. This work focuses on hypersonic reentry conditions where temperature can reach $T > 10000$ K and local chemistry processes have non-linear characteristics. In such settings, high accuracy observable are of vital importance for the simulation and modeling community, in particular with the lack of accurate experimental reference for all species and processes involved. Multi-scaled simulation can provide a solution for the in-depth accuracy needed for such coarse-grain observables.

The first chapter is a historical background of the previously conducted studies and modeling efforts. The second chapter focuses on the theoretical background of the construction and representation of high-fidelity potential energy surfaces (PES), ab-into electronic structure methods and a brief background into Quasi-Classical simulations (QCT).

The second part of the thesis shows the results and implementation of high-fidelity PESs in QCT simulations of atom + diatom reactions. The third chapter shows our results for the thermal and vibrational relaxation rates for the $N(^4S) + O_2(X^3\Sigma_g^-) \leftrightarrow O(^3P) + NO(X^2\Pi)$ reaction over a wide temperature range. The fourth chapter shows our investigation for the thermal and vibrational relaxation rates from 15 K to 20000 K for the $C(^3P) + O_2(^3\Sigma_g^-) \leftrightarrow CO_2 \leftrightarrow CO(^1\Sigma^+) + O(^1D)/O(^3P)$ reaction including five electronic states.

The third part of the thesis shows the implementation of our newly developed state-to-distribution (STD) model which predicts product state distributions from a given initial state. The fifth chapter shows the implementation of the STD model for the $N(^4S) + O_2(X^3\Sigma_g^-) \leftrightarrow O(^3P) + NO(X^2\Pi)$ reaction using the quartet electronic state and the sixth chapter is a further implementation to machine-learned (ML) based on spectroscopic assignment. In chapter seven we show the

initial steps in preparing an iterative model that can cycle through the different processes involved in a complete air chemistry system.

The last chapter shows the overall conclusion and discussion of this work.

Acknowledgements

Y dice ella: No hubo intento;
yo me fui no sé por qué.
Por las olas por el viento.
fui a la estrella y la corté.

Margarita - Rubén Darío

I will like to acknowledge and give my deepest gratitude to Prof. Dr. Markus Meuwly for giving me the opportunity to pursue my PhD studies in Switzerland. For giving me the guidance and support needed to work on such amazing projects. I'm forever thankful for the journey and where it has led me. My greatest gratitude to Prof. Dr. Raymond J. Bemish for our excellent exchanges and support throughout my studies.

I would like to thank Prof. Dr. Stefan Willitsch for accepting to be my second supervisor and Prof. Dr. Tom Schwartzentruber for kindly accepting to be my external examiner.

In the past years, I have had the amazing opportunity of working and collaborating with amazing researchers but also truly amazing people. I would like to first acknowledge Prof. Dr. Marco Panesi, Prof. Dr. Ad van der Avoird, Prof. Dr. Timothy K. Minton, and Prof. Dr. Hua Guo for the opportunity to be part of terrific research projects. Additionally, Dr. Alessandro Munafó, Dr. Adriana Caracciolo, Dandan Lu, and Dr. Sung Min Jo for our excellent scientific exchanges.

There are more internal collaborators without which this research will not be possible. I would like to acknowledge Dr. Narendra Singh for his great insights into the hypersonic and modeling aspects of our work and Dr. Max Schwilk for his devoted help and insight into the Ab-initio quantum calculations aspect of the research.

For my friends and close collaborators Prof. Dr. Debasish Koner, Dr. Sugata Goswami, and Julian Arnold there are not enough words to thank you for your contribution both scientifically and most importantly personally.

Thanks to all past and present members of the Meuwly group without which the PhD experience would lose its flavor: Dr. Oliver Unke, Dr. Leila Moham-

madzadeh, Dr. Marco Pezzella, Dr. Sebastian Brickel, Dr. Akshaya Das, Dr. Uxia Rivero, Dr. Jasmine Desmond, Dr. Kai Töpfer, Dr. Sarbani Patra, Dr. Maryam Salehi, Dr. Zhen-Hao Xu, Dr. Taylan Turan, Silvan Käser, Eric Boittier, Luis Itzá Vázquez Salazar and Meenu Upadhyay.

Special thank you to Dr. Michael Devereux for his friendship and being a good support.

Last but not least, to all my family, friends, and groups such as "Travis' Pals". This research work would not be possible without your constant support and encouragement. Thank you.

Contents

*This section is based on the book by N. E. Henriksen and F. Y. Hansen *Theories of Molecular Reaction Dynamics* (Oxford University Press, Oxford, 2012).

Chapter 1

Introduction

One of the most fundamental blocks of physical chemistry is the interaction between atoms and molecules. The characterization of this interaction has been fundamental in our current understanding of the chemical universe[1–3], the development of novelty materials[4], the design of new drugs[5], and the modelling of complex Non-Equilibrium systems[6, 7].

Complex system such as the flow around a hypersonic vehicle in reentry, presents numerous challenges for the scientific community on a different scale of study. The flight of a hypersonic space vehicle can usually reach a speed well past Mach 7[8], where the Mach value is the ratio of the speed of the flow surrounding the body in relation to the speed of sound in the surrounding medium. In this state, a strong shock wave is created which increases the temperature of the surrounding gas to over $>$ 10000 Kelvin[9]. The high temperature of the encompassing gas gives rise to the fragmentation into atomic species both within the shock wave and in a post-shock region. In this scenario, the time-scale of the chemical reactions matches the speed of the gas flowing over the body, creating a state of thermal and chemical non-equilibrium, and the conventional equilibrium chemistry is no longer accurate.

The study of the chemical processes that are present in the gas surface surrounding the vehicle is of vital importance since reproducing flight conditions in ground-test facilities is extensive, expensive and not feasible to try to reproduce the exact flight conditions. The heated gas surrounding the surface affects the heating rates and the overall gas-surface chemistry. Although some of the physical quantities such as reaction rates can be measured experimentally, a well

design hypersonic experiment will measure the overall effect of several processes, and a detailed understanding of all underlying processes will be missing. Thus, need a combined effort between experiment and theory to make further insights into the individual mechanism that influence such systems.

The non-linear nature of hypersonic flow, creates an almost instantaneous conversion of kinetic energy from the bulk of the gas into the different degrees of freedom, via collision thermal energy increases, and is deposited into the rotation and vibrational degrees of freedom. This process occurs at different time-scale where the vibrational energy excitation is slower than the rotational and is the realm of chemistry time-scales. Once the highest levels of vibrational and rotational energy are populated, dissociation or fragmentation into atomic species has a higher probability of occurrence. This creates a chain effect from the thermal energy, to the population of the internal degrees of freedom to a non-equilibrium dissociation. Thus, the phenomenon is closely to the internal energy processes and more specifically to the translational, vibrational and rotational distributions of the molecules. This chain-like process into dissociation will also be true for the reverse direction of recombination, where near the wall region atomic species are recombined into molecules, releasing heat into the system. The overall effect of both dissociation and recombination at high temperatures will affect quantifiable physical processes such the energy transport and momentum transport within the system and can have indirect effects on turbulence and radiation.

Numerical methods such as computational fluid dynamics (CFD) have made efforts in the study of hypersonic flow. Such simulations require a multi-scale approach that includes physicochemical modelling, incorporating phenomena such as the coupling between dissociation, recombination and internal energy and the ingrained non-equilibrium physical-chemical characteristics. Most modelling approaches can be divided into two approaches, either that model is fitted to known experimental quantities which is generally very limited or currently very difficult to measure. Alternatively, the model can be constructed from first principles which requires a large volume of data. At the same, this data needs to be consistent, accurate and available for the enormous amount of processes involved. Figure 1.1 shows the relevant processes and species involved for an Air Chemical Model[10].

In thermal non-equilibrium, the local population distributions of translational and internal energy of the gas cannot be effectively characterised by a single temperature T. Models that include the coupling between the vibration and dissociation have been around since the 1960's[11], these models incorporate the notion of a continuum-level rate expression by integrating the vibrational energy distribution which is assumed to be Boltzmann distribution. Then the effective dissociation rate was made to be a function of a single temperature T and the vibrational temperature T_{vib}.

With the shock tube experiment era of the 1980s, there was a realization that a new method was needed, since the new dissociation rates were obtained by shock tube experiments and the models were required to deduce the reaction rates, Park's model gave an explanation to the shock-tube data by calibrating a model that would be persistent with the data. This represented an improvement since previous models took reaction rates as given and built models around them. These newly generated rates in Arrhenius form were evaluated for an effective temperature ($\sqrt{TT_v}$) with T_v the vibrational temperature and T the one temperature translational/rotational temperature. It is important to note that the experimental raw data used for two temperature models has important levels of uncertainties (in cases one order of magnitude)[12–14], the other observation is that for low values of T_v the dissociation rate is suppressed, which is expected for a dissociation process[15]. More recently, an adaptation has been to include the vibrational relaxation constant from Millikan and White[16] to model translational-vibrational energy relaxation. In the last decades, this approach has been an effective modelling tool[17, 18]. In general, it requires: (1) the reaction rate of dissociation, (2) the vibrational relaxation rate and on occasions the rotational relaxation rate (τ_r, τ_v), (3) the average removal vibrational/rotational energy due to the dissociation, (4) the average addition vibrational/rotational energy due to recombination and (5) the reaction rate of recombination.

Although, it is vastly used the ($\sqrt{TT_v}$) has been shown to overestimate the N_2 dissociation for $T \leq 20000$ K in comparison to direct molecular simulation, however at large temperature ($T = 30000$ K) the two models converge[19]. Other examples show 1 order of magnitude difference between the vibrational relaxation from a modified Millikan-White model and vibrational relaxation obtained from methods such as quantum mechanical and quasiclasical simulations[20, 21]. The Park model is widely, not because it has been proven to be accurate across nu-

merous systems, but because the wide use is more oriented towards, the fact that historically it has been considered a straightforward implementation model.

Direct simulation Monte Carlo (DSMC) [7, 22] is a particle-based approach, in which particles (representing atoms and molecules) move and collide in space representing the temporal evolution of a gas ensemble. The particles in DSMC carry internal information such as the position, mass, velocity and internal state of molecules. Local properties of the particles can be averaged to get back macroscopic quantities such as concentration, density and pressure. For a sufficiently large number of particles (10^6 or larger), DSMC converges and simulates the Boltzmann equation[23]. One of the most widely used DSMC reaction model is the total collision energy model [22], although based on molecular properties which are involved at each collision, the most commonly used functional form is based on a modified Arrhenius equation in the continuum limit. One important note is that the TCE model assumes the probability of dissociation is inherently related to the total collision energy and there is not distinction on how the individual degrees of freedom (translational, vibrational and rotational) are distributed. In addition, the recombination probabilities can also be influenced by the uncertainties in the dissociation, since in most cases the microscopic reversibility principle is used to obtain such features. Additionally, it has been shown that typical statistical collision model that sample equilibrium distribution such as the Larsen and Borgnakke model[24] (LB) is not very accurate for post-collision properties when the system is away from equilibrium.

It is very evident that CFD simulations relying on shock-tube experiments which are not always reliable and very frequently not available is a huge limitation. Additionally, DSMC provides key modelling improvements although is parameterized to match the continuum models and would benefit from the introduction of additional microscopic physical chemistry properties to support the hypersonic flow modelling community. This detailed information can be obtained from quasiclassical trajectory simulations using high-fidelity state-of-the-art potential surfaces. Additional properties such as vibrational relaxation times and the product state distribution for the vibration, rotation and translational energy can explicitly calculated from meticulous simulations, which can then serve as input for more coarse grain models.

In recent times, it has become more and more useful the use of ab-initio computational chemistry methods to give further insight into the microscopic processes underlying the macroscopic models. A potential energy surface (PES) is a multidimensional component that encapsulates all the configurations and forces acting on all atoms involved. Starting from an initial condition the temporal evolution of the system can be obtained by integrating over time. This approach in solving the dynamical equations can be a quantum mechanical simulation approach (QM)[25] or a quasi-classical trajectory simulation (QCT)[26], which samples initial conditions from quantum states but the evolution in time is performed classically. Although QM methods are either time-independent or time-dependent and are very accurate and efficient, current limitations are centered around the speed of computation and the convergence of its main parameters. Furthermore, it has been shown that QCT can obtain comparable results to QM with a reduced computational cost and the advantage of conserving all the intermediate classical mechanic aspects of the collision[27].

Although the dynamical method is of crucial importance, the accuracy of the simulation will ultimately depend on the veracity of the underlying PES employed. In recent years, the capabilities to compute and represent a fully-dimensional PES have increased. It is now possible to study realistic chemical systems and thus chemical rate studies have considerably increased. Although analytical PESs provide solutions for a simpler system such as H_3[28] for larger systems with complex characteristics a more detailed characterization of the energy is required. Reactive processes require interaction potentials that are suitable to describe all the relevant asymptotic states for a given reaction partner. Multi reference character system, requires the inclusion of all the possible electronic states that could contribute to the accurate calculation of the energy. Typically used methods of theory are CCSD(T) or Multi reference configuration interaction (MRCI), additionally large basis sets are usually required (aug-cc-pVTZ) or larger are employed. To study the number of relevant electronic states involved in a collision, complete active space self-consistent field (CASSCF)[29] theory has been practical in generating an initial wave function. This wave function containing all the information relating to possible spin and spatial symmetries are the used as a starting guess for further MRCI calculation. This method has proven valuable in critical regions, such as crossings and asymptotics where single reference approaches would fail to converge. A state averaging (SA-CASSCF) is generally

prescribed to give weights to the different electronic states involved, Davidson-corrected MRCI (MRCI+Q)[30] which corrects for the size consistency error is then performed for a particular state. Other methods such as (MRCI-F12) have been implemented to correct for the finite size of the atomic basis set.

With several thousand electronic energy point calculations are required to uniformly cover the conformations space for systems such as atom + diatom and diatom + diatom reactions. For dynamic calculations, it is essential a smooth continuous PES, to access all the necessary configurations and energies required by the simulation. First attempts, where generally focused on representations using parametrization such as Shepard interpolation[31] or moving least-squares method[32], such approaches still present major obstacles in representing accurately reference points because of its inherent error. Other methods include permutation invariant polynomials (PIP)[33] or neural network approaches[34]. One of the most recent possibilities is to use Machine Learning for training on energy and/or force and predicting any desired conformation[35], although it has been very efficient for numerous systems[36, 37], it still has deficiencies in its application for multi-reference system and excited state system.

The reproducing kernel Hilbert space (RKHS) is a very accurate, fast, and efficient method to evaluate the entirety of the conformational space. RKHS representation is commonly preferable over other methods. First, because the kernel from the RKHS method will reproduce the ab-initio reference points with great accuracy even in scenarios where the ab-initio method is of the highest quality FCI[38], whereas most other methods will always carry an error on the actual reference points. Second, the robustness of RKHS is such that even if the error is present for "offgrid" evaluations, additional points can always be added in the regions where the error is unsatisfactory.

A full-dimensional PES that includes all the asymptotics, channels, and exhaustive search for all the required states involved is highly desirable and needed for accurate simulations. Thus, it is essential to obtain full-dimensional PESs that are highly accurate, well-represented, and consistent with the level of theory. In recent years, an effort has been made to generate such a database of PESs for atom-diatom collisions: [NO_2][39],[N_2O][40], [CNO][41] and [CO_2][42].

There are several ways that the modeling community can benefit from QCT simulations derived from using high-fidelity full-dimensional PESs. The first ap-

proach consists of averaged quantities such as reaction rate information or cross-sections at given temperatures. The reactant states are sampled using equilibrium (Boltzmann) distribution emulating the specific gas temperature. Additionally, a multi-temperature approach can be employed separating the temperature in corresponding degrees of freedom (T_r, T_v, and T_{trans}). The validation of such an approach has proven effective, due to the availability of thermal reaction rate generally measured by shock-tube experiments and macroscopic tables that include the forward and reverse rate of a reaction such as the equilibrium constant[39, 42].

The second approach consists of including state-specific information such as state-to-state cross-section and reaction rates. This input can then be incorporated into coarse-grain simulations such as master equations. Although for a full master equation approach a database of state-to-state data ($> 10^6$) need to be computed prior to the simulation. One way of validating such a state-specific approach is to emulate molecular bean experimental conditions, by assigning the same initial state condition as the experiment which has been proven effective for the [NO_2] system[43, 44]. The third approach is the include "on-the-fly" QCT calculations into Direct Molecular Simulation (DMS)[45]. All these modeling approaches account for how QCT data is of great value both for averaged and state-specific quantities. But, the use of QCT as a binding approach has been limited to the computational cost of QCT simulations, in particular for the demanding amount of PESs that are involved and for state-to-state approaches that demand an extensive amount of observables $> 10^{20}$ for diatom + diatom reaction for which each simulation requires at least 10^5 trajectories for convergence. This makes such an approach unfeasible for larger and larger poly-atomic reactions.

In recent years the enhancement of science has incorporated the use of statistical approaches to help tackle the most complex problems in chemistry[35–37]. Neural Network (NN) is one such approach. The basics behind NN is to learn to predict a particular property. The most basic transformation or "mapping" that we can make is a linear regression $\mathbf{y} = \mathbf{wx} + \mathbf{b}$. This mapping between an input and output property, denoted by the vector $\mathbf{x}$ and $\mathbf{y}$ respectively, with the mapping matrix ($\mathbf{w}$) and the parameter vector ($\mathbf{b}$).

As previously pointed the extensive number of state-to-state observables needed for the complete evaluation of a state-specific coarse grain model has limited the implementation of QCT simulations. A machine-learned model that can bridge

the gap in the computational cost of QCT while maintaining its accuracy is much needed. A recently developed state-to-state (STS)[46] model for the [N_2O] system was successfully implemented in predicting all the necessary state-to-state cross-section information while needing only a fraction of such observables from QCT reference data. A subsequent Distribution-to-Distribution model was later employed to effectively evaluated product state distribution given initial (T_{rot}, T_{vib} and T_{trans}) distributions for the [NO_2] system. An intermediate model which conserves the evaluation speed of DTD while having the inherent state-specific information is a requirement to be seamlessly incorporated into coarse modeling.

This thesis aims at presenting a multi-scale, in-depth approach to molecular simulations relevant to hypersonic flight. At each level of calculation exhaustive detail is placed in the accuracy of such calculations as this was required for high-fidelity observables that can be comparable to experiments at different scales of simulation.

In Chapter 3, shows an example for accurate simulations on the $N(^4S)+O_2(X^3\Sigma_g^-) \leftrightarrow O(^3P)+NO(X^2\Pi)$ reaction including 3 electronic states $^2A'$, $^4A'$ and $^2A''$, Chapter 4 focuses on the $C(^3P) + O_2(^3\Sigma_g^-) \leftrightarrow CO_2 \leftrightarrow CO(^1\Sigma^+)+ O(^1D)/O(^3P)$ reaction including 5 electronic states. The second part of the thesis focuses on applications that have the assistance of a recent state-to-distribution approach (STD) for an atom + diatom collision system, Chapter 5 explores a first implementation of the STD to the $N(^4S) + O_2(X^3\Sigma_g^-) \leftrightarrow O(^3P) + NO(X^2\Pi)$ reaction using the quartet state. Further implementation is made in Chapter 6 with the evaluation of a Model Hamiltonian (MH) constructed product state distributions and comparison with the standard semi-classical (SC) theory model. Finally, Chapter 7 shows the first step in the implementation of an iterative model to cycle through the different processes involved in a future complete air chemistry simulation.

A detailed introduction is provided at the beginning of each chapter. The final conclusion and observation are drawn in Chapter 8.

Regions with chemical and thermal nonequilibrium	
Region	Aerothermal phenomenon
Ⓐ	Chemical and thermal equilibrium
Ⓑ	Chemical nonequilibrium with thermal equilibrium
Ⓒ	Chemical and thermal nonequilibrium

Chemical species in high-temperature air		
Region	Air chemical model	Species present
Ⅰ	2 species	O_2, N_2
Ⅱ	5 species	O_2, N_2, O, N, NO
Ⅲ	7 species	$O_2, N_2, O, N, NO, NO^+, e^-$
Ⅳ	11 species	$O_2, N_2, O, N, NO, O_2^+, N_2^+, O^+, N^+, NO^+, e^-$

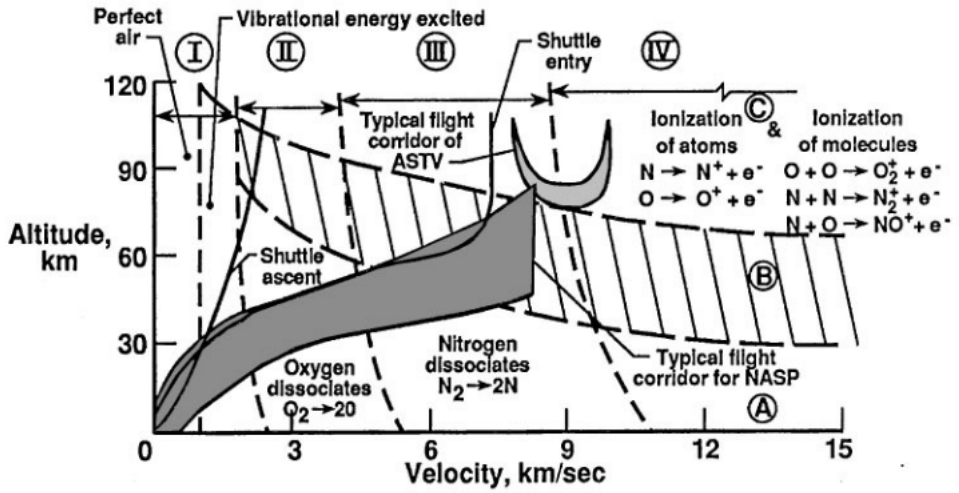

Figure 1.1: Critical regions, species, and processes for an Air Chemical Model that studies flow regimes of a 30.5 cm radius sphere flying in air. Figure extracted from Ref. [10]

Chapter 2

Theoretical Background

The different theoretical methods used in this thesis are summarized below, the chapter starts with a brief description of potential energy surfaces and quantum mechanical methods, Hartree-Fock and multireference configuration interaction (MRCI), and it continues with the description of the quasi-classical simulation method.

2.1 Potential Energy Surface Construction

The interactions between atoms and molecules are the fundamental building blocks of the chemical sciences. One of the most important aspects is the evolution of the species and their chemical properties in space and time. Just as sailors have long searched for a complete map of navigation that crosses the entirety of the planet, so to has scientific research focused on providing "chemical interaction maps" of different chemical systems. From lightweight atoms diatom reactions such as H + H_2 the field has now been involved to map heavy atom interaction and the inclusion of multiple electronic states. The topology of the PES varies depending on the elementary chemical reaction involved. there are surfaces with a single potential energy barrier and no wells and surfaces with multiple wells and barriers. The path from reactant to products can be of a “direct reaction” which takes place within a vibrational period and has a single saddle point, “indirect” which takes numerous vibrational periods and can have several saddle points along the path connecting reactant to product.

A saddle point is a critical point in a multidimensional potential energy surface. such a point has the uniqueness to be stable in all but one dimension, and thus the second-order derivative is negative. An important feature of the potential energy surface is the barrier height, this measure is indicative of how much energy is necessary for the reactant in order to be able to surpass the energetic threshold. Consideration needs to be made although the barrier height is an indication there are other effects such as vibrational zero-point energies and quantum tunneling that need to be considered and can affect the necessary energy needed to form the product specie.

The conjunction of wells, saddle points, and barrier height is often what defines the features of the topology of a potential energy surface. Although the complete energy surface is of much importance it is often the minimum energy or the path of the reaction that is most important for the reaction. The minimum-energy path is sometimes called the path of least resistance, this path will offer the lowest energetic values and a path from reactant to product. Such a path can be considered an "exothermic" reaction if the energy of the reactant is higher than that of the product or "endothermic" if the reactant's energy is lower than that of the product. Such definitions are very important because they have ramifications in the reaction at a larger scale, if the reaction is "exothermic" its excess energy can be distributed into the vibrational, rotational, and transnational degrees of freedom of the product molecule.

There are other critical features of a potential energy surface, such as the position of the barrier with respect to the reactant or product. A reaction barrier is called "early" or "reactant barrier" if the barrier is situated in the entrance channel while the reactant is still approaching one another, this can be associated with a high vibrational excitation in the product molecule. A "late" barrier occurs in the product channel while the product species are separating, this can lead to a low vibrational excitation in the product molecule. Local minimums and wells also can affect the dynamics of the reaction, a pronounced well can imply that a intermediate complex is formed with a long-live time before reaching the final product channel.

Potential energy surfaces are not limited to a particular electronic state, some will occur in the electronic ground states but others will have a presence in the

excited electronic states, and this brings the effective methods for calculating energies at the ground state and excited states.

In this section, we describe the elemental methods that play a role in the accurate calculation of the energy points that conform to a potential energy surface. Methods have roots in techniques solving the electronic Schrödinger equation. For molecules with a large number of electrons, it can be very difficult the calculation of the electronic energy of the molecule and thus the highly accurate calculation of the energy along the different internuclear configurations becomes increasingly difficult.

One of the most common approaches to solving the Schröndinger equation for a multi-electron system is the Hartree-Fock theory.

2.1.1 Hartree-Fock Theory

In quantum mechanics, one of the fundamental principles is the definition of a wave function. The wave function has a direct correlation with the energy of a particular molecule. The fundamental equation to obtain the energy is the time-dependent Schrödinger equation.

$$\hat{H}|\Psi_n >= E_n|\Psi_n > \tag{2.1}$$

Where $\hat{H}$ is the time-dependent Hamiltonian which is applied to the set of quantum states $|\Psi_n >$ and for which a real eigenvalue E_n is associated. The Hamiltonian operator can be express as $\hat{H} = \frac{-\hbar^2}{em}\Delta^2 + V(r)$, where Δ is the Laplacian and $V(r)$ the potential energy of the system.

Although the Schröndinger equation has an analytic solution for the Hydrogen atom, with only one electron. Other considerations and approximations need to be in place for solving the multi-electron system. One widely used approximation takes advantage of the distinctive difference in mass between the nuclei and electrons an thus is able to neglect the motion of the nuclei. The motionless nuclei will therefore not have any kinetic energy.

The Hartree-Fock approximation consists of considering the N electron wave function as a product of single orthogonal wave functions (Hartree Product), which is the interaction between individual electrons and the remaining electrons.

$$\Psi(x_1, x_2, \ldots, x_N) = \Psi_1(x_1)\Psi_2(x_2)\ldots\Psi_N(x_N) \tag{2.2}$$

An N electron wave function constructed by state determinants called "Slater determinant" is formulated.

$$\Psi(x_1, x_2, \ldots, x_N) = \frac{1}{\sqrt{N!}} \begin{vmatrix} \chi_1(x_1) & \chi_2(x_1) & \cdots & \chi_N(x_1) \\ \chi_1(x_2) & \chi_2(x_2) & \cdots & \chi_N(x_2) \\ \vdots & \vdots & \ddots & \vdots \\ \chi_1(x_N) & \chi_2(x_N) & \cdots & \chi_N(x_N) \end{vmatrix} \tag{2.3}$$

To obtain the lowest energy E_0 eigenstate, the variational principle is used.

$$E = \frac{<\Psi|\hat{H}|\Psi>}{<\Psi|\Psi>} \tag{2.4}$$

$E = E_0$ only for the lowest energy. Thus Eq. 2.4 needs to be solve interactive until the lowest energy is obtained.

For an N orbital system, the energy of the ith orbital can be obtained using a modified version of the Hamiltonian operator called the "Fock Operator".

$$\hat{F} = \hat{h_i} + \sum_{i=1}^{N/2}(\hat{J}_i - \hat{K}_i) \tag{2.5}$$

where $\hat{h_i}$ is the one-electron Hamiltonian for the ith orbital, $\hat{J}_i$ is the Coulomb electron-electron repulsion operator and $\hat{K}_i$ is the Exchange operator, which adds the quantum effects of interchanging electrons. Finding the energy ϵ_i of the ith orbital is reduced to solving the expression.

$$\hat{F}\Psi_i = \epsilon_i\Psi_i \tag{2.6}$$

Where $\hat{F}$ is the Fock operator and Ψ_i can be associated with a "Hartree-Fock Orbital".

2.1.2 Multireference configuration interaction

One of the major deficiencies of the Hartree-Fock approximation is its incapacity to consider the electron correlation in the multi-electron wave function. Using Hartree-Fock alone has been shown to have deficiencies in particular with the symmetry properties[47]. For the accurate calculation of molecular systems which are quasi-degenerate and have low-lying excited states the multireference approach has become a very useful tool.

Many electronic structure methods are classified as either a single reference (SR) or multireference (MR). For an SR calculation, a single reference function is chosen from the single Slater determinant, the Hamiltonian interaction with the reference function is generally derived from empirical procedures[48] or the use of other principles such as perturbation theory [49]. One of the main weaknesses in SR approaches is in describing multiple states since the reference function for one electronic state is usually not appropriate for other electronic states. Additionally, the potential energy surface is dominated by different determinants, which implies that the reference function based on one conformation will be inadequate for other conformations.

The multireference approach has the advantage of including all the most relevant configuration-state functions[50]. This generally implies a priory approach base on selecting the complete active space (CAS) reference, and thus all possible sets of active orbitals included are then the reference functions. The MR method has provided accurate results for systems with multi-reference characteristics[51, 52], showing the greatest advantage for excited states which need to include multiple states[53].

One MR method that has proven very effective for excite states[54] is the multireference configuration interaction (MRCI) method. One of the most important characteristics of MRCI calculation is the definition of the reference space which is constructed by correctly defining the set of frozen, reference, active and virtual orbitals (Fig. 2.1). This definition is critical as in practice the wave function from a previous complete active space self-consistent field (CASSCF)[29] is used as a reference for the MRCI calculation which uses the reference wave function from CASSCF exciting electrons out of this space.

One of the advantages of MRCI is the ability to tackle difficult systems with multiple electronic states involve and being able to accurately compute the corre-

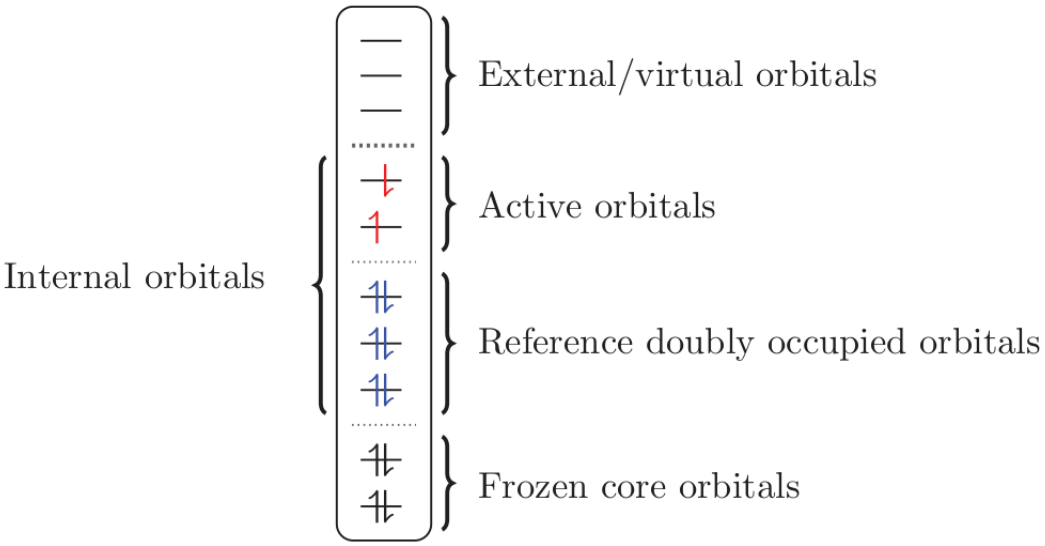

Figure 2.1: Classification of the orbital space into subspaces. Figure take from Ref. [55]

sponding excited states. From a technical perspective, including all the relevant states for a system with larger molecules or a number of electrons is still very computationally demanding. Additional challenges facing calculations using MRCI level of theory can be found in Ref. [53].

2.1.3 Representation of a Potential Energy Surface: RKHS Method

The generation and representation of potential energy surfaces have been a topic of interest in recent years. Dynamic simulations require complete coverage of the necessary energy evaluations, for a system such as atom + diatom collision (A + BC $\rightarrow$ AB + C) the necessary evaluations can reach over 10ˆ5 points. Thus, the necessity to find methods to represent continuous smooth potential energy surfaces covering all the necessary configurations that the simulations will require. The most commonly used methods include many-body expansion, permutationally invariant polynomials, and neural network (NN)-based representations. For tri and tetratomic system the many-body expansion has been an effective and accurate approach, but it has had difficulties when facing a higher-order system, as the expansion becomes complicated. PIP and NN methods shows good results for higher order system, but shows weakness in incorporating all the physics into

the surface in particular the long-range characteristics. The advantage of RKHS is its robustness, its reproduction of the reference or on-grid energies exactly, and its computational speed. It has effective characterization of the long-term interaction, creating a very reliable, smooth and continuous gradient PES for dynamic simulations.

As a grid base approach, RKHS has had limitations in scaling with the size of the grid or number of evaluations. A very efficient and fast approach, fast-evaluation method[56] has been design to exactly overcome the scaling issue. Until recently this method had limitations being implemented as a coded tool, but a very robust toolkit[57], has proven very efficient for the representation of PESs in numerous quasi-classical and quantum applications: NO_2[58], CO_2[27, 59], N_2^+-Ar[60], and CNO[41], this fast evaluation has the advantage of being independent of the number of data points, and hence a PESs with dense grid can be elaborated.

In its most basic representation, the generalized representer theorem[61] states that given the know values f_i of the function $f(x)$ for a set of N samples x_i, the function $f(x)$ can always be approximated by a linear combination of kernel products.

$$f(x) = \sum_{i=1}^{N} c_i K(x, x_i) \tag{2.7}$$

where c_i are coefficients and $K(x, x')$ is the reproducing kernel. The functional $f(x)$ can be represented as an inner product of $f(x)$ with $K(x, x')$. For a vector containing N observations K is a N X N matrix, which is symmetric and positive, the inverse matrix K^{-1} can be obtained by the Cholesky decomposition[62] and the coefficients c_i can be expressed.

$$c = \mathrm{K}^{-1}\mathrm{y} \tag{2.8}$$

where y is the vector constructed from the N y_i that are part of the know dataset $y = [y_1, \ldots, y_N]^T$ and c is the vector coefficient $\mathrm{c} = [c_i, \ldots, c_N]$. Once the coefficients have been determined for an arbitrary x^* value, which maps into $y^* = \hat{f(x^*)}$ from equation 2.7. If K is ill-conditioned then equation 2.8 becomes equation 2.9 from the Tikhonov regularization[63].

$$c = (\mathrm{K} + \lambda \mathrm{I})^{-1} \mathrm{y} \tag{2.9}$$

where $\lambda > 0$ and I is the identity matrix. For the application of kernels for the evaluation of a potential energy surface, equation 2.7 becomes for N configurations.

$$V(x) = \sum_{i=1}^{N} c_i K(x, x_i^{'}) \tag{2.10}$$

where c_i are the coefficients x_i', are the know values, for which ab-initio calculated energies have been determined. Using the same procedure as equation 2.8 the coefficients for an N configurations system can be determined.

$$\begin{vmatrix} K(x_1, x_1') & K(x_1, x_2') & \cdots & K(x_1, x_N') \\ K(x_2, x_1') & K(x_2, x_2') & \cdots & K(x_2, x_N') \\ \vdots & \vdots & \ddots & \vdots \\ K(x_N, x_1') & K(x_N, x_2') & \cdots & K(x_N, x_N') \end{vmatrix} \begin{vmatrix} c_1 \\ c_2 \\ \vdots c_N \end{vmatrix} = \begin{vmatrix} V_1 \\ V_2 \\ \vdots V_N \end{vmatrix} \tag{2.11}$$

This procedure generates n exact value for the reference points x_i'. For the (M) multidimensional case the kernel can be approximated by a product of one-dimensional kernels $K_j(x, x')$.

$$K(x, x') = \prod_{j=1}^{M} K_j(x, x') \tag{2.12}$$

The kernel can be represented by a polynomial of order (n), and other physical properties for the system can be included such as the long-range interaction[64, 65].

$$k^{n,m}(x, x') = n^2 x_{>}^{-(m+1)} B(m+1, n) {}_2F_1(-n+1, m+1; n+m+1; \frac{x_{<}}{x>} \tag{2.13}$$

where $x_{>}$ and $x_{<}$ are the larger and smaller value of x and x'. The values of n represent the smoothness of the kernel and m the asymptotic behavior or the long-range decay. In practice, it is common to use a reciprocal power decay with

$n = 2$ and $m = 6$ for the radial coordinates and a Taylor spline kernel for the angular part.

The complete kernel as a function of the interatomic distances r as:

$$V(r) = \sum_{i=1}^{N} c_i K(r, r') \tag{2.14}$$

and the corresponding derivatives can be obtained by substituting the kernels by their derivatives $K'(r, r')$.

$$\frac{dV}{dr_h} = \sum_{i=1}^{N} C_i K'(r, r') \tag{2.15}$$

2.2 Quasi Classical Trajectory Simulations*

The evolution in space and time of atoms and molecules can be described effectively by classical mechanics through its position and momentum. In a quasi-classical approach, the nuclei of a chemical specie moves in a force a field which is created by the adiabatic electronic energy of the system following the laws of classical mechanics. The term "quasi" refers to the way the system is prepared before a collision, molecules are assigned discrete internal energy states which are connected to different quantum states. Once the system is liberated from equilibrium and a trajectory, can be used as a trace of the motion, the assigned quantum restrictions are relaxed so that the trajectory is solely governed by the classical laws of motion. This same procedure is repeated when the trajectory reaches its product state and a "quantization" or assignment of the quantum properties is employed in the final analysis of molecular internal energy states. Thus a swarm of trajectories can have the common feature of having the same energy.

For a single trajectory of a A + BC(v,j) collision has specified initial quantized rotational and vibrational quantum state and a fixed initial translational energy. The Quasi classical Trajectory (QCT) approach which is described below, involves solving the Hamiltonian for the system.

*This section is based on the book by N. E. Henriksen and F. Y. Hansen *Theories of Molecular Reaction Dynamics* (Oxford University Press, Oxford, 2012).

2.2.1 The Hamiltonian

For a N-body system the Hamiltonian is described as:

$$H(r,p) = T_{kin}(p) + V(r) = \sum_{i=1}^{N} \frac{p_i^2}{2m_i} + V(r_1, \ldots, r_N) \tag{2.16}$$

The term $V(r_1, \ldots, r_N)$ is the potential energy of the N bodies from a fixed cartesian coordinate system. Each r_i are the position vector with respect to the reference frame and p_i are the respective momentum of body i

For a given reaction be an atom + diatom collision as A + BC $\rightarrow$ AB + C, where only three atoms, A , B, and C are involved, $N = 3$, the Hamiltonian becomes.

$$H(r,p) = \sum_{i=1}^{3} \frac{p_i^2}{2m_i} + V(r_1, r_2, r_3) \tag{2.17}$$

In collision processes, excluding external factors such as external fields, the relative motion of the atoms and molecules is the defining magnitude governing the process, not the absolute positions. It is naturally a best practice to choose a coordinate system that accommodates and reflects directly the relative motion of the atoms. One of the most common approaches is to use a Jacobi coordinate system, where the distance between atom BC is chosen as the first distance vector, the second vector will be the distance between the center of mass of the molecule BC and the A, and finally the third position vector will be the center-of-mass position vector for all three atoms. The advantage of choosing such a coordinate is the possibility to track the displacement of the incident atom A from the center of mass of the molecule BC. The Hamiltonian in reactant Jacobi coordinates can be written as:

$$H = \frac{1}{2\mu_{BC}} \sum_{i=1}^{3} p_i^2 + \frac{1}{2\mu_{A,BC}} \sum_{i=1}^{3} P_i^2 + \frac{1}{2M} \sum_{i=1}^{3} P_{S_i}^2 + V(q_1, q_2, q_3, Q_1, Q_2, Q_3) \tag{2.18}$$

where the diatomic reduced mass is $\mu_{BC} = \frac{m_B m_C}{(m_B + m_C)}$, the triatomic reduced mass $\mu_{A,BC} = \frac{m_A(m_B+m_C)}{M}$, where M is the total mass $M = m_A + m_B + m_C$, and m_i is the atomic mass of the individual species A, B, and C respectively.

The Hamiltonian is expressed in terms of the generalized coordinates q_i and Q_i ($i = 1, 2, 3$) represent the Cartesian coordinate of the BC distance and the distance vector from the center of mass of the molecule BC and the atom A. Similarly, p_i and P_i ($i = 1, 2, 3$) represent the momentum vector of the BC distance and center of mass of BC to A. S_i and P_{S_i} ($i = 1, 2, 3$) are the position and momentum of the triatomic ABC system in Cartesian coordinates. In the absence of an external field, V is the potential that depends on the relative coordinates q_i and Q_i.

The equations of motion in the reactant Jacobi coordinates are described by a set of Hamilton's differential equations.

$$\frac{\partial q_i}{\partial t} = \frac{p_i}{\mu_{BC}} \tag{2.19}$$

$$\frac{\partial Q_i}{\partial t} = \frac{P_i}{\mu_{A,BC}} \tag{2.20}$$

$$\frac{\partial S_i}{\partial t} = \frac{P_{S_i}}{M} \tag{2.21}$$

$$\frac{\partial p_i}{\partial t} = -\frac{V}{\partial q_i} \tag{2.22}$$

$$\frac{\partial P_i}{\partial t} = -\frac{V}{\partial Q_i} \tag{2.23}$$

$$\frac{\partial P_{S_i}}{\partial t} = 0 \tag{2.24}$$

Further reduction of the number of equations can be made by recognizing the total energy and total angular momentum (the three components) as constatants of motion. The reduction will be from 12 equations to 8 equations, the resulting equation will not be discussed here.

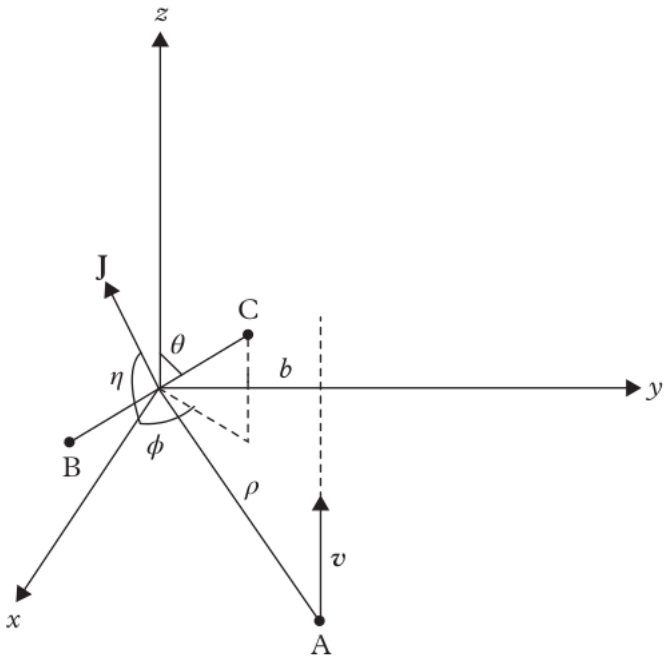

Figure 2.2: Initial conditions and arrangement of the A + BC collision, where ρ is the distance between the center of mass of the BC diatom and the atom A. b is the impact parameter, v is the relative velocity vector and θ, ϕ the spherical orientation and η the rotation angle of the angular momentum vector ($\mathbf{J_r}$) of the BC diatom. Figure extracted from [66]

2.2.2 Preparation of Initial Conditions

The initial values of the coordinates and momenta, are $q_i^0, Q_i^0, p_i^0, P_i^0; i = 1, 2, 3$ and must be specified. These initial conditions depend on the parameters chosen for the collision, which generally are the geometric parameter that characterizes the collision and differentiate one collision from another. It is important to note that from the center of mass of the diatomic molecule BC at any time t, $P_{S_i(t)} = S_i(t) = 0$. Thus, it is very important an efficient choice of the initial condition. For a collision for atom A with a selected vibrational-rotation state (v, j) of the molecule BC at some fixed center-of-mass collision energy E_{rel}, there are a total of five collision parameters. Figure 2.2 shows a schematic representation of the collision system, it is defined without losing generality that the origin of the coordinate system lies at the center of mass of the molecule BC. On the yz plane lies the distance vector from the center of mass of BC to A. The relative velocity vector (v), which is the relative velocity of A relative to BC is parallel to positive $z-$axis. The orientation of the molecule BC is given in spherical angles θ and χ. The angle that represents the rotation of the angular momentum (J_r of the

molecule BC is defined as ν. The distance from the center of mass of BC to A is defined as ρ, b is the impact parameter, b.

The set of equations that defines the positions and momenta of the relative motion between A and BC are as follows.

$$Q_1^0 = 0 \tag{2.25}$$

$$Q_2^0 = b \tag{2.26}$$

$$Q_3^0 = -(\rho^2 - b^2)^{\frac{1}{2}} \tag{2.27}$$

$$P_1^0 = 0 \tag{2.28}$$

$$P_2^0 = 0 \tag{2.29}$$

$$P_3^0 = (2\mu_{A,BC}E_{rel})^{\frac{1}{2}} = P^0 \tag{2.30}$$

The initial diatomic distance can vary from the two turning points of the molecule q_+ to q_-, the initial momentum is influenced by the initial separation of the diatom and the phase of the vibration. To include all possible phases of the vibrating diatom a random number is invoked ξ $(0 \leq \xi \leq 1)$ for each of the trajectories. In addition to integrating the equations of motions, the equation for a rotating and vibrating diatom molecule needs to be solved for a time interval of $\tau\xi$ if $\xi < 0.5$ or $\tau(\xi - 0.5)$ for $\xi \geq 0.5$. The period of the vibrational motion is denoted by τ, which is calculated by integrating the equation of motion for the rotating diatom between the two turning points q_+ and q_- respectively. It is worth noting that for a state-specific calculation the period τ and turning points q_+ and q_- only need to be calculated once.

2.2.3 Sampling the Initial Conditions

For sampling the initial conditions a standard Monte Carlo sampling scheme is used. Random numbers are invoked to initialize θ, ϕ, η, and ξ these new set of random θ', ϕ', η' and ξ' numbers have values between 0 and 1 and are related to θ, ϕ, η, and ξ as follows

$$\theta = \cos^{-1}(1 - 2\theta') \tag{2.31}$$

$$\phi = 2\pi\phi' \tag{2.32}$$

$$\eta = 2\pi\eta' \tag{2.33}$$

$$\xi = \xi' \tag{2.34}$$

Taken into consideration that first the equations of motions for the rotating oscillator are solved and the initial separation of the diatom BC can be q_+ or q_- depending if ξ is < 0.5 (q_-) or q_+ otherwise. The initial condition of the coordinate $(q_i(0))$ and momenta $(p_i(0))$ $i = 1, 2, 3$ are as follows.

$$q_1(0) = q_\pm \sin\theta \cos\phi \tag{2.35}$$

$$q_2(0) = q_\pm \sin\theta \sin\phi \tag{2.36}$$

$$q_3(0) = q_\pm \cos\theta \tag{2.37}$$

$$p_1(0) = \frac{J_r}{q_\pm}(\sin\phi\cos\eta - \cos\theta\cos\phi\sin\eta) \tag{2.38}$$

$$p_2(0) = -\frac{J_r}{q_\pm}(\cos\phi\cos\eta - \cos\theta\sin\phi\sin\eta) \tag{2.39}$$

$$p_3(0) = \frac{J_r}{q_\pm} \sin\theta \sin\eta \tag{2.40}$$

Where $J_r = \hbar\sqrt{j(j+1)}$

2.2.4 Analysis of Trajectories

There are several possible outcomes for a diatom + atom collision.

$$\mathrm{A} + \mathrm{BC}(v,j) \rightarrow \begin{cases} \mathrm{AB}(v',j') + \mathrm{C} \\ \mathrm{AC}(v',j') + \mathrm{B} \\ \mathrm{A} + \mathrm{B} + \mathrm{C} \\ \mathrm{A} + \mathrm{BC}(v',j') \end{cases} \tag{2.41}$$

There is the additional possibility that no reaction takes place $\mathrm{A} + \mathrm{BC}(v,j) \rightarrow \mathrm{A} + \mathrm{BC}(v,j)$ with no change in the final vibrational and rotational state, each one these possibilities usually refers to as "channels'. To decide whether a particular trajectory ends up in a particular channel, geometrical considerations are taken considering the inter-atomic distances. Since the original Jacobi coordinate was chosen from the perspective of the reactant molecule BC for the propagation of the trajectory for the product analysis it is convenient to do a transformation of the coordinates.

$$Q' = BQ \tag{2.42}$$

$$P'[B^T]^{-1}P \tag{2.43}$$

Where (Q,P) are the reactant coordinates and (Q',P') are the product states.

The reaction probability is taken as the fraction of trajectories that lead to a particular channel.

$$< P_{R(b;v,j,J)} >= \frac{N_{R(b;v,j,J)}}{N_{\mathrm{tot}}} \tag{2.44}$$

where N_R is the number of trajectories that lead to the desired channel and N_{tot} is the total number of trajectories. The choice of the total number of trajectories to run will depend on the initial condition considered, but generally at least 10^5 trajectories are necessary for reliable statistics.

The probability as constructed is dependent on the choosing of the impact parameter b, it will be very difficult to control the value of the impact parameter in an experiment, thus the most commonly used observable is the cross-section which has a direct relation with the probability. To obtain such a value we can simply sample the impact parameter from 0 to b_{max}, choosing b_{max} large enough so the probability is zero.

$$\sigma_R(v,j,J) = \pi b_{\text{max}}^2 \int_0^1 < P_R(b(b'),v,j,J) > db' = \pi b_{\text{max}}^2 \frac{N_R(v,j,J)}{N_{\text{tot}}(v,j,J)} \tag{2.45}$$

where b is the sampled value of the impact parameter $b = b_{\text{max}}\sqrt{b'}$ and b' is the random number from 0 to 1. $db' = \frac{2b}{b_{\text{max}}^2}$ and N_R are the number of trajectories leading to the desired channel and N_{tot} the total number of trajectories.

It is also of interest the the distribution of the rotational and vibrational state of the desire channel in particular the rotational and vibrational distributions of the product molecule. It is important to note that the meaning of a specific rotational and vibrational state is only meaningful if the coupling between the two modes is weak.

Chapter 3

NO_2: Thermal Rates and Cross Sections

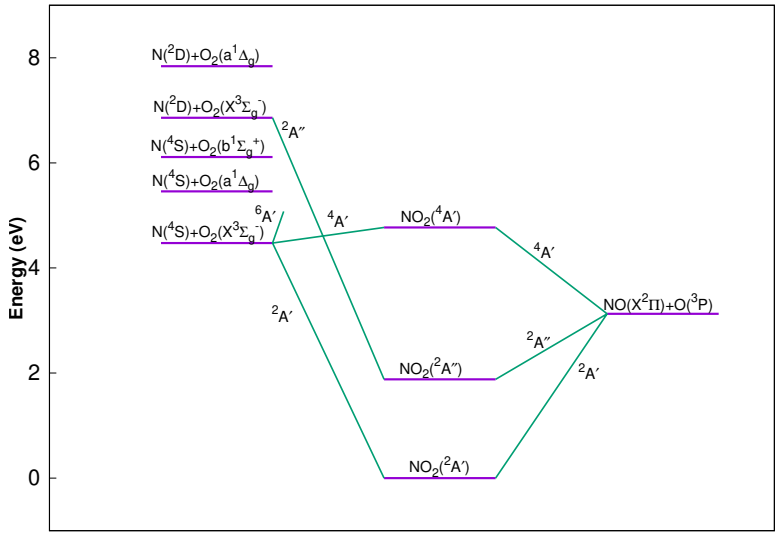

The results presented in this chapter have been previously published in:

Phys. Chem. Chem. Phys. 22 (2020) 3927

doi: 10.1039/c9cp06085e

***

Dr. Debasish Koner and Dr. Max Schwilk have contributed to this work as second and third author.

In this Chapter, the kinetics and vibrational relaxation of the $N(^4S)+O_2(X^3\Sigma_g^-) \leftrightarrow O(^3P)+NO(X^2\Pi)$ reaction is investigated over a wide temperature range based on quasiclassical trajectory simulations on 3-dimensional potential energy surfaces (PESs) for the lowest three electronic states. Reference energies at the multi reference configuration interaction level are represented as a reproducing kernel and the topology of the PESs is rationalized by analyzing the CASSCF wavefunction of the relevant states. The forward rate matches one measurement at 1575 K and is somewhat lower than the high-temperature measurement at 2880 K whereas for the reverse rate the computations are in good agreement for temperatures between 3000 and 4100 K. The temperature-dependent equilibrium rates are consistent with results from JANAF and CEA results. Vibrational relaxation rates for $O + NO(\nu = 1) \rightarrow O + NO(\nu = 0)$ are consistent with a wide range of experiments. This process is dominated by the dynamics on the $^2A'$ and $^4A'$ surfaces which both contribute similarly up to temperatures $T \sim 3000$ K, and it is found that vibrationally relaxing and non-relaxing trajectories probe different parts of the potential energy surface. The total cross section depending on the final vibrational state monotonically decreases which is consistent with early experiments and previous simulations but at variance with other recent experiments which reported an oscillatory cross section.

3.1 Introduction

Reactions involving nitrogen and oxygen play important roles in combustion, supersonic expansions, hypersonics, and in atmospheric processes. A particularly relevant process, which is part of the so-called Zeldovich process[67] are the NO + O or O_2 + N reactions[68, 69] that describe the oxidation of nitrogen. In the forward direction, the reaction also generates reactive atomic oxygen. These reactions, together with a range of other atom plus diatom and diatom plus diatom

reactions form the core of the 5- and 11-species model used in hypersonics.[70] At high temperatures ($\sim$ 20000 K), as present in thin regions of shock layers created at hypersonic speed flight[71], the reactive chemical processes can become very complex. This complexity is in part due to a significant degree of non-equilibrium. The lack of experimental information on the kinetics at these high temperatures makes numerical simulations for reaction cross sections as well as reaction and vibrational relaxation rates a very valuable source of information for characterizing hypersonic flow.

There is also much interest in correctly describing the vibrational distribution of the NO molecules after reactive or nonreactive collisions with atomic oxygen for atmospheric processes. The infrared emission of nitric oxide is one of the main tracers to follow and characterize the energy budget in the upper atmosphere.[72] This emission arises from relaxation of vibrationally excited NO after collisional excitation with atomic oxygen. This relaxation process has also been implicated in nighttime cooling of the thermosphere, above $\sim$ 100 km. Furthermore, nitric oxide is also formed in situ and used as a tracer for combustion and in hypersonic flows where it is commonly observed by Laser Induced Fluorescence (LIF).

Previous studies included experimental and computational characterizations of the reaction dynamics and final state distributions of the products. Using a pulsed beam of energetic nitrogen atoms at 8 km/s interacting with thermal oxygen under single collision conditions to mimic velocities seen in low earth orbit, distribution of vibrationally excited NO and state specific reaction cross sections for $N+O_2 \rightarrow NO+O$ were determined.[73] The analysis showed an oscillatory behaviour of the cross section with increasing final vibrational state, with minima at $\nu = 3$ and $\nu = 6$, with an uncertainty of a factor of two. An even earlier

experiment[74], using saturated multiphoton ionization spectroscopy, measured the NO product ground-state distribution, reporting a difference in the cross sections between odd ($\nu = 1, 3, 5$) and even ($\nu = 0, 2, 4, 6$) final vibrational levels.

From the perspective of computer based simulations[75–77] the vibrational state-dependent cross sections have been calculated using a variety of potential energy surfaces (PESs). In all of these computational studies, the maximum of the final state vibrational cross section is found to be at $\nu = 1$[75] or at $\nu = 2$[76, 77] with no notable oscillation. One PES for the $^2A'$ state used a fit[76] to electronic structure calculations at the complete active space SCF (CASSCF) level followed by multireference contracted configuration interaction and a modified Duijneveldt (11s6p) basis set.[78] Another PES was based on 1250 (for the $^2A'$) and 910 ($^4A'$) CASPT2 calculations and fitted to an analytical function.[79] Such an approach was also used for the $^2A''$ state.[80] This was followed by a PESs for the $^2A'$ state using a diatomics in molecules (DIM) expansion with the two-body terms based on extended Hartree-Fock calculations.[81] Then, a 2-dimensional PES with the NO bond length fixed at its equilibrium value of 2.176 a_0 was determined at the icMRCI+Q level of theory and a cc-pVQZ and represented as a cubic spline.[82] This work also presented a PES for the $^2A''$ state. More recently, a double many body expansion fit to 1700 points at the MRCI/aug-cc-VQZ level of theory for the $^2A''$ state was carried out.[83] In addition, quasi classical trajectory (QCT) calculations[68, 75, 79, 84] have been reported for the temperature dependent rate for the $N(^4S)+O_2 \rightarrow NO+O$ and its reverse reaction using different PESs.

Another important process is the energy transfer following the collision of vibrationally excited NO with oxygen atoms ($O_A + NO_B \rightarrow O_A + NO_B$) or ($O_A + NO_B \rightarrow O_B + NO_A$) to yield NO in its ground vibrational state. Using 355

nm laser photolysis of a dilute mixture of NO_2 in argon, the experiment[69] reports a vibrational relaxation rate of: $k_{\nu=1\to0} = 2.4 \pm 0.5(10^{-11})$ cm^{3}s^{-1} at a temperature of $T = 298$ K. Later, QCT simulations[85] reported a value of $k_{\nu=1\to0} = 2.124 \pm 0.73(10^{-11})$ cm^{3}s^{-1} at $T = 298$ K which is close to the experimentally reported rate. Another experiment[86] used a continuous wave microwave source to form O atoms combined with photolysis of trace amounts of added NO_2 to generate vibrationally excited NO. This experiment found a rate of $k_{\nu=1\to0} = 4.2 \pm 0.7(10^{-11})$ cm^{3}s^{-1} at $T = 295$ K which is larger by 75 % compared with the earlier experiments.[69] Quite recent QCT simulations using again the DIM-based PES[81] mentioned above reported a rate of $k_{\nu=1\to0} = 4.34 \pm 0.7(10^{-11})$ cm^{3}s^{-1} at $T = 298$ K from QCT simulations[87] which used the empirical DIM PES for the ^{2}A$'$ ground state[81] and a more recent, MRCI-based fitted PES for the ^{2}A$''$ state.[83]

Given the rather heterogeneous situation for the quality of the existing PESs for studying the N(^4S)+O$_2$($X^3\Sigma_g^-$) reaction and the vibrational relaxation of NO, the present work determines fully dimensional PESs using a consistent methodology to represent the 3 lowest electronic states, ^{2,4}A$'$ and ^{2}A$''$ as well as to evaluate the cross sections for the (forward)

$$\mathrm{N}(^4S) + \mathrm{O}_2(X^3\Sigma_g^-) \to \mathrm{O}(^3P) + \mathrm{NO}(X^2\Pi) \tag{3.1}$$

and (reverse)

$$\mathrm{O}(^3P) + \mathrm{NO}(X^2\Pi) \to \mathrm{N}(^4S) + \mathrm{O}_2(X^3\Sigma_g^-) \tag{3.2}$$

reaction. All three states are energetically accessible in the hypersonic regime, i.e. at temperatures up to 20000 K. Experimentally, cross sections and rates for the forward and reverse reactions have been measured and experimental data for

vibrational relaxation rates are available[69, 73, 74, 86, 88, 89] which serve as benchmarks for the present work.

In the following, the calculation and representation of the asymptotic PESs for the three electronic states and the two channels are described. These are combined to a set of fully-dimensional, reactive PESs which are suitable for quasiclassical trajectory simulations from which cross sections, reaction rates and rates for vibrational relaxation can be determined. The results of the simulations are discussed in the context of the limits of errors in the simulations and comparisons with available experimental data. Finally, the basis of the observables is discussed at an atomistic level, based on analyzing the trajectories.

3.2 Computational Methods

This section presents the generation and representation of the potential energy surfaces and the methodologies for the quasiclassical trajectory (QCT) simulations and their analysis. All PESs are computed at the multi reference CI (MRCI) level of theory together with large basis sets. These are then exactly represented using the reproducing kernel Hilbert space approach. The quality of the representation is then checked using additional MRCI calculated points.

3.2.1 The $^2A'$, $^2A''$ and $^4A'$ Potential Energy Surfaces

Ab initio energy calculations were carried out for the $^2A'$, $^2A''$ and $^4A'$ states. The energies were computed on a grid defined by Jacobi coordinates (r, R, θ) where r is the separation of the diatomic, R is the distance between the atom and the center of mass of the diatomic and θ is the angle between the two unit vectors $\vec{r}$

and $\vec{R}$. For R the grid included 28 points between 1.4 and 12.0 a_0, the distance r was covered by 20 points between 1.5 and 4.0 a_0 and the angular grid contained 13 angles from a Gauss-Legendre quadrature (169.796, 156.577, 143.281, 129.967, 116.647, 103.324, 90.100, 76.676, 63.353, 50.033, 36.719,23.423, 10.204). In order to consistently describe all relevant states and avoid numerical instabilities due to closely-lying states of the same symmetry, state-averaged CASSCF[90–92] calculations including the two lowest states of each symmetry (two spin symmetries and two spatial symmetries) were carried out. Hence, in total eight states are included in the CASSCF reference wave function. A subsequent MRCISD[93, 94] (referred to as MRCI+Q in the following) calculation of the lowest state for each symmetry then computes dynamical electron correlation contributions at a high order level. The augmented Dunning-type correlation consistent polarize triple zeta (aug-cc-pVTZ)[95] basis set is used in this work. All electronic structure calculations are done with the Molpro-2018 [96] software package. For each of the electronic states, *ab initio* energy calculations have been performed for total 7280 points for the NO+O channel and 3920 (including symmetry) points for the OO+N channel, i.e. overall $\sim$ 11000 points which is more than 5 times more reference calculations compared with previous efforts at a similar level of theory. It is to be noted that electronic structure calculations for a fraction of the geometries at large R and/or r converged to excited states. Those points were excluded from the training energy data set.

For certain geometries (< 0.5 %) outside the equilibrium region the CASSCF or MRCI calculations did not converge. In these cases, the missing grid points were reconstructed using a 2-dimensional reproducing kernel (R, r) (RKHS)[97] for each θ. This procedure of discriminating possible outliers was necessary before constructing the full dimensional PES. The 3-dimensional PES for each channel $V(R, r, \theta)$, is constructed using a reciprocal power decay kernel with $n = 2$ and

$m = 6$ for the two radial coordinates and an Taylor spline kernel with $n = 2$ for the angular part.[97] The regularization parameter used was $\lambda = 10^{-18}$.

The global, reactive 3D PES $V(r_1, r_2, r_3)$ for an electronic state is constructed by summing the individual PESs for each channel

$$V(r_1, r_2, r_3) = \sum_{j=1}^{3} w_j(r_j) V_j(R, r_j, \theta), \tag{3.3}$$

using an exponential switching function with weights

$$w_i(r) = \frac{e^{-(r_i/dr_i)^2}}{\sum_{j=1}^{3} e^{-(r_j/dr_j)^2}}. \tag{3.4}$$

Here, dr_i are switching function parameters for the two channels (I) O_2 + N and (II) NO + O. These parameters were optimized by a least square fit to obtain values of (1.25, 1.11, 1.11) a_0, (1.07, 0.87, 0.87) a_0 and (1.40, 1.35, 1.35) a_0 for the $^2A'$, $^4A'$ and $^2A''$ PESs, respectively.

The global, local minima and transition states between the minima and/or entrance channels supported by the PESs were determined using BFGS minimization and the nudged elastic band method[98] as implemented in the atomic simulation environment (ASE).[99]

3.2.2 Quasi-Classical Trajectory Simulations

The QCT simulations used in the present work have been extensively described in the literature[26, 100–102]. Here, Hamilton's equations of motion are solved using a fourth-order Runge-Kutta numerical method. The time step was $\Delta t = 0.05$ fs which guarantees conservation of the total energy and angular momentum.

Initial conditions for the trajectories are sampled using standard Monte Carlo sampling method.[26] The reactant and product ro-vibrational states are determined following semiclassical quantization. Since the ro-vibrational states of the product diatom are continuous numbers, the states are assigned by rounding to integer values. Two schemes were used 1) histogram binning (HB), i.e. rounding values to the nearest integers, or 2) Gaussian binning (GB), which weights each trajectory with a Gaussian shaped function (with a full width at half maximum of 0.1) centered on the integer values.[101, 103, 104] Here, both schemes were tested and found to yield comparable results. Therefore results obtained from GB are reported in the following.

The state-to-state reaction cross section at fixed collision energy E_c is $\sigma_{v,j\to v',j'}(E_\mathrm{c}) = 2\pi \int_0^{b_\mathrm{max}} P_{v,j\to v',j'}(b;E_c) b db$. This integral can be evaluated using Monte Carlo sampling[26] which yields

$$\sigma_{v,j\to v',j'}(E_\mathrm{c}) = \pi b_\mathrm{max}^2 \frac{N_{v',j'}}{N_\mathrm{tot}}, \tag{3.5}$$

where $N_{v',j'}$ is the number of reactive trajectories corresponding to the final state (v',j') of interest, N_tot is the total number of trajectories, $P_{v,j\to v',j'} = N_{v',j'}/N_\mathrm{tot}$ is the probability to observe a particular transition $(v,j) \to (v',j')$, and b_max is the maximum impact parameter for which a reactive collision occurs. Here, b_max is calculated by running batches of trajectories at different intervals of b. In the present work stratified sampling[26, 105] is used to sample the impact parameter $b \in [0 \leq b \leq b_\mathrm{max}]$. The sampling strategy is described in detail in previous work.[102]

The thermal rate for an electronic state (i) at a given temperature (T) is then obtained from

$$k_i(T) = g_i(T)\sqrt{\frac{8k_{\mathrm{B}}T}{\pi\mu}}\pi b_{\max}^2\frac{N_r}{N_{\mathrm{tot}}}, \tag{3.6}$$

where $g_i(T)$ is the electronic degeneracy factor of electronic state 'i', μ is the reduced mass of the collision system, k_{B} is the Boltzmann constant, and, depending on the specific process considered, N_r is the number of reactive or vibrationally relaxed trajectories. In the rate coefficient calculations, the initial ro-vibrational states and relative translational energy (E_{c}) of the reactants for the trajectories are sampled from Boltzmann and Maxwell-Boltzmann distribution at a given T, respectively. The sampling methodology is discussed in detail in Ref. [102].

For the forward reaction ($\mathrm{N}(^4\mathrm{S}) + \mathrm{O}_2(\mathrm{X}^3\Sigma_g^-) \rightarrow \mathrm{O}(^3\mathrm{P}) + \mathrm{NO}(\mathrm{X}^2\Pi)$) the rate $k_+(T)$ is calculated using degeneracies of 1/6 and 1/3 for the $^2\mathrm{A}'$ and $^4\mathrm{A}'$ states, respectively, whereas for the reverse reaction ($\mathrm{O}(^3\mathrm{P}) + \mathrm{NO}(\mathrm{X}^2\Pi) \rightarrow \mathrm{N}(^4\mathrm{S}) + \mathrm{O}_2(\mathrm{X}^3\Sigma_g^-)$) the degeneracies are

$$g_{^2A'}(T) = \frac{2}{(5 + 3\cdot e^{\frac{-227.8}{T}} + e^{\frac{-326.6}{T}})(2 + 2e^{\frac{-177.1}{T}})} \tag{3.7}$$

and

$$g_{^4A'}(T) = \frac{4}{(5 + 3\cdot e^{\frac{-227.8}{T}} + e^{\frac{-326.6}{T}})(2 + 2e^{\frac{-177.1}{T}})} \tag{3.8}$$

The terms in Eqs. 3.7 and 3.8 are the degeneracies of the J or spin states and the exponential parameters 227.8, 326.6 and 177.1 are the energy differences (in units of K) between two neighboring states. The equilibrium constant is then

$$K_{eq}(T) = \frac{k_+(T)}{k_-(T)}. \tag{3.9}$$

3.3 Results

3.3.1 The Potential Energy Surfaces

An overview of the PESs, see Figure 3.1, and Table 3.1, for all three states investigated (^{2}A$'$, ^{4}A$'$, and ^{2}A$''$ from bottom to top) is given as 2-dimensional projections with the two asymptotes (N+OO and O+NO) on the left and right columns in Figure 3.1, respectively. It should be noted that these representations are all for diatomic separations (O_2 and NO, respectively) at values of critical points (see Figures 3.2 to 3.4) and therefore do not exhibit all features of the full 3-dimensional PES.

All PESs for OO+N are symmetric with respect to $\theta = 90°$, as expected. For the ^{2}A$'$ state and the O_2+N dissociation limit the 2d-PES was generated for TS1 in Figure 3.2, i.e. for $R^{(\mathrm{OO})} = 2.33$ a$_0$. The two symmetry related minima are at $R_e^{(\mathrm{NO})} = 3.23$ a$_0$ and $\theta = 34°$ and $\theta = 146°$, respectively. For the NO+O dissociation limit the PES with $R^{(\mathrm{NO})} = 2.26$ a$_0$ (corresponding to MIN3 in Figure 3.2) displays two minima. They are at ($R^{(\mathrm{OO})} = 3.38$ a$_0$, $\theta = 35°$) and ($R^{(\mathrm{OO})} = 3.22$ a$_0$, $\theta = 150°$).

For the ^{4}A$'$ state the surface for the O_2+N dissociation limit has $R^{(\mathrm{OO})} = 2.39$ a$_0$ for TS1 in Figure 3.3 and the 2-dimensional PES in Figure 3.1 has the minimum at $R^{(\mathrm{NO})} = 3.19$ a$_0$ with $\theta = 56°$ and $\theta = 124°$, respectively. Conversely, at the NO+O asymptote, the PES is almost purely repulsive for $R^{(\mathrm{NO})} = 2.36$ a$_0$ (TS2 in Figure 3.3). In Jacobi coordinates, a faint minimum is at ($R^{(\mathrm{OO})} = 3.48$ a$_0$, $\theta = 146°$).

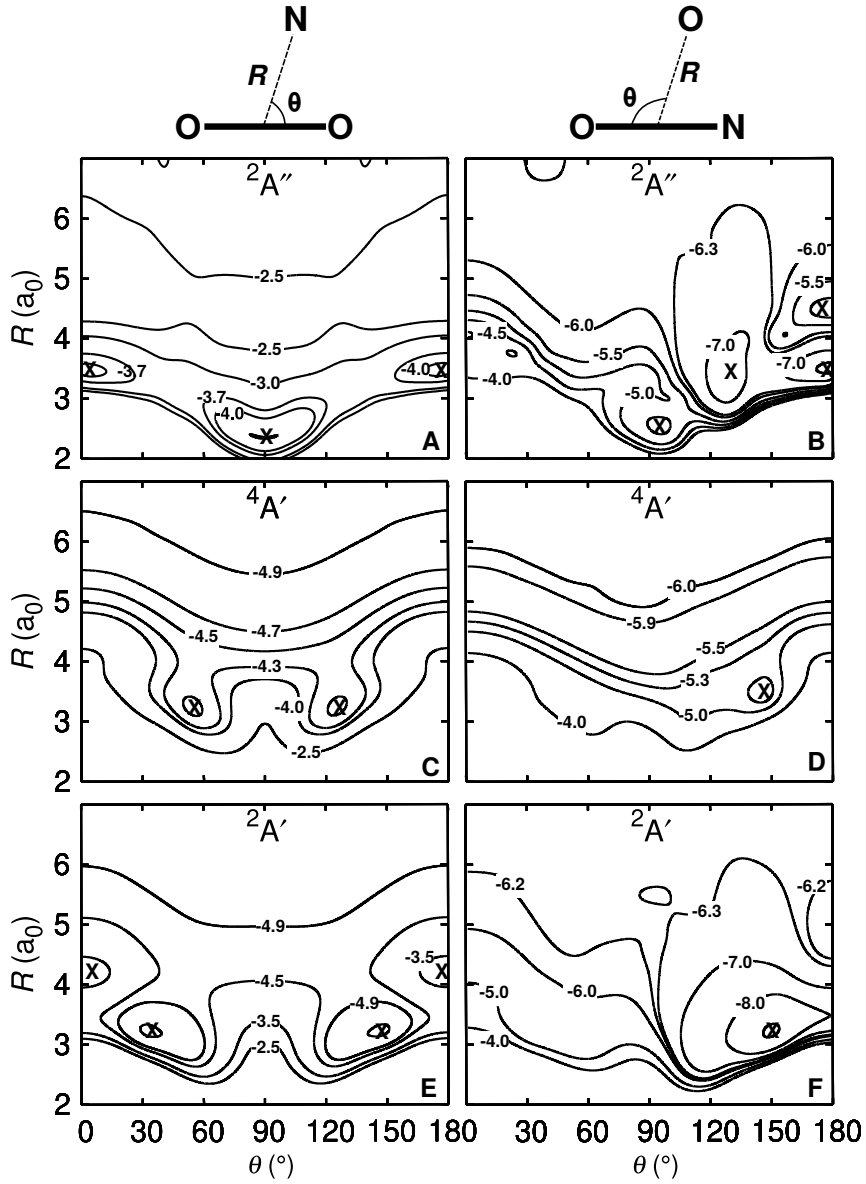

Figure 3.1: Two-dimensional cuts through the 3-d PES for the OO+N (left and the NO+O (right) channels. The OO and NO diatomics are at their equilibrium bond lengths of the respective states, see Figures 3.2 to 3.4. They are $R^{(\mathrm{OO})} = 2.33$ Å, $R^{(\mathrm{OO})} = 2.39$ Å, $R^{(\mathrm{OO})} = 2.30$ Å, and $R^{(\mathrm{NO})} = 2.26$ Å, $R^{(\mathrm{NO})} = 2.36$ Å, $R^{(\mathrm{NO})} = 2.28$ Å for the ^{2}A′, ^{4}A′, and ^{2}A″ states, respectively, from bottom to top. Specific contours with energies in eV are indicated. The zero of energy is for dissociation into atomic fragments O(^{3}P)+O(^{3}P)+N(^{4}S). The symbols indicate the minima discussed in the text and the definition of the coordinates is given on top of the Figure. For the NO+O asymptote the OON geometry corresponds to $\theta = 0$ whereas ONO has $\theta = 180°$.

Finally, for the ^{2}A″ state the 2-dimensional PES is reported for $R^{(\mathrm{OO})} = 2.30$ a$_0$ in the OO+N channel (TS1 in Figure 3.4). It exhibits two minima at ($R^{(\mathrm{NO})} = 2.36$ a$_0$, $\theta = 90°$), and ($R^{(\mathrm{NO})} = 3.55$ a$_0$, $\theta = (0, 180)°$). At the NO+O asymptote

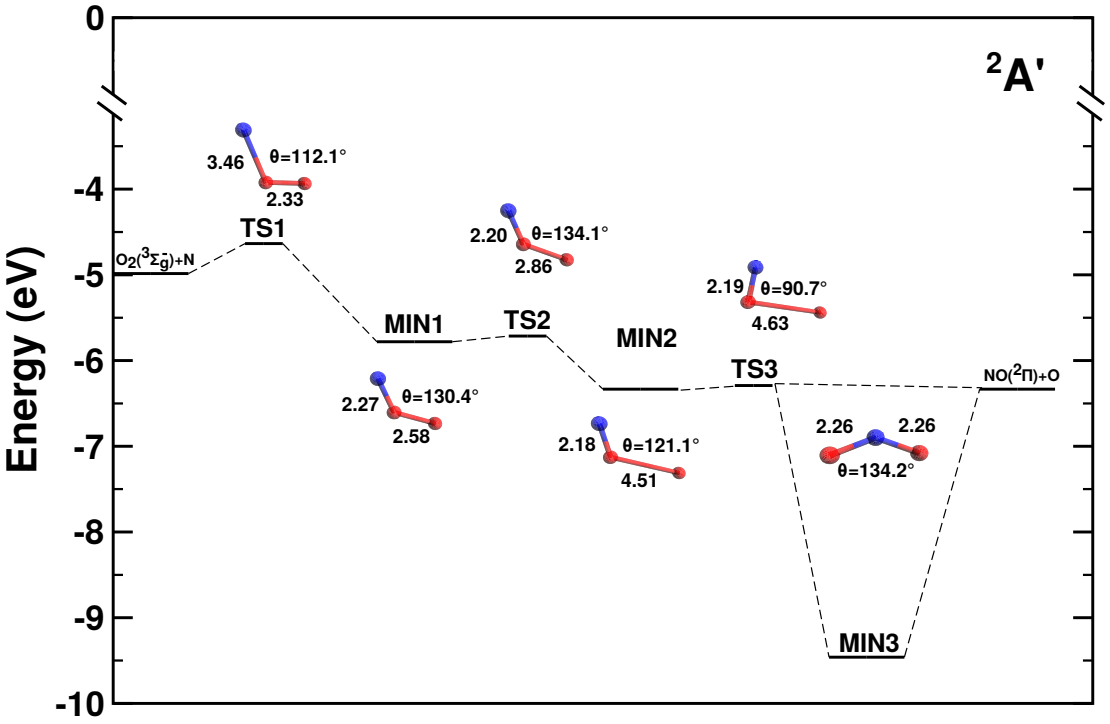

Figure 3.2: The minima (MINi) and transition states (TSi) for the ^{2}A′ state as found from minimization and the nudged elastic band calculations.[98, 106] The geometrical parameters are also given (bond distances in a_0).

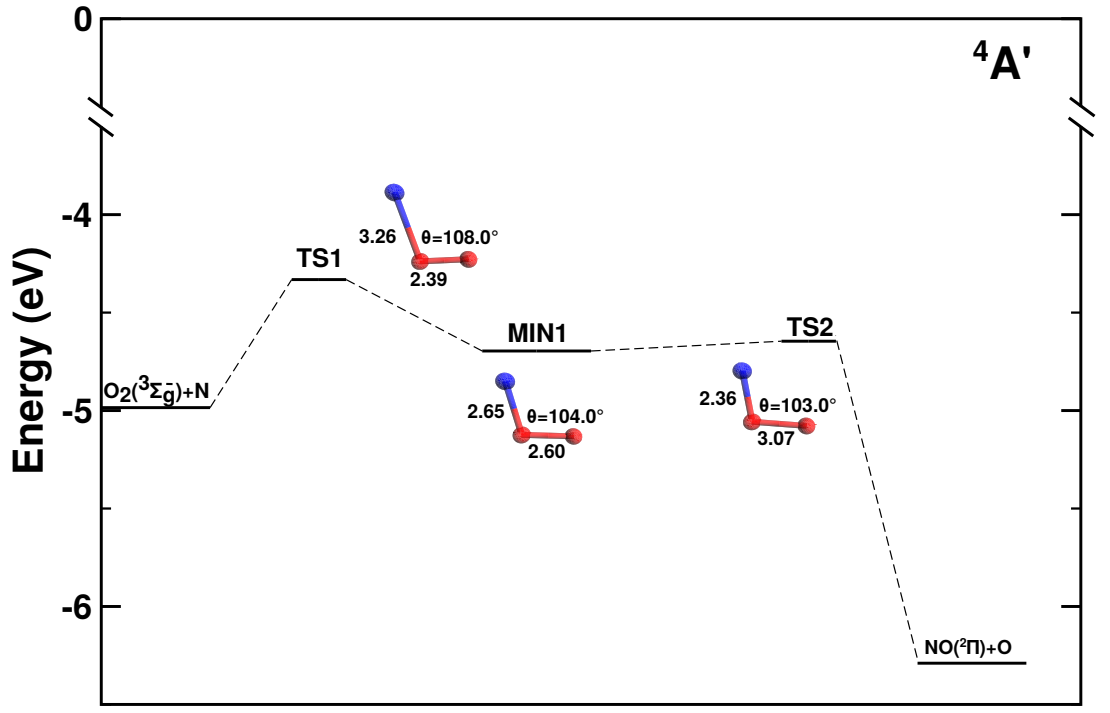

Figure 3.3: The minima (MINi) and transition states (TSi) for the ^{4}A′ state as found from minimization and the nudged elastic band calculations.[] The geometrical parameters are also given (bond distances in a_0).

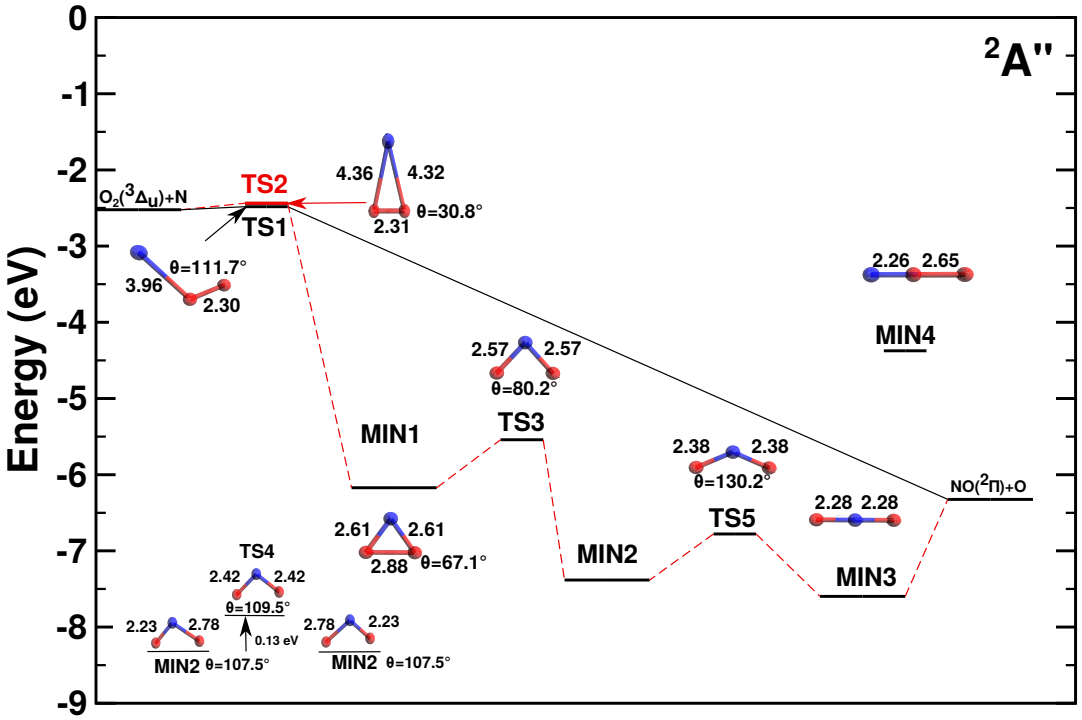

Figure 3.4: The minima (MINi) and transition states (TSi) for the ^{2}A″ state as found from minimization and the nudged elastic band calculations.[98] The geometrical parameters are also given (bond distances in a_0).

the PES has multiple minima, see Figure 3.1. For $R^{(NO)} = 2.28$ a_0 they are at ($R^{(OO)} = 3.69$ a_0, $\theta = 0°$), ($R^{(OO)} = 2.53$ a_0, $\theta = 95°$), ($R^{(OO)} = 3.28$ a_0, $\theta = 128°$), and ($R^{(OO)} = 3.50$ a_0, $\theta = 180°$).

All minima and transition states together with their connectivities on the 3d PES are given in Figures 3.2 to 3.4. Several paths which include a number of minima and transition states can be found on the ^{2}A′ and ^{2}A″ PESs for the forward and reverse reaction while both reactions follow rather simple paths on the ^{4}A′ PES. It is worthwhile to note that there are no crossings between the ^{2}A′ and ^{2}A″ PESs as well as between ^{2}A′ and ^{4}A′ electronic states which differs from, e.g., the [CNO]-system.[102]

^{2}A′	$R_e^{(NO)}$	R_e^{OO}	<NOO	ΔE_1	ΔE_2	ΔE_2[79]
MIN1	2.27	2.58	130.4	–5.78	–18.34	–28.50
TS1	3.46	2.33	112.1	–4.64	8.07	6.87
TS2	2.20	2.86	134.1	–5.71	–16.82	–27.42
TS3	2.19	4.63	90.7	–6.29	–30.12	–34.26
MIN2	2.18	4.51	121.1	–6.33	–31.10	–37.64
MIN3	2.26	4.17	22.9	–9.46	–103.20	–108.68
^{4}A′						ΔE_2[79]
MIN1	2.65	2.60	104.0	–4.69	6.67	5.43
TS1	3.26	2.39	108.0	–4.33	15.01	12.74
TS2	2.36	3.07	103.0	–4.68	8.75	7.81
^{2}A″						ΔE_2[83]
MIN2	2.23	4.06	107.5^a	–7.37	–111.79	–113.95
TS1	3.96	2.30	111.7	–2.48	0.93	0.63
TS2	4.35	2.31	30.8^a	–2.44	1.95	2.07
TS3	2.57	4.35	80.2^a	–5.54	-69.61	–77.81
TS4	2.42	3.99	109.4^a	–7.22	–108.34	–113.14
TS5	2.39	4.31	130.2^a	–6.78	18.60^b	32.25^b
MIN1	2.61	2.88	67.1^a	–6.16	–83.93	–85.59
MIN3	2.28	4.56	180.0^a	–7.58	–29.06^c	–38.41^c

Table 3.1: Minima (MINi) and transition states (TSi) were calculated using the Nudged Elastic Band (NEB)[98, 106] method. Equilibrium distances in a_0, angle in degree for ∠(NOO) and ^{a}∠(ONO), and energies ΔE_1 (in eV) with respect to the N+O+O asymptote and ΔE_2 (in kcal/mol) relative to the N + O_2 limit, except for ^{b}(with respect to the global minimum), and ^{c}(relative to the O+NO limit) to compare with the literature. For the energy level diagram and the connectivities, see Figures 3.2 to 3.4.

One-dimensional cuts along the O_2+N and NO+O coordinates for constant angle θ for the three different electronic states are reported in Figure 3.5. All angular cuts correspond to off-grid points, i.e. data not explicitly used in generating the RKHS. Therefore, the RKHS energies (solid lines) are predictions and are found to compare well with the true energies calculated at the MRCI+Q/aug-cc-pVTZ level of theory. Nevertheless, for a few points on the $\theta = 175.0°$ cut around $R \sim 4$ a_0 for the ^{2}A′ state (see Figure 3.5A) the RKHS-predicted energies differ slightly from the true energies.

The quality of all three PESs for both, on- and off-grid points is reported in Figure 3.6 as correlation plots. The correlation between the reference (*ab initio*

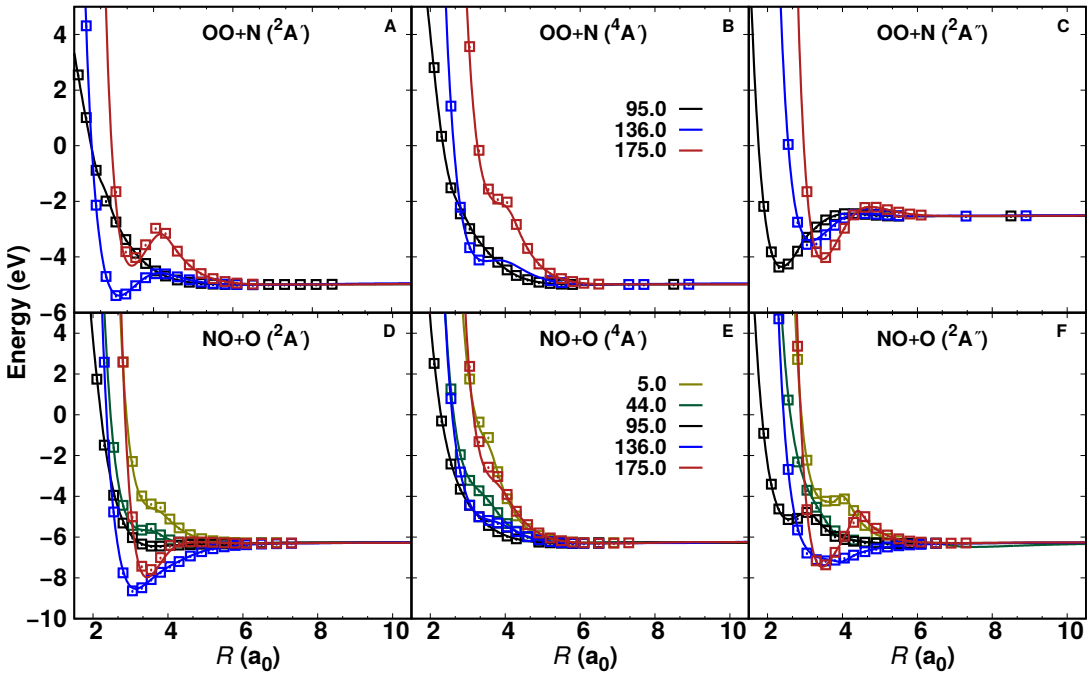

Figure 3.5: Quality of the RKHS representation of the 3d PESs at off-grid points. The MRCI+Q/aug-cc-pVTZ reference energies (open symbols) and the RKHS interpolated energies (lines) for the ^{2}A′, ^{4}A′ and ^{2}A″ for the OO+N (top, $r^{(\mathrm{OO})} = 2.30$ a$_0$) and NO+O (bottom, $r^{(\mathrm{NO})} = 2.19$ a$_0$) channels are reported.

energies) and RKHS energies ranges from $R^2 = 0.9996$ to 0.9999 for grid points and from $R^2 = 0.9992$ to 0.9997 for off-grid points for the three electronic states. The corresponding root mean squared errors for the on-grid points range from 0.022 to 0.043 eV and off-grid points from 0.033 to 0.057 eV. It should be noted that all the RKHS energies are evaluated on the mixed, fully reactive PES, see Eq. 4.1. The agreement between reference and RKHS energies is even better if the channels are considered separately.

To rationalize the observed topology of the NO+O channel of the MRCI+Q PES (Figure 3.1 panels B, D, and F), the orbital diagram of the natural orbitals as obtained from the CASSCF calculations are analyzed. Figure 3.7 shows the evolution of the natural orbitals and the energies for $R = 3.4$ a$_0$ and $r_{\mathrm{NO}} = 2.183$ a$_0$ (equilibrium NO separation) with varying values of θ. Only natural orbitals with significant change in occupation number are shown along the path. Figure

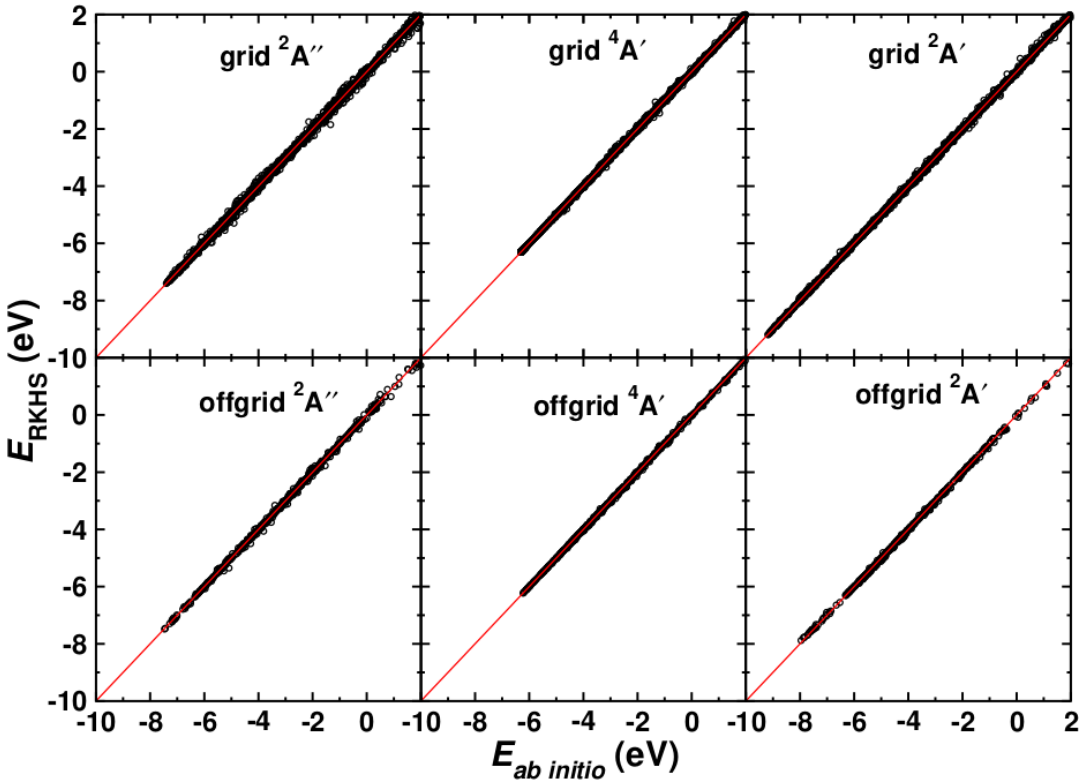

Figure 3.6: Correlation between MRCI/aug-cc-PVTZ ($E_{abinitio}$) and RKHS energies up to a values of 2 eV for 7435 (^{2}A′), 6869 (^{4}A′) and 7275 (^{2}A″) grid points and 537, 533 and 596 offgrid points for the ^{2}A′, ^{4}A′ and ^{2}A″ surfaces, respectively. The zero of energy is the O+O+N dissociation limit. The R^2 value for the grid points are (0.99984, 0.99989, 0.99965) and for off-grid points (0.99959, 0.99966, 0.99922) for the (^{2}A′, ^{4}A′, ^{2}A″) surfaces, respectively. The corresponding root mean squared errors (RMSE) for the ^{2}A′, ^{4}A′ and ^{2}A″ surfaces are (0.65, 0.49, 0.99) kcal/mol (0.028, 0.022, 0.043) eV for the grid points and (0.86, 0.76, 1.31) kcal/mol (0.038, 0.033, 0.057) eV for offgrid points.

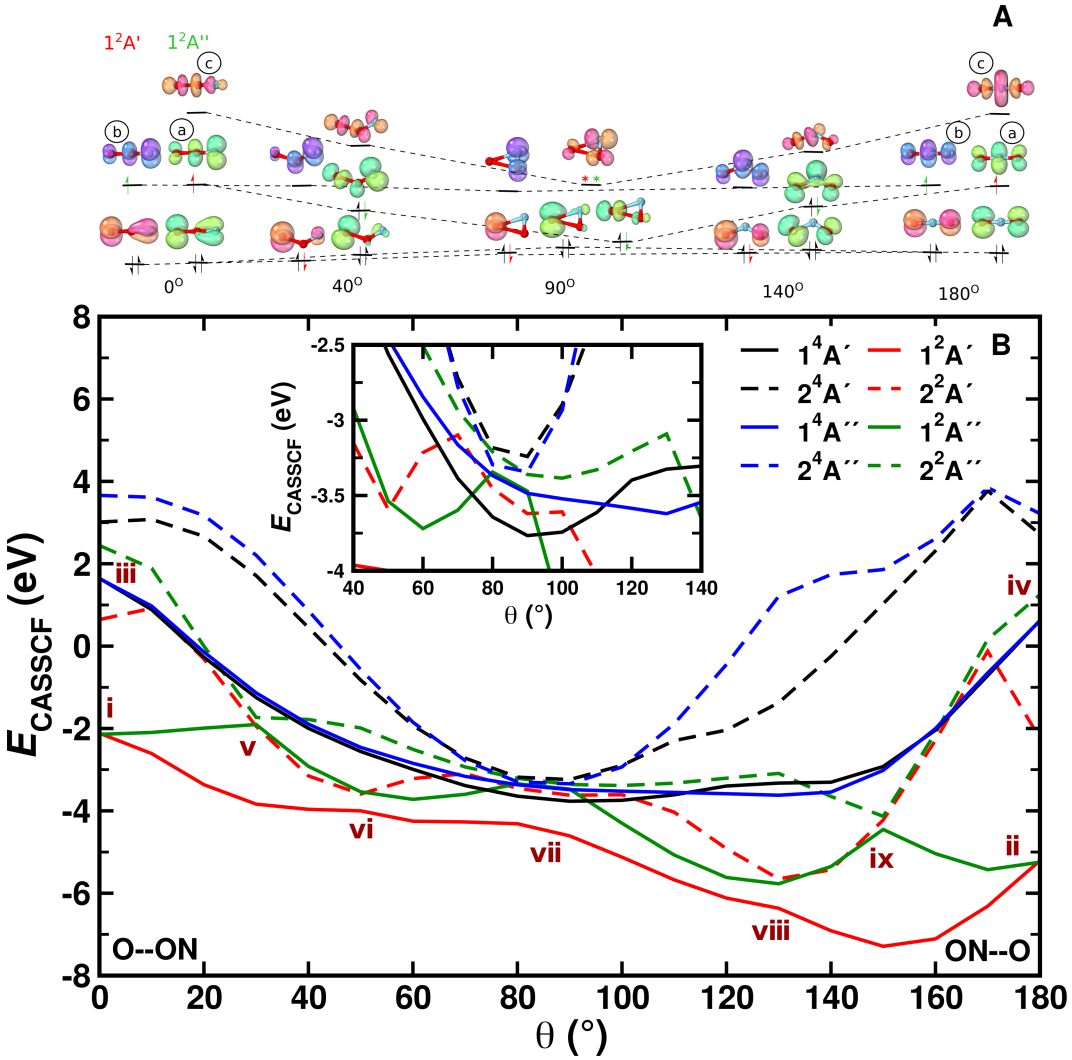

Figure 3.7: Panel A: MO diagram of NO_2 for the doublet ground state for varying values of θ. The dominant configurations at selected angles are shown for the lowest $^2A'$ and $^2A''$ states (in black occupations occurring for both states, state-specific orbital occupations are colour-coded). An asterisk indicates significant (additional) occupation of an orbital due to strong electron correlation. Details for each of the states are provided in Figure 3.8 Panel B: Energies in eV relative to separated atoms. The inset shows details of the states around the T-shaped geometry. Features i through ix are discussed in the text.

3.9 shows a complete MO diagram of the valence space. The dominant configurations for the lowest $^2A'$ and $^2A''$ states are indicated in the MO diagrams, and an illustration of all main configurations along the path is given in Figure 3.8. The cut qualitatively includes most of the stationary states of the 2-dimensional PESs of the NO+O channel (see Figures 3.1 and 3.6). For the linear structures (Figure 3.7A) two perpendicular π_3-systems arise with one electron in an anti-

bonding π_3* orbital. The bonding orbital of the π-system shows a more equal contribution from all three atomic centers for the linear ONO structure than for the linear OON structure, making the bonding situation more stable in this case (see Figure 3.9). Bending of the linear structures leads to a transformation of the in-plane antibonding orbitals of the π-system ("a" in Figure 3.7A) into a non-bonding p-orbital on the oxygen at $\theta = 90°$. The two non-bonding orbitals of the linear π-systems transform also into $p-$orbitals on the oxygen. Hence, at $\theta = 90°$ three natural orbitals close in energy with mostly $p-$orbital contribution on the oxygen atom arise. Their energy fine-ordering depends on the amount of residual antibonding character they bear. The out-of-plane antibonding orbital of the linear $\pi-$systems ("b" in Figure 3.7A) however transform into an antibonding π^* NO-orbital upon bending. Finally, the antibonding orbital with dominant σ^*-character for the linear structures ("c" in Figure 3.7A) also transforms into an antibonding π^* NO-orbital at 90°, considerably lowering its orbital energy. The fine-ordering of the two π^* NO-orbitals again depends upon their remaining additional antibonding character. Thus, for a T-shaped structure ($\theta = 90°$) the quasi-degeneracies lead to a large number of configurations with similar energy and lead to small energy differences for the eight states included in the CASSCF wavefunction (see Figure 3.7B).

Two additional interesting observations on the NO+O channel can be made from the MO diagram: 1) No stable covalent bonding between the oxygen and the N-O fragment in the T-shaped structure is observed at the CASSCF level of theory. This explains the almost fully repulsive character of the NO+O channel along R for θ close to 90° (cf. Figure 3.5). 2) Upon bending, the in-plane π_3* orbital ("a" in Figure 3.7A) significantly lowers its energy. As the π_3* orbitals are partially occupied for the linear structures, bending makes lower energy configurations accessible, yielding minima on the PESs of the NO+O channel for slightly bent

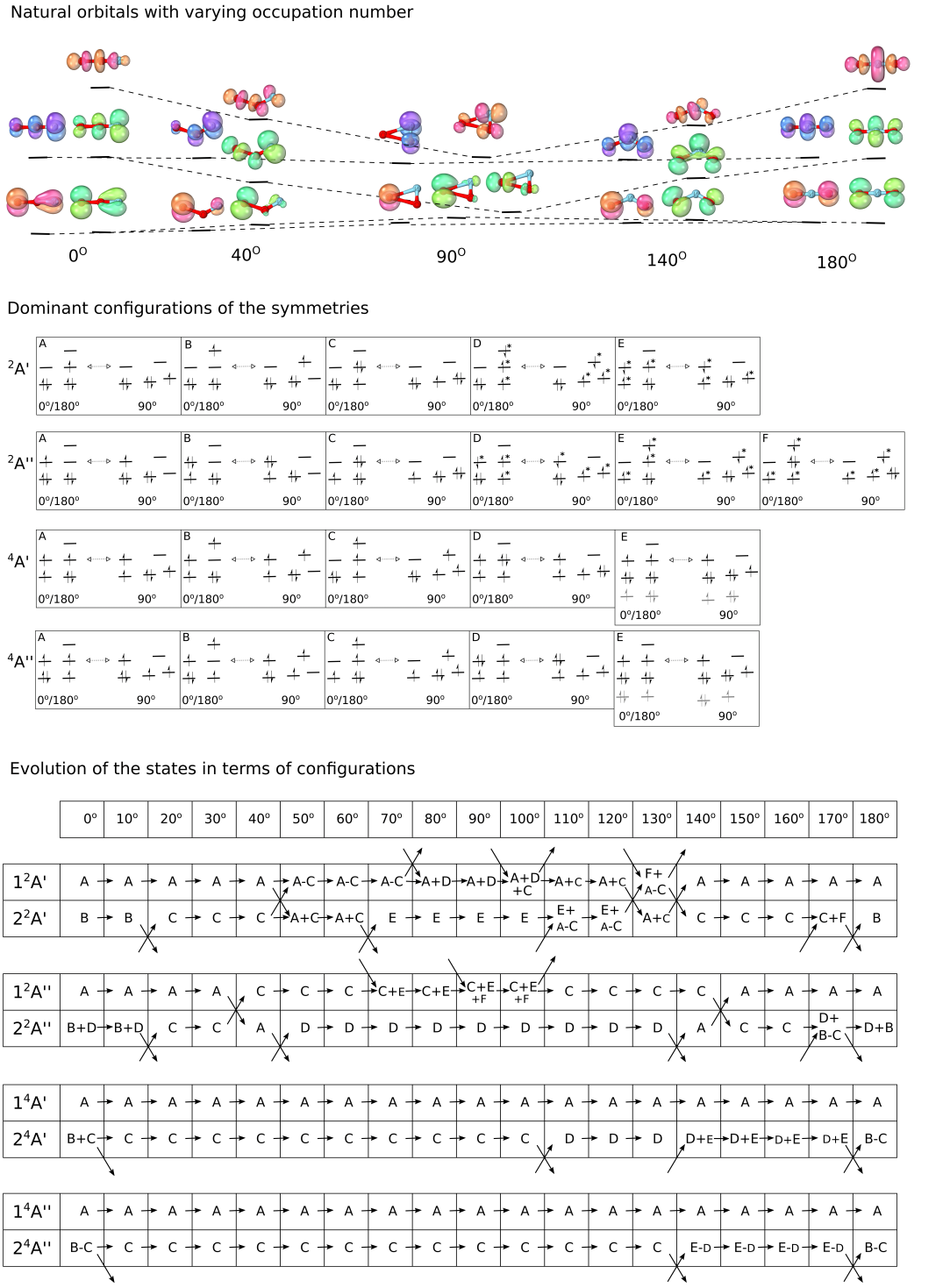

Figure 3.8: MO diagram of the NO +O channel at fixed values of R and r together with details of the orbital occupancies. This Figure complements Figure 3 in the main text. The most important configurations with >10% contribution to the CASSCF wave function for each state are given in the middle panel of the figure.

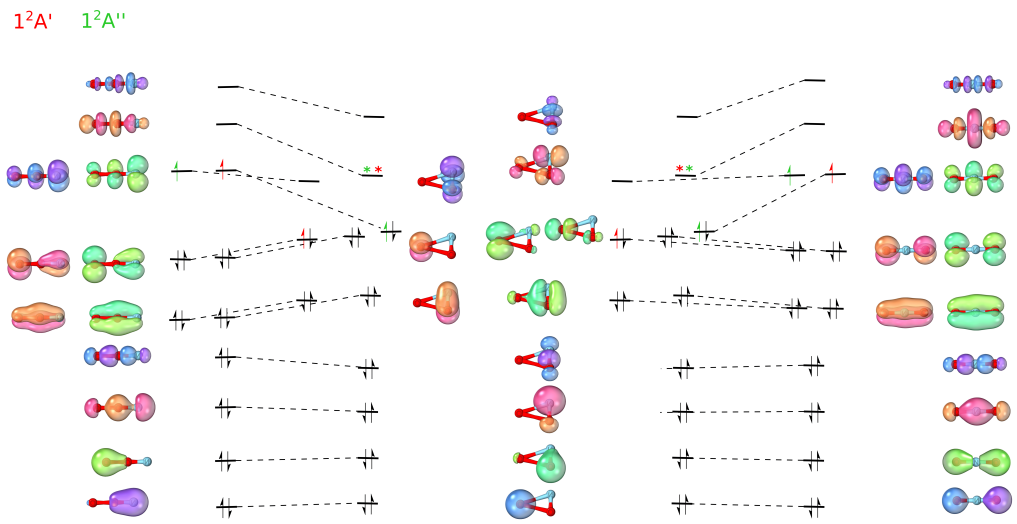

Figure 3.9: MO diagram of NO_2 for the doublet ground state for the two linear configurations (left OON, right ONO) and for $\theta = 90$ (middle). The full valence orbital basis is shown. The dominant configurations at selected angles are depicted for the lowest $^2A'$ and $^2A''$ states. Black arrows for occupancies in both states, red for $^2A'$ and green for $^2A''$. Asterisks for significant additional occupancies due to strong correlation.

structures (cf. Figure 3.1).

The CASSCF energies for the eight states along the bending coordinate are shown in Figure 3.7B. In the following significant features (i to ix) of the PESs are discussed. For the linear structures (OON ($\theta = 0$) and ONO ($\theta = 180°$)) the orbital degeneracy leads to $^{2,4}A'$ and $^{2,4}A''$ lowest states of equal energy (see points i to iv in Figure 3.7B). Bending away from the linear geometry leads to an approach and avoided crossing of the $1^2A''$ and $2^2A''$ states ($\theta = 30°$, point v), each of which is described by one dominant configuration outside the crossing region. A similar observation is made for the $1^2A'$ and $2^2A'$ states ($\theta = 50°$, point vi). The $1^2A'$ state has a strong multi-reference character with various configurations contributing in an extended region $50° \leq \theta \leq 100°$. As indicated in Figure 3.7A, the quasi degeneracies in the T-shaped structures gives rise to a large number of configurations with similar energies and to seven states within 0.9 eV for $\theta = 90°$ (point vii). The characteristics of points vii and ix can be described along the

same lines as for points vi and v, respectively. The full and detailed analysis of changes in configurations of the states along the path is given in Figure 3.8. It is noted that the two lowest ^{4}A states do not show an avoided crossing and have each one dominant configuration along θ. This explains the rather simple topology of the 1^4A' PES in Figure 3.1. The inset in Figure 3.7 amplifies the subtle changes in state order around $\theta = 90°$. Various additional avoided crossings can be observed (their analysis is given in Figure 3.8.)

3.3.2 Thermal Rates and Reaction Cross Sections

Thermal rates for the forward ($N(^4S) + O_2(X^3\Sigma_g^-) \rightarrow O(^3P) + NO(X^2\Pi)$) and reverse ($O(^3P) + NO(X^2\Pi) \rightarrow N(^4S) + O_2(X^3\Sigma_g^-)$) reaction are determined between 300 and 20000 K. A total of 50000 trajectories was calculated at each temperature for each reaction on each electronic states. The individual contributions of the ^{2}A$'$ and ^{4}A$'$ states are reported in Figure 3.10 panels A and B. The forward rates are about one order of magnitude higher than the reverse rates for both electronic states.

Parameter	^{2}A$'$	Lit.[75]	^{4}A$'$	Lit.[75]	Total	Lit.[68]	Lit.[79]
Forward							
n	0.83	0.63	0.56	0.97	1.18	1.18	1.60
A [10^{-14} cm^3/s]	3.58	34.0	117.2	2.31	0.370	0.414	0.014
B[K]	4105	4043	8722	7459	4090	4005	2894
Reverse							
n	0.74	–	0.64	–	0.40	–	1.51
A [10^{-14} cm^3/s]	1.77	–	12.1	–	190.3	–	0.01
B[K]	19653	–	23505	–	24520	–	19115

Table 3.2: Arrhenius 3-parameter model (Eq. 3.10) for $600 \leq T \leq 20000$ K for the forward ($N(^4S) + O_2(X^3\Sigma_g^-) \rightarrow O(^3P) + NO(X^2\Pi)$) and reverse ($O(^3P) + NO(X^2\Pi) \rightarrow N(^4S) + O_2(X^3\Sigma_g^-)$) reaction. A in units of 10^{-14} cm^3/(s molecule).

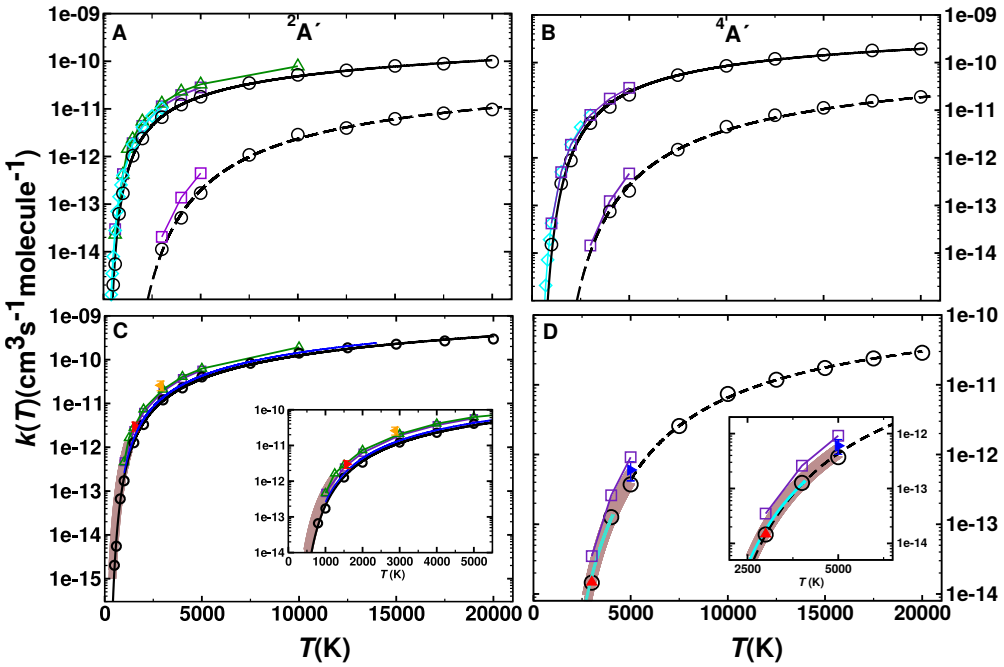

Figure 3.10: (Top) Forward and reverse rate coefficients for the $^2A'$ (panel A) and $^4A'$ (panel B) states. Rates for the forward ($N(^4S) + O_2(X^3\Sigma_g^-) \rightarrow O(^3P) + NO(X^2\Pi)$, open circles and solid black line) and reverse ($O(^3P) + NO(X^2\Pi) \rightarrow N(^4S) + O_2(X^3\Sigma_g^-)$ open circles and dashed lines) reaction are given separately. Results from previous computations based on VTST (green open triangle)[75], ICVT (violet open square)[79] and quantum treatments (cyan open diamond)[107] are also shown for comparison. (Bottom) Total rates $k(T)$ for the forward ($N(^4S) + O_2(X^3\Sigma_g^-) \rightarrow O(^3P) + NO(X^2\Pi)$, panel C) and reverse ($O(^3P) + NO(X^2\Pi) \rightarrow N(^4S) + O_2(X^3\Sigma_g^-)$, panel D) reaction. The black open circles are the data from GB and the fit to a 3-parameter Arrhenius model is the solid black line. The fitting parameters are reported in Table 3.2. Results from VTST (green open triangle up)[75], ICVT (violet open square)[79], quantum (cyan open diamond)[107] and evaluation (blue solid line)[68]. Experimental values are also reported in Panel C ((red solid right triangle)[108], (orange solid left triangle)[109]) and Panel D ((blue solid right triangle)[110], (red solid triangle up)[111], (blue cyan line)[112]) together with fits to experiment with errors (brown shaded areas in panels C[113] and D[114]).

Figures 3.10 C and D show the total rate $k(T)$ for the forward and reverse reaction. The total rate is calculated by summing the contributions from ^{2}A$'$ and ^{4}A$'$ surfaces. For practical applications, such as discrete sampling Monte Carlo (DSMC) simulations,[115] it is also useful to fit the data to an empirical, modified Arrhenius relationship

$$k(T) = A \cdot T^n \cdot e^{(-\frac{B}{T})} \tag{3.10}$$

The fitted parameters are given in Table 3.2. Additional fits for N+O_2 on the ^{4}A$'$ state yield[75] $A = 1.41\ 10^{-14}$ cm^3/(s molecule), $n = 1.04$, $B = 6112$ K based on VTST data.[79] Fitting of earlier QCT data[68] yields remarkably similar values to the present results, see Table 3.2 and blue trace in Figure 3.10C, which, however, differ both substantially from a more recent study.[79] Experimental rates at higher temperatures are rare. One study was carried out at 1575 K[108] which is in quite good agreement within typical[114] uncertainties of 25 % with the present simulations (Figure 3.10C) whereas the rate from an experiment at higher temperature (2880 K)[109] is larger than the rate from the present and earlier[68] simulations by about a factor of two. One possible explanation is that for experiments above $T \sim 2000$ K there is interference between the O+N_2 and N+O_2 reactions and the analysis required a reaction network both of which introduce uncertainties in the rate.[109] For the reverse rate the present simulations accurately describe those measured experimentally.[110, 111, 114]

The reverse rate (O+NO) in Ref.[75] was not determined from QCT simulations but rather by first computing the equilibrium constant $K_{\mathrm{eq}}(T)$ according to statistical mechanics and then using $k_-(T) = k_+(T)/K_{\mathrm{eq}}(T)$. The Arrhenius values from Ref.[75] are $A = 0.114\ 10^{-14}$ cm^3/(s molecule), $n = 1.13$, and $B = 19200$ K. To the best of our knowledge the present work determined $k_-(T)$ for the first

time from QCT simulations.

In addition, the equilibrium constant $K_{eq}(T)$ as defined in Eq. 4.5 is also calculated (see Figure 3.11) as it can be compared directly with experimental work. For $K_{\mathrm{eq}}(T)$ the present calculations agree favourably with the JANAF and CEA values over the entire temperature range, as can be expected since K_{eq} is also determined from the difference in Gibbs free energy between the initial and final states.

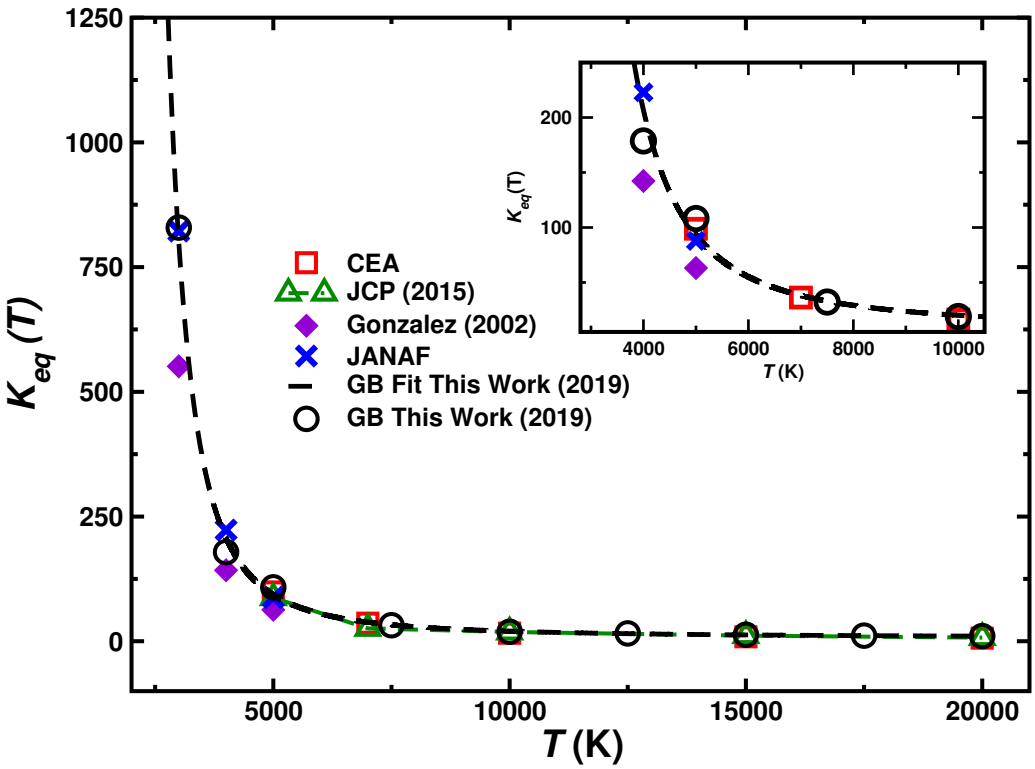

Figure 3.11: Equilibrium constant $K_{eq}(T)$. QCT results calculated in this work (circles), fit to a modified Arrhenius model (solid lines) for temperatures between 1000 and 20000 K. Previous QCT[116], JANAF tables [89] and Chemical Equilibrium with Application (CEA) results [88] are also included for comparison. The inset shows an enlarged view for lower temperatures.

To determine the cross sections depending on the final vibrational state v', additional simulations were carried out. For this 2×10^5 independent trajectories on each of the three electronic states were run starting from the $N+O_2$ asymp-

tote with a distribution of O_2 internal (v, j) states at 1000 K to follow $N(^4S)$ + $O_2(X^3\Sigma_g^-) \rightarrow O(^3P)$+ $NO(X^2\Pi)(\nu', j)$. Then, total reaction cross sections for the individual final vibrational states (ν', j) were determined. The cross section as a function of the vibrational level (ν') is reported in Table 3.3 and compared with previous experimental[73] and theoretical[75] work. Of particular interest is the dependence of σ on the final vibrational state ν' of NO because experimentally, an oscillating total cross section had been found with minima at $\nu' = 3$ and $\nu' = 5$.[73] However, earlier experiments[117, 118] report the rate constant for formation of NO for the N + $O_2 \rightarrow$ NO + O reaction for vibrational levels $\nu = 2 - 7$. Using Eq. 3.6 these rates converted into cross sections which are monotonically decreasing with ν except for $\nu = 2$.[117] Rates for $\nu = 0$ and $\nu = 1$ were reported to be larger compared to $\nu \geq 2$.[117] A comprehensive comparison of the present results for the cross sections is given in Table 3.3.

State ν'	Exp.[119]	Exp.[117]	$^2A'$	$^4A'$	Total	Lit.[76]	Lit.[77]	Lit.[75]
0	–	–	0.17	0.67	0.84	—	0.28	0.50
1	0.49	–	0.16	0.48	0.64	0.37	0.41	0.53
2	0.65	0.37	0.14	0.31	0.45	0.42	0.46	0.48
3	0.20	0.39	0.14	0.22	0.36	0.39	0.44	0.43
4	0.69	0.22	0.12	0.16	0.28	0.36	0.37	0.32
5	0.37	0.16	0.10	0.10	0.20	0.31	0.32	0.26
6	0.20	0.04	0.09	0.07	0.16	0.27	0.28	0.20
7	0.25	0.03	0.07	0.05	0.12	0.23	0.24	0.18

Table 3.3: Individual and total cross sections (in $Å^2$) for the N + $O_2(\nu) \rightarrow NO(\nu')$ + O process as a function of the final vibrational state (ν') from Gaussian binning. The total cross sections are also compared with experimental results (Exp.)[119] and rates for NO formation (Exp.)[117] converted to cross sections according to Eq. 3.6. Additionally, comparison with other computational work (Lit.).[75–77] is also provided.

No oscillating behaviour of the cross section was found from the present simulations, see Figure 3.12. This finding agrees with previous simulations[75] based on a DIM PES for the $^2A'$ state[81] and a fitted MBE to CASPT2 calculations for the $^4A'$ state.[79] The present calculations find a decaying cross section with

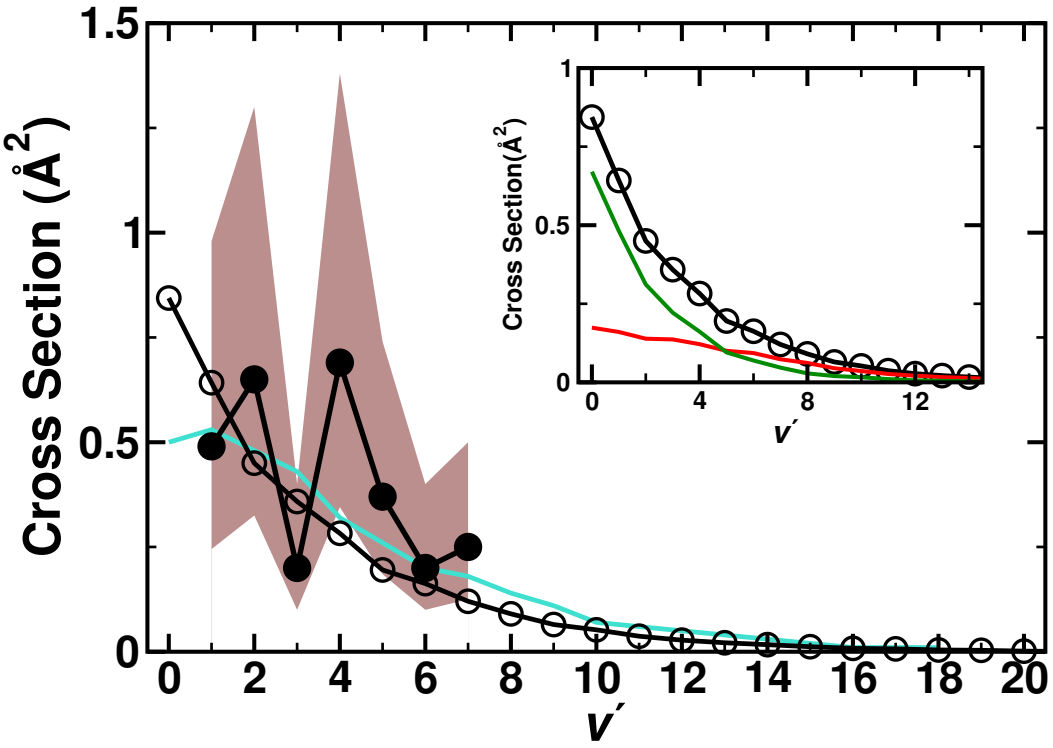

Figure 3.12: Vibrational state-dependent, total cross sections (in Å^2) for the N + $O_2(\nu) \rightarrow NO(\nu')$ + O process as a function of the final ν'. Total contribution (^{2}A′ + ^{4}A′) (open circles and black line) compared with previous computations (turquoise line)[75] and experiment (black solid circles)[73] with error region (brown shaded area) results. The inset reports the individual contributions from the present work for the ^{2}A′ (red) and ^{4}A′ (green), together with the total cross section.

higher vibrational state. The individual contributions of the (^{2}A′) and (^{4}A′) state are calculated in addition to the total cross sections. The previous computational work[75] also used the contribution of both the ^{2}A′ and ^{4}A′ states and found a small population inversion peaking at $\nu' = 1$. But overall, the findings from both simulation studies are consistent and suggest that the experimental findings[73] should be reconsidered.

3.3.3 Vibrational relaxation

As a third observable reactive (Oxygen exchange) and non-reactive vibrational relaxation of O + $NO(\nu = 1) \rightarrow$ O + $NO(\nu = 0)$ was studied on the RKHS PESs for all three electronic states as a function of temperature. An early experiment[69]

determined the rate for NO($\nu = 1$) vibrational relaxation by O atoms at room temperature. The vibrationally excited NO and relaxer O atoms were formed using 355 nm laser photolysis of a dilute mixture of NO_2 in an argon bath gas. The reported total rate was $k_{\nu=1\to0} = 2.4 \pm 0.5\ 10^{-11}$ cm^{3}s^{-1} at $T = 298$ K. It was argued that this value is 2 to 3 times lower than the generally accepted value of K used in atmospheric modeling.[120, 121] Subsequent QCT simulations[85] on the ^{2}A$'$ and ^{2}A$''$ states, find a value of $k_{\nu=1\to0}(T = 298\text{K}) = 2.124 \pm 0.73(10^{-11})$ cm^{3}s^{-1}. It should be noted that the PESs for these two states are based on different approaches. For the ^{2}A$'$ PES it is based on a DIM ansatz[81] whereas the ^{2}A$''$ PES is a MBE fit to CASPT2 calculations.[80] Even earlier calculations using the ^{2}A$'$ PES obtained a somewhat smaller rate of $k_{\nu=1\to0}(T = 298\text{K}) = 1.7(10^{-11})$ cm^{3}s^{-1}.[122]

A more recent experiment[86] used a continuous wave microwave source to generate oxygen atoms, combined with photolysis of trace amounts of added NO_2 to produce vibrationally excited NO. The rate for vibrational relaxation is $k_{\nu=1\to0}(T = 295\text{K}) = 4.2 \pm 0.7(10^{-11})$ cm^{3}s^{-1} which is an increase by 75 % compared with the earlier results.[69] Later QCT simulations[87] based on the DIM PES for the ^{2}A$'$ state[81] and a fitted DMBE PES based on 1681 MRCI/AVQZ calculations for the ^{2}A$''$ state[83] report a value of $k_{\nu=1\to0}(T = 298\text{K}) = 4.34 \pm 0.7(10^{-11})$ cm^{3}s^{-1}. Another computational study[123] reported a value of $k_{\nu=1\to0}(T = 300\text{K}) \sim 5(10^{-11})$ cm^{3}s^{-1}.

As to compare with the more recent experiments[86] the individual contributions of the ^{2}A$'$, ^{4}A$'$, and ^{2}A$''$ states towards vibrational relaxation of O + NO($\nu = 1$) $\rightarrow$ O + NO($\nu = 0$) were determined here. Additionally, the total rate is compared with previous theoretical[85, 87] and experimental[69, 86] results, see Figure 3.13.

In particular for low temperature the agreement with the more recent[86] experiments and the only high-temperature experiment (at 2700 K)[124] is noteworthy. The results from the simulations based on high-level, 2-dimensional PESs[82] for the ^{2}A′ and ^{2}A″ states are also in good agreement with the experiments and the present simulations.

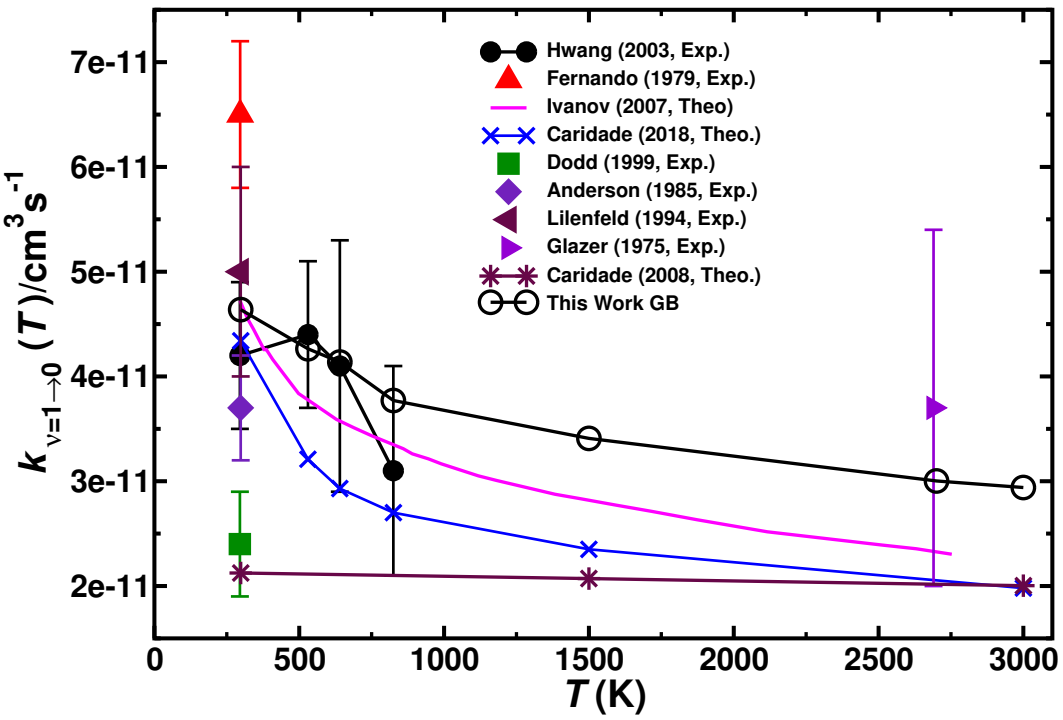

Figure 3.13: Total vibrational relaxation rate for O+NO($\nu = 1$) → O+NO($\nu = 0$). Present data from Gaussian binning are open black circles and literature values are the symbols indicated.[69, 82, 85–87, 120, 124–126]

	298 K	530 K	640 K	825 K	1500 K	2700 K	3000 K
^{2}A″	2.21	1.98	1.82	1.63	1.42	1.13	1.16
^{4}A′	0.00	0.00	0.00	0.00	0.01	0.08	0.12
^{2}A′	2.43	2.28	2.32	2.15	1.98	1.80	1.66
Total	4.64	4.26	4.14	3.77	3.41	3.00	2.94
Exp.[86]	4.2 ± 0.7	4.4 ± 0.7	4.1 ± 1.2	3.1 ± 1.0	–	–	–

Table 3.4: Electronic state-dependent vibrational relaxation rates (in units of 10^{11})$k_{\nu\to\nu'}$: O+NO($\nu = 1$) → O+NO($\nu' = 0$) for the ^{2}A′, ^{4}A′ and ^{2}A″ states and the total contribution using GB.

As can be seen in Table 3.4, trajectories run on the ^{2}A′ state contribute most to the vibrationally relaxing (VR) rates. Hence, to explore whether and how the

process of vibrational relaxation (O+NO($\nu = 1$) $\rightarrow$ O+NO($\nu' = 0$)) and sampling of the underlying PES are related, another 25000 independent trajectories were run for the ^{2}A$'$ state at 530 K. Out of those, 5722 relaxed to $\nu' = 0$ whereas for 13311 trajectories either the internal state of NO was changed to ($\nu' \neq 0, j'$) or O_2 was produced. For the remaining 5967 (nonreactive) trajectories the initial ro-vibrational state is not changed. All the trajectories were saved and rigorous analysis have been carried out to investigate the relaxation process.

The probability distributions of different O+NO configurations for different types of trajectories have been computed in (R, θ) space. Structures are included in the computation only if any of the NO bond is within 2.03 to 2.39 a_0 (the turning points for the $\nu = 1$ state of NO are $r_{\min} = 2.046$ a_0 and $r_{\max} = 2.370$ a_0). Gaussian binning with bin size $\Delta R = 0.1$ a_0 and $\Delta\theta = 3^\circ$ was used and contributions from 2.03 $a_0 < r_{\rm NO} < 2.39$ a_0 are excluded. Individually normalized distributions for relaxing (Figure 3.18A) and nonrelaxing (Figure 3.18B) trajectories are then projected on an $r-$relaxed 2D PES. This PES was computed by determining the minimum energy for given (R, θ) with $r \in [2.03, 2.39]$. Such an $r-$relaxed PES is a more realistic way for this comparison as it also incorporates the varying NO bond length during the dynamics instead of restricting it to one specified value.

Figure 3.18 demonstrates that the two families of trajectories sample distinct regions of the interaction potential. The VR trajectories have a high density in the deep potential well area (dark blue) of the PES and sample mostly $\theta > 90^\circ$ region. This suggests formation of a long lived, tightly bound collision complex. However, the non-relaxing (NR) trajectories spend less time in the potential well region and the density map is rather flat, more uniformly distributed along the

angular coordinate with slightly larger sampling in the low-θ region.

To check the initial (before collision) angular dependence of the trajectories and role of long-range anisotropic interactions between the atomic collider and the diatomic target, similar density maps like Figure 3.18 have been computed for the VR and NR trajectories only up to the time satisfying the criterion that the sum of the three inter-nuclear distances is less than 9.5 a_0. Those are shown for the NR trajectories in Figure 3.14 and for the relaxing in Figure 3.15. It can be seen that at a separation of $\sim$ 8.5 a_0 the distribution $P(\theta)$ already has "structure" for the NR trajectories and in that a large fraction samples the range $\theta \sim 50°$ while the NR trajectories scarcely sample the high-θ region. However, for the relaxing trajectories the distribution is much more even and lacks a specific high-probability characteristic for a particular angle. Since the low-θ region of the PES is repulsive, most of the trajectories are reflected with only changing the rotational state of the NO and resulting NR events. A large fraction of those NR trajectories could not even visit the short-range interaction region ($R < 6.0$ a_0) and they fly by from the target contributing twice (incoming and outgoing trajectories) more in the density map which is obvious in Figure 3.14.

In Figure 3.16, ten randomly selected VR (red) and NR (black) trajectories from each of the data set plotted in Figure 3.14 and 3.15 are projected on similar 2D PES as in Figure 3.18. The dashed lines represent the reactive (oxygen exchange or O_2 formation) trajectories. It can be seen that all VR trajectories sample the potential well region which supports a collision complex. Out of the 10 VR trajectories 3 involve a reactive, oxygen exchange event. The ratio 7:3 is representative of all trajectories (3890:1832, for relaxing non reactive vs. relaxing reactive trajectories). Thus, oxygen exchange events contribute almost one third to VR. On

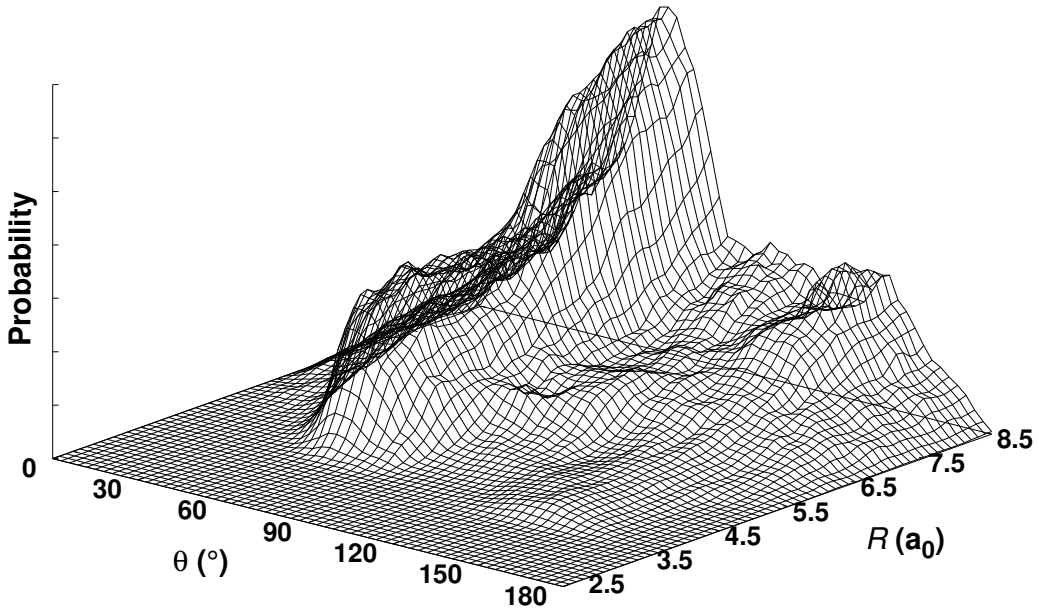

Figure 3.14: Distribution of the vibrationally nonrelaxing trajectories in (R, θ), i.e. O + NO($\nu = 1$) $\rightarrow$ O + NO($\nu \neq 0$), with or without oxygen atom exchange and N+O_2. The distance R is the oxygen atom-to-NO(center of mass) distance. Probability densities are calculated for all nonrelaxing trajectories and only up to the time satisfying the criterion that the sum of the three inter-nuclear distances is less than 9.5 a_0.

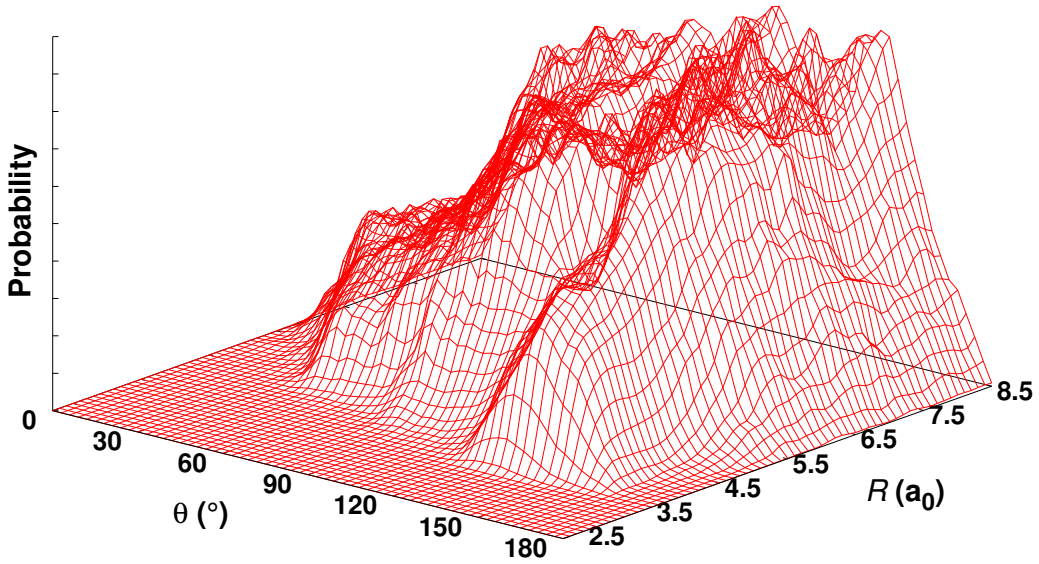

Figure 3.15: Distribution of the vibrationally relaxing trajectories in (R, θ), i.e. O + NO($\nu = 1$) $\rightarrow$ O + NO($\nu = 0$), with or without oxygen atom exchange. The distance R is the oxygen atom-to-NO(center of mass) distance. Probability densities are calculated for all relaxing trajectories and only up to the time satisfying the criterion that the sum of the three inter-nuclear distances is less than 9.5 a_0.

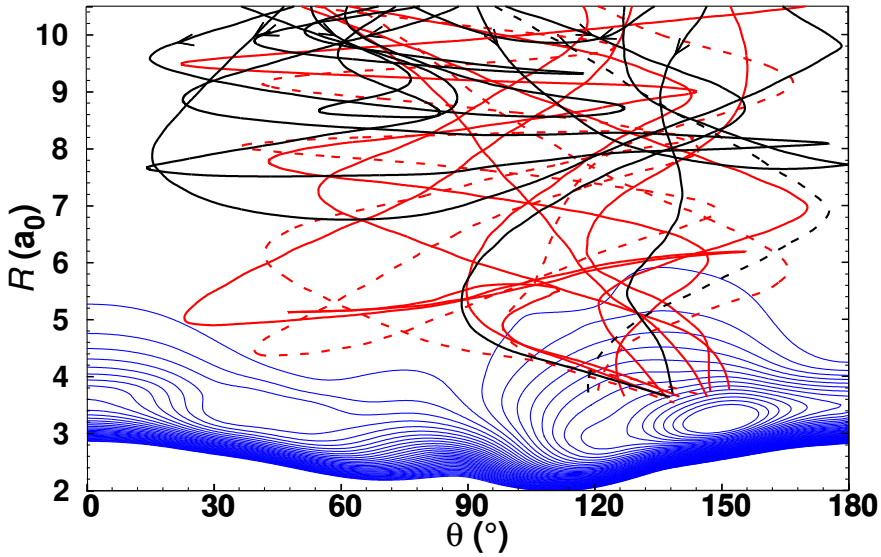

Figure 3.16: Projection of vibrationally relaxing (red) and nonrelaxing (black) O+NO collision trajectories onto the $^2A'$ PES (blue isocontours) as a function of (R, θ). For each (R, θ) combination the energy of the structure with lowest energy for $r \in [2.03, 2.39]$ (covers the classical turning points of the $v_{NO} = 1$ vibration, which are at $r_{min} = 2.046$ a_0 and $r_{max} = 2.370$ a_0) is used. Ten random trajectories are shown for each of the cases. Trajectories are shown only up to the time satisfying the geometrical criterion that the sum of the three inter-nuclear distances is less than 9.5 a_0. Reactive (oxygen exchange or O_2 formation) trajectories are shown as dashed lines.

the other-hand, among the NR trajectories a certain fraction accesses the global minimum of the PES but most of them do not continue beyond $R < 6.0$ a_0 but are reflected at longer R.

The results above suggest that relaxing and non-relaxing trajectories probe different parts of the PES. Hence, in order to be able to realistically describe vibrational relaxation the relevant regions, especially the potential well of the PES, have to be described sufficiently accurately. Figure 3.17 reports the same PES together with the positions in (R, θ) for which MRCI+Q calculations were carried out. It can be seen that the relevant regions sampled by vibrationally relaxing and non-relaxing trajectories are covered by the electronic structure calculations. Thus the current PES is expected to provide an accurate description of the interaction potential for relaxation dynamics, which is also supported when comparing the

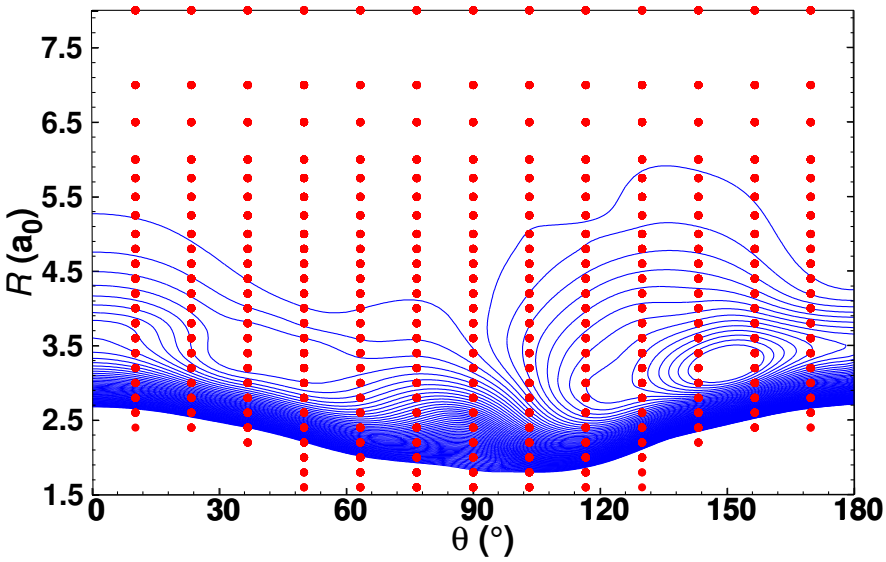

Figure 3.17: Contour diagram of the relaxed PES (as a function of R, θ and $r = 2.03 - 2.39$ a_0) of the $^2A'$ PES for the O+NO channel. The *ab initio* grid points used in constructing the RKHS are shown as red filled circles at which MRCI+Q calculations were carried out.

computed rates with experiments.

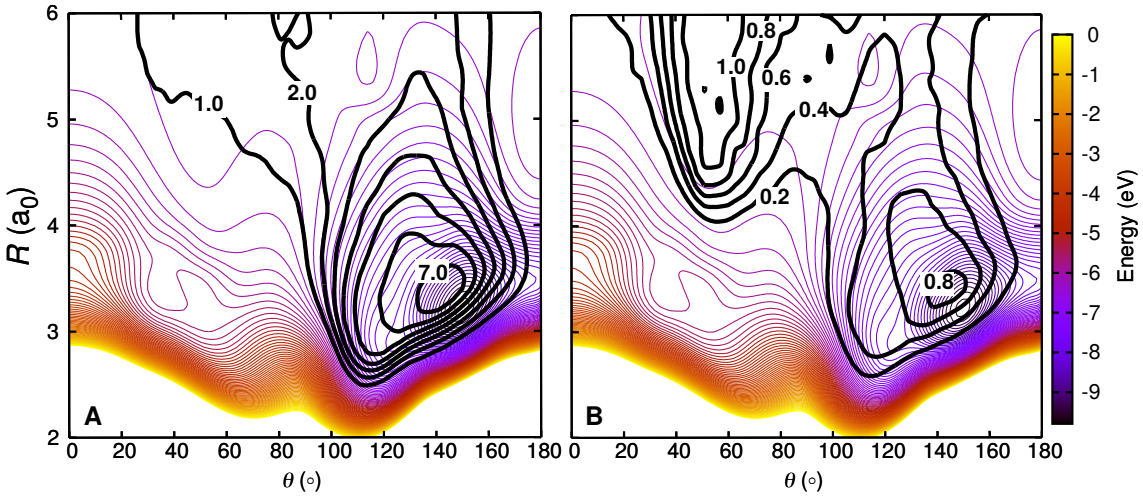

Figure 3.18: Density trajectory map for the vibrationally relaxing (left) and non-relaxing (right) for O+NO($\nu = 1, j$) collisions on the $^2A'$ PES. Vibrationally relaxing trajectories includes both, reactive and non-reactive trajectories, i.e. O_A+NO_B $\rightarrow$ O_B+NO_A and O_A+NO_B $\rightarrow$ O_A+NO_B, whereas for the non-relaxing trajectories we excluded the trajectories for which the initial ro-vibrational state is not changed. The density map for the trajectories is superimposed on a relaxed 2D RKHS PES (see text for details). The two different classes of trajectories access different regions in configuration space, corresponding to different angular anisotropies.

3.4 Conclusion

QCT calculations were carried out on the ^{2}A$'$, ^{4}A$'$ and ^{2}A$''$ electronic states of NO_2 for both, the forward and reverse reaction. The total rates agree favourably with experiment for the forward and reverse reaction (Figures 3.10C and D), except for the experiment for the forward rate at 2880 K for which interference with other reactions render the analysis more difficult.[109] The $T-$dependent equilibrium constants are close to those reported in the JANAF tables [89] and to those from results reported in Chemical Equilibrium with Application (CEA)[88]. This latter fact suggests that the forward rate $k_+(T)$ is in fact preferred over the single available experimental result at higher temperature (2880 K).[109] Vibrational relaxation rates were computed for the O + NO($\nu = 1$) $\rightarrow$ O + NO($\nu = 0$) process. Both states, ^{2}A$'$ and ^{2}A$''$, contribute to vibrational relaxation whereas the contribution from the ^{4}A$'$ state is small at low temperature ($k \approx 10^{-14}$) but increases for higher temperatures (Table 3.4).

For VR to occur, the force on the NO oscillator must act along the chemical bond, not orthogonal to it. Hence, the PES along the $\theta = 0$ and $\theta = 180°$ directions are most relevant to convert translational energy of the oxygen atom into relaxation of the vibrational motion of the NO diatomic, see Figure 3.18. As around $\theta = 0$ the PES is repulsive it is primarily the region around $\theta = 180°$ to which VR is sensitive to. The present work highlights that different parts of the PESs are probed depending on the observable considered, which can even be demonstrated explicitly. For example, using the DIM PES for the ^{2}A$'$ state for computing the N+O_2 $\rightarrow$O+NO temperature-dependent rate coefficients together with contributions for the ^{4}A$'$ state from the literature, acceptable agreement with experiment can obtained whereas for the temperature dependent vibrational relaxation the DIM PES finds a T-independent rate (see Figure 3.13) which considerably un-

derestimates that reported from experiments.

The fact that different observables provide information about different parts of the PES has already been highlighted for van der Waals complexes. As an example, the morphed PESs for the Ne–HF complex[127] demonstrated that observables from high resolution spectroscopy about the lowest stretching and bending states along the van der Waals coordinate provide sensitive information about the linear Ne–HF approach but no information about the antilinear Ne–FH part of the PES. Hence, it will be interesting to relate the space sampled by trajectories leading to particular final states with specific features such as to better understand what parts of a PES are crucial for reliably characterizing experimental observables from high-level computational studies.

It is expected that the temperature dependence of the rates computed in the present work extrapolate more reliably to higher temperature than the experimental data because, as the collision energy increases, the simulations sample the near vertical repulsive wall of the diatomic, determining its size. As this is an exponentially increasing curve, errors in the exponent will make little difference in the radius that is accessible at a given energy.

The present work uses one of the highest affordable levels of theory for the electronic structure calculations (MRCI+Q) and the validity of their representation as a RKHS is thoroughly tested using a large number of off-grid points. No relevant crossings between the PESs were found which would require the inclusion of nonadiabatic effects into the dynamics as had been done for the [CNO] system.[102] As with previous work for which quantum and classical nuclear dynamics studies were carried out and found to agree with one another[102], no

quantum effects are expected for the present system.

In summary, the reactive dynamics, thermal rates and vibrational relaxation for the $N(^4S) + O_2(X^3\Sigma_g^-) \leftrightarrow O(^3P) + NO(X^2\Pi)$ reaction on the three lowest potential energy surfaces was studied based on QCT simulations. The results are consistent with most of the available experiments. This provides a solid basis for a molecularly refined picture of vibrational relaxation and extrapolation of thermal rates to higher temperatures relevant at the hypersonic flight regime which can be used for more coarse grained studies such as DSMC simulations.

Chapter 4

CO_2: Rates and Vibrational Relaxation

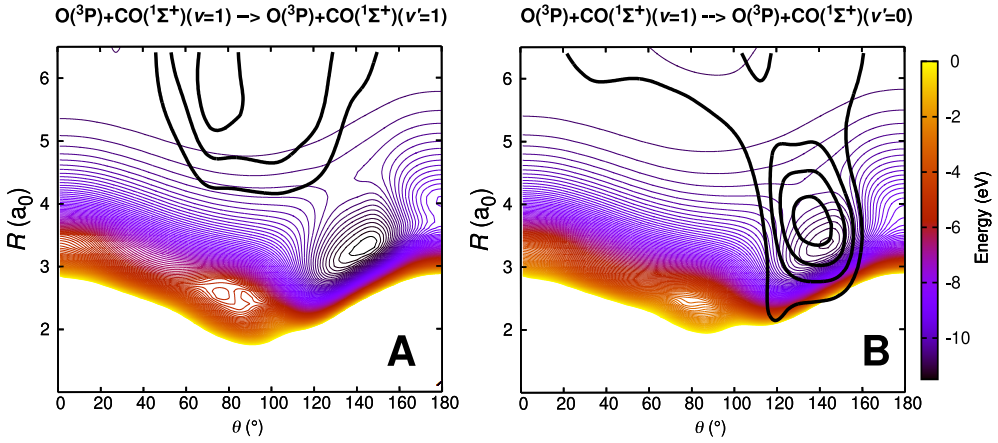

The results presented in this chapter have been previously published in:

Phys. Chem. Chem. Phys. 23 (2021) 11251

doi: 10.1039/d1cp01101d

***

Dr. Debasish Koner and Dr. Max Schwilk have contributed to this work as second and third author.

In this Chapter, thermal rates for the $C(^3P) + O_2(^3\Sigma_g^-) \leftrightarrow CO(^1\Sigma^+) + O(^1D)/O(^3P)$ reaction are investigated over a wide temperature range based on quasi classical trajectory (QCT) simulations on 3-dimensional, reactive potential energy surfaces (PESs) for the $^1A'$, $(2)^1A'$, $^1A''$, $^3A'$ and $^3A''$ states. These five states are the energetically low-lying states of CO2, the PES is computed at the MRCSISD+Q/aug-cc-pVTZ level of theory using a state-average CASSCF reference wave function. The forward rate matches measurements at 15 K to 295 K whereas the equilibrium constant determined from the forward and reverse rates are consistent with those derived from statistical mechanics at high temperature. Vibrational relaxation, $O+CO(\nu = 1, 2) \rightarrow O+CO(\nu = 0)$, is found to involve both, non-reactive and reactive processes. The contact time required for vibrational relaxation to take place is $\tau \geq 150$ fs for non-reacting and $\tau \geq 330$ fs for reacting (oxygen atom exchange) trajectories and the two processes are shown to probe different parts of the global potential energy surface. In agreement with experiments, low collision energy reactions for the $C(^3P) + O_2(^3\Sigma_g^-, v = 0) \rightarrow CO(^1\Sigma^+) + O(^1D)$ lead to $CO(^1\Sigma^+, v' = 17)$ with an onset at $E_c \sim 0.15$ eV, dominated by the $^1A'$ surface with contributions from the $^3A'$ surface. Finally, the barrier for the $CO_A(^1\Sigma^+) + O_B(^3P) \rightarrow CO_B(^1\Sigma^+) + O_A(^3P)$ atom exchange reaction on the $^3A'$ PES yields a barrier of ~ 7 kcal/mol (0.300 eV), consistent with an experimentally reported value of 6.9 kcal/mol (0.299 eV). A CASSCF wave function analysis of the different electronic states for the $CO_2 \rightarrow CO+O$ dissociation channel is used to rationalize the topography of this region of the PESs and to validate our genergal computational approach.

4.1 Introduction

Reactions involving carbon and oxygen atoms play important roles in combustion, hypersonic flow, and planetary atmospheres.[128] Among those, the thermal

rates for the $C(^3P)+O_2(^3\Sigma_g^-)$, $O(^3P)+CO(^1\Sigma^+)$, and $O(^1D)+CO(^1\Sigma^+)$ reactions going through various electronic states of CO_2 (see Figure 4.1) are particularly relevant. Similarly, the vibrational deactivation of $CO(^1\Sigma^+)$ through collisions with $O(^3P)$ is a relevant pathway for relaxation and redistribution of energy in nonequilibrium flow.[129]

Several independent studies have determined thermal rates for the forward $C(^3P) + O_2(^3\Sigma_g^-)$ reaction.[130–132] Using the CRESU (Cinétique de Réaction en Ecoulement Supersonique Uniforme) technique[132] the thermal rate from experiments between 15 and 295 K was measured. At 298 K the rate was $4.8 \pm 0.5 \cdot 10^{-11}$ cm^3 $molecule^{-1}$ s^{-1} which is within a factor of two to three of other, previous experiments.[130, 131, 133, 134] In all three laval nozzle experiments it was found that the rate increases with decreasing temperature between 15 and 295 K.[132, 135, 136] The product detection techniques included vacuum ultraviolet laser-induced fluorescence[132, 136], and chemiluminescence[135].

Shock tube experiments of the $C+O_2$ reactions were also carried out at higher temperatures (from 1500 to 4200 K) and reported a rate of $k_f(T) = 1.2 \times 10^{14} \exp(-2010\text{K}/T)$ cm^3 mol^{-1} s^{-1} (corresponding to $1.9\times10^{-10} \exp(-2010\text{K}/T)$ cm^3 $molecule^{-1}$ s^{-1}) with an overall uncertainty of ±50 % and a standard deviation for the activation energy of ±15 % and ±13 %, respectively.[137] Yet earlier emission spectra in a discharge flow found that the $C(^3P) + O_2(^3\Sigma_g^-)$ reaction generates CO in high vibrationally excited states (up to $v' = 17$) and that the transition state has the configuration COO rather than OCO.[138] Such a COO intermediate was also proposed from the interpretation of the $C+O_2$ reaction[139] and has been described in multiconfiguration SCF calculations.[140] Also, no evidence was found that the $C+O_2$ reaction passes through the region where the

quenching of $O(^1D)$ to $O(^3P)$ by CO occurs as a non-adiabatic process, as had been proposed earlier.[141, 142]

For the reverse reactions, $O(^3P)$+$CO(^1\Sigma^+)$, and $O(^1D)$+$CO(^1\Sigma^+)$ leading to $C(^3P)$ + $O_2(^3\Sigma_g^-)$, the onset for the rates $k_r(T)$ to form C+O_2 is expected to occur at considerably higher temperature than that for k_f due to the large energy difference of $\sim$ 6 eV between the O+CO and the C+O_2 asymptotes, see Figure 4.1. There are, however, computational investigations of the oxidation of CO to form CO_2 following the $O(^3P)$ + $CO(^1\Sigma^+) \rightarrow CO_2(^1\Sigma_g^+)$ route, usually involving a third particle M.[143] The rates for formation of CO_2 along the $^3A'$ and $^3A''$ pathways starting from $O(^3P)$+$CO(^1\Sigma^+)$ ranged from 10^{-13} to 10^{-12} cm^3 molecule^{-1} s^{-1}, depending on temperature, compared with $\sim 10^{-14}$ cm^3 molecule^{-1} s^{-1} from earlier work.[144] These were non-Born-Oppenheimer dynamics simulations of the $O(^3P)$+$CO(^1\Sigma^+) \rightarrow CO_2(^1\Sigma_g^+)$ reaction involving the $^1A'$, $^3A'$, and $^3A''$ potential energy surfaces (PESs).[143] The spin-forbidden fraction in this study was, however, found to be small ($\sim$ 1 %). Experimentally, the forward reaction has not been probed so far, to the best of our knowledge. Direct experiments involving [$O(^3P)$, $O(^1D)$] and $CO(^1\Sigma^+)$ concern the vibrational deactivation of CO upon collision with atomic oxygen.[129, 145–148] Finally, the rate for collisional spin relaxation for the $O(^1D)$ to $O(^3P)$ spin relaxation by $CO(^1\Sigma^+)$ at temperatures between 113 and 333 K was determined.[149] The rates were found to vary monotonically from about 7.6×10^{-11} to 5.2×10^{-11} cm^3 molecule^{-1} s^{-1} over the temperature range. Earlier modeling based on collisions with CO and other small molecules obtained a rate of $8 \times 10 - 11$ cm^3 molecule^{-1} s^{-1}.[150]

Computationally, the ground and excited state PESs for CO_2 have been studied in some detail.[140, 151–156] Early configuration interaction calculations established[151]

that there must be four states (two singlet and two triplet) of CO_2 below the $CO(^1\Sigma^+)$+$O(^3P)$ asymptote which is also what is found in the present work (Figure 4.1). CO_2 does not show strong absorptions below 11 eV[151] which makes direct comparison difficult also, because often vertical and not adiabatic transition energies were measured. A low-lying adiabatic electronic transition to a triplet state was reported at 39412 cm^{-1} (4.89 eV) above the ground state,[157] in qualitative agreement with the position of the $^3A'$ state, 4.62 eV above the ground state, see Figure 4.1.

An early classical MD study[158] of the forward reaction using an analytical potential energy surface found a rate of $k_f = 1.92 \times 10^{-11}$ cm^3 $molecule^{-1}$ s^{-1}. In dynamics studies[143, 145, 155, 159, 160] the reference energies from electronic structure calculations were either represented as parametrized fits,[145, 159, 160] cubic splines,[155] or interpolated moving least squares.[143] Reference calculations were carried out at the CASSCF-MP2/631G+(d),[145] and MRCI+Q/aug-cc-pVQZ levels of theory.[143, 155, 160] The dynamics simulations either concerned the O-induced collisional dissociation of CO,[160] CO vibrational relaxation,[145] the O-exchange dynamics in reactive O+CO collisions, non-Born-Oppenheimer effects in CO_2 formation from O+CO collisions,[143] or the final state distributions from the O+CO reactive scattering[159] but not the entire $C(^3P)$ + $O_2(^3\Sigma_g^-)$ $\leftrightarrow$ CO_2 $\leftrightarrow$ $CO(^1\Sigma^+)$+ $O(^1D)/O(^3P)$ reaction involving several electronic states.

A schematic of the states derived from the present calculations and considered in the present work is provided in Figure 4.1. The left hand side is the $C(^3P)$ + $O_2(^3\Sigma_g^-)$ (entrance) channel which connects to all bound CO_2 states in the middle. This asymptote is 11.22 eV above the global minimum which is the linear $CO_2(^1A')$ structure. The right hand side of Figure 4.1 shows the two product

channels considered: the lower CO($^1\Sigma^+$) + O(^{3}P) state, 5.30 eV above the minimum energy of the CO$_2$(^{1}A′) ground state, and the CO($^1\Sigma^+$) + O(^{1}D) asymptote another 1.97 eV higher in energy. The final state involving O(^{3}P) connects with the triplet states (^{3}A′ and ^{3}A″) of CO$_2$ whereas that leading to O(^{1}D) correlates with the ^{1}A′, ^{1}A″, and (2)^{1}A′ states, see Figure 4.1.

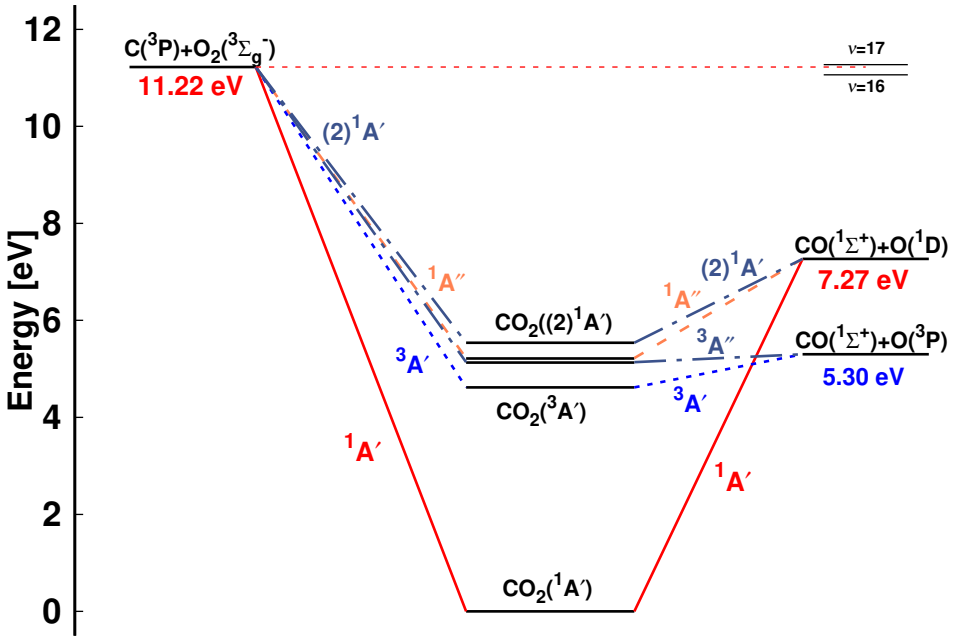

Figure 4.1: Energy level diagram for the C+O$_2$ ↔ CO+O reaction: C(^{3}P)+O$_2$($^3\Sigma_g^-$) ↔ CO($^1\Sigma^+$)+O(^{3}P) and C(^{3}P)+O$_2$($^3\Sigma_g^-$) ↔ CO($^1\Sigma^+$)+O(^{1}D). The energies of the dissociating species are reported: the O(^{1}D)/O(^{3}P) separation is 1.97 eV, consistent with experiment, and the total energies for CO$_2$ are ^{1}A′ ($^1\Sigma_g$ in D$_{\infty h}$) (0 eV), ^{3}A′ (4.62 eV), ^{3}A″ (5.14 eV), ^{1}A″ (5.22 eV), and (2)^{1}A′ (5.53 eV). The relative positions of the CO($v'=16$)+O(^{1}D) and CO($v'=17$)+O(^{1}D) asymptotes, relevant for discussing the low energy collision C(^{3}P)+O$_2$($^3\Sigma_g^-$) ↔ CO($^1\Sigma^+$)+O(^{1}D) reaction,[161] are indicated on the right hand side. The correlation of the (2)^{1}A′ state of CO$_2$ based on state-averaged SA-CASSCF calculations are consistent with earlier work[135] but differs from others.[140]

Except for the shock tube experiments[162] on C+O$_2$ → O+CO (1500-4200 K) and the computations[143] for CO$_2$ formation from O+CO (between 1000 K and 5000 K) there is little information on the high-temperature dynamics of either, the C+O$_2$ or the O+CO reactive processes. The present work extends this by performing QCT simulations on the 5 lowest states of CO$_2$, represented as a

reproducing kernel Hilbert space (RKHS),[97, 163] and focusing on the forward and reverse reactions and vibrational relaxation. First, the methods are presented and the potential energy surfaces for all 5 states are discussed. Then the thermal rates are determined along the singlet pathway. Next, vibrational relaxation for the O+CO collision is considered for CO($v = 1$) and CO($v = 2$) and the distributions for relaxing/nonrelaxing reactive/nonreactive trajectories are mapped onto the PES. Finally, conclusions are drawn.

4.2 Computational methods

This section presents the generation and representation of the potential energy surfaces and the methodologies for the QCT simulations and their analysis.

4.2.1 Electronic Structure Calculations

All PESs are computed at the multi reference CI singles and doubles (MRCISD) level of theory[93, 94] including the Davidson quadruples correction[164] (MRCISD+Q) together with the aug-cc-pVTZ basis set[95] using the MOLPRO 2019.1 software.[96] In order to consistently describe all relevant states and avoid numerical instabilities due to closely-lying states of the same symmetry, state-averaged CASSCF[90–92, 165] calculations including the two lowest states of each symmetry (two spin symmetries and two spatial symmetries) were carried out. Hence, in total eight states are included in the CASSCF reference wave function. MRCI+Q calculations for both asymptotic channels followed for the 5 lowest CO_2 states, namely $^1A'$, $^3A'$, $^3A''$, $^1A''$, and $(2)^1A'$, see Figure 4.1.

The energies were computed on a grid defined by Jacobi coordinates (r, R, θ) where r is the separation of the diatomic, R is the distance between the atom

and the center of mass of the diatomic and θ is the angle between the two unit vectors $\vec{r}$ and $\vec{R}$. For channel I ($C(^3P) + O_2(^3\Sigma_g^-)$) the $R-$grid included 28 points between 1.4 and 11 a_0 and the distance r was covered by 20 points between 1.55 and 4.10 a_0 whereas for channel II ($O(^3P/^1D) + CO(^1\Sigma^+)$) the $R-$grid included 26 points between 1.8 and 11 a_0, and the distance r was covered by 20 points between 1.55 and 4.00 a_0. The angular grid for both channels contained 13 angles from a Gauss-Legendre quadrature (169.796°, 156.577°, 143.281°, 129.967°, 116.647°, 103.324°, 90.100°, 76.676°, 63.353°, 50.033°, 36.719°,23.423°, 10.204°).

The reference points are then represented using reproducing kernel Hilbert space (RKHS) techniques.[97, 163, 166] The quality of the representation is further checked using energies from additional, off-grid geometries. The global, reactive 3D PES $V(r_1, r_2, r_3)$ for an electronic state is constructed by summing the weighted individual PESs for each channel

$$V(r_1, r_2, r_3) = \sum_{j=1}^{3} w_j(r_j) V_j(R, r_j, \theta), \tag{4.1}$$

using an exponential switching function with weights

$$w_i(r) = \frac{e^{-(r_i/\sigma_i)^2}}{\sum_{j=1}^{3} e^{-(r_j/\sigma_j)^2}}. \tag{4.2}$$

Here, σ_i are switching function parameters for channels I and II. These parameters were optimized by a least squares fit and yielded values of (0.90, 1.00, 1.00) a_0, (1.10, 1.05, 1.05) a_0, (0.9, 1.00, 1.00) a_0, (0.85, 1.25, 1.25) a_0 and (1.05, 1.00, 1.00) a_0 for the $^1A'$, $(2)^1A'$, $^1A''$, $^3A'$, and $^3A''$ PESs, respectively.

The - global and local - minima and transition states between the minima and/or entrance channels supported by the PESs were determined using BFGS mini-

mization and the nudged elastic band method[98] as implemented in the atomic simulation environment (ASE)[99].

4.2.2 Quasi-Classical Trajectory Simulations

The QCT simulations used in the present work have been extensively described in the literature[26, 41, 100, 101]. Here, Hamilton's equations of motion are solved using a fourth-order Runge-Kutta method. The time step was $\Delta t = 0.05$ fs which guarantees conservation of the total energy and angular momentum. Initial conditions for the trajectories are sampled using standard Monte Carlo methods.[26] The reactant and product ro-vibrational states are determined following semiclassical quantization with quantum bound state calculations for the two diatomics. Since the ro-vibrational states of the product diatom are continuous numbers, the states need to be assigned to integer values for which a Gaussian binning (GB) scheme was used. For this, Gaussian weights centered around the integer values with a full width at half maximum of 0.1 were used.[101, 103, 104] It is noted that using histogram binning (HB) was found to give comparable results for a similar system.[41]

The thermal rate for an electronic state (i) at a given temperature (T) is then obtained from

$$k_i(T) = g_i(T)\sqrt{\frac{8k_{\mathrm{B}}T}{\pi\mu}}\pi b_{\max}^2\frac{N_r}{N_{\mathrm{tot}}}, \tag{4.3}$$

where $g_i(T)$ is the electronic degeneracy factor of state 'i', μ is the reduced mass of the collision system, k_{B} is the Boltzmann constant, and, depending on the specific process considered, N_r is the number of reactive or vibrationally relaxed trajectories. In the rate coefficient calculations, the initial ro-vibrational states and relative translational energy (collision energy E_{c}) of the reactants for the tra-

jectories are sampled from Boltzmann and Maxwell-Boltzmann distributions at given T, respectively. The sampling methodology is discussed in detail in Ref. [41]

For the forward $C(^3P) + O_2(^3\Sigma_g^-) \rightarrow CO(^1\Sigma^+) + O(^1D)$ and reverse reactions $CO(^1\Sigma^+) + O(^1D) \rightarrow C(^3P) + O_2(^3\Sigma_g^-)$ with rates $k_f(T)$ and $k_r(T)$, respectively, the degeneracy factor is

$$g_{(^1A',(2)^1A',^1A'')}(T) = \frac{1}{(1 + 3 \cdot e^{\frac{-23.6}{T}} + 5 \cdot e^{\frac{-62.4}{T}})} \tag{4.4}$$

where the terms are the degeneracies of the J states for which the energy differences between the ground and the excited states are –23.6 K and –62.4 K, respectively. For the reactions leading to $O(^3P)$ and going through triplet CO_2 the degeneracies are $g_{(^3A',^3A'')} = \frac{1}{3}$. From $k_f(T)$ and $k_r(T)$ the equilibrium constant

$$K_{eq}(T) = \frac{k_f(T)}{k_r(T)}. \tag{4.5}$$

is determined.

4.3 Results and Discussion

4.3.1 The Potential Energy Surfaces

Two-dimensional contour plots of the PESs are shown in Figure 4.2 and the positions and relative energies of the critical points are summarized in Table 1. The left hand column in Figure 4.2 reports the PESs for the $C+O_2$ asymptote whereas the right hand column that for the CO+O channel, including the linear ground state structure for CO_2 (Figure 4.2b). All PESs for the $C+O_2$ asymptote are manifestly symmetric with respect to $\theta = 90°$ with moderate anisotropies for the $^1A'$ and $^3A'$ states and increased anisotropies for all other PESs. Conversely, all

PESs for the O+CO channel are single-minima PESs with their minima around 140° , except for the $^1A'$ state which has a minima for the OCO (180°) and OOC (0°) structures. The energy of the OOC state is 170.0 kcal/mol (7.37 eV) above the OCO minimum and the barrier height for transition between the OOC and OCO minima is 8.5 kcal/mol (0.369 eV). In addition, the existence of the local OOC minimum was confirmed at the MRCI+Q and CCSD(T) levels of theory and was suggested earlier from experiments[138, 139] and calculations.[140]

All root mean squared errors for both, on-grid and off-grid points are below 1 kcal/mol (0.043 eV), except for the $^1A''$ PES for which it is 1.04 kcal/mol (0.045 eV), all evaluated on the mixed PESs, see Eqs. 4.1 and 4.2. For the individual channels the performance of the RKHS is even better. Importantly, for off-grid points that were not used to construct the PESs but to independently validate the RKHS representations, the RMSEs are all below 1 kcal/mol (0.043 eV), too.

For a better understanding of the shapes of the PESs, the SA-CASSCF/aug-cc-pVTZ wave functions were analyzed in more detail for the different states at a bent geometry (θ = 117.65°), see Figure 4.3, for r_{CO} = 2.14 a_0 and varying R. Figure 4.3A shows the valence molecular orbitals that are relevant for the description of the eight states in the SA-CASSCF calculations along the $CO_2 \rightarrow$ CO + O dissociation for this bent geometry. Figure 4.3B depicts the dominant configuration state functions along this dissociation path. All states except for the energetically high lying $(2)^3A'$ state resolve with one dominant CASSCF configuration state function for the eight computed states of SA-CASSCF and keep their characteristic configuration along the entire dissociation path. Hence, no avoided crossing of two states with the same symmetry is observed. Figure 4.3C shows the relative energetics (taking the C(^{3}P) + O(^{3}P) + O(^{3}P) ground state

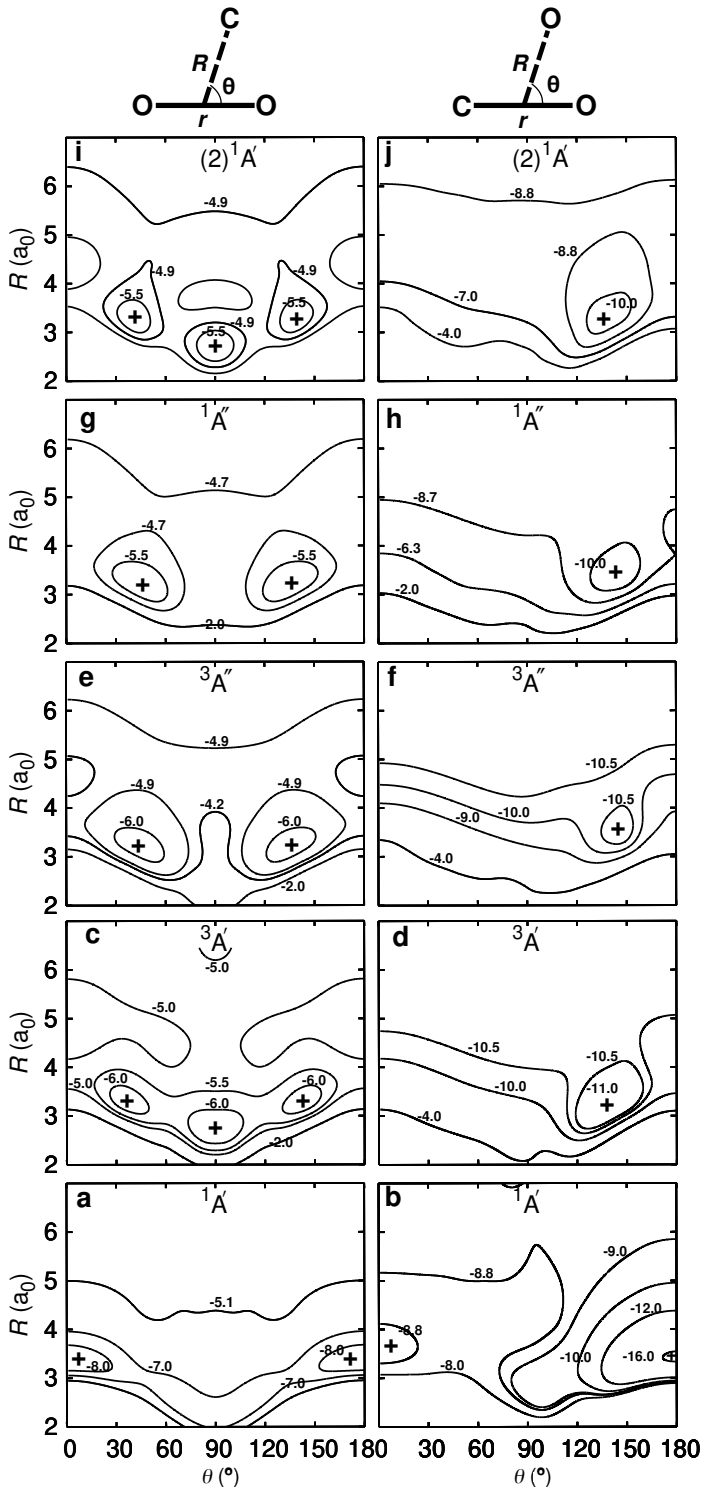

Figure 4.2: Two-dimensional cuts through the 3-d PES for the OO+C (left) and the CO+O (right) channels. Energy contours (in eV) for the ^{1}A′ (panels a,b), ^{3}A′ (panels c,d), ^{3}A″ (panels e,f), ^{1}A″ (panels g,h), and (2)^{1}A′ (panels i,j) states. The OO and CO diatomic distance are fixed at $r = 2.14$ and $r = 2.29$ a$_0$ for the CO+O and OO+C channels, respectively. The zero of energy is the dissociation into atomic fragments (C(^{3}P) + O(^{3}P) + O(^{3}P)). The symbol ("+") indicates local and global minima on each PES.

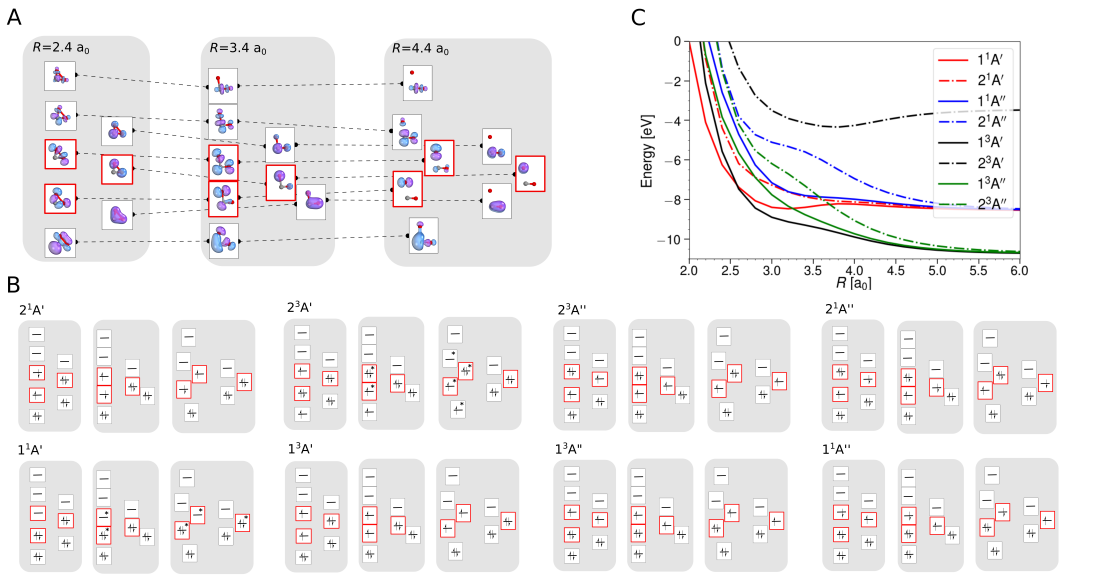

Figure 4.3: Analysis of the all-valence active space SA-CASSCF/aug-cc-pVTZ wave functions for a bent geometry with $\theta = 117.65°$, $r_{CO} = 2.14$ a_0 and for $R = 2.4, 3.4, 4.4$ a_0 ($CO_2 \rightarrow CO + O$ dissociation path). A: Valence molecular orbitals (natural orbitals) energetically close to the three frontier orbitals (red frames) whose occupation defines the five lowest lying electronic states considered for the dynamics on the CO_2 PES. The three depicted geometries are oriented with the symmetry plane parallel to the paper plane. Orbitals symmetric and antisymmetric with respect to the plane in the left and right columns of each diagram, respectively. B: Dominant configuration state functions of the eight states included in the SA-CASSCF calculation depicted as MO diagrams of the orbitals presented in panel A. If other configurations contributed with a weight > 0.05, the orbitals involved in the entanglement are marked by an asterisk (i. e. these orbitals have an occupation number that deviates significantly from the depicted integer value). C: Energy curves of the eight states for the $CO_2 \rightarrow CO + O$ dissociation at this bent geometry. The ground state C + O + O energy computed at the same level of theory is the reference energy.

	Present Work				Literature[143, 145, 167–169]			
PES	$r_1(CO_A)$	$r_2(CO_B)$	∠(OCO)	E (eV)	r_1 (a_0)	r_2 (a_0)	∠(OCO)	E (eV)
$(2)^1A'$ MIN	2.368	2.368	119.0	0.23	–	–	–	–
$^1A''$ MIN	2.374	2.374	130.5	–0.13	–	–	–	–
$^3A''$ MIN	2.374	2.374	130.6	–0.14	2.364 2.399	2.364 2.399	127.2 127.0	–0.23 –0.22
$^3A''$ TS	2.165	3.431	135.8	0.47	2.147 2.192	3.515 3.496	126.2 122.0	0.35 0.30
$^3A'$ MIN	2.356	2.356	126.3	–0.69	2.381 2.349	2.381 2.349	118.0 118.0	–0.94 –0.92
$^3A'$ TS	2.163	3.544	116.3	0.39	2.143 2.192	3.628 3.779	120.8 112.0	0.28 0.20
$^1A'$ (Global-M)	2.206	2.206	180.0	–5.30	2.196 2.194	2.196 2.194	180.0 180.0	–5.45 –5.64
$^1A'$ (MIN1)	2.527	2.527	70.6	0.74	2.522	2.522	72.9	0.61
$^1A'$ (MIN2)	2.192	4.798	0.0	1.88	2.220	4.716	0.0	1.72
$^1A'$ (TS1)	2.502	2.430	88.4	1.05	2.600	2.309	91.8	1.04
$^1A'$ (TS2)	2.164	4.279	68.9	2.15	2.203	4.537	41.0	2.22

Table 4.1: Minima (MINi) and transition states (TSi) on the CO_2 PESs towards the $CO(^1\Sigma^+)$ + $O(^3P)$ asymptote using the Nudged Elastic Band (NEB) method.[98] The PESs are in ascending energetic order, see Figure 4.2. Distances are in a_0 and Energy in eV. Energies relative to the $CO(^1\Sigma^+)$ + $O(^3P)$ dissociation limit. Present values are compared with previous work: for triplet states top row Ref.[143], bottom row Ref.[145]. For the global minimum in the $^1A'$ state: top row experiment[167], bottom row Ref.[143] and for the remaining minima and transition states Ref.[168]. Where necessary, literature values were converted to a_0 and eV.

computed with the same level of theory as the reference).

Upon bending, the doubly degenerate π_3 non-bonding [doubly occupied in $^1A'$], as well as the π_3 antibonding [unoccupied in $^1A'$] orbitals for collinear CO_2 undergo a splitting due to the lifted degeneracy. This results in a Jahn-Teller splitting of the states $^1A''$, $^3A''$, $^3A'$, and $(2)^1A'$ of CO_2 with their energy minimum at a bent geometry, see right hand column in Figure 4.2. The splitting of the degenerate HOMO and LUMO π_3 orbitals upon bending leads to three frontier orbitals, similar in energy, and with overall occupation of four electrons in all five energetically low-lying states (red frames in Figure 4.3A). One of these three frontier orbitals has σ^* character along the O-O bond (see Figure 4.3A) and is somewhat higher in energy. States that involve double occupation of this orbital lie higher in energy.

Along the same line, states that involve single occupation of one of the strongly bonding orbitals below the frontier orbitals also lie energetically higher.

The $^3A'$ and $^3A''$ states are lower in energy than the $^1A'$ state for certain bent geometries (see Figures 4.2 and 4.3C), as the triplet states gain from increased Pauli exchange, as well as reduced Coulomb repulsion due to the single occupations of orbitals. The corresponding open shell singlet states [$(2)^1A'$ and $^1A''$] lie slightly higher in energy than their triplet counterparts due to reduced Pauli exchange.

All CO_2 singlet states connect to $CO(^1\Sigma^+)+O(^1D)$ upon dissociation whereas the $^3A'$, $^3A''$, and $(2)^3A''$ states connect to the $CO(^1\Sigma^+)+O(^3P)$ state. On the other hand, the $(2)^3A'$ connects to the energetically high-lying excited $CO(^3\Pi)+O(^3P)$ state. The low-lying triplet CO_2 states have no or rather low barriers towards their dissociation across the entire PES (see Figure 4.2 and Figure 4.3C). Specifically, the $(2)^3A''$ state connects to the ground state of CO + O and crosses the singlet states upon dissociation. The crossing should nevertheless only lead to negligible non-adiabatic transition rates, as they are spin-forbidden. Since this state involves double occupation of an orbital with σ^* character of the O-O bond, it correlates with high lying excited states in the C + O_2 channel and is energetically well separated from the $^3A''$ state whenever there are short O-O distances. It is therefore sufficient to take its occupation only into account via the degeneracy of $O(^3P)$ in the quasi-classical treatment of the CO + O dissociation channel.

4.3.2 Forward and Reverse Rates and the Equilibrium Constants

The forward reaction $C(^3P) + O_2(^3\Sigma_g^-)$ (Figure 4.1) generates ground and excited state oxygen (^3P and ^1D). The pathway to yield ^3P involves the $^3A'$ and $^3A''$ CO_2 PESs whereas that to form ^1D goes through the $^1A', (2)^1A'$, and $^1A''$ states. For each of the reactions on each PES a minimum of 5×10^5 trajectories was run at each temperature.

Figure 4.4 shows the total thermal rates for formation of $O(^1D)$ and $O(^3P)$. The rates for formation of $O(^1D)$ start at 1.72×10^{-10} cm^3 molecule^{-1} s^{-1} at 15 K, drop to 5.19×10^{-11} cm^3 molecule^{-1} s^{-1} for $T \sim 600$ K and then monotonically increase to 3.23×10^{-10} cm^3 molecule^{-1} s^{-1} for higher temperatures, see red line for the total rate in Figure 4.4 with explicit numerical values reported in Table A.1 which also reports the number of reactive trajectories that contribute to the rate. Experimentally, the total rate for this process was determined over the temperature range from 1500 K to 4000 K. [162] Evaluating the reported expression $k(T) = 1.2 \times 10^{14} e^{\frac{-2010K}{T}} (\pm 50\%)$ cm^3 molecule^{-1} s^{-1} at 1500 K and 4000 K yields rates of $k(1500) = 5.22 \times 10^{-11}$ cm^3 molecule^{-1} s^{-1} and $k(4000) = 1.21 \times 10^{-10}$ cm^3 molecule^{-1} s^{-1} . This compares with $k(1500) = 5.96 \times 10^{-11}$ cm^3 molecule^{-1} s^{-1} and $k(4000) = 1.05 \times 10^{-10}$ cm^3 molecule^{-1} s^{-1} , respectively, from the present simulations. A high temperature measurement at 8000 K, associated with a substantial uncertainty, yields $k \sim 5 \times 10^{-10}$ cm^3 molecule^{-1} s^{-1} .[170]

The inset of Figure 4.4 reports the low-temperature results. Starting at 15 K the rate first decreases, goes through a minimum (at $\sim$ 600 K) before it raises again for higher temperatures. Such a behaviour is indicative of a submerged barrier[173] which, based on the rates for individual surfaces, appears to be dom-

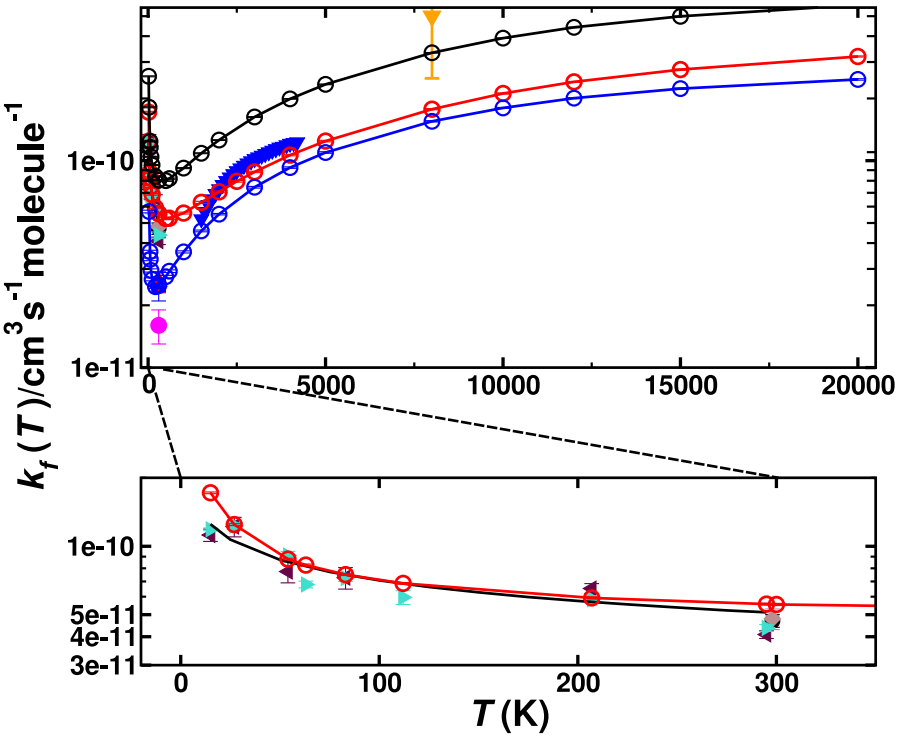

Figure 4.4: Thermal rate for the forward reaction (k_f) C(^{3}P) + O$_2$($^3\Sigma_g^-$) $\rightarrow$ CO($^1\Sigma^+$) + O(^{1}D)/O(^{3}P). The sum of the contribution of the singlet (red circles) and triplet (blue circles) states and the total rate (black circles). Comparison with forward rates from experiments: Ref. [162] (solid blue triangles) Ref. [135] (solid green right triangle), Ref. [134] (solid magenta circle), Ref. [133] (solid black circle), [171] (solid blue square), Ref. [132] (grey diamond), Ref. [170] (solid orange triangle down) and Ref. [172] (red triangle). The bottom panel shows an enlarged view for $0 < T < 300$ K for the total singlet rate (solid red line) together with the experimental results and a fit using Arrhenius parameters provided in the literature[132] (inset, black solid line).

inated by the ^{1}A$'$ and ^{3}A$'$ states. Compared with experiments all computed rates are within 2 % to 20 % at 50 K and 30 % to 40 % for Ref. [136] and 4 % to 30 % at 300 K for Ref.[132] which can be considered good agreement. For the process to yield O(^{3}P) the individual rates from the contribution of both triplet PESs (^{3}A$'$ and ^{3}A$''$) as well as the total weighted sum from the process to yield O(^{1}D) and O(^{3}P) are also reported in Figure 4.4 (blue and black lines), with numerical values given in Table A.2.

For the reverse reaction, CO($^1\Sigma^+$)+ O(^{1}D)/O(^{3}P) $\rightarrow$ C(^{3}P) + O$_2$($^3\Sigma_g^-$), similar simulations were carried out. As this is an uphill process (Figure 4.1), this

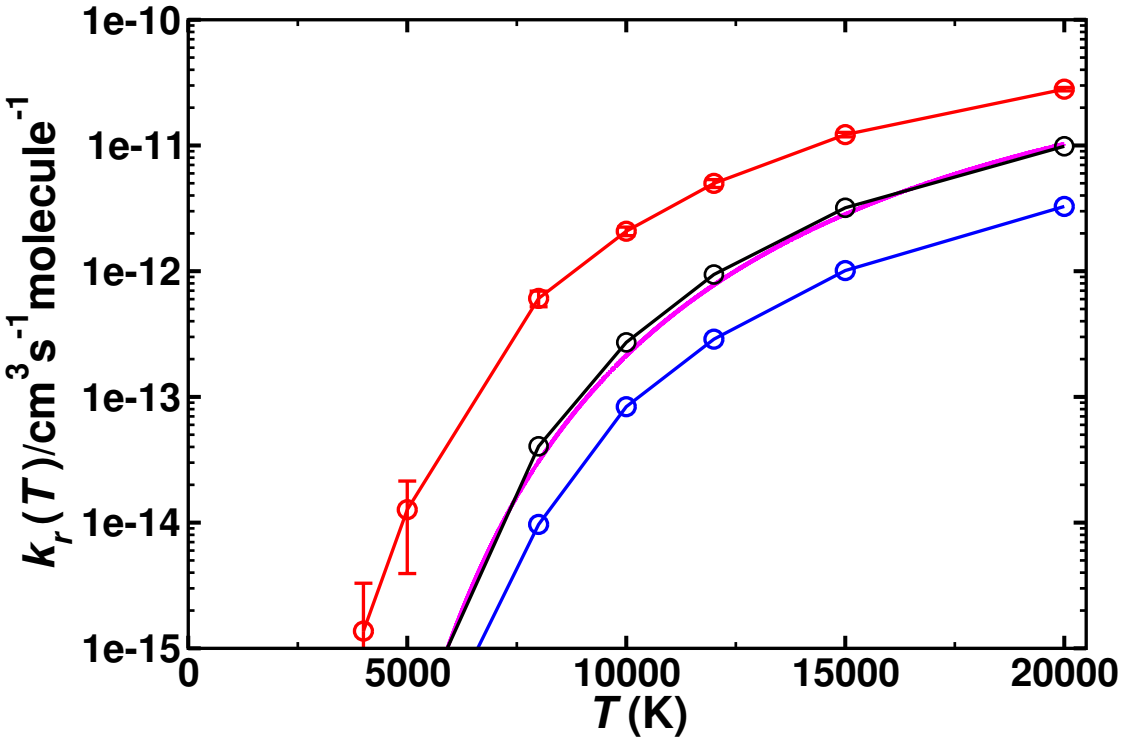

Figure 4.5: Thermal rate for the reverse (k_r) reaction CO($^1\Sigma^+$)+ O(^{1}D) $\rightarrow$ C(^{3}P) + O$_2$($^3\Sigma_g^-$). The sum of the contributions of the singlet (red circles, with error bars from bootstrapping) and triplet (blue circles) states and their Boltzmann-weighted sum (black circles). The temperature range is from 5000-20000 K. Comparison with recent theoretical work[160] (magenta solid line).

channel only opens at higher temperature, see Figure 4.5. The dynamics for CO($^1\Sigma^+$)+ O(^{1}D) $\rightarrow$ C(^{3}P) + O$_2$($^3\Sigma_g^-$) involves the ^{1}A$'$, (2)^{1}A$'$, and ^{1}A$''$ states (for numerical values see Table A.3), whereas that for CO($^1\Sigma^+$)+ O(^{3}P) $\rightarrow$ C(^{3}P) + O$_2$($^3\Sigma_g^-$) is related to the ^{3}A$'$ and ^{3}A$''$ states, given in Table A.4. Compared with the forward rates, those for the reverse reaction is typically 1 to 5 orders of magnitude smaller. The reverse rates starting from O(^{1}D) are larger by 1 to 2 orders of magnitude at high T than those from O(^{3}P) which is consistent with the Boltzmann-weighted energy difference for the two asymptotes.

Table 4.2 summarizes the parameters from fitting the raw data to a modified Arrhenius expression $k(T) = AT^n \exp(-\epsilon/T)$ for the forward and reverse processes for all five PESs. It is noted that all forward processes involve a comparatively

Forward	A	n	ϵ
$C(^3P) + O_2(^3\Sigma_g^-) \rightarrow CO(^1\Sigma^+) + O(^1D)$	4.12×10^{-12}	0.45	2209
$^1A'$	2.42×10^{-12}	0.40	116
$(2)^1A'$	1.21×10^{-12}	0.47	4506
$^1A''$	1.06×10^{-11}	0.27	6639
$C(^3P) + O_2(^3\Sigma_g^-) \rightarrow CO(^1\Sigma^+) + O(^3P)$	3.50×10^{-11}	0.22	3513
$^3A'$	1.60×10^{-11}	0.22	1891
$^3A''$	5.49×10^{-11}	0.11	6789
Total	1.56×10^{-11}	0.30	3018
Reverse			
$O(^1D) + CO(^1\Sigma^+) \rightarrow C(^3P) + O_2(^3\Sigma_g^-)$	1.15×10^{-10}	0.11	49965
$^1A'$	1.25×10^{-12}	0.42	42273
$(2)^1A'$	4.60×10^{-12}	0.32	50111
$^1A''$	5.28×10^{-13}	0.53	46836
$O(^3P) + CO(^1\Sigma^+) \rightarrow C(^3P) + O_2(^3\Sigma_g^-)$	1.52×10^{-12}	0.50	68903
$^3A'$	8.92×10^{-14}	0.70	64167
$^3A''$	7.80×10^{-09}	–0.37	83013
Total	1.55×10^{-10}	0.09	71735

Table 4.2: Modified Arrhenius 3-parameter model for the forward $C(^3P) + O_2(^3\Sigma_g^-) \rightarrow CO(^1\Sigma^+) + O(^1D)/O(^3P)$ and reverse $O(^1D)/O(^3P) + CO(^1\Sigma^+) \rightarrow C(^3P) + O_2(^3\Sigma_g^-)$ reaction. A in units of $cm^3\ s^{-1}$ molecule^{-1} and ϵ in Kelvin. The temperature range for the modified Arrhenius fit is 5000 to 20000 K.

small activation energy ϵ of a few hundred to a few thousand Kelvin. All reverse rates have activation energies that are at least one order of magnitude larger. The number of trajectories that contribute to these rates varies from less than 1 % to 55 %. For the slowest process, the reverse reaction on the $^3A'$ and $^3A''$ PESs originating from $O(^3P)$, at least an additional 5×10^5 trajectories were run at each temperature between 3000 K and 20000 K and close to 10^6 trajectories for $T \leq 1000$ K.

From the forward and reverse rates the equilibrium constant $K_{eq}(T)$ can also be determined, see Figure 4.6. This equilibrium constant was determined from the total forward and reverse fluxes of the weighted sum of the singlet and triplet pathways according to the data summarized in Table 4.2. Error bars for the individual rates have been determined from bootstrapping and are compared with

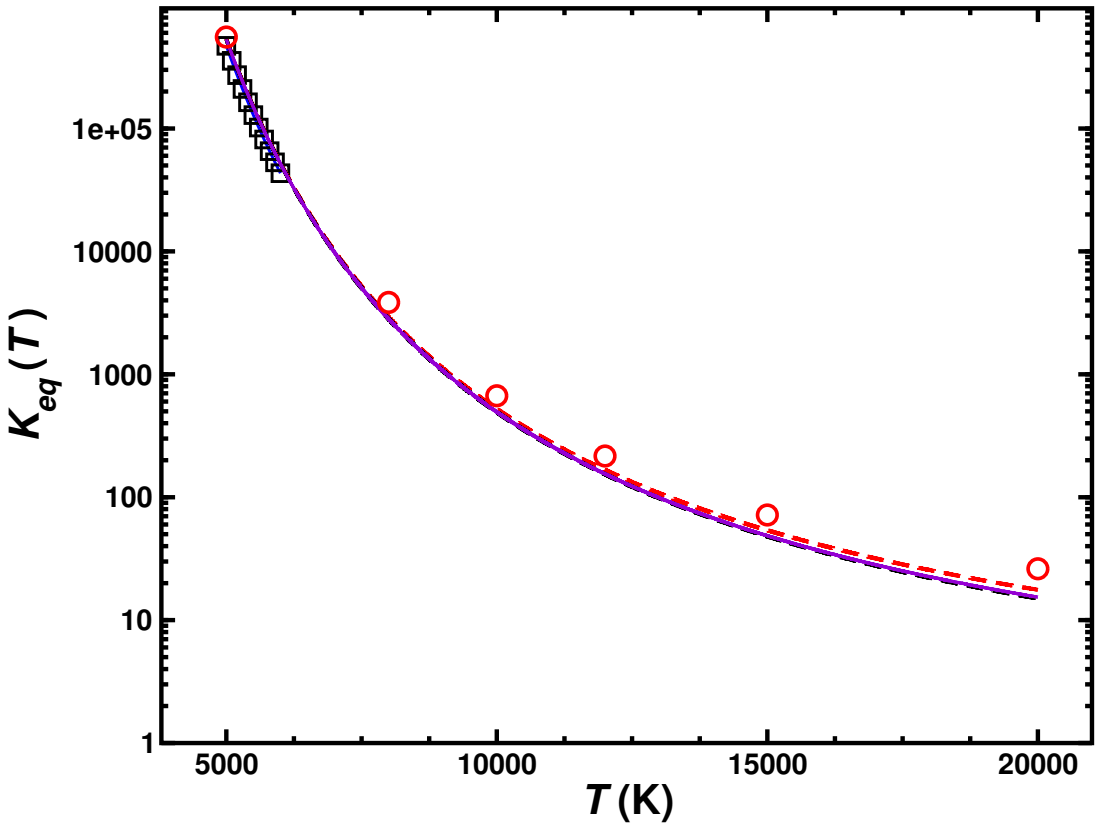

Figure 4.6: Equilibrium constant for the $C(^3P) + O_2(^3\Sigma_g^-) \leftrightarrow CO(^1\Sigma^+) + O(^1D_1)$ (k_1) and $C(^3P) + O_2(^3\Sigma_g^-) \leftrightarrow CO(^1\Sigma^+) + O(^3P)$ (k_2) reactions. The results from the JANAF tables[174] (black open squares), those derived from equilibrium statistical mechanics (k_1 (red open circles and red dashed line), k_2 (black dashed line) and their Boltzmann-weighted total $wk_1+(1-w)k_2$ (purple solid line)) with those from the QCT simulations are compared.

results determined from statistical mechanics. The equilibrium constant is only reported for temperatures 5000 K and higher as the reverse reaction only opens at these temperatures, see Figure 4.5.

A final process considered is the atom exchange reaction $CO_A(^1\Sigma^+) + O_B(^3P) \rightarrow CO_B(^1\Sigma^+) + O_A(^3P)$. For this process, on the $^3A'$ state, rates ranging from 5×10^{-16} cm^3 molecule^{-1} s^{-1} to 6×10^{-11} cm^3 molecule^{-1} s^{-1} between 500 K and 20000 K were found, see Table A.5. The rate increases monotonically from values $\sim 10^{-16}$, consistent with those measured experimentally,[175] as a function of T and is smaller than the measurement at 1820 K.[176] This experimental value

was an indirect measurement that required the decomposition rate for N_2O and is presented without derived error bars. The barrier for the atom exchange reaction inferred from the low-temperature experiments is 6.9 kcal/mol (0.299 eV), which is also what is found from the present work.

A summary of all forward and reverse rates is provided in Tables A.1 to A.5 which report all numerical values for the temperature-dependent rates.

4.3.3 Vibrational Relaxation

Vibrational relaxation (VR) of CO in its $v = 1$ and $v = 2$ states was investigated for both, the singlet and triplet manifolds separately. VR was investigated by running 5×10^5 trajectories at each temperature, ranging from 300 K to 5000 K, see Table 4.3. The final vibrational state was determined using Gaussian binning (GB) which has been shown to yield similar results as histogram binning.[103, 104, 177] Figure 4.7 compares the individual and total VR rates with those measured experimentally and Table 4.3 reports the rates. The computed rates are consistently lower than those from experiments at lower temperatures. For $T > 2000$ K the rates are in good agreement with experiments, though. In order to verify that the underestimation is not due to neglect of higher electronically excited states, the $(2)^3A''$ PES was also determined. This PES (not shown) is mainly repulsive. Therefore, the VR rates for this state only contribute ~ 10 % of the rates for the $^3A'$ and $^3A''$ states at the highest temperatures. Hence, the differences between experiment and simulations at lower temperatures are not due to neglect of contributions from higher-lying electronic states.

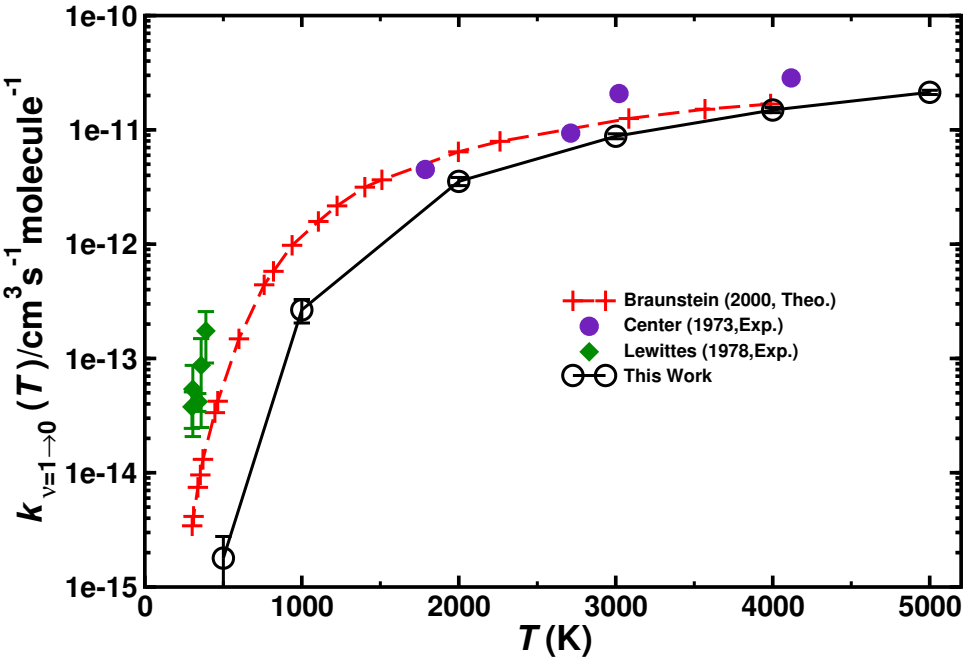

Figure 4.7: Total vibrational relaxation rate for O+CO($\nu = 1$) $\rightarrow$ O+CO($\nu = 0$). Total contribution (^{3}A$'$+^{3}A$''$) (closed black circles) ($g(e) = 1/3$). Literature values are the symbols as indicated.[129, 145, 147]. 5×10^5 trajectories were run at every temperature.

In order to better characterize to which parts of the PESs the individual processes are sensitive to, density maps were determined as follows. For each initial condition a trajectory can be attributed to one of the 4 possible outcomes: a) no vibrational relaxation, no reaction: O+CO($\nu = 1$) $\rightarrow$ O+CO($\nu' = 1$) b) vibrational relaxation without reaction: O+CO($\nu = 1$) $\rightarrow$ O+CO($\nu' = 0$), c) no vibrational relaxation but with atom exchange: O_A+CO_B($\nu = 1$) $\rightarrow$ O_B+CO_A($\nu' = 1$), and d) vibrational relaxation with atom exchange: O_A+CO_B($\nu = 1$) $\rightarrow$ O_B+CO_A($\nu' = 0$). Then, all trajectories for a given class were combined and a 2-dimensional histogram was generated and smoothed using kernel density estimation (KDE).[178] The resulting 2-dimensional distribution was then projected onto the relaxed PES for the corresponding state, see Figure 4.8.

Panel 4.8A shows that nonrelaxing trajectories sample regions in the long range without penetrating into the strongly interacting region around ($R = 3.2a_0, \theta =$

	500 K	1000 K	2000 K	3000 K	4000 K	5000 K
$^3A'$	0.01	1.51	18.61	43.62	74.44	101.95
$^3A''$	0.01	1.08	14.90	39.70	67.00	99.30
$(2)^3A''$	0.00	0.07	1.90	4.71	7.83	11.73
Total	0.02	2.66	35.41	88.03	149.27	212.98

Table 4.3: Vibrational relaxation rates (in units of 10^{13}cm^3 molecule^{-1} s^{-1}) $k_{\nu\to\nu'}$ for the collision of O(^{3}P) with CO($^1\Sigma_g$): O+CO($\nu = 1$) $\rightarrow$ O+CO($\nu' = 0$) for the $^3A'$, $^3A''$, and $(2)^3A''$ states and the total contribution using GB.

	relaxing			nonrelaxing	
reacting	$\nu = 2 \to 1$	$\nu = 2 \to 0$	$\nu = 1 \to 0$	$\nu = 2 \to 2$	$\nu = 1 \to 1$
N	300	230	681	340	745
τ_c	210	207	333	241	301
non-reacting					
N	480	440	1579	65790	117367
τ_c	67	155	156	33	36

Table 4.4: Average contact time (τ_c in fs, for definition see text) and number N of trajectories for each final state for $N_{\text{tot}} = 5 \times 10^5$ trajectories for each of the processes considered. In each case the difference ($N_{\text{tot}} - N$) are fly-by trajectories. This table reports the cases $\nu = 2 \to$ x and $\nu = 1 \to$ x for both reactive and non-reactive events.

150°). Contrary to that, nonreactive, relaxing trajectories of the type O+CO($\nu = 1$) $\rightarrow$ O+CO($\nu' = 0$) access the strongly interacting region and sample it before leaving this region again, see Figure 4.8B. For the reactive trajectories (O_A+CO_B $\rightarrow$ O_B+CO_A), see Figures 4.8C and D, all trajectories enter the strongly interacting region along $\theta \sim 160°$ (black density).

After the reaction, the product (CO_A) can either remain vibrationally excited (Figure 4.8C; no relaxation), or its vibrational state can change ($CO_A(v' = 0)$ or $CO_A(v' = 2)$). The highest vibrational state in the products after reaction in these trajectories (run at 1000 K) is $v' = 3$. The probability distributions of the products from reactive collisions in Figures 4.8C and D are in red (for $v' = 0$, relaxation) and in blue (for $v' = 2$, further excitation). The shape of the red and blue probability distributions in Figures 4.8C and D can already be anticipated from the relaxed PES for the CO+O channel. A different perspective that

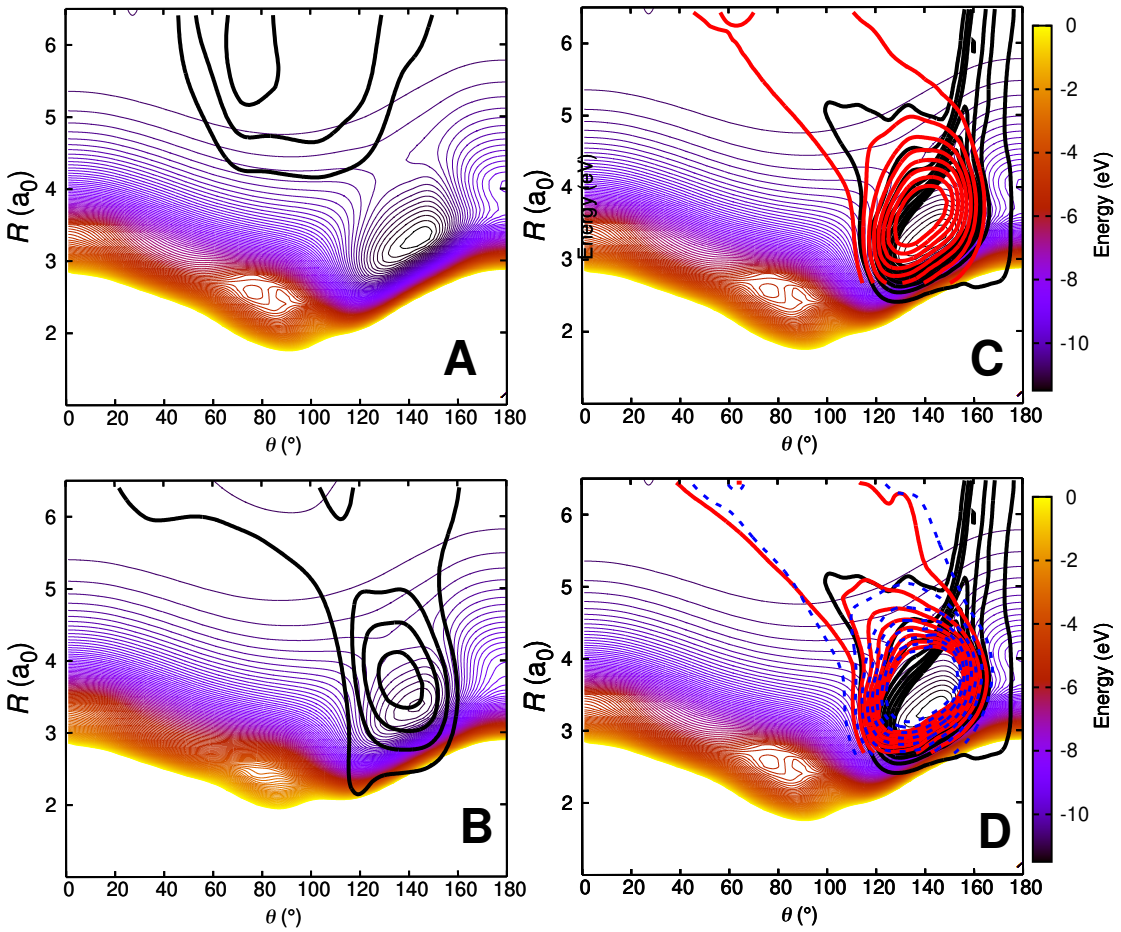

Figure 4.8: Density map for O+CO($\nu = 1$) collisions at 1000 K on the relaxed ^{3}A′ PES. Panel A: O+CO($\nu = 1$) → O+CO($\nu' = 1$); Panel B: O+CO($\nu = 1$) → O+CO($\nu' = 0$); Panel C: O_A+CO_B($\nu = 1$) → O_B+CO_A($\nu' = 1$) and Panel D: O_A+CO_B($\nu = 1$) → O_B+CO_A($\nu' = 0$). For the reactive trajectories (panels C and D), two coordinate systems are used: one for the reactant (black density) in which the CO_B diatom is the distance r and the separation of atom O_A from the center of mass is the distance R; the second coordinate system is for the product state (red density) for which the CO_A diatom is the distance r' and the separation of atom O_B from the center of mass is the distance R'. The dashed blue isocontours in panel D are for O_A+CO_B($\nu = 1$) → O_B+CO_A($\nu' = 2$). The density map for the trajectories is superimposed on a relaxed 2D RKHS PES where $2.00 < r < 2.30$ a_0 (turning points). For all density maps 1500 trajectories were used to generate the 2d densities which were smoothed using kernel density estimation (KDE) as implemented in the R software package[179].

could be taken is to refer to all reactive trajectories as "vibrationally relaxing" because the quanta initially present in CO_B are destroyed upon dissociation of CO_B. However, experimentally, the final states $CO_B(v' = 1)$ and $CO_A(v' = 1)$ can not be distinguished. Hence separation into 4 separate cases is meaningful in

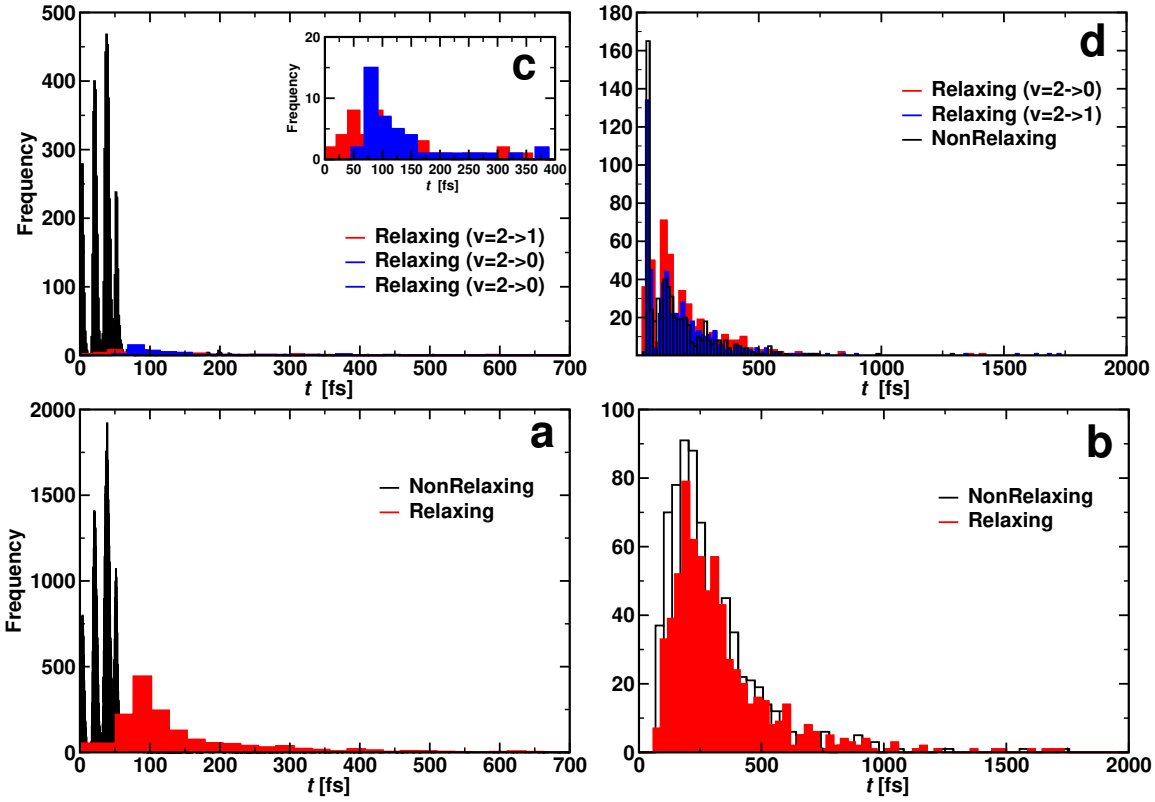

Figure 4.9: Contact time histogram for O_A+CO_B $\rightarrow$ O_B+CO_A (reacting: panel a and c) and O_A+CO_B $\rightarrow$ O_A+CO_B (non reacting: panel b and d). Bottom panels for CO($v = 1$) and top panel for CO($v = 2$). Panel c inset illustrates that relaxing two quanta ($\nu = 2 \rightarrow 0$, blue distribution) takes longer than relaxing one quantum ($\nu = 2 \rightarrow 1$, red distribution). Rates for the atom exchange reaction are given in Table A.5.

analyzing the trajectories.

It is also of interest to consider the distribution of contact times τ_c for each of the scenarios. This quantity was taken as the first instance along the trajectory for which the sum σ of all three atom distances is smaller than 12 a_0 in the entrance channel until the point at which $\sigma > 12$ a_0 along the exit channel. This was done for CO initially in its $v = 1$ and $v = 2$ states, respectively. The average contact times are reported in Table 4.4 and their distributions are shown in Figure 4.9. It should, however, be noted that the average τ_c only incompletely characterize the underlying distribution $P(\tau_c)$ because the distributions are either structured (Figures 4.9a and c) or extend to times more than 10 times the most probable

value as in Figures 4.9b and d.

For reacting trajectories and non-reacting but relaxing trajectories, the contact time τ_c decreases with increasing vibrational excitation. This differs for non-reacting, relaxing trajectories. Their average contact times appear to be determined by the final vibrational state. For relaxation to $v' = 0$ the average vibrational relaxation time is $\sim$ 150 fs which shortens to $\sim$ 70 fs for relaxation to $v' = 1$ with initial $v = 2$. This is in contrast to the non-relaxing non-reacting trajectories which appear to be independent of vibrational excitation. The τ_c for these trajectories is of the order of 30 fs which is roughly the minimum time required for one collision.

When considering the lifetime distributions it is found that those involving reacting trajectories display a regular pattern of peaks, see Figures 4.9a and c. It is noticeable that the probability to find trajectories that react but do not relax $P(\tau_c)$ can be zero and reaches maximal values for other values for the lifetime. Fourier transformation of this signal yields frequencies between 1824 cm^{-1} and 2529 cm^{-1}. These frequencies, which are in the range of typical CO stretch frequencies, can be understood as "gating modes" that allow the reaction to occur, similar to what was found for proton transfer in protonated ammonia dimer.[180]

It is also of interest to consider the geometries sampled for the $C(^3P) + O_2(^3\Sigma_g^- \longrightarrow CO(^1\Sigma^+) + O(^1D)$ reaction on the $^1A'$ PES depending on the temperature from which the initial conditions were generated. This was done for $T = 15$ K and $T = 10000$ K. For reactive trajectories at low temperatures the global minimum is extensively sampled (see Figure 4.10A) whereas at high temperature this region is not sampled at all as shown in Figure 4.10B. Hence, collisions at dif-

ferent temperatures are expected to sample complementary regions of the 3d PES.

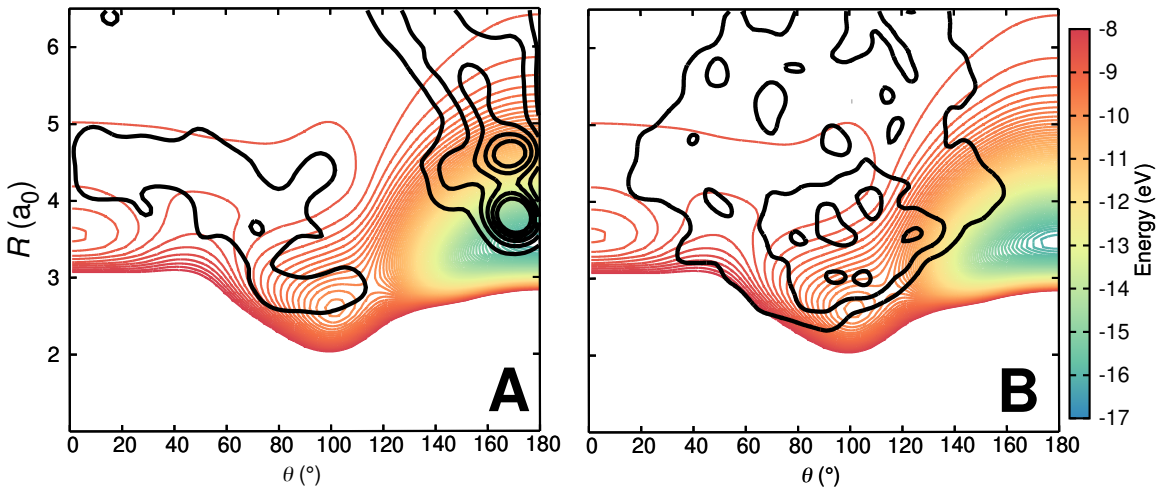

Figure 4.10: Density trajectory map at 15 K (panel A) and 10000 K (panel B) for the $C+O_2 \longrightarrow CO+O(^1D)$ reactive collisions on the ground state $^1A'$ PES. The density map for the trajectories is superimposed on a relaxed 2D RKHS PES where $2.00 < r < 2.30$ a_0 (turning points). 300 reacting trajectories were taken for each case and represented as a KDE. It is found that although both sets of trajectories describe the same physical process (atom exchange reaction) they are sensitive to and sample different parts of the PES.

4.4 Discussion and Conclusions

The present work reports thermal and vibrational relaxation rates from QCT simulations on the five lowest PESs of the [COO] systems. Comparison with experiment is favourable for thermal rates and vibrational relaxation rates at high temperatures. For the atom exchange rate, agreement is rather more qualitative, with an overall offset in the energetics of 300 K (0.026 eV). Additional analyses are carried out in the following to provide an understanding of remaining disagreements between experiment and simulations.

One interesting comparison can be made with state-to-state cross section measurements for the $C(^3P) + O_2(^3\Sigma_g^-) \leftrightarrow CO(^1\Sigma^+) + O(^1D)$ reaction at small collision energies.[161] These experiments used a pulsed nozzle through which the

O_2 expanded into the vacuum. The O_2 internal state distribution was not measured directly but expected to be very cold.[161] Hence, it is likely that mostly $O_2(v = 0)$ with low j_{max} was populated. Such experiments found that excitation of $CO(v' = 16)$ occurs for all collision energies E_c whereas population of $CO(v' = 17)$ is only possible with an excess of $E_c > 0.04$ eV. Using bound state energies for CO derived from experiment[181] and accounting for the 0.04 eV required to open the $CO(v' = 17)$ channel, the energy difference between $CO(v = 0)$ and $CO(v' = 17)$ is 4.037 eV. Including zero point energy for CO and O_2, the difference between the $C(^3P)$ + O_2 and $CO+O(^3P)$ channels from experimental data is 4.075 eV. This differs by 0.085 eV from the value at the MRCI level of theory which is 3.990 eV.

From semiclassical calculations on the present PESs the $CO(v' = 17)$ state is at 4.140 eV. This compares with the difference in electronic energies (3.990 eV) and differences in the CO and O_2 zero point energies of 3.952 eV. Hence, $E_c = (4.140 - 3.952) = 0.188$ eV is required to open the $CO(v' = 17)$ channel. QCT simulations starting from Boltzmann-distributed (v, j) initial conditions find that the population of the $CO(v' = 16)$ decays exponentially with increasing E_c (Figure 4.11 left panel) which is consistent with experiments.[161] Because expansion through a nozzle does not necessarily yield Boltzmann-distributed initial conditions and the experimental beam was deemed "very cold",[161] the final state distributions were also separated into those originating from $O_2(v = 0)$ (open circles in Figure 4.11) and those from $O_2(v > 0)$ (solid line in Figure 4.11). For $CO(v' = 16)$ all distributions follow the same overall behavior.

Conversely, for $CO(v' = 17)$ considering the final state distribution from initial $O_2(v = 0)$ has an onset at $\sim$ 0.05 eV (inset Figure 4.11 right panel) with a

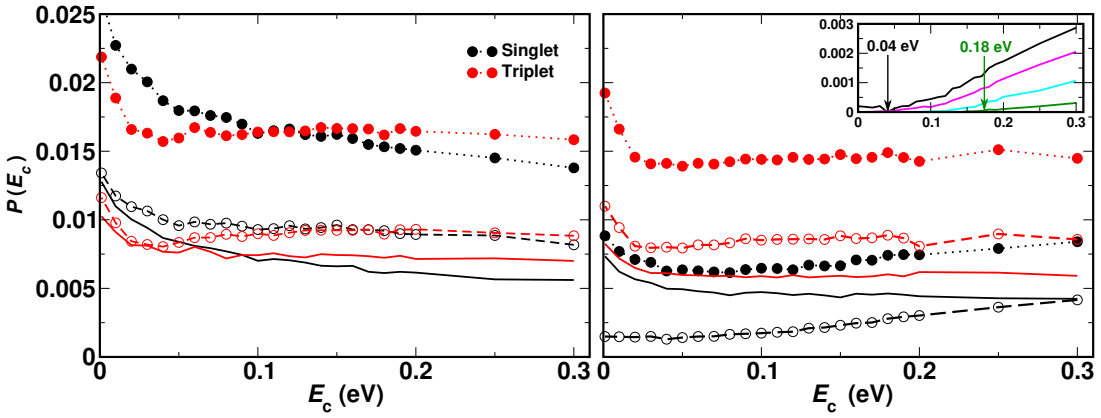

Figure 4.11: Reaction probability $P(E_c)$ as a function of collision energy E_c for the $C(^3P) + O_2(^3\Sigma_g^-) \longrightarrow CO(^1\Sigma^+) + O(^1D)$ (singlet (black), $^1A'$ PES) and $C(^3P) + O_2(^3\Sigma_g^-) \longrightarrow CO(^1\Sigma^+) + O(^3P)$ (triplet (red), $^3A'$ PES) reaction. Left panel for final vibrational state CO ($v' = 16$) and right panel for CO($v' = 17$). At least 10^5 trajectories were run for each collision energy (0.001-0.300 eV). Filled circles: total reaction probability; open circles: reaction probability originating from $O_2(v = 0)$; solid line: reaction probability originating from $O_2(v > 0)$. The inset in the right hand panel shows an enlargement for the singlet channel (forming $O(^1D)$) and highlights the threshold energy observed from experiment[161] to open this product channel at $E_c = 0.04$ eV. The green, cyan, magenta, and black traces correspond to initial $O_2(v = 0, j_{max} < 10)$, $O_2(v = 0, j_{max} < 20)$, $O_2(v = 0, j_{max} < 30)$, and $O_2(v = 0)$ for all $j-$values.

dependence on E_c consistent with experiment[161] whereas including all initial $v-$states for O_2 and those starting from $O_2(v > 0)$ again show a decaying probability distribution with increasing E_c. Because both, initial v and j are probably "cold", it is meaningful to consider final CO($v' = 17$) distributions originating from different j_{max} values for the parent O_2 molecule. With decreasing j_{max} the CO($v' = 17$) channel opens with increasing values of E_c. For $j_{max}^{O_2} < 30$, the onset occurs at 0.05 eV and shifts to ~ 0.15 eV for $j_{max}^{O_2} < 10$, which is consistent with the estimate of 0.188 eV based entirely on energetic arguments above. A temperature of $T = 300$ K corresponds to $O_2(j = 12)$ but the corresponding (nonequilibrium) distribution probably extends to higher $j-$values. Hence an estimated onset of generating CO($v' = 17$) for $E_c \in [0.05, 0.10]$ eV is expected from the present simulations. This corresponds to a difference of 0.01 eV to 0.06 eV from experiment on a scale of 4 eV, which is an error of 1 % at most.

For the deactivation of $O(^1D)$ to $O(^3P)$ in the atmosphere early models performed well for the observed data available at that time.[150] The CO case was categorized as one that is dominated by the configuration of a critical region where a crossing between the single PESs originating from the $O(^1D)$ channel cross the triplet PESs leading to $O(^3P)$. For the crossing dynamics a Landau-Zener model was assumed. This simple approach lead to a predicted rate of 8.0×10^{-11} cm^3 molecule^{-1} s^{-1} at 300K which was within the error of experimental measurements of 7.6 and 7.3×10^{-11} cm^3 molecule^{-1} s^{-1} .[141, 182] Following this, the deactivation of $O(^1D)$ by CO was measured and the rate obtained was fit by the expression $(4.7 \pm 0.9) \times 10^{-11} \exp\left((126 \pm 33)/RT\right)$ which yields a rate of 5.8×10^{-11} cm^3 molecule^{-1} s^{-1} at 300 K. Assuming $\sim 5 \times 10^{-10}$ cm^3 molecule^{-1} s^{-1} for the collision rate, this implies a $\approx 10\%$ efficiency for deactivation of $O(^1D)$ to $O(^3P)$ at 300 K. Based on this low efficiency the crossings between the singlet and triplet manifolds are not expected to have a large impact on the formation, exchange or relaxation of the reaction.

As Tully pointed out, deactivation depends on the specific crossing geometry of the PESs; in this case the singlet and triplet surfaces. When starting from the CO_A+O_B side of the reaction, as was previously mentioned, Figure 4.8 shows that the active reactions sample a channel near 140° that brings the outgoing O_A atom into approximately $R = 3.5$ a$_0$. At low temperature, starting from CO+$O(^3P)$, it would be possible to cross from any of the ^{3}A surfaces onto the ^{1}A$'$ surface to lead to ground state CO_2. However, in a collisionless environment the complex will still have sufficient energy to return to the ^{1}A$'$ PES and will have to cross with a ^{3}A surface to leave as $O(^3P)$. This may affect vibrational energy transfer or the exchange reaction and may be the reason for the shifts in the onset seen between the experiment and QCT such as in Figure 4.7 at low temperature. Starting from CO+$O(^1D)$ and traveling along the ^{1}A$'$ surface crosses all ^{3}A surfaces while the

$(2)^1A'$ and $^1A''$ surfaces only cross the repulsive $(2)^3A''$ surface. At temperatures lower than that required to form $C(^3P)+O_2$ these trajectories can potentially cross on to the ^3A surfaces and then return to the $CO+O(^3P)$ state although it would be at high CO vibrational state.

One finding of the present work is the role "gating" plays in the different processes considered here. For one, vibrational relaxation with atom exchange displays gating in the contact time distributions which hints at a time-dependent barrier in the [COO] collision complex. This is explicitly seen in the barriers for the $CO_A(^1\Sigma^+) + O_B(^3P) \rightarrow CO_B(^1\Sigma^+) + O_A(^3P)$ atom exchange reaction on the $^3A'$ PES. Depending on the phase of the CO vibration at which the impinging oxygen atom collides with the diatomic molecule, the barrier for formation of the collision complex is either high or low. Such processes are particularly susceptible to zero-point vibrational effects which can not be captured in QCT simulations. Specifically, the vibrational wavefunction does not produce the same spatial probability distribution at low v as the classical trajectory. This results in differences in sampling times for when the gate is open versus closed. The rates from QCT simulations should, therefore, underestimate the true rates, in particular at low temperatures. This is indeed found for vibrational relaxation, see Figure 4.7. As the vibrational relaxation rates include both, processes with and without atom exchange, and the CO vibration-dependent barriers only affect trajectories with atom exchange, it is conceivable that vibrational relaxation without atom exchange is not affected by these effects.

Including zero-point effects is likely to improve the comparison between calculations and experiments. Furthermore, nonadiabatic effects may further improve comparison with experiment, in particular for the processes leading from CO_2

to the O+CO asymptotes. Analysis of vibrational relaxation demonstrates that depending on the process considered (with or without reaction), different parts of the fully-dimensional PES are sampled. This is also true for reactions at low (15 K) and higher (1000 K) temperatures, respectively. Together with suitable information from experiment the underlying PESs could be further improved from techniques such as morphing[183, 184] or Bayesian inference.[185]

In conclusion, the present work provides a comprehensive characterization of the energetics and dynamics of the reactive [COO] system involving the lowest five electronic states. Many findings provide good agreement between simulations and experiments but it is also found that disagreements can be traced back to neglecting quantum mechanical effects at low temperatures. Additional experiments for this important system will provide a more complete understanding of the reactions involving both asymptotes.

Chapter 5

State to Distribution Model

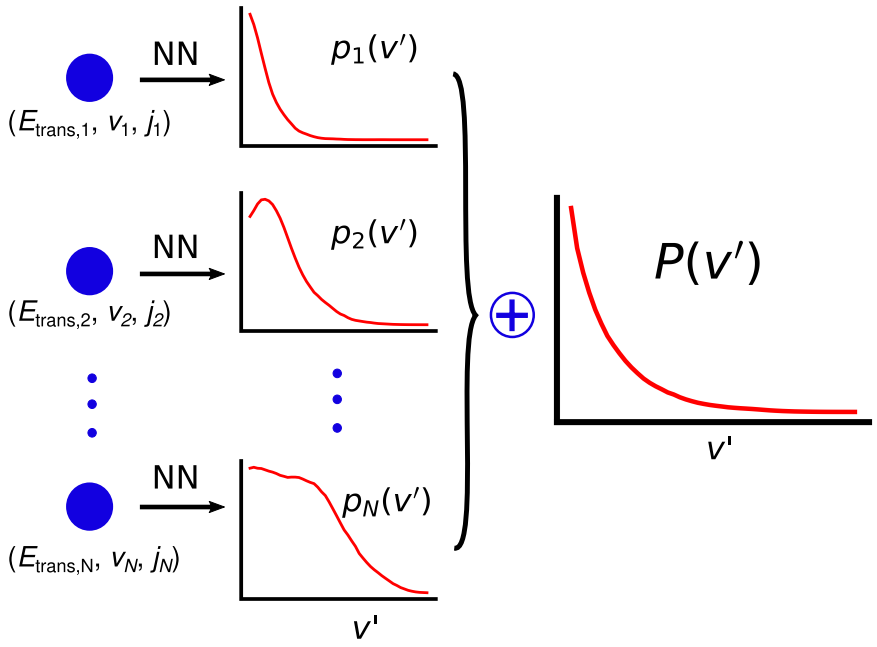

The results presented in this chapter have been previously published in:

J. Chem. Phys. 156 (2022) 034301

doi: 10.1063/5.0078008

Julian Arnold, Dr. Debasish Koner and Dr. Narendra Singh have contributed to this work as first, third and fourth author.

In this Chapter, a machine learned (ML) model for predicting product state distributions from specific initial states (state-to-distribution or STD) for reactive atom-diatom collisions is presented and quantitatively tested for the $N(^4S) + O_2(X^3\Sigma_g^-) \rightarrow NO(X^2\Pi) + O(^3P)$ reaction. The reference data set for training the neural network (NN) consists of final state distributions determined from explicit quasi-classical trajectory (QCT) simulations for $\sim$ 2000 initial conditions. Overall, the prediction accuracy as quantified by the root-mean-squared difference (~ 0.003) and the R^2 (~ 0.99) between the reference QCT and predictions of the STD model is high for the test set and off-grid state specific initial conditions and for initial conditions drawn from reactant state distributions characterized by translational, rotational and vibrational temperatures. Compared with a more coarse grained distribution-to-distribution (DTD) model evaluated on the same initial state distributions, the STD model shows comparable performance with the additional benefit of the state resolution in the reactant preparation. Starting from specific initial states also leads to a more diverse range of final state distributions which requires a more expressive neural network to be used compared with DTD. Direct comparison between explicit QCT simulations, the STD model, and the widely used Larsen-Borgnakke (LB) model shows that the STD model is quantitative whereas the LB model is qualitative at best for rotational distributions $P(j')$ and fails for vibrational distributions $P(v')$. As such the STD model can be well-suited for simulating nonequilibrium high-speed flows, e.g., using the direct simulation Monte Carlo method.

5.1 Introduction

Predicting the outcomes of chemical reactions is one of the essential tasks for efficient material design, engineering, or reaction planning.[186] Understanding chemical reactions at a molecular level can also shed light on the mechanisms underlying chemical transformations. However, the exhaustive characterization of reactions at the microscopic (i.e. state-to-state or STS) level quickly becomes computationally intractable using conventional approaches due to the rapid growth of the underlying state space.[187, 188] As an example, even for a reactive atom+diatom system (A+BC→AB+C) the number of internal states for diatoms AB and BC is $\sim 10^4$ which leads to $\sim 10^8$ state-to-state cross sections $\sigma_{v,j\rightarrow v',j'}(E_{\text{trans}})$ between initial (v, j) and final (v', j') rovibrational states at a given relative translational energy E_{trans}.[188] The estimated number of classical trajectories required for converged STS cross sections is $\sim \mathcal{O}(10^{13})$ assuming that 10^5 classical trajectories are sufficient for one converged cross section. For reactive diatom+diatom systems this number increases to $\sim \mathcal{O}(10^{20})$ which is currently unfeasible.[189]

Machine learning (ML) methods are well suited for such tasks as they are designed for large data sets and generalize well towards unseen input data.[186, 190] In particular, neural network (NN)-based models have successfully been used to predict the STS cross sections of reactive atom-diatom collision systems.[188] These models were trained on data obtained from explicit quasi-classical trajectory (QCT) simulations. Similarly, NN-based models were constructed at the distribution-to-distribution (DTD) level.[191] For a given set of distributions of initial states of reactants ($P(E_{\text{trans}})$, $P(v)$, $P(j)$), a DTD model aims at predicting the relative translational energy distribution $P(E'_{\text{trans}})$, together with the vibrational $P(v')$ and rotational $P(j')$ state distributions of the product. Compared with a STS

model, state specificity is lost in a DTD model as it follows how a distribution of initial reactant states is processed through interactions on a potential energy surface (PES), but does not keep track of the interrelations between individual initial and final states. This information loss makes DTD models computationally cheaper compared with STS models.

Motivated by these findings, the present work explores the possibility to conceive an intermediate model between the STS and DTD models which retains state specific information for the reactants. In the following it is demonstrated how a NN-based state-to-distribution (STD) model for a reactive atom+diatom system can be developed. The STD model is shown to predict product state distributions $P(E'_{\text{trans}}), P(v')$, and $P(j')$ given a specific initial reactant state (E_{trans}, v, j). The necessary reference data to train such a NN-based STD model was obtained from explicit quasi-classical trajectory (QCT) simulations for the $\text{N}(^4\text{S})+\text{O}_2(\text{X}^3\Sigma_\text{g}^-) \rightarrow \text{NO}(\text{X}^2\Pi) + \text{O}(^3\text{P})$ collision system as a proxy. As such, an STD model may be constructed from a STS model through coarse graining, i.e. by integration of the final states. Similarly, a DTD model can be obtained from an STD model by further coarse graining of the state-specific initial conditions. Note that such a coarse graining by means of integration does, however, incur a computational overhead. Moreover, the increase in information content going from a DTD model to a STD model, and finally to a STS model, also comes at an increased number of trainable parameters and, hence, increased computational cost both in training and evaluation of the model. Therefore, it is crucial to choose the appropriate model resolution for a given task. Finally, it is shown that the STD model realizes a favourable trade-off between computational cost and accuracy, i.e., information content. In particular, the STD model provides information at an appropriate resolution to be utilized as input for methods such as Direct Simulation Monte

Carlo (DSMC)[192] or computational fluid dynamics (CFD) simulations.[193]

This work is structured as follows. First, the methods including the data generation based on quasi-classical trajectory simulations, as well as the neural network architecture and its training are described. Next, the ability of the STD model to predict product state distributions from unseen, specific initial states of the reactant is assessed. Then, the differences between DTD and STD models at predicting product state distributions from initial state distributions is discussed. Finally, the performance of the STD model is compared with the widely used Larsen-Borgnakke [24] for simulations of nonequilibrium, high-speed flows, and then conclusions are drawn.

5.2 Methods

5.2.1 Quasi-Classical Trajectory Simulations

Explicit QCT calculations for the N + O_2 $\rightarrow$ NO + O reaction were carried out following previous work.[26, 39, 100–102] Specifically, the reactive channel for NO formation ($N(^4S)+O_2(X^3\Sigma_g^-) \rightarrow NO(X^2\Pi) + O(^3P)$) was considered here. For this, the $^4A'$ PES was chosen as NO formation is dominated by contributions from the $^4A'$ electronic state.[39] Hamilton's equations of motion were solved in reactant Jacobi coordinates using a fourth-order Runge-Kutta method with a time step of $\Delta t = 0.05$ fs, which guarantees conservation of the total energy and angular momentum.[102, 194]

For generating the training, test, and validation data set for the NN the following *state-specific* initial conditions were used: $(0.5 \leq E_{\text{trans}} \leq 8.0)$ eV with $\Delta E_{\text{trans}} = 0.5$ eV; $v = [0, 2, 4, 6, 8, 10, 12, 15, 18, 21, 24, 27, 30, 34, 38]$; and $0 \leq j \leq 225$ with

$\Delta j = 15$, resulting in 2184 different states. The impact parameter b was sampled from 0 to $b_{\max} = 12$ a_0 using stratified sampling.[26, 195] Ro-vibrational states of the reactant (O_2) and product diatom (NO) are determined from the semiclassical theory of bound states.[194] First, final vibrational and rotational states were determined as real numbers from the diatomic internal energy and angular momentum, respectively, whereas the translational energy is obtained from the relative velocity of the atom+diatom system. Ro-vibrational quantum numbers are then assigned as the nearest integers (v', j') using the histogram binning method. To conserve total energy, the ro-vibrational energy $E_{v'j'}$ is recomputed from semiclassical quantization[26, 194] using the quantum numbers (v', j') and the final translational energy for the atom+diatom system is adjusted using $E'_{\text{trans}} = E_{\text{tot}} - E_{v'j'}$. Product states were assigned using histogram binning ($0.1 \leq E'_{\text{trans}} \leq 19.8$) eV; $0 \leq v' \leq 47$ with $\Delta v' = 1$; $0 \leq j' \leq 240$ with $\Delta j' = 1$. Out of the 2184 initial reactant states, 7 (with $E_{\text{trans}} = 0.5$ eV) resulted in product state distributions with zero or negligible probability ($\max(P) < 10^{-5}$) which were not considered for the subsequent analysis. Consequently, 2177 initial reactant states together with the corresponding product state distributions obtained by QCT simulations constitute the reference data to train and test NN-based STD models in this work.

To evaluate the trained models, a second set of initial conditions was generated from reactant *state distributions*. For each trajectory they were randomly chosen using standard Monte Carlo methods.[26, 100] The initial relative translational energies E_{trans} were sampled from Maxwell-Boltzmann distributions ($0.0 \leq E_{\text{trans}} \leq 19.8$) eV with $\Delta E_{\text{trans}} = 0.1$ eV. Vibrational (v) and rotational (j) states were sampled from Boltzmann distributions, where $0 \leq v \leq 38$ with $\Delta v = 1$; and $0 \leq j \leq 242$ with $\Delta j = 1$. These distributions are characterized by T_{trans}, T_{vib}, and T_{rot}, respectively.[26, 195] For each set of temperatures $\boldsymbol{T} = (T_{\text{trans}}, T_{\text{vib}},$

T_{rot}), 80000 trajectories were run to obtain the product state distributions. First, models were constructed with $T_{\mathrm{rovib}} = T_{\mathrm{rot}} = T_{\mathrm{vib}}$, for which QCT simulations were performed at T_{trans} and T_{rovib} ranging from 5000 K to 20000 K in increments of 250 K. This yielded 3698 sets of reactant states and corresponding product state distributions. Next, for the more general case $T_{\mathrm{rot}} \neq T_{\mathrm{vib}}$, additional QCT simulations were performed for $T_{\mathrm{trans}} = 5000, 10000, 15000, 20000$ K with T_{vib} and T_{rot} each ranging from 5000 K to 20000 K in increments of 1000 K. Combining these additional 960 data sets with the 3698 sets from above leads to a total of 4658 data sets.

5.2.2 Data Preparation

An important step in conceiving a ML model is the preparation, representation and featurization of the data. For featurization the following properties were chosen as input to the NN: 1.) E_{trans}, 2.) vibrational quantum number v of the diatomic, 3.) rotational quantum number j of the diatomic, 4.) relative velocity of diatom and atom, 5.) internal energy $E_{v,j}$, of the diatom, 6.) vibrational energy $E_{v,j=0}$, of the diatom, 7.) rotational energy $E_{v=0,j}$, of the diatom, 8.) angular momentum of the diatom, 9-10.) the two turning points at each of the vibrational states of the reactant diatom, and 11.) the vibrational time period of the diatom. These features were already used successfully for the STS model.[188]

To represent the product state distributions, a grid-based (G-based) approach was used.[191] In a G-based approach, each product state distribution is characterized by its values at discrete grid points, referred to as "amplitudes" in the following. Figure 6.2 shows the product state distributions from QCT simulations (solid line) and their G-based representation (open symbols) for two exemplar re-

actant states. The G-based representation closely follows the true, underlying data from the QCT simulations. Thus, G-based product state distributions (i.e. amplitudes) are suitable to train the NN and the amplitudes also constitute the output of the trained NN. Calculating the product state amplitudes for all available data sets then allowed to train and test the NN. Subsequently, inter- and extrapolation can be performed to obtain a continuous prediction. This is referred to as the "STD model" in the following.

For the product state distributions it was found to be advantageous to consider the set $(P(E'_{\mathrm{int}}), P(v'), P(j'))$ instead of $(P(E'_{\mathrm{trans}}), P(v'), P(j'))$. Here, $E'_{\mathrm{int}} = E_{\mathrm{tot}} - E'_{\mathrm{trans}}$ is the internal energy after removing the translational energy. Note that $P(E'_{\mathrm{int}})$ and $P(E'_{\mathrm{trans}})$ contain the same information and can be interconverted because the total energy E_{tot} of the system is conserved. However, for representing $P(E'_{\mathrm{int}})$ fewer grid points are required than for representing $P(E'_{\mathrm{trans}})$. This is illustrated in Figure 5.2, where $P(E'_{\mathrm{trans}})$ and $P(E'_{\mathrm{int}})$ obtained

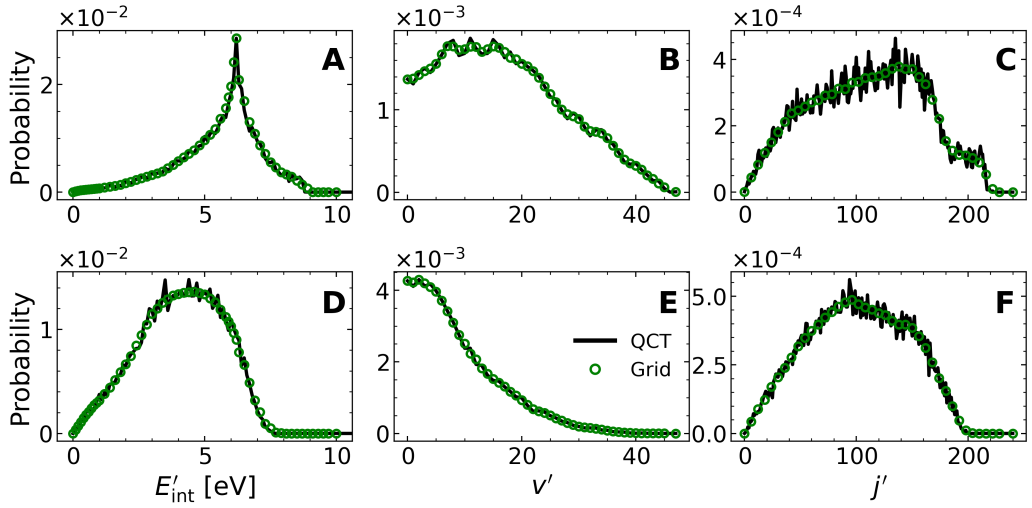

Figure 5.1: Product state distributions $P(E'_{\mathrm{int}})$, $P(v')$, and $P(j')$ obtained from QCT simulations (QCT), as well as the corresponding amplitudes that serve as a reference for training and testing the NN-based STD models (Grid). The product state distributions correspond to initial reactant states characterized by: (A to C) ($E_{\mathrm{trans}} = 3.0$ eV, $v = 34$, $j = 0$; $E_{\mathrm{int}} = 4.8$ eV), (D to F) ($E_{\mathrm{trans}} = 5.0$ eV, $v = 6$, $j = 45$; $E_{\mathrm{int}} = 1.5$ eV).

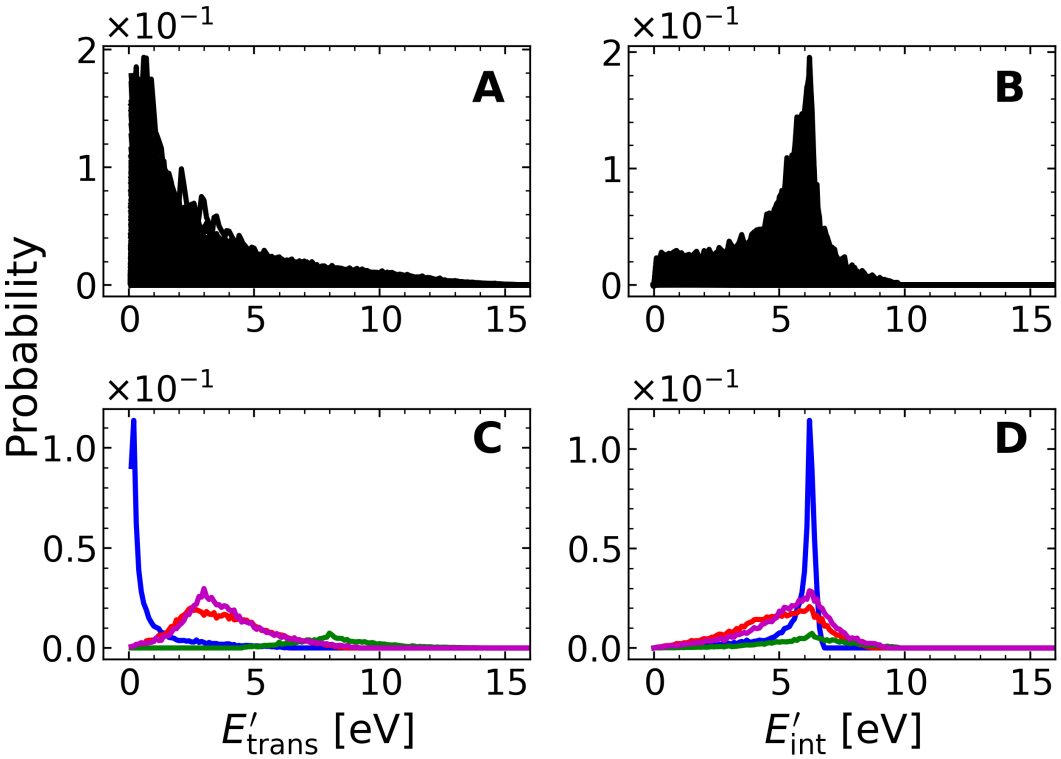

Figure 5.2: Distributions $P(E'_{\text{trans}})$ (panel A) and $P(E'_{\text{int}})$ (panel B) obtained from QCT simulations for each of the 2184 initial reactant states considered in this work displayed on top of each other. Panels C and D: a few selected distributions $P(E'_{\text{trans}})$ and $P(E'_{\text{int}})$ to highlight their different shapes that motivate the choice of $P(E'_{\text{int}})$ over $P(E'_{\text{trans}})$.

from explicit QCT simulations for all 2184 initial reactant states used to train and validate in this work are shown. While there are distributions $P(E'_{\text{trans}})$ which are non-zero at $E'_{\text{trans}} > 10$ eV, all $P(E'_{\text{int}})$ are zero for $E'_{\text{int}} > 10$ eV and grid points are only used up to this value.

The location and number of grid points to represent the product state distributions was motivated after inspection of the overall shape of these distributions. In particular, it was observed that a large number of $P(E'_{\text{int}})$ distributions exhibit a sharp peak for $E'_{\text{int}} \sim 6.2$ eV which is the dissociation energy of the product diatom NO (see Figures 6.2A, 5.2B and D).[196] Non-zero contributions to $P(E'_{\text{int}})$ at E'_{int} larger than the dissociation energy of the product diatom NO can be

attributed to the presence of quasi-bound states. Additionally, $P(E'_{\text{int}})$ can also increase rapidly for $E'_{\text{int}} < 1.0$ eV. Consequently, the grid for $P(E'_{\text{int}})$ was chosen more densely for $E'_{\text{int}} < 1.0$ eV and $E'_{\text{int}} \sim 6.2$ eV to capture these features ($E'_{\text{int}} = [0.0, 0.1, \cdots, 1.0], [1.2, 1.4, \cdots, 6.0], [6.1, 6.2, 6.3], [6.5, 6.7, \cdots, 9.7, 10.0]$ eV).

A considerable number of the final state vibrational distributions, $P(v')$, show a maximum for $v' \sim 0$ (see Figures 6.2B and 6.2E). For higher v', $P(v')$ typically decays rapidly but in general, the distributions display a variety of shapes. Hence, the corresponding grid was dense ($0 \leq v' \leq 47$ with $\Delta v' = 1$). Final state rotational distributions, $P(j')$, are closer in overall shape to one another compared with $P(E'_{\text{int}})$ or $P(v')$. In particular, $P(j')$ typically does not exhibit sharp features (see Figures 6.2C and D). Taking this into consideration, the grid for $P(j')$ was equidistant ($0 \leq j' \leq 240$ with $\Delta j' = 6$) and less dense than for the other two final state distributions.

The number of grid points for $(E'_{\text{int}}, v', j')$ was $(58, 47, 40)$, respectively. This is significantly more dense than the DTD model,[191] for which $(16, 16, 12)$ grid points were used and is attributed to the fact that the distributions considered here are more diverse and exhibit more detail, including sharp features. The shapes of the distributions $P(E'_{\text{int}})$, $P(v')$ or $P(j')$ are generally smooth across the ranges of E'_{int} and quantum numbers v' and j'. They also tend to vary smoothly as the initial state changes. However, when reaction channels open there can be sharp features in the probability distribution, see Figure 5.9. Because the grids used here are dense, linear interpolation can be used to obtain a continuous NN-based prediction of product state distributions at off-grid points.

Instead of directly sampling the product state distributions $P(x)$ at the grid points x_i to obtain the amplitudes in the G-based representation, local averaging according to

$$\bar{P}(x_i) = \frac{1}{2n+1} \sum_{j=i-n}^{i+n} P(x_j), \tag{5.1}$$

was performed. Here, the number of neighbouring data points x_j (not necessarily grid points) considered for averaging is $n \in [0, n_{\max}]$. If there are fewer neighbouring data points to the right and/or to the left of grid point x_i when compared with $n_{\max}$, n was chosen as the maximum number of neighbouring data points available to both sides, otherwise $n = n_{\max}$. Consequently, the first and last data points were assigned unaveraged values. Note, that the value of $n_{\max}$ can differ for each of the 3 degrees of freedom $(E'_{\text{int}}, v', j')$. Additionally, no local averaging was performed for "sharp" peaks and only a reduced amount was applied at nearby points. A maximum was classified as "sharp" if the slopes of the two lines fit to neighbouring data points to the left and right of it exceeded a given threshold, see Section 5.4 in the SI for details.

5.2.3 Neural Network

The NN architecture for the STD model is shown in Figure 6.1 and is inspired by ResNet.[197] The input and output layers consist of 11 inputs (the 11 features, see above) and $58+47+40 = 145$ output nodes for the amplitudes characterizing the product state distributions. The main part of the NN consists of 7 residual layers, each of which is again composed of two hidden layers, and two separate hidden layers. The shortcut connections, characteristic for residual layers, help to address the vanishing gradient problem.[197] Hidden layers 1 to 14 are each composed of 11 nodes, whereas hidden layers 14 to 16 are each composed of 44 nodes which leads to a "funnel-like" NN architecture that helps to bridge the

gap between the small number of inputs (11) and the large number of outputs ($58 \times 47 \times 40 = 109040$). The NN for the STD model has 3746 trainable parameters compared with ≈ 140 parameters that are used in the DTD model.[191] The larger number of trainable parameters for STD can be attributed to the larger diversity of product state distributions requiring a denser grid, i.e., a wider output layer. Moreover, the decrease in the number of free model parameters in going from STD to DTD reflects the reduced information content which is the state-specificity on the reactant side.

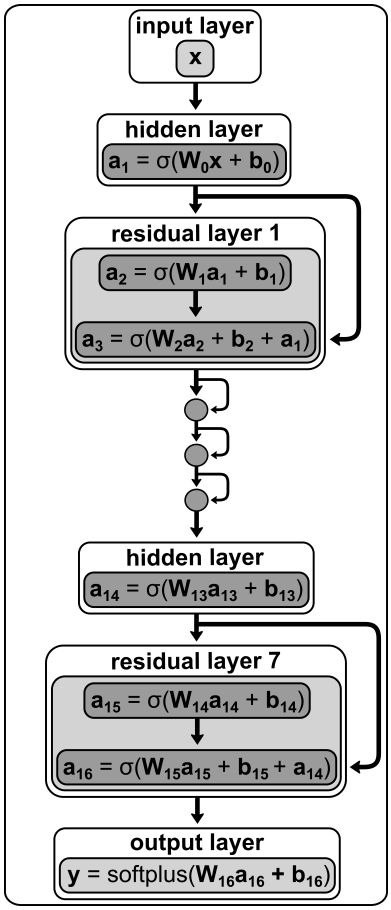

Figure 5.3: Schematic for the NN architecture underlying the STD model. The activation vector of each layer is denoted as $\mathbf{a}_i$, and the input and output vectors are $\mathbf{x}$ and $\mathbf{y}$. The weight matrix and bias vector for each layer are denoted by $\mathbf{W}_i$ and $\mathbf{b}_i$, respectively. The activation function of the hidden layers is $\sigma(\boldsymbol{z})$ and corresponds to a shifted softplus[198] function $\sigma(\boldsymbol{z}) = \ln(1 + e^{\boldsymbol{z}}) - \ln(2)$, where softplus($\boldsymbol{z}$)= $\ln(1 + e^{\boldsymbol{z}})$.[199, 200] Activation functions act element-wise on vectors.

Before training the NN inputs were standardized via the transformation

$$x_i' = (x_i - \bar{x}_i)/\sigma_i, \tag{5.2}$$

and the NN outputs are normalized

$$x_i' = x_i/\sigma_i, \tag{5.3}$$

where x_i denotes the i-th input/output (as specified above), and $\bar{x}_i$ and σ_i are the mean and standard deviation of the distribution of the i-th input/output over the entire training data. Standardization results in distributions of the transformed inputs x_i' over the training data that are characterized by ($\bar{x}_i' = 0$, $\sigma_i' = 1$) and allows prediction of high- and low-amplitude data with similar accuracy. Also, standardization generally yields faster convergence of the gradient-based optimization.[200] The distributions of the transformed outputs x_i' over the training data have ($\bar{x}_i' = \bar{x}_i$, $\sigma_i' = 1$) through normalization. This enables the use of a root-mean-squared deviation (RMSD) loss function

$$\mathcal{L} = \sqrt{\frac{1}{N}\sum_{i=1}^{N}(y_i - y_i')^2}. \tag{5.4}$$

where y_i and y_i' denote the value of the i-th predicted and reference amplitude, respectively. Unnormalized output may drastically differ in amplitude and spread which can lead to poor performance of the RMSD loss. However, this ignores inherent sampling noise arising from potentially unconverged QCT simulations, a point considered explicitly in the following. Using a softplus activation function for the output layer was found to significantly increase the NN prediction accuracy compared in contrast to a scaled hyperbolic tangent. Specifically, using softplus removes unphysical undulations and unphysical negative probabilities which would arise in the predicted product distributions in regions where the

corresponding reference distributions are small or zero.

The weights and biases of the NN were initialized according to the Glorot scheme[201] and optimized using Adam[202] with an exponentially decaying learning rate. The NN was trained using TensorFlow[203] and the set of weights and biases resulting in the smallest loss as evaluated on the validation set were subsequently used for predictions. From the total number of $N_{\text{tot}} = 2177$ data sets, $N_{\text{train}} = 1700$ were randomly selected for training, $N_{\text{valid}} = 400$ were used for validation and $N_{\text{test}} = 77$ were used as the test set.[188] All NNs underlying the STD models in this work were trained on a 3.6 GHz Intel Core i7-9700k CPU resulting in training times shorter than 4 minutes.

5.3 Results

First, the performance of the STD model in predicting product state distributions given specific initial reactant states is discussed. This is done for the test set ($N_{\text{test}} = 77$) and a considerably broader set of initial conditions not covered in training or validation (off-grid). In a next step, the capability of the STD model to predict product state distributions given distributions over initial reactant states is assessed. These include distributions with $T_{\text{trans}} = T_{\text{vib}} = T_{\text{rot}}$, $T_{\text{trans}} \neq T_{\text{vib}} = T_{\text{rot}}$, $T_{\text{trans}} = T_{\text{rot}} \neq T_{\text{vib}}$ as the most relevant case for hypersonics, and $T_{\text{trans}} \neq T_{\text{vib}} \neq T_{\text{rot}}$ as the most general case. The results for $T_{\text{vib}} \neq T_{\text{rot}}$ are also compared with those from the DTD model[191].

5.3.1 Performance for Given Initial States

The performance measures to assess the quality of the STD model considered are $\text{RMSD} = \sqrt{\sum_{i=1}^{N} \frac{(P_i - O_i)^2}{N}}$ and $R^2 = 1 - \sum_{i=1}^{N} \frac{(P_i - O_i)^2}{(O_i - \langle O \rangle)^2}$ where P_i is the predicted value i from STD, O_i is the observed (reference) value i from QCT, and $\langle O \rangle$ is the average for a given initial condition and a given degree of freedom. The performance measures are determined for all three degrees of freedom individually and for their entirety. The subscript "LG" refers to evaluating the STD and QCT models only on the locally averaged grid points, whereas the subscript "FG" refers to using all grid points at which QCT data is available (full grid). For this comparison the reference and predicted amplitudes are first normalized with the normalization calculated by numerical integration of the reference QCT distributions. Predictions for STD at off-grid points are obtained through linear interpolation.

STD model	RMSD_{LG}	${R^2}_{\text{LG}}$	RMSD_{FG}	${R^2}_{\text{FG}}$
overall	0.0039	0.9886	0.0033	0.9890
E'_{int}	0.0095	0.9915	0.0077	0.9906
v'	0.0020	0.9885	0.0018	0.9895
j'	0.0003	0.9860	0.0003	0.9867

Table 5.1: Performance measures RMSD and R^2 for the test set ($N_{\text{test}} = 77$). The mean error is calculated separately using the distributions of E'_{int}, v', or j' and then averaged to obtain an overall performance measure. Subscripts "LG" and "FG" refer to the "local grid" (on which STD is evaluated) and "full grid" (on which the reference QCT results are available).

The performance measures of the STD model on the test set are summarized in Table 5.1. Overall, $\text{RMSD}_{\text{LG}} = 0.0039$ and $R^2_{\text{LG}} = 0.9886$ values confirm that the NN gives highly accurate predictions of the amplitudes on a grid characterizing the product state distributions. The performance is preserved even for the "full grid" (FG). The decreasing performance for predicting $P(E'_{\text{int}})$ compared to $P(v')$ or $P(j')$ (see RMSD and R^2 in Table 5.1) can be attributed to the fact that

$P(E'_{\text{int}})$ varies strongly in shape but is typically peaked which is challenging to capture using a G-based approach. In contrast, $P(j')$ varies least and can thus be predicted with the highest accuracy as can be seen from the lowest RMSD and R^2 values. The small difference in accuracy when comparing RMSD_{LG} and R^2_{LG} to RMSD_{FG} and R^2_{FG} arises because linear interpolation is used to obtain predicted amplitudes between the designated grid points.

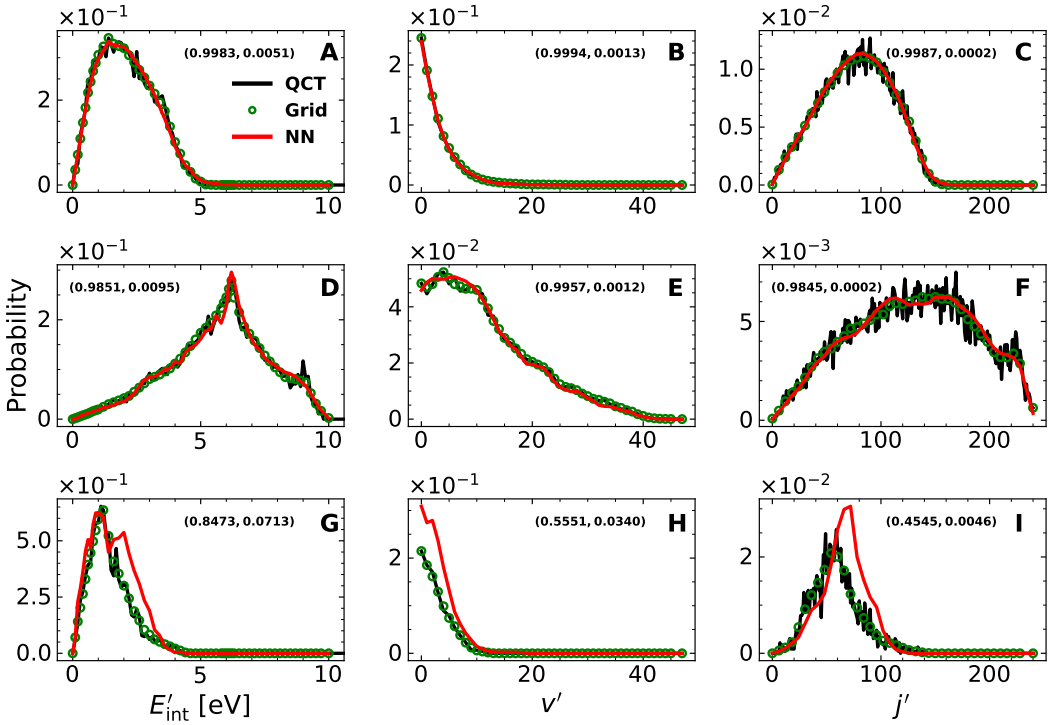

Figure 5.4: Product state distributions obtained from explicit QCT simulations (QCT), and the corresponding reference amplitudes (Grid) and STD model predictions (NN) for three initial conditions from the test set (77 sets) not used in the training. The predictions for these three data sets are characterized by (A to C) a R^2_{LG} value closest to the mean R^2_{LG} value as evaluated over the entire test set, (D to F) the largest and (G to I) smallest R^2_{LG} value in the test set, respectively. (A to C) ($E_{\text{trans}} = 3.5$ eV, $v = 0$, $j = 45$, $E_{v,j} = 0.85$ eV), (D to F) ($E_{\text{trans}} = 6.0$ eV, $v = 21$, $j = 0$, $E_{v,j} = 1.11$ eV), (G to I) ($E_{\text{trans}} = 0.5$ eV, $v = 0$, $j = 135$, $E_{v,j} = 0.32$ eV). For each distribution $(R^2_{\text{LG}}, \text{RMSD}_{\text{LG}})$ values are provided.

Predictions of the STD model for three different sets of initial reactant states from the test set are shown in Figure 6.5. These data sets are characterized by 1) a R^2_{LG} value closest to the average R^2_{LG} value over the entire test set (77 sets) (pan-

els A to C), and R^2_{LG} values corresponding to 2) the largest (panels D to F; "best performing") and 3) the smallest (panels G to I; "worst performing") R^2_{LG} values in the test set, respectively. The amplitudes of the product state distributions in panels D to F (lowest overall R^2_{LG}) are roughly one order of magnitude smaller compared to the other two data sets (panels A to F). This can be explained by the fact that the corresponding initial reactant state is characterized by $E_{\mathrm{trans}} = 0.5$ eV, which results in a low reaction probability and renders a reactive collision a "rare" event. Consequently, the uncertainty arising from finite sample statistics in the QCT simulations is largest for such data sets. Moreover, 7 data sets with $E_{\mathrm{trans}} = 0.5$ eV had already been excluded from the data set prior to training the NN because the reaction probability obtained from QCT was negligible. This naturally biases the NN training and predictions towards data sets with a larger reaction probability.

The product state distributions shown in Figure 6.5 demonstrate the variety of shapes and features that are present. This is a major difference compared to the product state distributions that were considered for the DTD models. There, only $P(v')$ was subject to significant variations, whereas $P(E'_{\mathrm{trans}})$ and $P(j')$ showed less variability. Even for $P(v')$, three major classes of distributions could be distinguished which is not the case for STD. This variability explains the need for a denser grid and a more expressive NN in the present work.

Next, the performance of the STD model on a larger grid including parts of the training, test, validation set and additional initial (v, j) combinations is considered. For this, QCT simulations were carried out for $v \in [0, 15]$ with $\Delta v = 1$ and for $j = [0, 7, 15, 22, ..., 157, 165]$. The entire grid considered included 368 points and 50000 QCT simulations for every (v, j) combination were run at $E_{\mathrm{trans}} = 4.0$

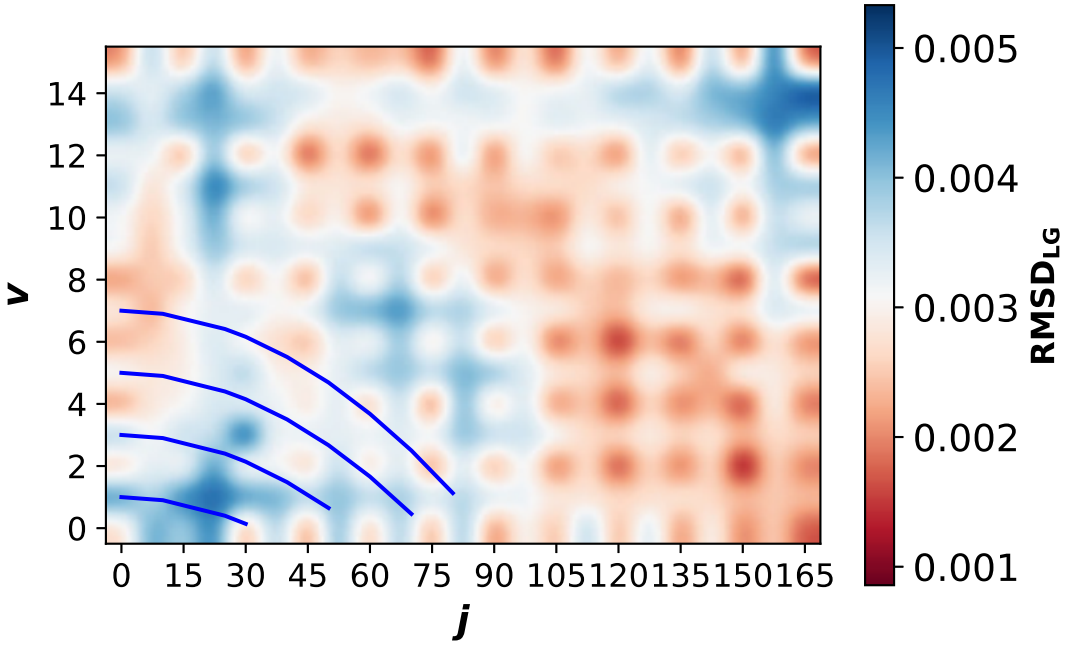

Figure 5.5: 2D map for $\mathrm{RMSD}_{\mathrm{LG}}(v, j)$ between QCT and STD predictions for the product state distributions $P(E'_{\mathrm{int}})$, $P(v')$, and $P(j')$ for given initial (v, j). The STD model was evaluated at fixed $E_{\mathrm{trans}} = 4.0$ eV for the grid points $v = [0, 2, \cdots, 14]$ and $j = [0, 15, \cdots, 165]$ used for training, validation, and test. For the off-grid points, the $(v, j)-$combinations included $v = [1, 3, \cdots, 15]$ and $j = [7, 22, \cdots, 157]$. The solid blue lines indicate constant rovibrational energies of 0.2850 eV, 0.6552 eV, 1.0142 eV, and 1.3622 eV. For the initial condition $(v = 13, j = 157)$ a comparatively high RMSD (~ 0.005) is obtained (blue).

eV. Figure 6.6 reports the $\mathrm{RMSD_{LG}}$ between the product state distributions obtained from QCT and those predicted by the STD model. The two-dimensional surface $\mathrm{RMSD_{LG}}(v, j)$ (for R^2_{LG} see Figure 5.10) exhibits a visible checkerboard pattern that reflects states (v, j) used for training (on-grid) and off-grid points which were not included in the training. Across the entire (v, j) state space the performance of STD is good. Despite the low overall $\mathrm{RMSD_{LG}}$, there are regions (blue) that are associated with larger differences between the reference QCT amplitudes and those from the STD model. For low (v, j) one reason for the somewhat larger $\mathrm{RMSD_{LG}}$ is the low reaction probability whereas for high (v, j) neglecting ro-vibrational coupling may lead to increased errors. A comparison of the final state distributions from QCT and the STD model for ($E_{\mathrm{trans}} = 4.0$ eV, $v = 13, j = 157$) and ($E_{\mathrm{trans}} = 4.0$ eV, $v = 1, j = 22$) is reported in Figures 5.11 and 5.12, respectively. A similar deterioration of performance in the high temperature regime was, for example, found from the surprisal model applied to the N_2+N reaction[204].

5.3.2 Performance for Initial Conditions from Reactant State Distributions

Next, the ability of the STD model to predict product state distributions given initial reactant state distributions is assessed. For this, the STD model is tested for different types of initial conditions by comparing reference product state distributions from explicit QCT simulations with those predicted by the model. For a given set of initial reactant state distributions initial conditions $(E_{\mathrm{trans}}, v, j)$ are generated through Monte Carlo sampling. In the limit of a sufficient number of samples, the average of the product state distributions predicted by the STD model will converge to the product state distributions associated with the given

reactant state distributions. Sampling 10000 initial conditions is sufficient to converge the product state distributions obtained from STD (see Figure 5.13A). This compares with $\sim 10^6$ that are required for QCT simulations shown in Figure 5.13B. The decrease in the number of samples required for convergence is due to the more coarse-grained nature of the STD model compared to QCT as the STD model lacks state-to-state specificity for the products.

Four distinct cases of thermal distributions are considered in the following: $T_{\text{trans}} = T_{\text{vib}} = T_{\text{rot}}$, $T_{\text{trans}} \neq T_{\text{vib}} = T_{\text{rot}}$, $T_{\text{trans}} = T_{\text{vib}} \neq T_{\text{rot}}$, and $T_{\text{trans}} \neq T_{\text{vib}} \neq T_{\text{rot}}$. The performance measures of STD evaluated for the four cases are summarized in Table 5.2. In all cases the STD model provides an accurate prediction of product state distributions given thermal reactant state distributions with $\text{RMSD}_{\text{FG}} \approx 0.003$ and $R^2_{\text{FG}} \approx 0.996$. No significant differences in STD model performance for the different cases is observed which demonstrates that the STD model is generic in nature and applicable to reactant state distributions of arbitrary shape with significant weight over the range of initial reactant states considered in training. The decreased level of performance for predicting $P(E'_{\text{int}})$ distributions compared to $P(v')$ or $P(j')$ is again attributed to stronger variation in shapes and peaks near the NO dissociation as was already found for final state distributions from individual initial reactant states, see Table 5.1. Moreover, the cutoff at $E_{\text{trans}} = 8.0$ eV in the training data of the STD model becomes relevant for $P(E'_{\text{int}})$ distributions at high temperatures and may lead to a decrease in performance.

For the most general case $T_{\text{trans}} \neq T_{\text{rot}} \neq T_{\text{vib}}$, 840 temperature combinations were generated. As Figure 6.7 demonstrates the STD model reliably captures overall shapes and features such as the position of maxima even for the worst

	$\mathrm{RMSD_{FG}}$				R^2_{FG}			
	Overall	$P(E'_{\mathrm{int}})$	$P(v')$	$P(j')$	Overall	$P(E'_{\mathrm{int}})$	$P(v')$	$P(j')$
$T_{\mathrm{trans}} = T_{\mathrm{vib}} = T_{\mathrm{rot}}$	0.0029	0.0079	0.0007	0.0001	0.9965	0.9912	0.9993	0.9990
$T_{\mathrm{trans}} \neq T_{\mathrm{vib}} = T_{\mathrm{rot}}$	0.0028	0.0078	0.0007	0.0001	0.9961	0.9904	0.9990	0.9990
$T_{\mathrm{trans}} = T_{\mathrm{vib}} \neq T_{\mathrm{rot}}$	0.0030	0.0083	0.0007	0.0001	0.9961	0.9900	0.9992	0.9990
$T_{\mathrm{trans}} \neq T_{\mathrm{vib}} \neq T_{\mathrm{rot}}$	0.0030	0.0081	0.0007	0.0001	0.9953	0.9885	0.9985	0.9989

Table 5.2: Performance comparison of the STD model in terms of $\mathrm{RMSD_{FG}}$ and R^2_{FG} for the 4 different temperature sets: $T_{\mathrm{trans}} = T_{\mathrm{vib}} = T_{\mathrm{rot}}$ (61 sets), $T_{\mathrm{trans}} \neq T_{\mathrm{vib}} = T_{\mathrm{rot}}$ (3637 sets), $T_{\mathrm{trans}} = T_{\mathrm{vib}} \neq T_{\mathrm{rot}}$ (60 sets), and $T_{\mathrm{trans}} \neq T_{\mathrm{vib}} \neq T_{\mathrm{rot}}$ (840 sets).

performing data set (panels G to I). This is remarkable as the shapes of $P(E'_{\mathrm{int}})$ and $P(v')$ can vary appreciably. The distribution of R^2 values for all 840 data sets also demonstrates high prediction accuracy, in particular for $P(v')$ and $P(j')$. The specific case $T_{\mathrm{trans}} \neq T_{\mathrm{vib}} = T_{\mathrm{rot}}$ is considered in Figure 5.14. Panels 5.14A to C are for the best performing STD model compared with QCT data whereas panels D to F are representative for the average R^2_{FG}. Both examples demonstrate that shapes and location of maxima are reliably captured by predictions based on the STD model. Even for the worst performing STD model (panels G to I) the important features of the distributions are still captured reliably. Finally, Figures 5.14 J to L report the distribution $P(R^2_{\mathrm{FG}})$ for all 3637 models evaluated for $T_{\mathrm{trans}} \neq T_{\mathrm{vib}} = T_{\mathrm{rot}}$. For all distributions $R^2_{\mathrm{FG}} > 0.95$ with $P(j')$ performing best.

A direct comparison of the STD and DTD models is reported in Table 5.3. The two models perform on par for all measures and all degrees of freedom except for E'_{int}. This is despite the fact that the DTD model was explicitly trained on these thermal distributions (4658 data sets in total) and further underlines the predictive power of the STD model. Also, it should be noted that for the DTD model E'_{trans} instead of E'_{int} was used for training. Given the excellent performance of both models, the differences appear to be negligible. As such, STD represents a highly accurate approach to obtain product state distributions given

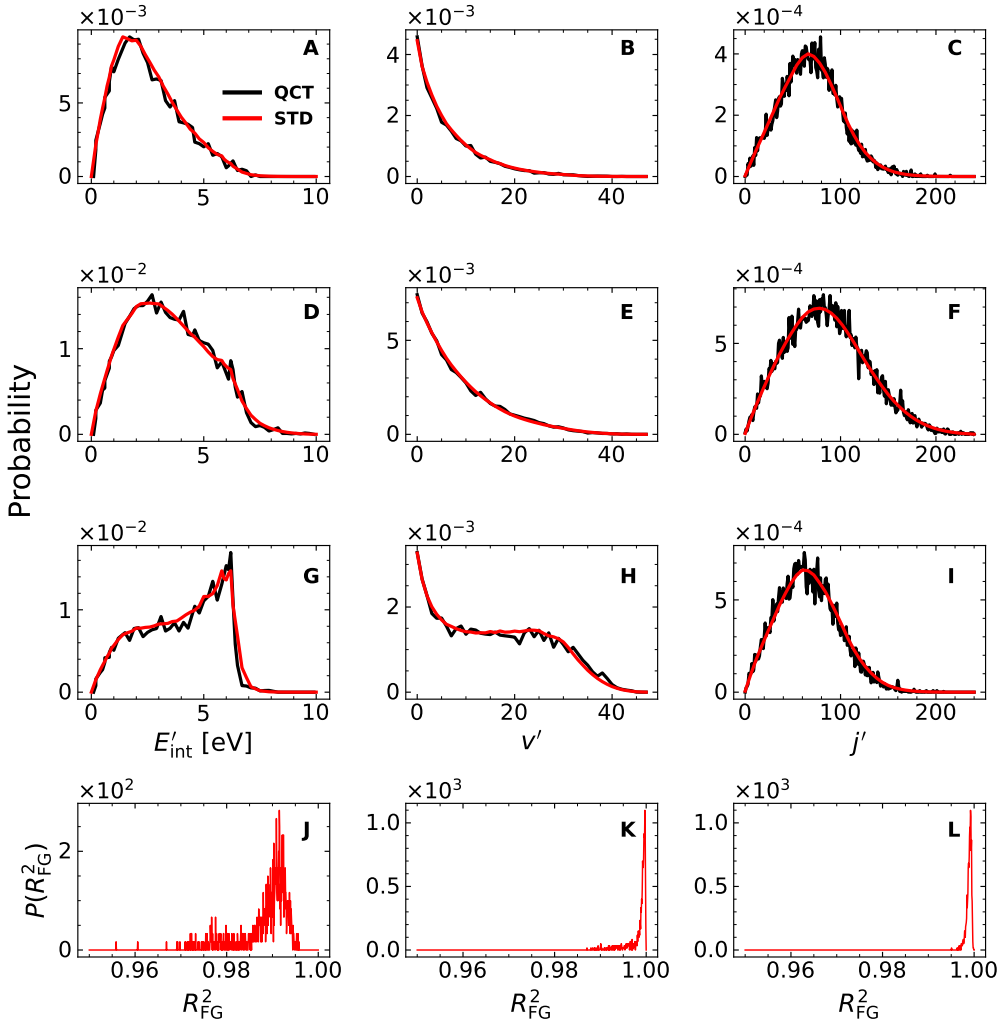

Figure 5.6: Product state distributions for $T_{trans} \neq T_{rot} \neq T_{vib}$ obtained from STD and compared with explicit QCT simulations. Panels A-C: best performing prediction (largest R^2_{FG}) for T_{trans} = 10000 K, T_{vib} = 6000 K , T_{rot} = 5000 K; panels D-F: prediction closest to the mean R^2_{FG} for T_{trans} = 5000 K, T_{vib} = 8000 K, T_{rot} = 13000 K; panels G-I: worst performing model (smallest R^2_{FG}) value for T_{trans} = 5000 K, T_{vib} = 18000 K, T_{rot} = 8000 K. Panels J-L: normalized distributions $P(R^2_{FG})$ for the complete set of 840 temperatures ($T_{trans} \neq T_{rot} \neq T_{vib}$), respectively, (J) $P(E'_{int})$, (K) $P(v')$ and (L) $P(j')$.

initial state specific reaction states. The decreased level of performance for predicting $P(E'_{int})$ distributions compared to $P(v')$ or $P(j')$ (see $RMSD_{FG}$ and R^2_{FG}) has several origins. First, $P(E'_{int})$ distributions vary strongly in shape and are typically peaked (see Figure 5.2) which is challenging to capture using a G-based approach. Secondly, for highly excited (v', j') states rovibrational coupling in the diatomic product molecule becomes more important. Explicitly accounting

for this coupling during the data preparation may further improve the predictive power of STD. In contrast to $P(E'_{\mathrm{int}})$, rotational distributions $P(j')$ vary least and can thus be predicted with the highest accuracy. Moreover, the cutoff at $E_{\mathrm{trans}} = 8.0$ eV in the training data of the STD becomes relevant for $P(E'_{\mathrm{int}})$ distributions at high temperatures and may lead to a decrease in performance. The small decrease in accuracy when comparing $\mathrm{RMSD}_{\mathrm{LG}}$ and R^2_{LG} to $\mathrm{RMSD}_{\mathrm{FG}}$ and R^2_{FG}, see Table 5.3, arises because of the linear interpolation to obtain predicted amplitudes between the designated grid points.

	$\mathrm{RMSD}_{\mathrm{FG}}$		R^2_{FG}	
	STD|QCT	DTD|QCT	STD|QCT	DTD|QCT
overall	0.0030	0.0017	0.9953	0.9988
E'_α	0.0081	0.0042	0.9885	0.9985
v'	0.0007	0.0008	0.9985	0.9988
j'	0.0001	0.0001	0.9989	0.9991

Table 5.3: Performance of STD and DTD models for $T_{\mathrm{rot}} \neq T_{\mathrm{vib}}$ (960 data sets) compared with QCT results for initial conditions from initial thermal distributions. For the STD model $\alpha = \mathrm{int}$ and for DTD $\alpha = \mathrm{trans}$. Performance measures (averaged over the all data sets) $\mathrm{RMSD}_{\mathrm{FG}}$ and R^2_{FG} are computed by comparing QCT data with the STD or DTD model predictions over the grid for which explicit QCT data is available. For $T_{\mathrm{trans}} = 5000, 10000, 15000, 20000$ K a set of 960 temperatures is evaluated with $T_{\mathrm{rot}} \neq T_{\mathrm{vib}}$ ranging from 5000 to 20000 K with $\Delta T = 1000$ K.

It is also of interest to compare the performance of STD in predicting QCT data with the fidelity of the QCT data itself. As training of the NN is based on final state distributions from 8×10^4 trajectories for each initial condition it is likely that the training set does not contain fully converged reference information. To this end, a much larger number ($N_{\mathrm{C}} = 5 \times 10^6$) of QCT simulations was carried out for a few initial conditions to determine the "ground truth" and were compared with final state distributions from only $N_{\mathrm{U}} = 5 \times 10^4$ samples. The correlation for the bin-occupation between the "ground truth", i.e. "converged" distributions from N_{C} samples, and the unconverged distributions using N_{U} samples is $R^2 \sim 0.99$ or better for all four initial conditions considered and all three

degrees of freedom, see Figure 5.15. Hence, the quality of the QCT reference data used for training the NN is comparable to the performance of the NN itself. The relative error between distributions from "ground truth" and the unconverged samples is around 0.2, see Figure 5.16. Thus, the χ^2 (rescaled mean squared error) between STD and reference QCT simulations accounting for the fact that the QCT input to train the NN is not fully converged is about 5 times larger than the RMSD, which yields $\chi^2 \sim 0.005$. One possible way of looking at this is to consider the amount of information (or signal) compared to the amount of noise. This "signal-to-noise ratio" should increase $\propto \sqrt{N}$ where N is the number of samples, assuming that the noise is stochastic and arising from insufficient sampling. As seen in Figure 5.16, when the number of samples in a channel is above ~ 10, the noise/signal is 0.1.

The relevance of "rare events" is a major difference when considering product state distributions from individual initial reactant states compared to initial conditions from reactant state distributions. When applied to individual initial conditions it was found that the STD model performance decreases for $E_{\text{trans}} \leq 1.0$ eV, i.e. for initial conditions with low reaction probability. The corresponding product state distributions are noisy and show large variations due to finite sample statistics from QCT. This may be improved in future work through importance sampling of the impact parameter. While rare events are crucial for an accurate description of certain physical phenomena, such as plasma formation,[205] they do *not* constitute a significant contribution to product state distributions. As such, for observables that involve integration of a product state distribution, such as reaction rates, the decrease of performance of the STD model with regards to rare events is also negligible.

From the STD-predicted product state distributions, $T-$dependent reaction rates can be obtained and compared with rates from explicit QCT simulations. In general, such a rate is determined from

$$k(T) = g(T)\sqrt{\frac{8k_{\mathrm{B}}T}{\pi\mu}}\pi b_{\mathrm{max}}^2 P_{\mathrm{r}}, \tag{5.5}$$

where P_{r} is the probability for a reaction to occur. For QCT simulations $P_r = \frac{N_{\mathrm{r}}}{N_{\mathrm{tot}}}$ where N_{r} is the number of reactive trajectories and N_{tot} is the total number of trajectories run. For the STD model, $P_{\mathrm{r}} = \int_{E=0}^{E_{\mathrm{max}}} P(E)dE$ where $E = E'_{\mathrm{int}}$. For the forward $\mathrm{N}(^4\mathrm{S})+\mathrm{O}_2(\mathrm{X}^3\Sigma_{\mathrm{g}}^-) \rightarrow \mathrm{NO}(\mathrm{X}^2\Pi) + \mathrm{O}(^3\mathrm{P})$ reaction on the $^4\mathrm{A}'$ electronic state the degeneracy factor $g(T) = 1/3$ and μ is the reduced mass of the reactants.[58] The two approaches are compared in Figure 5.7 and favourable agreement is found over a wide temperature range. Hence, the STD model can also be used to determine macroscopic quantities such as realistic reaction rates which is essential. The decrease in prediction accuracy at the highest temperatures may be attributed to the cutoff at $E_{\mathrm{trans}} = 8.0$ eV in the training data of the STD. Cross sections $\sigma = \pi b_{\mathrm{max}}^2 P_{\mathrm{r}}$ were also determined for the test set ($N_{\mathrm{test}} = 77$). Typical values for σ from the QCT simulations are $\sigma \sim 9 \times 10^{-15}$ cm^2 which compares with those from the STD model of $\sigma \sim 8.5 \times 10^{-15}$ cm^2.

Finally, it is also of interest to compare the computational cost for evaluating the STD and DTD models. Here, a single evaluation refers to the prediction of the product state distributions at 201, 48, and 241 evenly spaced points for E'_{int} (for STD) or E'_{trans} (for DTD) between 0 and 20 eV, $v' = 0 - 47$, and $j' = 0 - 240$, respectively, for a given reactant state distribution. The evaluation time for processing 50 reactant state distributions randomly selected from the total set of 4658 distributions is (98.01 ± 5.95) s using the STD model and (1.03 ± 0.01) s using the DTD model on a 3.6 GHz Intel Core i7-9700K CPU. The difference of

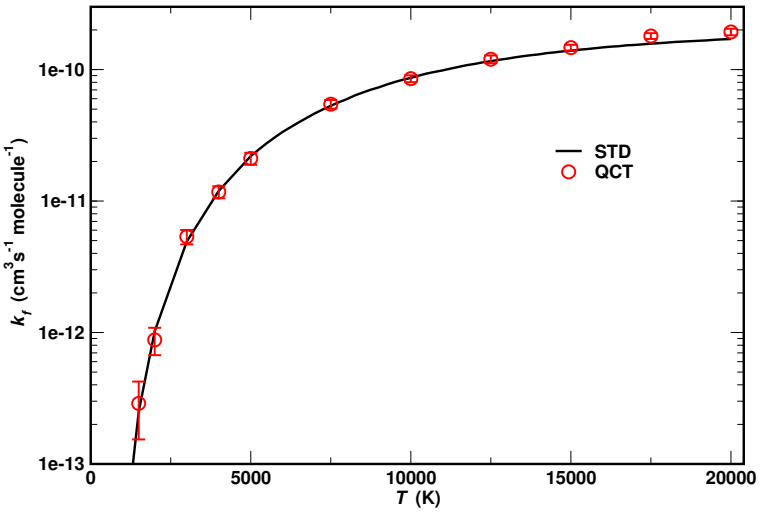

Figure 5.7: The thermal forward rate k_f calculated from QCT (open red circle) and STD model (solid black line) for the $^4A'$ state of the $N(^4S)+O_2(X^3\Sigma_g^-) \rightarrow NO(X^2\Pi) + O(^3P)$ reaction between 1500 and 20000 K. The present rates agree quantitatively with those directly obtained from QCT simulations.[58] It is interesting to note that significant differences between the rates from QCT simulations and those from the STD model arise only for the highest temperatures for which pronounced $v - j$ coupling is expected.

two orders of magnitude is explained as follows. For the STD model the NN is considerably larger and STD requires 10000 NN-evaluations for a given reactant state distribution. Contrary to that, for DTD only one evaluation is required. On the other hand, for STD linear interpolation is used to obtain an amplitude whereas DTD needs to evaluate a computationally costly kernel-based interpolation.

5.4 Discussion and Conclusion

The present work introduces a machine-learned state-to-distribution model for predicting final state distributions from specific initial states of the reactants. The STD model achieves a good performance, see Tables 5.1 and 5.3, and accurately predicts product state distributions as compared with reference QCT simulations. The model also allows to determine observables such as thermal

reaction rates, see Figure 5.7.

One specific motivation to develop such an STD model is for generating meaningful input for direct simulation Monte Carlo [22] (DSMC) simulations. DSMC is a computational technique to simulate nonequilibrium high-speed flows and is primarily applied to dilute gas flows. The method is particle-based, where each particle typically represents a collection of real gas molecules, and transports mass, momentum, and energy. Models are required to perform collisions between particles by which they exchange momentum and energy with one another. For instance, given the internal energy states and relative translational energy of reactants in a colliding pair of particles, the total collision energy (TCE) model proposed by Bird is a widely used quantity to estimate the reaction probability [22]. Once a colliding pair is selected for a collision, a key model output is the post-collision energy distribution from which product states are subsequently sampled. The state-of-the-art model for such a purpose is a phenomenological model proposed by Larsen-Borgnakke [24] (LB). The explicit form of the LB model for sampling the rotational and vibrational energy after a reaction is

$$f_{\mathrm{LB}} = \frac{\left[1 - \dfrac{\varepsilon_i'}{\varepsilon_{coll}}\right]^{\zeta_{\mathrm{tr}}/2-1}}{\sum_i \left[1 - \dfrac{\varepsilon_i'}{\varepsilon_{coll}}\right]^{\zeta_{\mathrm{tr}}/2-1}}, \tag{5.6}$$

where ε_i' corresponds to ε_v' or ε_j' for post-reaction vibrational and rotational energy respectively and $\varepsilon_{\mathrm{coll}} = \varepsilon_{\mathrm{v}}' + \varepsilon_{\mathrm{j}}' + \varepsilon_{\mathrm{t}}'$. That is, the collision energy is the sum of the internal energy and translational energy post-collision (or pre-collision, due to conservation of total energy in the system the two coincide). In Eq. 5.6, $\zeta_{\mathrm{tr}} = 5 - 2\omega$ is related to the translational degrees of freedom and the collision

cross section parameter ω which is obtained by fitting collision cross sections such that the viscosity $\mu \propto T^{\omega}$. of a gas is recovered. In essence, the LB model is not based on state-specific probabilities of product states in reactions. Figure 5.8 reports the LB model results together with predictions from the STD model and reference QCT simulations. The significant discrepancies are not surprising as the LB model samples post-collision states from a local equilibrium distribution. This is the advantage of the STD model which is based on state-specific reference calculations from QCT simulations.

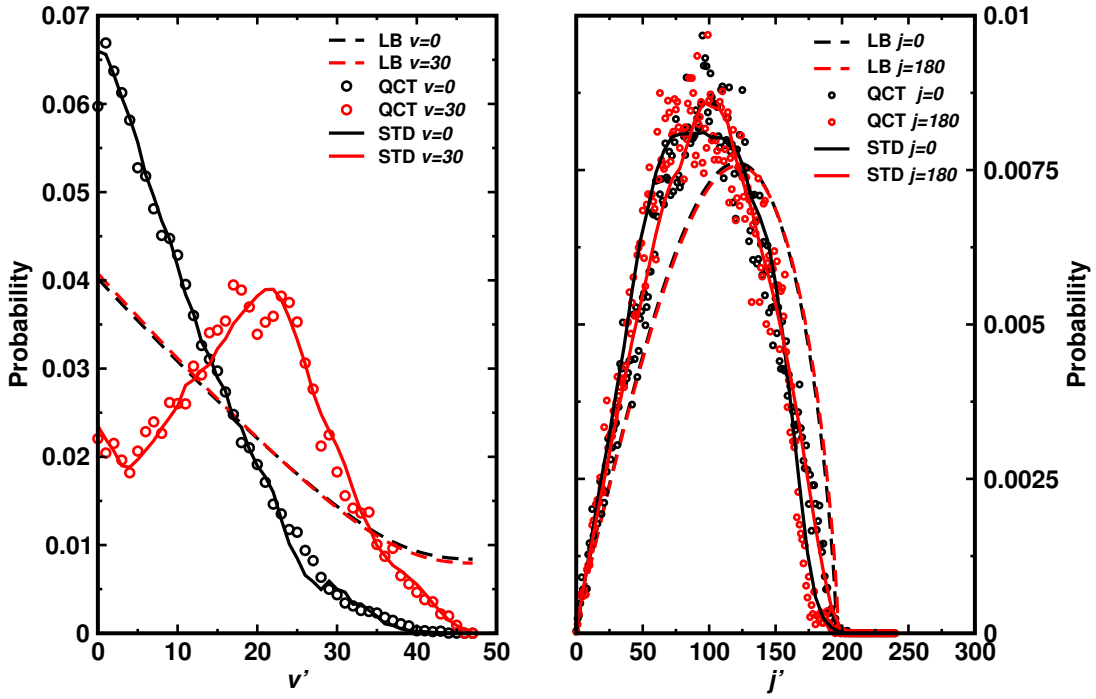

Figure 5.8: Comparison of the final state distributions from the STD model and those from the Larsen-Borgnakke model which is often used in DSMC simulations. The initial conditions used are: $(E_{\text{trans}} = 7.0$ eV $v = 0, j = 0); (E_{\text{trans}} = 2.5$ eV,$v = 30, j = 0); (E_{\text{trans}} = 2.0$ eV$, v = 0, j = 180)$, all at the same $\varepsilon_{\text{coll}}$ or E_{tot}.

One additional refinement of the present method concerns preparation of the data set for training the NN. Including rotation/vibration coupling is likely to improve the overall model specifically for high (v, j) states. Furthermore, generating initial conditions from stratified sampling of the impact parameter may more broadly cover low-energy initial translational energies to further extend the

range of applicability of the trained NN.

In conclusion, an initial state-resolved model to predict final state distributions for chemical reactions of type A+BC→AB+C based on machine learning is formulated and tested. The prediction quality of the model compared with explicit QCT simulations is characterized by RMSD ~ 0.003 and $R^2 \sim 0.99$. Final state distributions from STD can be sampled again using Monte Carlo simulations for generating input for more coarse grained simulations, such as DSMC. Furthermore, the STD model complements the DTD model when predicting product from reactant state distributions. At the cost of an increased evaluation time the STD model allows for accurate predictions given arbitrary nonequilibrium reactant state distributions. This is a regime for which DTD models trained on a given set of (equilibrium) reactant state distributions may underperform. In conjunction, these two models can enable the efficient and accurate simulation of molecular systems over time undergoing multiple reactive collisions.

Supporting Information: Machine Learning Product State Distributions from Initial Reactant States for a Reactive Atom-Diatom Collision System

Detection of "sharp" peaks

When constructing the training, validation, and test data from the raw QCT data no local averaging was performed around "sharp" peaks and averaging over fewer points was done at nearby points. This was done to conserve the sharp peaks, as they would otherwise be washed out. A maximum of a given distribution was classified as "sharp" based on the following criteria:

For $P(E'_{\text{int}})$ if there were 2, 1, or 0 points to either side of the maximum, it was classified as sharp. Otherwise two linear fits were done to the 3 points (or 4 points, if available) to the left and right of a maximum, respectively, including the maximum itself. If the magnitude of both slopes exceeded a critical value $|a_{\text{crit}}| = 0.001$, the maximum was classified as "sharp". Subsequently, averaging over neighbouring data points was performed: The maximum was not averaged, the nearest and next-nearest neighbours of the maxima were averaged with $n_{\text{max}} = 2$, and all other points were averaged with $n_{\text{max}} = 3$.

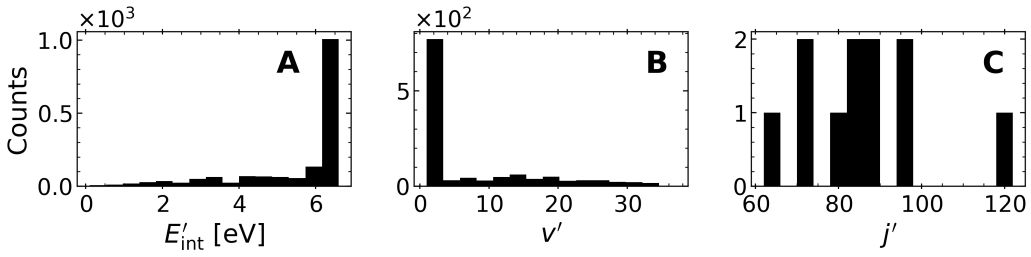

Figure 5.9: Histograms showing the distribution of "sharp" peaks for (A) $P(E'_{\text{int}})$, (B) $P(v')$ and (C) $P(j')$ obtained by QCT simulations, considering all 2184 initial reactant states considered in the present work.

For $P(v')$ if there were 2, 1, or 0 points to either side of a maximum, it was classified as sharp. Otherwise two linear fits were performed for the 3 points to the left and right of the maximum including the maximum itself. If the magnitude of both slopes exceeded a critical value $|a_{\text{crit}}| = 0.000143$, the maximum was classified as "sharp". Subsequently, averaging over neighbouring data points was performed: The maximum was not averaged, and all other points were averaged with $n_{\text{max}} = 1$. The same procedure applied to $P(j')$ with $n_{\text{max}} = 7$ and $|a_{\text{crit}}| = 0.000005$. Figure 5.9 shows the distribution of "sharp" peaks for all 2184 explicit initial reactant states considered in this work.

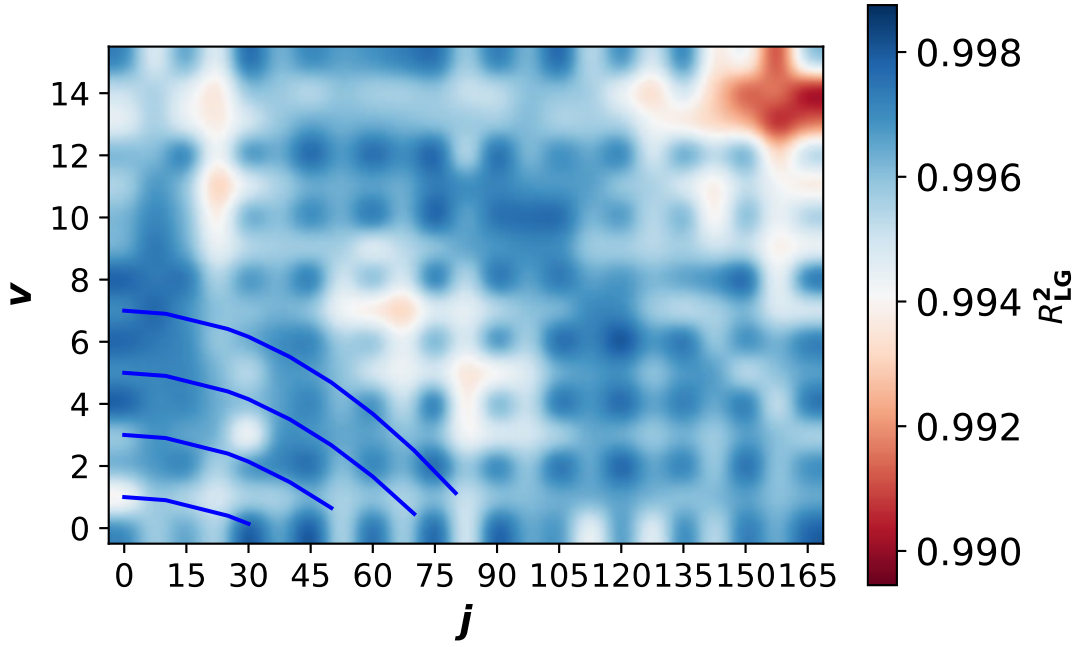

Figure 5.10: 2D map of the R^2_{LG} values between QCT and STD predictions for the product state distributions $P(E'_{\text{int}})$, $P(v')$, and $P(j')$ for given initial (v, j). The STD model was evaluated at fixed $E_{\text{trans}} = 4.0$ eV for the grid points $v = [0, 2, 4, 6, 8, 10, 12, 14]$ and $j = [0, 15, 30, 45, 60, 75, 90, 105, 120, 135, 150, 165]$ used for training, validation, and testing. For the offgrid points, the $(v, j)-$combinations included $v = [1, 3, 5, 7, 9, 11, 13, 15]$ and $j = [7, 22, 37, 52, 67, 82, 97, 112, 127, 142, 157]$. The red lines are for constant rovibrational energies of 0.2850 eV, 0.6552 eV, 1.0142 eV, and 1.3622 eV. For the initial condition $(v = 13, j = 160)$ a low value of $R^2 = 0.94$ is obtained (red); the direct comparison between the final state distributions from QCT and those predicted from STD is given in Figure 5.11.

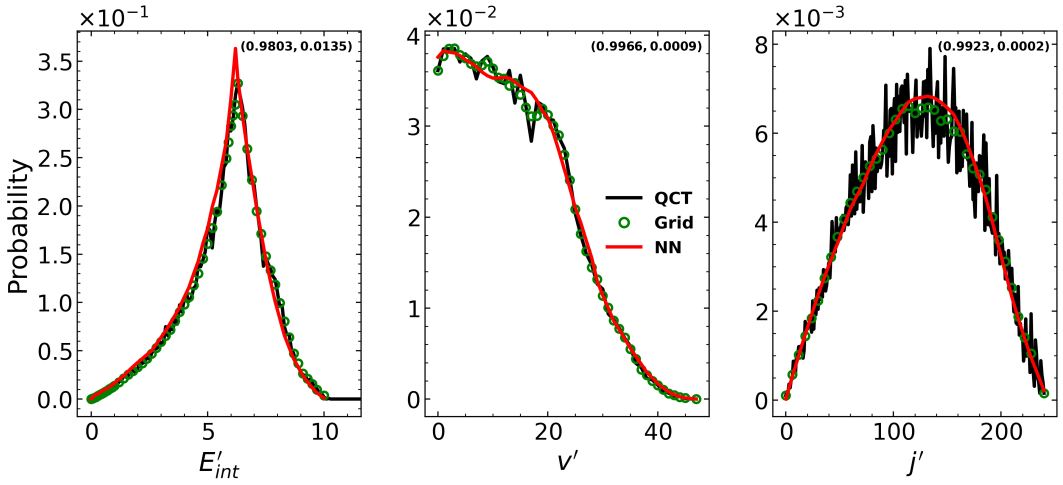

Figure 5.11: Direct comparison between final state distributions from QCT simulations (black solid line) and those predicted from the STD model (red solid line) for (E_{trans} = 4.0 eV, v = 13, j = 157). The R^2_{LG} and RMSD_{LG} for $P(E'_{\text{int}})$, $P(v')$ and $P(j')$ are shown in parenthesis. The overall R^2_{LG} and RMSD_{LG} are 0.9897 and 0.0049, respectively.

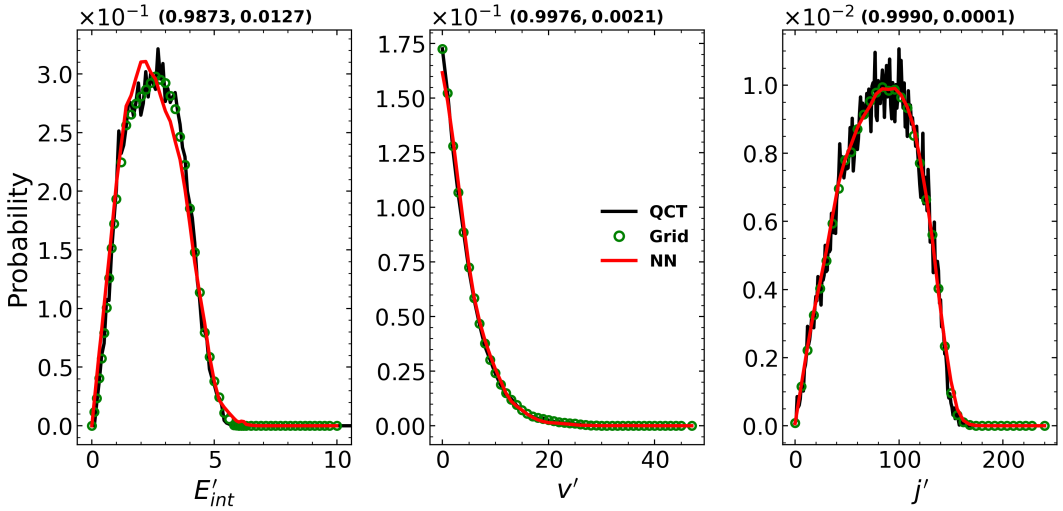

Figure 5.12: Direct comparison between final state distributions from QCT simulations (black solid line) and those predicted from the STD model (red solid line) for initial condition (E_{trans} = 4.0 eV, v = 1, j = 22). The R^2_{LG} and RMSD_{LG} for $P(E'_{\text{int}})$, $P(v')$ and $P(j')$ are shown in parenthesis. The overall R^2_{LG} and RMSD_{LG} are 0.9946 and 0.0050, respectively.

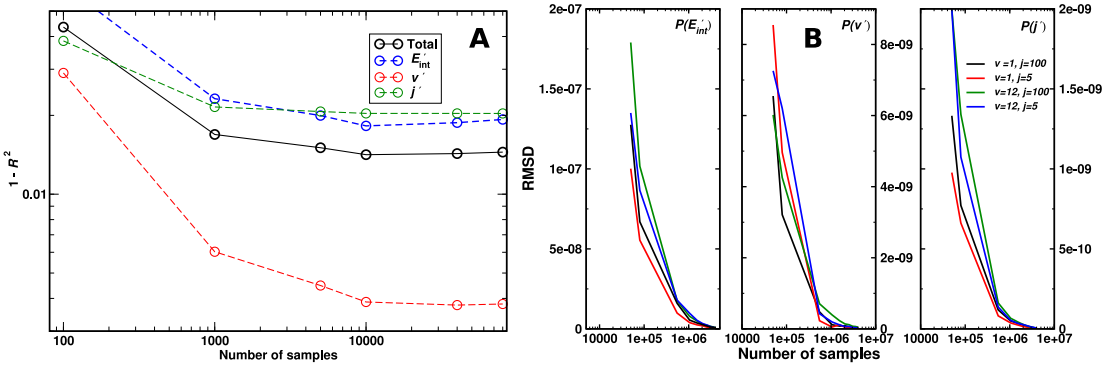

Figure 5.13: Panel A: Error of the STD model in predicting product state distributions as a function of the number of samples drawn from the reactant state distributions. The error is reported as $1 - R^2_{\mathrm{FG}}$, where R^2_{FG} is obtained by averaging over the entire set of temperatures with $T_{\mathrm{trans}} \neq T_{\mathrm{vib}} \neq T_{\mathrm{rot}}$. The error saturates at ≈ 10000 samples. Panel B: RMSD of QCT data as a function of different trajectories sample size with (5×10^6) trajectories as reference. Four different initial conditions $(v = 1, j = 100; v = 1, j = 5; v = 12, j = 100; v = 12, j = 5)$ at $E_{\mathrm{trans}} = 4.0$ eV are evaluated for $P(E'_{\mathrm{int}})$, $P(v')$, and $P(j')$.

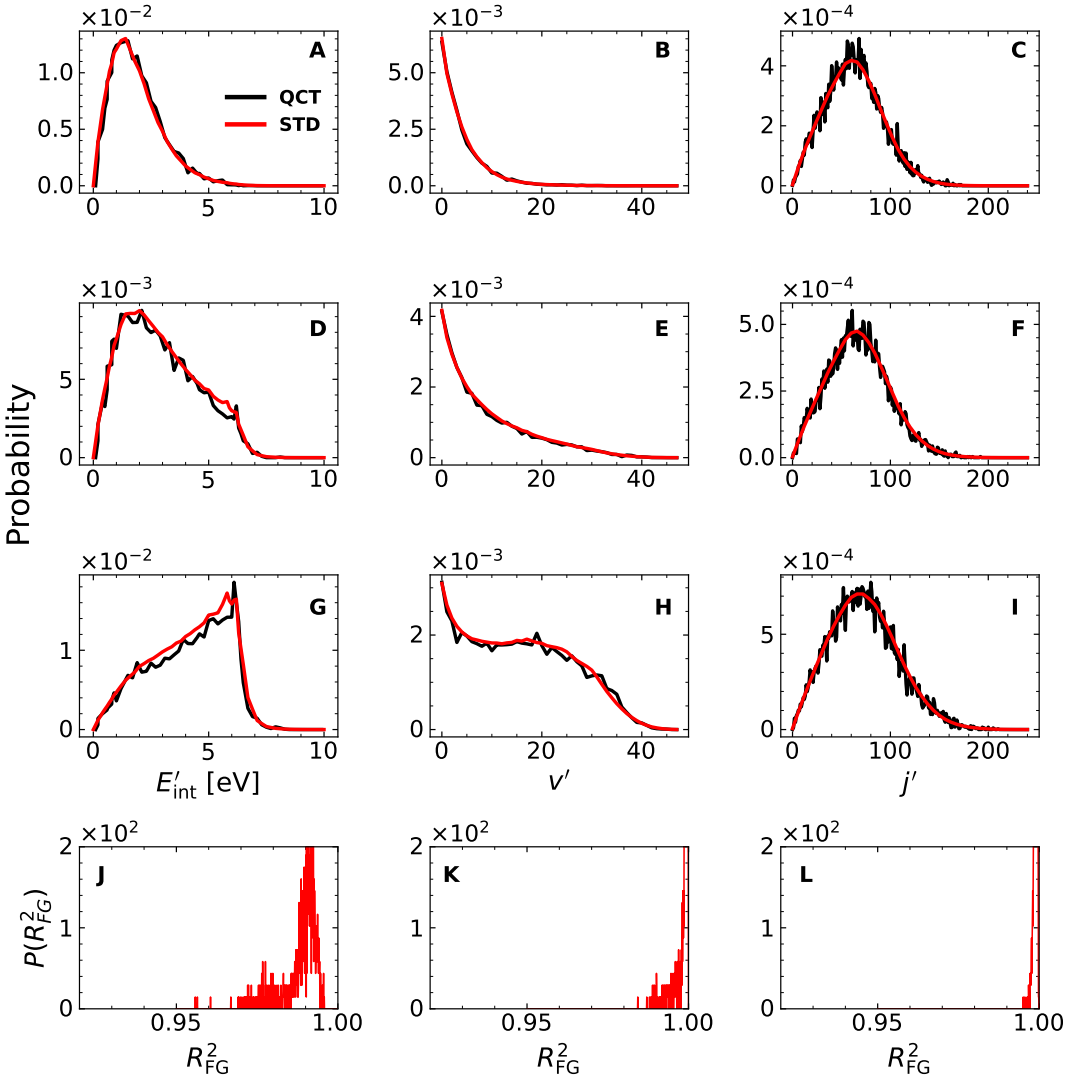

Figure 5.14: Product state distributions for $T_{\mathrm{trans}} \neq T_{\mathrm{rot}} = T_{\mathrm{vib}}$ from QCT simulations compared with predictions from the STD model for a set of temperatures between 5000 and 20000 K in steps of 250 K. For each set of temperatures 10000 reactant initial conditions are generated from Monte Carlo sampling of $(P(E_{\mathrm{trans}}), P(v), P(j))$. Then, final state distributions $(P_i(E'_{\mathrm{int}}), P_i(v'), P_i(j'))$ for each initial condition i are obtained from evaluating the STD model and averaged to obtain the final state distribution $(P(E'_{\mathrm{int}}), P(v'), P(j'))$ for the particular set of temperatures. These distributions are then compared with the results from QCT simulations. Panels A-C: best performing (largest R^2_{FG}) for $T_{trans} = 6500$ K, $T_{\mathrm{rot,vib}} = 5000$ K; panels D-F: closest to the mean of all models for $T_{trans} = 5250$ K, $T_{\mathrm{rot,vib}} = 9250$ K; panels G-I: worst performing (smallest R^2_{FG}) for $T_{trans} = 5000$ K, $T_{\mathrm{rot,vib}} = 19000$ K. Panels J to L report the distribution of R^2_{FG} values for the complete set $T_{\mathrm{trans}} \neq T_{\mathrm{rot}} = T_{\mathrm{vib}}$ containing for $P(E'_{\mathrm{int}})$, (K) $P(v')$ and (L) $P(j')$, from left to right.

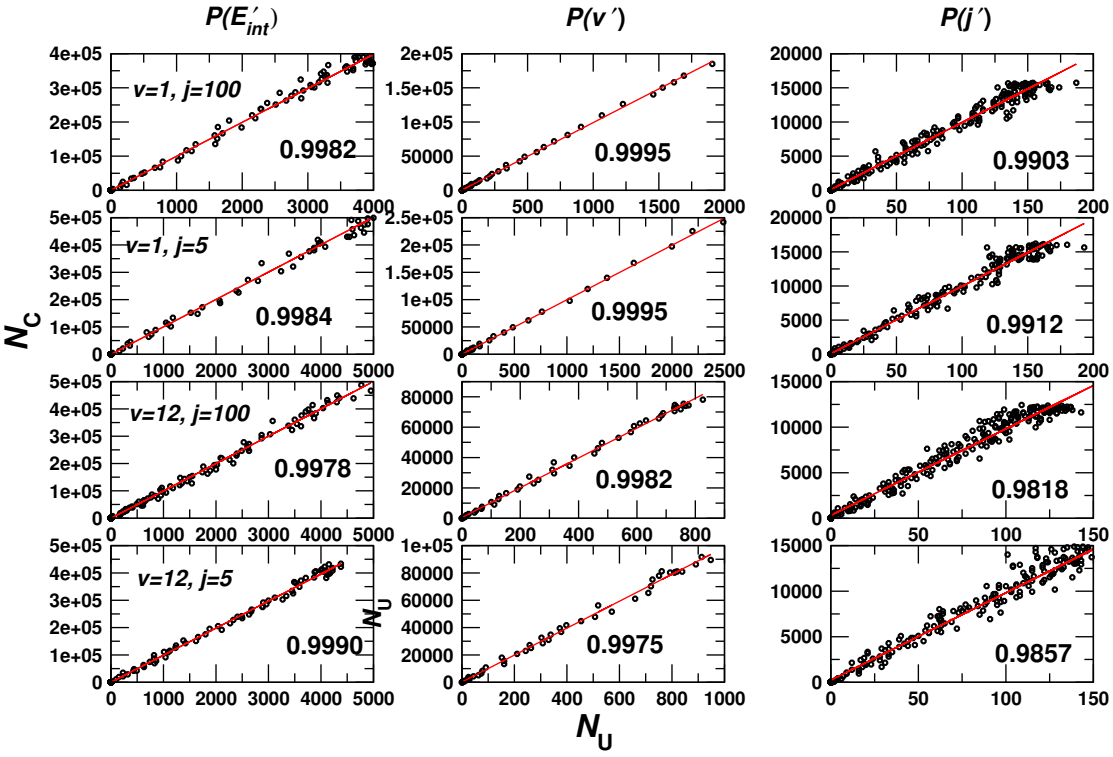

Figure 5.15: Correlation between converged ("ground truth", $y-$axis) and unconverged ($x-$axis) QCT simulations for four different initial conditions with $E_{\text{trans}} = 4.0$ eV as indicated. The "ground truth" is from 5×10^6 trajectories and the unconverged data is from 5×10^4 trajectories. The reported data compares occupation for the same bin for $P(E'_{\text{int}})$ (left), $P(v')$ (middle), and $P(j')$ (right). All correlation coefficients are close to 0.99 showing quantitative agreement.

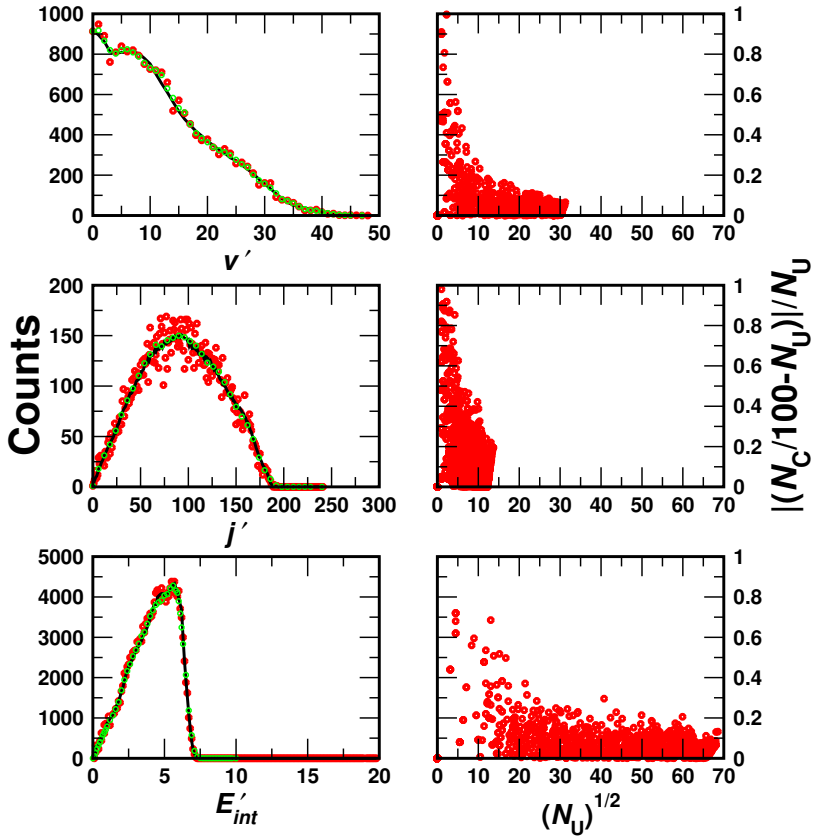

Figure 5.16: Product state distributions $P(v')$, $P(j')$, and $P(E'_{\text{int}})$ for initial condition ($E_{\text{trans}} = 4.0$ eV, $v = 12, j = 5$), from $N_{\text{U}} = 5 \times 10^4$ (red, number of unconverged samples) and $N_{\text{C}} = 5 \times 10^6$ (black, "ground truth" number of converged samples) trajectories. The green dots are obtained by performing local averaging over the red data points. The reference curve obtained by local averaging of the unconverged QCT data matches the converged QCT data closely. This motivates the local averaging procedure performed as a data preparation step in this work. It allows for STD models to be trained on unconverged QCT data while the resulting models yield predictions that match the converged data closely. The right column reports the noise to signal ratio $\frac{(N_{\text{C}}/100 - N_{\text{U}})/N_{\text{C}}}{N_{\text{C}}}$ of the unconverged set relative to "ground truth" as a function of $\sqrt{N_{\text{U}}}$.

Chapter 6

STD + Spectroscopy to Model Reactive Collisions

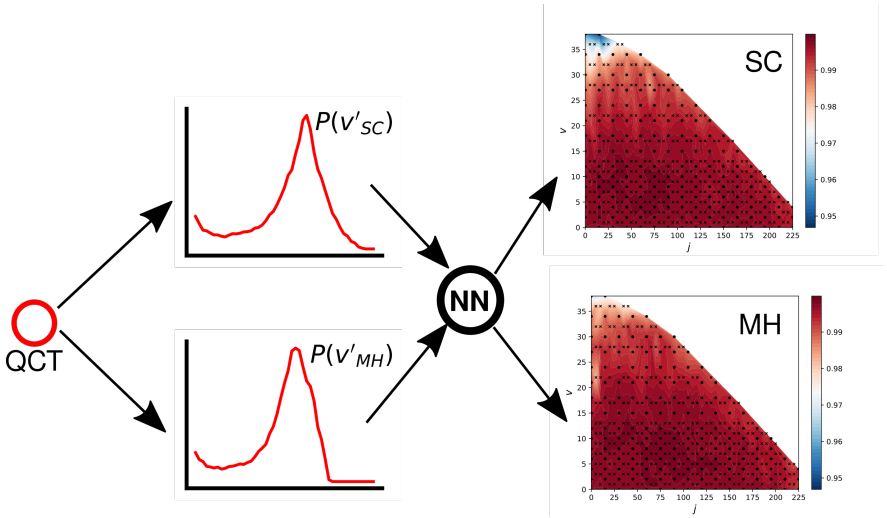

The results presented in this chapter have been previously published in:

J. Phys. Chem. A. (2022) 7971

doi: 10.1021/acs.jpca.2c06267

***

Julian Arnold has contributed to this work as second author.

In this Chapter, the prediction of product translational, vibrational, and rotational energy distributions for arbitrary initial conditions for reactive atom+diatom collisions is considered. Due to the large number of accessible states, determination of the necessary information from explicit (quasi-classical or quantum) dynamics studies is impractical. Here, a machine-learned (ML) model based on translational energy and product vibrational states assigned from a spectroscopic, ro-vibrational coupled energy expression based on the Dunham expansion is developed and tested quantitatively. All models considered in this work reproduce final state distributions determined from quasi-classical trajectory (QCT) simulations with $R^2 \sim 0.98$. As a further validation, thermal rates determined from the machine-learned models agree with those from explicit QCT simulations and demonstrate that the atomistic details are retained by the machine learning which makes them suitable for applications in more coarse-grained simulations. More generally, it is found that ML is suitable for designing robust and accurate models from mixed computational/experimental data which may also be of interest in other areas of the physical sciences.

6.1 Introduction

Atom-diatom collisions at high collision energy are complex due to the multitude of possible ways in which the available energy can be redistributed. Relevant processes include reactions, exchange of energy into translation, rotation, and vibration and depending on the energy, low-lying electronic states. The number of possible states that are accessible increases exponentially with the available energy. To be able to understand bulk energy transfer in high-energy processes, the probabilities of these processes need to be quantified and understood.

For a reactive atom-diatom collision, determining all state-to-state cross sections is computationally very challenging even when treating the process within classical mechanics. This is due to the large number of reactant states ($\sim 10^4$) that can combine with any product state (also $\sim 10^4$) which gives rise to $\sim 10^8$ state-to-state cross sections. If such cross sections are determined from quasi-classical trajectory (QCT) simulations, typically 10^4 to 10^5 simulations are required for converged results which yields an estimated 10^{12} to 10^{13} QCT simulations that would have to be run at a given collision energy. Depending on the range of relevant collision energies ($\sim$ 5 eV in hypersonics) the number of required QCT simulations can further increase by one or two orders of magnitude. This is usually not possible nor desirable. With individual QCT calculations taking roughly one second, even parallelization and Moore's law scaling for improvement in processor speed will not provide sufficient speedup for exhaustive calculations in the next decades. Current computer technology limits tractable calculations to 10^8 meaning that any complete model for the probabilities determined from QCT simulations would be supported by one in $\sim 10^7$ outcomes. In other words: either many final state distributions are unconverged or the final states are not covered at all, or both. This sparse representation creates a challenge for accurately modeling the molecular dynamics in a way that is useful to larger scale simulations. However, because state-to-state cross sections are of paramount importance to determine rates for the process of interest, alternative ways to address the problem are required as this information is further used in reaction networks to model more complicated chemistries.

One application for which this is particularly relevant, is the high temperature, high enthalpy flow prevalent in hypersonics. It is not uncommon to find nominal temperatures that exceed 10000 K in shocks and expansions that cause local non-equilibrium in the rovibrational states of the chemically active molecules.

Following the dynamics and chemical development of rarefied gas flows employs primarily two strategies. One uses computational fluid dynamics (CFD)[193] which is based on the Navier Stokes formulation of fluid dynamics and is valid for small Knudsen number (ratio of the mean free path length to a physical length scale), whereas direct simulation Monte Carlo (DSMC)[192] is more broadly applicable and is also valid for high Knudsen number. In DSMC, particles (representing the physical atoms and molecules) move and collide in physical space to which techniques from statistical mechanics can be applied.[206] Particles in DSMC carry information about their position, velocity, mass, size, and internal state (for molecules) and move in cells within which they can collide and exchange energy.

DSMC cycles through the following steps: 1.) moving particles over a time step Δt smaller than the local mean free collision time; 2.) moving particles across cell boundaries or reflecting them at solid boundaries; 3.) changing their internal states as a consequence of collisions or reactions; 4.) sample average particle information.[206] Step 3 is where microscopic information about thermal reaction rates, state-to-state cross sections, and vibrational relaxation rates enters. For chemical reactions most often the "total collision model", based on a modified Arrhenius equation, is used,[207] although more refined models are also available.[208] A more detailed and accurate description is afforded by state-to-state or state-to-distribution models. However, experimentally, it is very challenging or even impossible to determine the relevant quantities at sufficiently high temperature. Most cross sections presently used are derived from chemical kinetics, many of which have not been measured at and above 3000 K, or can not be measured but are required at even higher temperatures. Alternatively, the essential information can also be obtained from quasi-classical trajectory (QCT) simulations using state-of-the-art potential energy surfaces. Such an approach

provides all necessary information but implicitly assumes that the PESs and the classical dynamics underlying QCT simulations are meaningful. In the present work information from experimental spectroscopy is blended into such a model.

A widely used model for describing microscopic details of hypersonic flow including chemical and relaxation processes is due to Park.[18, 209] This approach considers separate temperatures T_{v} and T_{t} for the vibration and rotation/translation, respectively. In application to kinetics the temperature is taken to be the geometric mean of these, the so-called "$T - T_v$ model". "Chemistry" enters such models through forward and reverse reaction rates in the law of mass action for interacting chemical species which are often determined from temperature-dependent (modified) Arrhenius expressions. Following and extending the approach from Millikan and White,[210] an important intuitive correction established a framework for including vibrational non-equilibrium in vibrational relaxation.[211]

One problematic aspect of the Park model is that vibrational energy becomes "frozen" above the translational energy because vibrational relaxation is only included within the limits of Landau-Teller theory[210, 212, 213] but the contribution that accounts for removal of vibrational energy due to dissociation of the product is neglected as is the movement of large amounts of translational energy to vibrational energy via atom exchange reactions. Including the contribution arising from dissociation of the diatomic products was addressed and corrected in a recent kinetic model which, however, neglected explicit coupling between intramolecular rotation and vibration.[214, 215] Also, with larger computational platforms, it has been possible to investigate the underlying physics on which the Park approach rests, namely the two-temperature assumption and the preferential dissociation model[216] which assumes that the amount of vibrational energy

removed during dissociation is large. For N_2 + N and N_2 + N_2 it was shown that the $T - T_v$ model predicts a much faster N_2 dissociation for $T \leq 20000$ K than that obtained with direct molecular simulation (DMS) whereas for $T = 30000$ K the two models agree.[217]

Machine-learned (ML) models have proven to be effective in predicting product distributions based on information about initial states (E_{trans}, v, j). For one, a neural network (NN) based state-to-state (STS) model was conceived that predicts the cross section for a given transition $(E_{\text{trans}}, v, j) \rightarrow (E'_{\text{trans}}, v', j')$. This was demonstrated for the [NNO] reactive system[218] in that not only the cross sections for transitions that were not part of the training set were correctly predicted, but also quantities derived from the cross sections – such as the total thermal rate $k(T)$ – are in very good agreement with those determined directly from QCT simulations. Conversely, a distribution-to-distribution (DTD) model is capable of describing the map between initial and final state distributions.[191]

From a practical perspective the most useful model is a state-to-distribution (STD) model from which final state distributions $P(E'_{\text{trans}})$, $P(v')$, and $P(j')$ can be determined for every initial state (E_{trans}, v, j). This is what is required for more coarse-grained simulations, such as DSMC. The present work presents state-to-distribution models for the $N(^4S)+O_2(X^3\Sigma_g^-) \rightarrow NO(X^2\Pi) + O(^3P)$ reaction based on translational energy E_{trans} (instead of the diatom's internal energy E_{int}, see Ref.[219]) and final vibrational state assignment including mechanical ro-vibrational coupling. It has been suspected earlier[219] that including such coupling may benefit model performance for high (v, j) states. The trained ML models are based on data used for the earlier STD model[219] to allow for direct

comparison between the different approaches.

The present work is structured as follows. First, the methods used are presented. This is followed by an analysis of the data based on product vibrational state assignments v' using semiclassical mechanics or from a model Hamiltonian (here a truncated Dunham expansion). Then, the performance of NN-trained models based on translational energy together with the two possibilities for assigning final vibrational quantum numbers is assessed and compared. Finally, thermal rates obtained via the two approaches are compared.

6.2 Methods

6.2.1 Quasi-Classical Trajectory Simulations and Analysis

The necessary data for ML-based models characterizing atom + diatom collisions are based on quasi-classical trajectory (QCT) simulations. The QCT data and an earlier STD model were used and provided a means to compare the different approaches.[219] Additional QCT simulations were run as needed using the same procedures as discussed before.[219]

Initial conditions for QCT simulations were generated from semiclassical quantization.[26, 194] Such an approach couples vibration and rotation in the sense that the initial vibrational state is assigned from the numerical solution of an integral involving the rotational barrier $j(j+1)/r^2$ where r is the diatomic bond length. After propagation of a specific initial condition (E_{trans}, v, j) for a given impact parameter b, the final states (v', j') for the diatomic need to be determined and the final translational energy E'_{trans} is obtained from the relative velocities and reduced masses

of the products. Assigning (v', j') quantum numbers is based on final momenta and positions which are transformed to suitable coordinates. The internal final angular momentum $\mathbf{j}' = \mathbf{q}' \times \mathbf{p}'$ for the product diatomic species is determined from the final position $\mathbf{q}'$ and momentum $\mathbf{p}'$. Then the quadratic equation

$$j' = -\frac{1}{2} + \frac{1}{2}\left(1 + 4\frac{\mathbf{j}' \cdot \mathbf{j}'}{\hbar^2}\right)^{\frac{1}{2}} \tag{6.1}$$

is solved to determine the rotational quantum number (j') as a *non-integer* number.[26, 194]

Using semiclassical (SC) mechanics, the non-integer vibrational quantum number (v') of the final diatomic species is calculated according to[26, 194]

$$v'_{\mathrm{SC}} = -\frac{1}{2} + \frac{1}{\pi\hbar}\int_{r^-}^{r^+} \left\{2\mu\left(E_{\mathrm{int}} - V(r) - \frac{\mathbf{j}\cdot\mathbf{j}}{2mr^2}\right)\right\}^{\frac{1}{2}} dr, \tag{6.2}$$

where r is the diatomic bond length, r^+ and r^- are the turning points of the diatomic species on the effective potential with rotational state j' for internal energy E'_{int}, μ is the reduced mass, and $V(r)$ is the potential energy curve of the product diatom.

Integer ro-vibrational quantum numbers are then assigned as the nearest integers (v', j') using histogram binning. To ensure conservation of total energy, the ro-vibrational energy E'_{int} is recomputed from semiclassical quantization[26, 194] using the integer quantum numbers (v', j') and the final translational energy for the atom+diatom system is adjusted according to $E'_{\mathrm{trans}} = E_{\mathrm{tot}} - E'_{\mathrm{int}}$ where the final total internal energy is determined from the final momenta and positions of the two atoms forming the diatomic.

For high j' quantum numbers the angular momentum causes the potential energy surface of the system to distort, changing the characteristic frequency of the vibrations. A first-order approximation to the energy based on the Dunham expansion is shown in Eq. 6.3. To include mechanical coupling between vibration and rotation for the products, as afforded by a model Hamiltonian ("MH"), the assignment of the final angular momentum $j^{'}$ is retained as in Eq. 6.1 but v' is determined from solving

$$\begin{aligned} E(v'_{\mathrm{MH}}, j') =& \omega_e(v'_{\mathrm{MH}} + 1/2) - \frac{\omega_e^2}{4D_e}(v'_{\mathrm{MH}} + 1/2)^2 + B_e j'(j'+1) + D_e[j'(j'+1)]^2 \\ & - \alpha_e(v'_{\mathrm{MH}} + 1/2)j'(j'+1) \end{aligned} \tag{6.3}$$

for v'. Here, $E(v', j') = E_{\mathrm{tot}} - E'_{\mathrm{trans}}$, ω_e is the harmonic frequency, $\omega_e x_e$ is the first order correction, B_e is the rotational constant, D_e is the centrifugal constant, and α_e is the ro-vibrational coupling constant. For NO the data is $\omega_e = 1904.20$ cm^{-1}, $\omega_e x_e = 14.08$ cm^{-1}, $B_e = 1.672$ cm^{-1}, $D_e = 0.00000054$ cm^{-1}, and $\alpha_e = 0.0171$ cm^{-1}.[220] The corresponding parameters on the MRCI/aug-cc-pVTZ curve for NO are $\omega_e = 1871.0$ cm^{-1} and $\omega_e x_e = 14.04$ cm^{-1}.

6.2.2 Neural Network

One approach to creating a model that spans all of the possible probabilities for the outcome of a collision between an atom and a diatom is to use a neural network (NN) representation. Such an approach was used previously in earlier STD work.[219] This NN consists of seven residual layers with two hidden layers per residual layer, and uses 11 input and 254 output nodes corresponding to the 11 features representing the initial reactant state and the 254 amplitudes characterizing the product state distributions. For training, the NN inputs were standardized which ensures that the distributions of the transformed inputs x'_i

over the entire training data are each characterized by ($\bar{x}_i' = 0$, $\sigma_i' = 1$). The NN outputs were normalized which ensures that the distributions of the transformed outputs x_i' over the entire training data being characterized by ($\bar{x}_i' = \bar{x}_i$, $\sigma_i' = 1$). Standardization of the data generally yields a faster convergence.[200] The loss function was the root-mean-squared deviation between reference QCT data and model predictions. As the NN outputs are probabilities, being non-negative even after normalization, a softplus function is used as an activation function of the output layer.

The weights and biases of the NN were initialized according to the Glorot scheme[201] and optimized using Adam[202] with an exponentially decaying learning rate. The NN was trained using TensorFlow [203] and the set of weights and biases resulting in the smallest loss as evaluated on the validation set were subsequently used for predictions. Overall, final state distributions from 2184 initial conditions on a grid defined by ($0.5 \leq E_{\text{trans}} \leq 5.0$) eV with $\Delta E_{\text{trans}} = 0.5$ eV ($5.0 \leq E_{\text{trans}} \leq 8.0$) eV with $\Delta E_{\text{trans}} = 1.0$ eV, $v = [0, 2, 4, 6, 8, 10, 12, 15, 18, 21, 24, 27, 30,$
$34, 38]$, and and $0 \leq j \leq 225$ with step size $\Delta j = 15$ were generated, of which 7 were excluded due to low reaction probability. This "on-grid" set of size $N = 2184$, of which 7 data points were excluded due to low reaction probability, was randomly split into $N_{\text{train}} = 1700$ for training, $N_{\text{valid}} = 400$ for validation, and $N_{\text{test}} = 77$ for testing.[219] The "on-grid" set used for training, validation and test is distinguished from "off-grid" data which refers to initial conditions for which at least one of the entries in (E_{trans}, v, j) differs from an "on-grid" initial condition. All NNs in this work were trained on a 3.60 GHz X 8 Intel Core i7-9700K CPU resulting in training times shorter than 3 minutes. For additional technical details, see Ref.[219]

6.3 Results

6.3.1 Data Preparation

A first important task in designing a ML model is the selection and preparation of the data. Among other aspects, the present work assesses whether a reliable and predictive STD model can be conceived from training on / predicting of a) the translational energy E'_{trans} and b) the final vibrational quantum number v'_{MH} determined from a model Hamiltonian. The reason for this is that E'_{trans} contains independent physical information from (v', j') states about the collision system whereas E'_{int} and the (v', j') states, as used in the previous model,[219] are somewhat redundant. Similarly, while assignment of v' from semiclassical quantization is one possibility, such an approach neglects part of the mechanical (v, j) coupling. Furthermore, using a model Hamiltonian (such as a Dunham expansion[221] or a Watson Hamiltonian,[222] based on coefficients fit to represent spectroscopically measured line positions or transitions) for computing v'_{MH} includes valuable information from experiment and makes the model somewhat less dependent on the level of theory at which the intermolecular interactions have been / can be determined in practice. This is the reason to explore changes in the final vibrational distribution if a model Hamiltonian (here the Dunham expression up to first order in coupling vibration and rotation) is used. Retaining higher order terms is also possible to further refine the approach but is not expected to fundamentally change the findings.

E'_{int} versus E'_{trans}: The reason to employ E'_{int} for training the original STD model[219] was that the number of grid points required to faithfully represent $P(E'_{\mathrm{int}})$ was smaller than for $P(E'_{\mathrm{trans}})$ due to the smaller span of energies and smoother features. Figures 6.1A and B report $P(E'_{\mathrm{trans}})$ and $P(E'_{\mathrm{int}})$ for all 2184 initial reactant conditions ("on-grid") considered. It appears that $P(E'_{\mathrm{trans}})$ ex-

tends to higher energies than $P(E'_{\text{int}})$. This is illustrated by considering a few select final state distributions, see panels E and F in Figure 6.1.

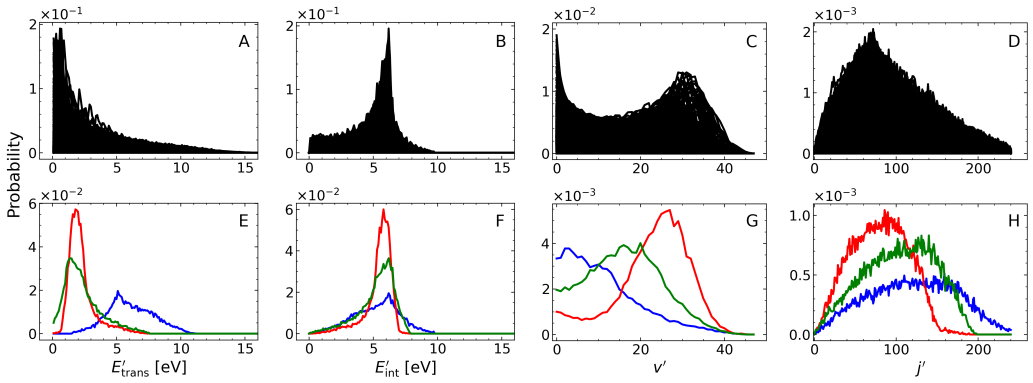

Figure 6.1: Final state distributions $P(E'_{\text{trans}})$ (panel A), $P(E'_{\text{int}})$ (panel B) $P(v')$ (panel C) and $P(j')$ (panel D) from semiclassical quantization for NO_2 from QCT simulations for all 2184 initial reactant states. Panels E to H report selected distributions $P(E'_{\text{trans}})$, $P(E'_{\text{int}})$, $P(v')$, and $P(j')$ to highlight their different shapes.

Vibrational Quantum Number from Semiclassical Assignment and Ro-vibrational Energy Expression: Final state distributions $P(v')$ and $P(j')$ from using semiclassical quantization in the final state analysis are reported in Figure 6.1. Panels C and D show product state distributions corresponding to all 2184 initial reactant states considered. For $P(v')$ they are found to extend out to $v' \leq 45$ whereas for $P(j')$ the highest final state is $j' \sim 240$ with maximum values $v'_{\text{max}} = 47$, $j'_{\text{max}} = 240$. Figures 6.1G and H show individual final state distributions and highlight the various shapes of these distributions encountered depending on the initial condition.

Next, the distributions from using SC and MH final states v'_{SC} and v'_{MH} are presented for all initial conditions, see Figure 6.2A. The black symbols denote $P(v'_{\text{SC}})$ and extend up to $v'_{\text{SC}} = 46$. This compares with a final state distribution $P(v'_{\text{MH}})$ from using the mechanically coupled energy expression for the assignment of the final state (red symbols) which only extends up to $v'_{\text{MH}} = 36$. The differ-

ence (green) between the two assignment schemes is reported in Figure 6.2B. For $v' \leq 20$ the difference in the population is ~ 10 % which increases to considerably higher values for $v' \sim 30$ and above.

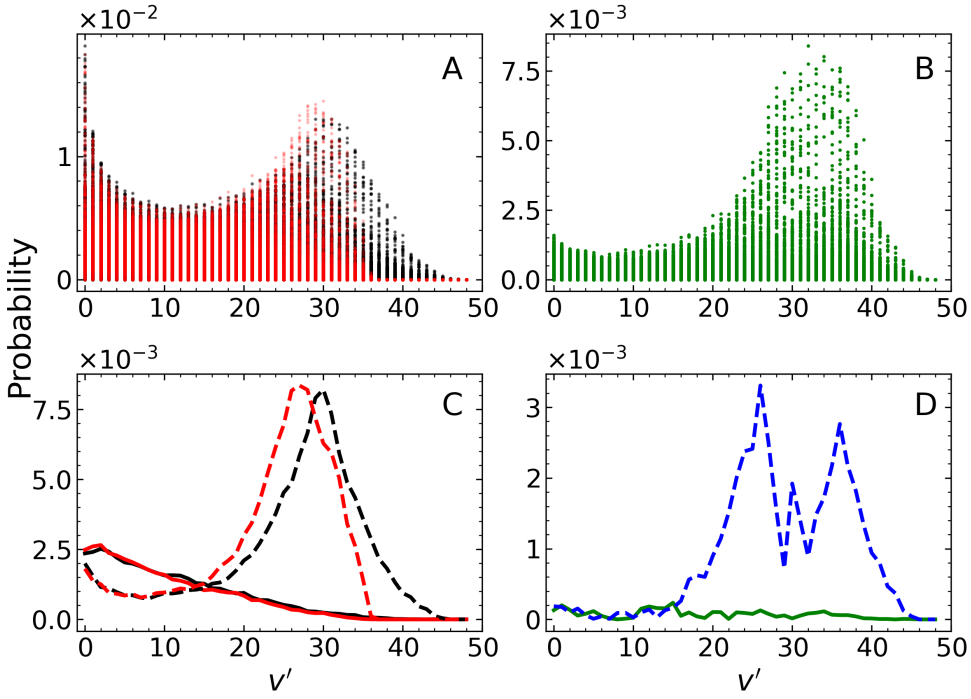

Figure 6.2: Complete distribution for $P(v'_{\mathrm{SC}})$ (black) and $P(v'_{\mathrm{MH}})$ (red) for the set of 2184 initial conditions (Panel A) and for selected individual contributions (Panel C). The absolute difference between $P(v'_{\mathrm{SC}})$ and $P(v'_{\mathrm{MH}})$ is given in panels B (for complete set) & D (for selected individual distributions). Selected test initial conditions: $E_{\mathrm{trans}} = 8.0, v = 0, j = 0$ (solid lines) and $E_{\mathrm{trans}} = 1.0, v = 30, j = 0$ (dashed lines).

Panels C and D of Figure 6.2 compare final state distributions $P(v'_{\mathrm{SC}})$ and $P(v'_{\mathrm{MH}})$ for two specific initial states. For $E_{\mathrm{trans}} = 8.0, v = 0, j = 0$ (solid lines) the two final vibrational state distributions are almost indistinguishable, see also their absolute difference (green) in Figure 6.2D. On the other hand, for initial $E_{\mathrm{trans}} = 1.0, v = 30, j = 0$ (dashed lines) the maximum for $P(v'_{\mathrm{SC}})$ (black) is at $v'_{\mathrm{SC}} = 30$ which shifts to $v'_{\mathrm{MH}} = 26$ for $P(v'_{\mathrm{MH}})$. Evidently, the two distributions also differ, see blue dashed line in Figure 6.2D. The general finding is that including mechanical ro-vibrational coupling in assigning the final vibrational state

v'_{MH} populates lower states compared with an analysis based on a semiclassical approach.

Assignment of the final state to integer values (v'_{MH}, j') leads to differences in the corresponding internal energy $E'_{\mathrm{int}}(v'_{\mathrm{MH}}, j')$ from the value obtained when considering $E'_{\mathrm{int}} = E_{\mathrm{tot}} - E'_{\mathrm{trans}}$ based on energy conservation. Hence, the difference $E'_{\mathrm{int}}(v'_{\mathrm{MH}}, j') - E'_{\mathrm{int}}$ has to be redistributed into E'_{trans} which leads to $E'_{\mathrm{trans,MH}}$ from including mechanical coupling in the rovibrational energy. Figure 6.3A compares the final translational energy distributions $P(E'_{\mathrm{trans,SC}})$ (black) and $P(E'_{\mathrm{trans,MH}})$ (red). The overall shapes of the two distributions are comparable but when considering the absolute difference between the two distributions (Figure 6.3B, green) variations up to 50 % are found. For high translational energy the absolute differences decay to zero.

Focussing on two specific initial conditions ($E_{\mathrm{trans}} = 8.0, v = 0, j = 0$ and $E_{\mathrm{trans}} = 8.0, v = 24, j = 120$, see Figure 6.3C) indicate that the overall shapes of the final translational energy distributions depend little on whether mechanical coupling was included or not to determine v'. For initial ($E_{\mathrm{trans}} = 8.0, v = 0, j = 0$) nonzero probability at low translational energy starts at a higher value for an analysis based on MH (red) compared with SC (black). A similar behaviour is seen for the initial condition given by ($E_{\mathrm{trans}} = 8.0, v = 24, j = 120$) (dashed lines in Figure 6.3C). Absolute differences are reported in Figure 6.3D and reach a maximum of ~ 20 %.

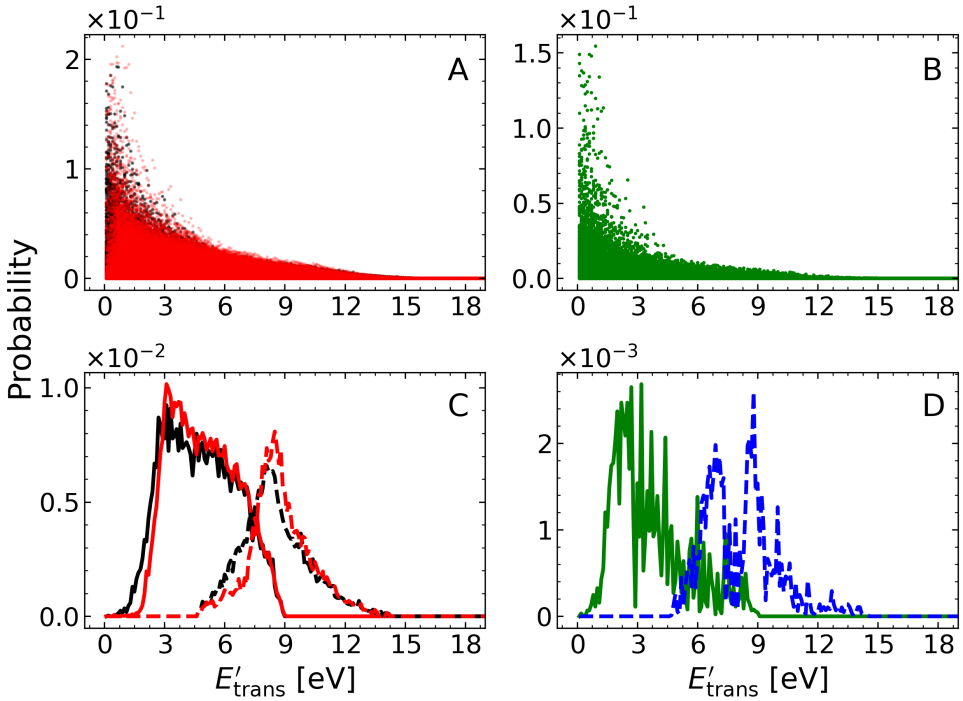

Figure 6.3: Complete distribution for $P(E'_{\mathrm{trans,SC}})$ (black) and $P(E'_{\mathrm{trans,MH}})$ (red) for the set of 2184 initial conditions (Panel A) and for selected individual contributions (Panel C). The absolute difference between $P(E'_{\mathrm{trans,SC}})$ and $P(E'_{\mathrm{trans,MH}})$ is given in panels B (for complete set) & D (for selected individual distributions) for initial conditions $E_{\mathrm{trans}} = 8.0, v = 0, j = 0$ (solid lines) and $E_{\mathrm{trans}} = 8.0, v = 24, j = 120$ (dashed lines).

6.3.2 Trained STD Models

Next, full STD models were trained based on assignment of the final vibrational state from semiclassical analysis (v'_{SC}) or using a first-order Dunham expansion (v'_{MH}) together with E_{trans}, respectively. In the following, "on-grid" values refer to initial conditions that were used for training the NN (training, validation, test data - see Methods) and "off-grid" corresponds to initial conditions that differed from "on-grid" values in at least one of the initial conditions $(E_{\mathrm{trans}}, v, j)$.

The performance of the trained models in terms of R^2 and RMSD is summarized in Tables 6.1 and 6.2. The analysis is carried out for all on-grid-values, excluding seven distributions with low probabilities ($P(v') < 0.005$)), and excluding the

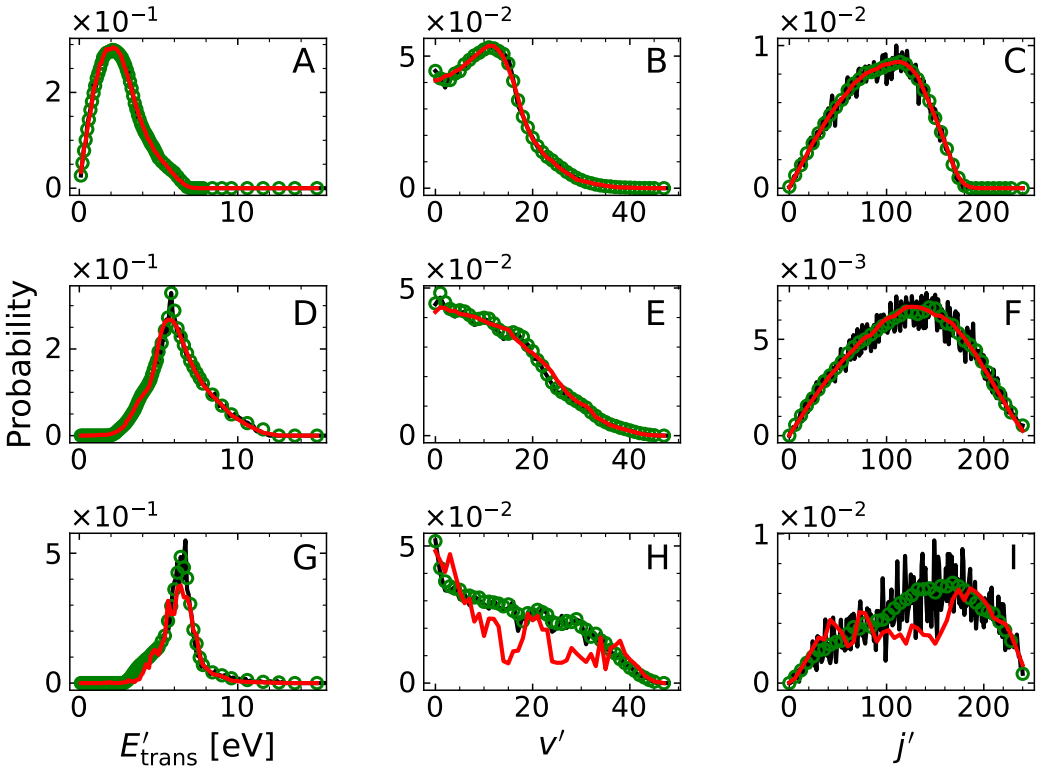

Figure 6.4: Comparison of product state distributions from QCT (symbols) and STD model evaluation (red solid line) for SC, for initial conditions from the "on-grid" set (excluding $E_{\mathrm{trans}} = 0.5$ eV). STD predictions are for the initial condition for which the prediction is best (top, largest R^2), is closest to the average R^2 (middle), and worst (bottom, lowest R^2), respectively. The corresponding R^2 values for ($P(E'_{\mathrm{trans}})$, $P(v')$, $P(j')$) are: [0.9985,0.9985,0.9995] (best); [0.9880,0.9954,0.9895] (closest to mean) and [0.9307,0.4082,0.3578] (worst). The corresponding reaction probabilities $P_r = N_r/N_{\mathrm{tot}}$ are 0.378, 0.217, and 0.064 for the best, average and worst prediction, respectively. Here, N_{tot} and N_r the total number and number of reactive trajectories, respectively.

lowest translational energy $E_{\mathrm{trans}} = 0.5$ eV because the number of QCT simulations may be insufficient to fully converge these final state distributions. In addition, this analysis was also carried out for initial conditions off-grid in (v, j) and at fixed $E_{\mathrm{trans}} = 4.0$ eV. For all degrees of freedom and all test sets $R^2 > 0.97$ which indicates reliable statistical models. Such R^2 measures are also comparable to the performance if instead of using E_{trans} the models are trained on E_{int} for which $R^2 > 0.98$ was found.[219] If simulations at the lowest translational energy (0.5 eV) are excluded, the performance is somewhat improved for all degrees of freedom. Finally, whether the final vibrational state v' was assigned from a semi-

classical treatment or a mechanically coupled energy expression has negligible influence on the performance of the models. When using the RMSD as the measure to compare reference distributions with predictions from the trained STD models (see Table 6.2) similar conclusions are drawn as for R^2.

	On-grid (All)	On-grid (test)	On-grid*	Off-grid*
$P(E'_{\mathrm{trans,SC}})$	0.9878	0.9844	0.9949	0.9918
$P(E'_{\mathrm{trans,MH}})$	0.9737	0.9840	0.9959	0.9942
$P(v'_{\mathrm{SC}})$	0.9881	0.9835	0.9949	0.9961
$P(v'_{\mathrm{MH}})$	0.9834	0.9817	0.9966	0.9972
$P(j'_{\mathrm{SC}})$	0.9845	0.9816	0.9940	0.9950
$P(j'_{\mathrm{MH}})$	0.9879	0.9882	0.9950	0.9951
"SC" (overall)	0.9868	0.9832	0.9946	0.9943
"MH" (overall)	0.9817	0.9846	0.9959	0.9955

Table 6.1: R^2 between QCT results and the trained STD model based on E_{trans} and either semiclassical or mechanically coupled determination of v'. On-grid (All) is for all initial conditions from the training, validation and test set for all translational energies considered. The numbers in bracket are from the test set (77 initial conditions) only. On-grid* and Off-grid* are for initial conditions with $E_{\mathrm{trans}} = 4.0$ eV only and Off-grid* contains all initial conditions for which either v, j, or both (v, j) differed from the values used for the training, validation and test sets.

An explicit comparison of final state distributions from models based on SC (Figure 6.4) and MH (Figure 6.5) for assigning the final vibrational state is provided for the best-performing, for an average-performing, and for the least performing distribution. The QCT final state distributions are shown as green open circle and the STD predictions as the red solid line. For the best-performing prediction the STD model closely follows the target data. This is still the case for a prediction that represents an average performance. It is also notable that the shape of the distributions for the same degree of freedom can change appreciably, depending on the initial condition. For the worst-performing prediction it is found that SC (see Figure 6.4) leads to a visually inferior model compared to using MH (Figure 6.5). In both worst-performing cases, the number of reactive trajectories N_r as a fraction of the total number of trajectories N_{tot} is only ~ 5 % and increasing the

sampling may also lead to better reference data.

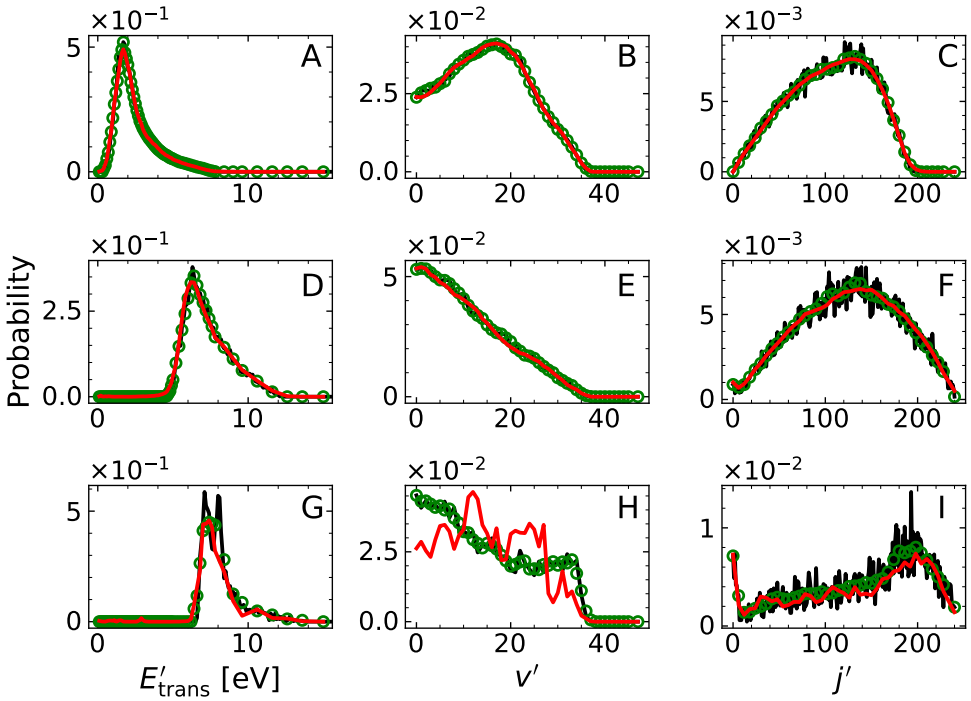

Figure 6.5: Comparison of product state distributions from QCT (symbols) and STD model evaluation (red solid line) for MH, for initial conditions from the "on-grid" set (excluding $E_{\mathrm{trans}} = 0.5$ eV). STD predictions are for the initial condition for which the prediction is best (top, largest R^2), is closest to the average R^2 (middle), and worst (bottom, lowest R^2), respectively. The corresponding R^2 for ($P(E'_{\mathrm{trans}})$, $P(v')$, $P(j')$) are: [0.9987,0.9987,0.9991](best); [0.9911,0.9971,0.9911](closest to mean) and [0.9741,0.5043,0.8305](worst). The corresponding reaction probabilities $P_r = N_r/N_{\mathrm{tot}}$ are 0.365, 0.308, and 0.044 for the best, average and worst prediction, respectively. Here, N_{tot} and N_r the total number and number of reactive trajectories, respectively.

For a more global characterization of the final states for the entire range of possible initial states (v, j), 5 independent models were trained from reference data for SC (Figure 6.6A) and MH (Figure 6.6B). The averaged R^2 over all 5 models using "on-grid" (see Methods; black circles) and "off-grid" (see caption Figure 6.6; crosses) data for each of the initial states considered shows a uniformly high performance for both approaches with typical $R^2 \sim 0.98$ or better. For the highest $v-$values the absolute difference between using MH and SC expressions for v' becomes most apparent. There, using a "MH" model appears to slightly out-

perform an analysis based on a "SC" energy expression. But the differences are insignificant.

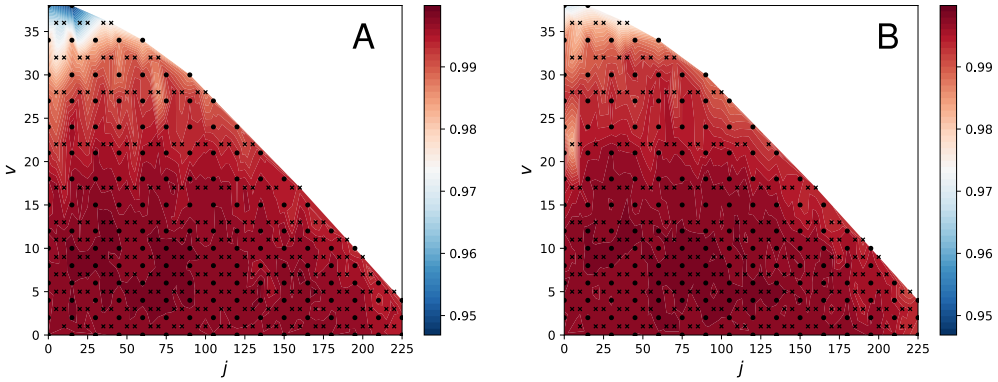

Figure 6.6: 2D map of the averaged (over 5 independently trained STD models) R^2 values between QCT data $(P(E'_{\mathrm{trans}}), P(v'), P(j'))$ and STD evaluation for initial conditions "on-grid" (see Methods, circles) and "off-grid" ($[v = 1, 3, 5, 7, 9, 11, 13, 17, 22, 28, 32, 36]$, $j = [10, 20, 25, 35, 40, 50, 55, 65, 70, 80, 85, 100, 110, 115, 125, 130, 140, 145, 155, 160, 170, 175, 185, 200, 205, 215, 220]$, crosses). Panel A for "SC" and panel B for "MH" assignment of the final vibrational state. All QCT simulations were carried out at $E_{\mathrm{trans}} = 4.0$ eV.

6.3.3 Thermal Rates

It is also of interest to determine thermal rates from the trained models. In general, such a rate is determined from the reaction probability P_r according to

$$k(T) = g(T)\sqrt{\frac{8k_{\mathrm{B}}T}{\pi\mu}}\pi b_{\mathrm{max}}^2 P_r. \tag{6.4}$$

For QCT simulations based on stratified sampling of the impact parameter b, $P_r = \sum_{k=1}^{K} V_k \frac{N_k^r}{N_k^{\mathrm{tot}}}$ where N_k^r and N_k^{tot} are the number of reactive and total trajectories, respectively, for stratum k with impact parameter b_k. The fractional volumes $V_k = \frac{b_k^2 - b_{k-1}^2}{b_{\mathrm{max}}^2}$ of stratum k obey $\sum_{k=1}^{K} V_k = 1$. For the STD model the reaction probability can be obtained as $P_r = \int_{E=0}^{E_{\mathrm{max}}} P(E)dE$ where $E = E'_{\mathrm{trans}}$ and $E_{\mathrm{max}} = 15.0$ eV. For the forward $\mathrm{N}(^4\mathrm{S}) + \mathrm{O}_2(\mathrm{X}^3\Sigma_{\mathrm{g}}^-) \rightarrow \mathrm{NO}(\mathrm{X}^2\Pi) + \mathrm{O}(^3\mathrm{P})$ reaction in the $^4\mathrm{A}'$ electronic state the degeneracy factor $g(T) = 1/3$ and μ is the

reduced mass of the reactants.[58] The two approaches are compared in Figure 6.7 and favourable agreement is found over a wide temperature range. Hence, the STD model can also be used to determine macroscopic quantities such as realistic reaction rates which is essential.

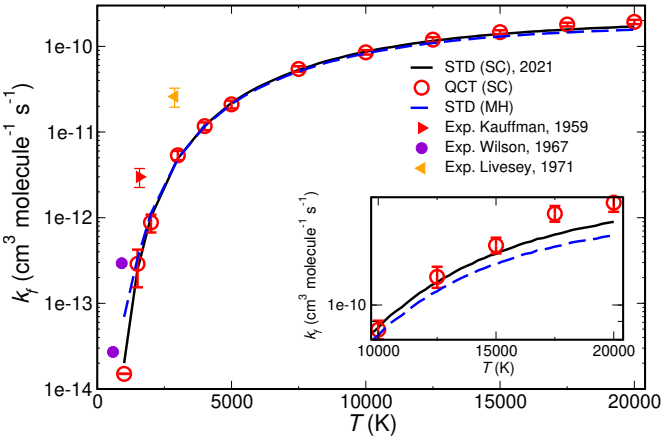

Figure 6.7: The thermal forward rate k_f calculated from QCT (open red circle) and STD model (solid black line) for the $^4A'$ state of the N(^{4}S) + O$_2$($X^3\Sigma_g^-$) $\rightarrow$ NO($X^2\Pi$) + O(^{3}P) reaction between 1000 and 20000 K. Additional simulations were made with the STD model based on E_{trans} and "MH" (blue dashed line). The present rates agree quantitatively with those directly obtained from QCT simulations, in particular considering the reduction of required compute time by 7 orders of magnitude or more. Rates for "MH" are expected to change slightly if higher-order terms in the Dunham expansion are included. Experimental total forward reaction rate k_{f} (including contributions from the doublet and the quartet states) are also shown for comparison: (red triangle)[108], (orange triangle)[109] and (magenta circle)[223].

6.4 Conclusion

The present work discusses a rapid, accurate, and physics-based model to determine final state distributions for given initial conditions (E_{trans}, v, j) for atom+diatom reactions. It is shown that training on E'_{trans} and v' from an energy expression including mechanical coupling (Dunham expression) yields a model performance of $R^2 \sim 0.98$ or better compared with rigorous QCT reference simulations. Models based on (E_{trans}, v, j) are more physically meaningful than those using (E_{int}, v, j) because E_{int} and (v, j) are partly redundant whereas E_{trans} contains new, com-

plementary, and physically relevant information. The gain in speed compared to explicit QCT simulations is about 7 orders of magnitude required for inference (i.e., excluding training the NN which is minutes, and generating the required QCT reference data for training) assuming that 10^5 QCT trajectories are sufficient for converged final state distributions. Hence, this is a promising avenue to be used in more coarse-grained simulations of reaction networks relevant to hypersonics and combustion.

Including coupling in determining the final v' state of the diatomic by means of a truncated Dunham expansion as a typical model Hamiltonian (MH) leads to population of lower v' states than assignment from semiclassical mechanics (SC). The overall shapes of the final state distributions $P(v'_{\mathrm{SC}})$ and $P(v'_{\mathrm{MH}})$ do not change appreciably, see for example Figure 6.2. However, final vibrational distributions from SC extend to higher values v' than those from using a Dunham expansion. The influence of this effect is illustrated in Figure 6.8 which compares final internal energy distributions from the two assignment schemes (SC and MH) for all on-grid initial conditions. The relevant NO dissociation energies from the SC and MH models are also indicated and allow to determine the fraction of final states that are above this threshold to be 21 % and 14 %, respectively, for SC and MH.

If larger products than diatomics are produced in such reactions, it is expected that the MH approach for assigning final vibrational states is more convenient than an assignment based on semiclassical mechanics. Furthermore, using effective Hamiltonians to determine internal final states of molecular fragments opens the possibility to blend accurate spectroscopic information into such models which makes them less dependent on the level of quantum chemical theory at

which the intermolecular interactions can be practically described. For example, multi-reference configuration interaction (MRCI) calculations with extended basis sets (triple zeta and larger) for molecules with more than 3 atoms can quickly become computationally prohibitive. However, it should also be noted that both schemes have their advantages and drawbacks. For experimental observables, such as thermal rates, both models perform on par, see Figure 6.7.

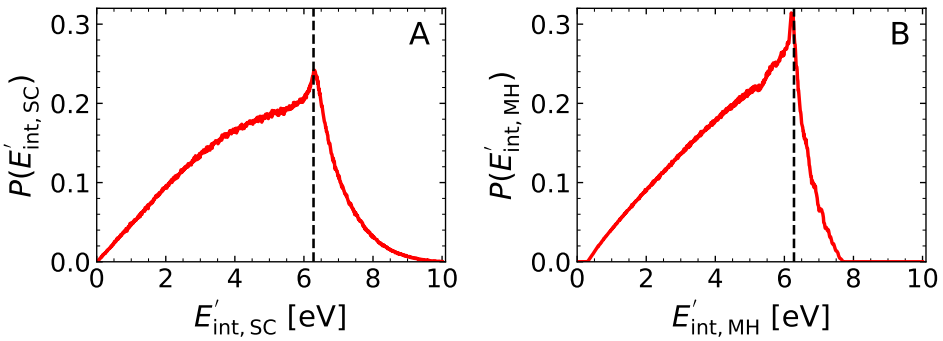

Figure 6.8: Final internal energy distribution $P(E'_{\text{int}})$ depending on the assignment scheme (SC, MH) used. Distributions are generated from the complete data set (on-grid and off-grid) used as initial conditions in the QCT simulations. The dissociation energy for NO (dashed black) is shown as well (6.27 eV and 6.29 eV for SC and MH, respectively, compared with 6.50 eV from experiment.[220]) and the percentage of population above dissociation is 21 % and 14 % for SC and MH, respectively. The D_e value for MH was determined from using a scaling factor between experimental D_e, and $D_e = \omega_e^2/(4\omega_e x_e)$ using spectroscopic constants.[220]

The actual population of highly excited states in the product diatom is particularly relevant for hypersonics because such states can easily dissociate during the next collision and the ensuing products (free atoms at high translational energy) induce rich chemistry. In general, highly vibrationally excited states are correlated with facile dissociation whereas high $j-$values prevent and delay breakup of the diatomic. Furthermore, the vibrational coordinate can also lead to electronic state relaxation rate differences in subsequent reactions.[224] Hence, overall, depending on the assignment scheme used for (v, j) the energy partitioning into

other degrees of freedom (translation, electronic) will be affected, too.

In summary, the present work demonstrates that it is possible to construct machine-learned models for final state distributions given state-specific information for the reactants for atom + diatom reactions. The trained models are accurate, rapid to evaluate, and can be extended as needed for other applications, e.g. combustion, by supplying suitable training data. It is anticipated that such approaches are beneficial to perform more coarse-grained modeling to applications in hypersonic flow and computational combustion studies.

Supporting Information: STD + Spectroscopy to Model Reactive Collisions

	On-grid (All)	On-grid (test)	On-grid*	Off-grid*
$P(E'_{\mathrm{trans,SC}})$	0.0110	0.0134	0.0053	0.0080
$P(E'_{\mathrm{trans,MH}})$	0.0143	0.0151	0.0056	0.0081
$P(v'_{\mathrm{SC}})$	0.0015	0.0019	0.0011	0.0011
$P(v'_{\mathrm{MH}})$	0.0019	0.0025	0.0011	0.0010
$P(j'_{\mathrm{SC}})$	0.0002	0.0003	0.0002	0.0002
$P(j'_{\mathrm{MH}})$	0.0002	0.0003	0.0002	0.0002
"SC" (overall)	0.0042	0.0052	0.0022	0.0031
"MH" (overall)	0.0055	0.0059	0.0028	0.0031

Table 6.2: RMSD between QCT results and the trained STD model based on E_{trans} and either semiclassical or mechanically coupled determination of v'. On-grid (All) is for all initial conditions from the training, validation and test set for all translational energies considered. The numbers in bracket are from the test set (77 initial conditions) only. On-grid* and Off-grid* are for initial conditions with $E_{\mathrm{trans}} = 4.0$ eV only and Off-grid* contains all initial conditions for which either v, j, or both (v, j) differed from the values used for the training, validation and test sets.

Chapter 7

Next Steps: Iterative Cycle Model

In this Chapter, we explore and give a brief introduction on our current efforts to construct an iterative cycle model for air chemistry simulations based on STD evaluations.

7.1 Introduction

Machine learning- (ML) based models to generate product state distributions from given reactant states for atom-diatom collisions are presented and quantitatively tested characterizing Stationary Non-Equilibrium Distributions at Hypersonic Conditions

The chemistry and dynamics in high energy gas flows, as they occur during hypersonic flight or in combustion, is dominated by thermal non-equilibrium. The behaviour of matter, such as spacecraft or meteorites, upon re-entry into atmospheres of planets depends to a large extent on the internal state (vibration, rotation) of the surrounding molecules, and the amount and composition of gases

produced by the ablation process in the reactive flow. Because the timescales and velocities of the flow do not allow full relaxation to chemical and thermal equilibrium[225] at the solid/gas interface, complex chemistry at high temperature in thermodynamic non-equilibrium takes place. Temperatures of the medium around re-entry objects can easily reach several thousand Kelvin.[226] Interactions between gases, in equilibrium or not, at these temperatures with surfaces are essentially uncharacterized and the experimental methodologies capable of probing the molecularly resolved details are essentially unavailable. Given this, computational methods based on quantum and molecular dynamics techniques and machine learning approaches provide a powerful means to determine the relevant quantities to characterize the non-equilibrium rates and internal state distributions for gas-gas and gas-surface chemistry in such rarefied flows.

Over the past ten years, the group has been at the forefront of quantitative simulations of reactive, high-energy collisions for atom-diatom systems involving ground and electronically excited states for the [NNO][227, 228], [NOO][39, 229, 230], [CNO][231], and $[NNN]^+$ systems relevant to hypersonics. For this, generic and broadly applicable techniques including a reproducing kernel Hilbert space (RKHS)-based,[232] machine learning technique to accurately represent high-level electronic structure calculations have been developed and made publicly available. Also, a versatile quasi-classical trajectory (QCT) program for adiabatic and non-adiabatic dynamics studies were developed and used for computing thermal, equilibrium, and vibrational relaxation rates.[231] Comparisons with experiments, wherever possible, provide a stringent validation of the methods employed and valuable empirical relationships as modified Arrhenius models which are widely used in combustion models. In very recent work, powerful ML-based state-to-state (STS), distribution-to-distribution (DTD), and state-to-distribution (STD) models for cross-sections were developed.[233–235] Such models provide accurate

and computationally efficient ways to determine necessary[204, 236] microscopic information for reaction network modeling.[192]

7.2 Methods

The stationary nonequilibrium distributions for the diatomics, $P(v_\mathrm{f}, j_\mathrm{f}, E_\mathrm{t,f})$, for the [N,O] reactive system including the 5 species [O,N,O_2,N_2,NO], will be determined from machine-learned models (STD[235] and DTD[234]) trained on state-to-distribution data from QCT simulations. These models are based on a large number of QCT simulations and predict the final state distribution for given initial state (v, j, E_t) with high accuracy. First, a simplified reaction model will be considered as a test which only involves [N,O,NO,O_2] according to the following scheme

$$\mathrm{N} + \mathrm{O_2}(v, j) \rightarrow \mathrm{O} + \mathrm{NO}(v', j') \tag{7.1}$$

$$\mathrm{N} + \mathrm{O_2}(v, j) \rightarrow \mathrm{N} + \mathrm{O_2}(v', j') \tag{7.2}$$

$$\mathrm{O} + \mathrm{NO}(v, j) \rightarrow \mathrm{N} + \mathrm{O_2}(v', j') \tag{7.3}$$

$$\mathrm{O} + \mathrm{NO}(v, j) \rightarrow \mathrm{O} + \mathrm{NO}(v', j') \tag{7.4}$$

For this, final state models for the $\mathrm{N}(^4\mathrm{S})+\mathrm{O_2}(\mathrm{X}^3\Sigma_\mathrm{g}^-) \leftrightarrow \mathrm{NO}(\mathrm{X}^2\Pi) + \mathrm{O}(^3\mathrm{P})$ are required which are already available. Eqs. (1) and (3) are reactions whereas Eq. (2) is a collision between N and O_2 that potentially changes the the internal state of the diatomic. The decision of whether Eq. (1) or Eq. (2) is followed is based on Monte Carlo sampling of the the state-dependent branching ratio between the two processes that can also, be determined from QCT simulations.

A somewhat extended set of equations

$$\mathrm{N} + \mathrm{O_2}(v, j) \rightarrow \mathrm{O} + \mathrm{NO}(v', j') \tag{7.5}$$

$$\mathrm{N} + \mathrm{NO}(v, j) \rightarrow \mathrm{O} + \mathrm{N_2}(v', j') \tag{7.6}$$

$$\mathrm{O} + \mathrm{N_2}(v, j) \rightarrow \mathrm{N} + \mathrm{NO}(v', j') \tag{7.7}$$

$$\mathrm{O} + \mathrm{N_2}(v, j) \rightarrow \mathrm{O} + \mathrm{N_2}(v', j') \tag{7.8}$$

$$\mathrm{N} + \mathrm{NO}(v, j) \rightarrow \mathrm{N} + \mathrm{NO}(v', j') \tag{7.9}$$

$$\mathrm{N} + \mathrm{O_2}(v, j) \rightarrow \mathrm{N} + \mathrm{O_2}(v', j') \tag{7.10}$$

$$\mathrm{O} + \mathrm{NO}(v, j) \rightarrow \mathrm{N} + \mathrm{O_2}(v', j') \tag{7.11}$$

$$\mathrm{O} + \mathrm{NO}(v, j) \rightarrow \mathrm{O} + \mathrm{NO}(v', j') \tag{7.12}$$

is considered next. This network will require a final state distributions for the $\mathrm{N}(^4\mathrm{S})+\mathrm{O_2}(\mathrm{X}^3\Sigma_\mathrm{g}^-) \leftrightarrow \mathrm{NO}(\mathrm{X}^2\Pi) + \mathrm{O}(^3\mathrm{P})$ and $\mathrm{N}(^4\mathrm{S})+\mathrm{NO}(\mathrm{X}^2\Pi) \leftrightarrow \mathrm{O}(^3\mathrm{P})+\mathrm{N_2}(\mathrm{X}^1\Sigma_g^+)$ reactions. Again, several non-reactive, state-changing processes will be included as well and the probability to follow a non-reactive or a reactive the pathway is determined from QCT simulations.

The strategy is to start by sampling an initial distribution of (v, j, E_t) states, evaluate the NN to predict (v', j', E_t') for the relevant diatomic product distributions. These are sampled from equilibrium Monte Carlo simulations to provide input for the next reaction. One of the questions we will like to tackle is whether a quasi-equilibrium distribution for each of the diatomic species is ever reached and, if yes, how these quasi-equilibrium (quasi-stationary) vibrational and rotational distributions are characterized.

7.3 Results

7.3.1 Available PESs and STD trained models

The available PESs all at the MRCI+Q/aug-cc-pVTZ level of theory and represented as a RKHS are the ^{2}A$'$, ^{4}A$'$, ^{2}A$''$ PESs for the [NOO][39] system and the ^{3}A$'$ and ^{3}A$''$ PESs for the [NNO][228] system.

$$O(^3P) + NO(X^2\Pi) \leftrightarrow N(^4S) + O_2(X^3\Sigma_g^-)[^2A', ^4A', ^2A''] \tag{7.13}$$

$$N(^4S) + NO(X^2\Pi) \leftrightarrow O(^3P) + N_2(X^1\Sigma_g^-)[^3A', ^3A''] \tag{7.14}$$

$$O(^3P) + NO(X^2\Pi) \leftrightarrow O(^3P) + NO(X^2\Pi)[^2A', ^4A', ^2A''] \tag{7.15}$$

$$N(^4S) + O_2(X^3\Sigma_g^-) \leftrightarrow N(^4S) + O_2(X^3\Sigma_g^-)[^2A', ^4A', ^2A''] \tag{7.16}$$

$$N(^4S) + NO(X^2\Pi) \leftrightarrow N(^4S) + NO(X^2\Pi)[^3A', ^3A''] \tag{7.17}$$

$$O(^3P) + N_2(X^1\Sigma_g^-) \leftrightarrow O(^3P) + N_2(X^1\Sigma_g^-)[^3A', ^3A''] \tag{7.18}$$

7.3.2 STD trained models

$$N(^4S) + O_2(X^3\Sigma_g^-) \rightarrow O(^3P) + NO(X^2\Pi)[^4A'] \tag{7.19}$$

$$N(^4S) + O_2(X^3\Sigma_g^-) \rightarrow N(^4S) + O_2(X^3\Sigma_g^-)[^4A'] \tag{7.20}$$

$$O(^3P) + NO(X^2\Pi) \rightarrow N(^4S) + O_2(X^3\Sigma_g^-)[^4A'](\text{In Progress}) \tag{7.21}$$

$$N(^4S) + O_2(X^3\Sigma_g^-) \rightarrow O(^3P) + O(^3P) + N(^4S)(\text{In Progress}) \tag{7.22}$$

7.3.3 Branching Ratios

Using the output from QCT simulations, a very straightforward approach to determine the probabilities or branching ratios is determined for each of the individual processes. Examples of the expected branching ratios for the N+O_2 and O+NO system given an initial condition is shown in Table 7.1. The branching ratio is taken as the fraction between $\frac{N(i)}{N_{\text{tot}}}$, where N_{tot} is the total number of trajectories and $N(i)$ is the number of trajectories for a particular process: Non-Reactive, Reactive or Dissociation. Figure 7.1 shows a complete 3D map of the branching ratio for the N+O_2 system using 2184 initial conditions.

N+O_2	N+O_2 (Non-reactive)	O+NO (Reactive)	O+O+N (Dissociation)
(2, 120, 1.5)	0.67	0.33	0.00
(6, 135, 4.0)	0.59	0.35	0.06
(0, 135, 8.0)	0.64	0.25	0.11
O +NO	O + NO (Non-reactive)	N+O_2 (Reactive)	N+O+O (Dissociation)
(0, 105, 1.5)	0.95	0.05	0.00
(4, 120, 5.0)	0.84	0.13	0.03
(6, 135, 8.0)	0.76	0.10	0.13

Table 7.1: Branching ratios ($\frac{N_i}{N_{\text{tot}}}$) for specific (v, j, E_{trans}) states. E_{trans} in eV

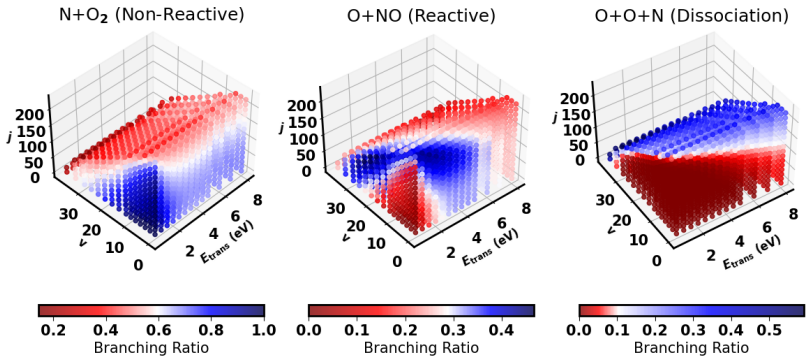

Figure 7.1: Branching Ratio for the: $N(^4S) + O_2(X^3\Sigma_g^-) \rightarrow N(^4S) + O_2(X^3\Sigma_g^-)$ (left); $N(^4S) + O_2(X^3\Sigma_g^-) \rightarrow O(^3P) + NO(X^2\Pi)$ (middle) ; and $N(^4S) + O_2(X^3\Sigma_g^-) \rightarrow N(^4S) + O(^3P) + O(^3P)$ (right) Processes. A grid of 2184 initial conditions is considered.

7.4 Sampling from a Distribution

7.4.1 Reactive: $N+O_2 \rightarrow NO+O$

A first attempt has been made to effectively model the $N(^4S) + O_2(X^3\Sigma_g^-) \rightarrow O(^3P)+NO(X^2\Pi)[^4A']$ reaction. This has been done by starting from a Boltzmann distribution at ($T_{\text{trans}} = T_{\text{rot}} = 10000$ K, and different scenarios of T_{vib}=5000, 100000 and 200000 K). The initial conditions used for the STD evaluation are initially sampled from the equilibrium Boltzmann distribution and in the case of T_{vib} allowed to evolve in K cycles by evaluation the initial conditions via STD. Thus, generating a new product distribution $P(v')_K$. In this first attempt the other two degrees of freedom ($T_{\text{trans}} = T_{\text{rot}} = 10000$ K are kept frozen, by throwing away the sampled values for $P(j')_K$ and $P(E_{\text{trans}})_K$ and re-sampling the initial distribution. Figure 7.2 shows the evolution of the vibrational energy $< E_v >$ calculated as $< E_v >= \sum_{i=0}^{i=vmax} P(v_i) * E_{v_i}$. The number of extracted samples for each K cycle was choosen to be $N = 10^3$ and $N = 10^4$ in order to check the necessary number of samples needed for convergence. Other attempts have been made to study the inelastic $N+O_2 \rightarrow N+O_2$ process, but so far the efforts have not proven successful.

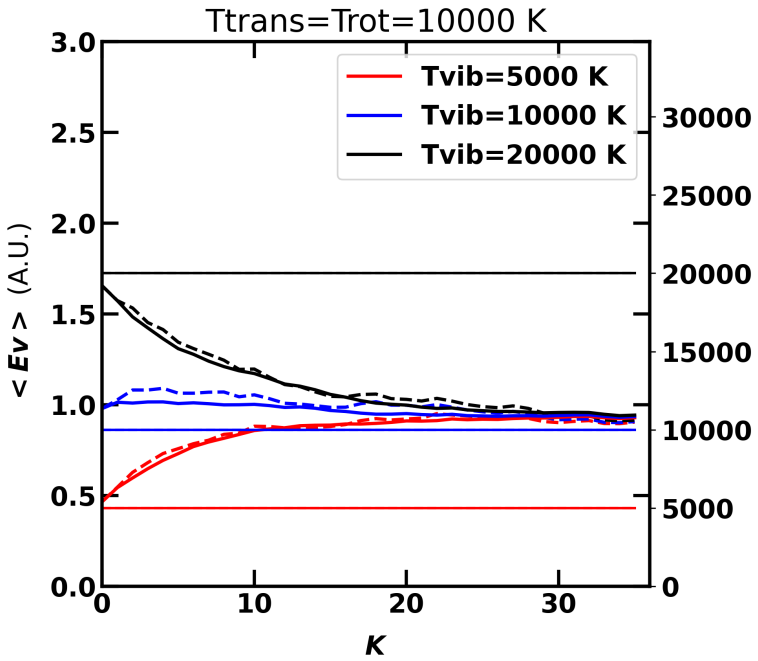

Figure 7.2: $< E_v >$ as a function of K. $T_{\text{trans}} = T_{\text{rot}} = 10000$ K and T_{vib} is initially sampled at different vibrational temperatures $= 5000, 10000, 20000$ K for $K = 0$ and then allow to evolve freely for each K step. The number of initial conditions sampled at each K is 10^3 (dash line) and 10^4 (solid lines).

Chapter 8

Conclusion and Outlook

In this work, we focused on a multi-scale approach in the construction of potential energy surfaces, quasi-classical simulations, and implementation of a Neural Network model to predict the distributions of the internal degrees of freedom. Future development is described in the implementation of a iterative model that can give a temporal evolution of the associated internal degrees of freedom, and can in future be able to effectively reproduce macroscopic observables in addition to being comparable to state-to-state master equation models.

This work gives insight into the observables used in hypersonic reentry such as reaction rates, cross sections, and vibrational relaxation rates with an extreme degree of accuracy and within the error of the experimental measurement for most cases observed. In such an approach, it was necessary for an exhaustive detailed construction and representation of high-fidelity potential energy surfaces, which incorporated all the states involved in the reaction and the relevant physics. These landscapes provided surfaces that were calculated with the same level of theory (MRCI+Q/aug-cc-pVTZ) and accuracy in most cases of ($<$ 1 kcal/mol) with respect to reference ab-initio data. This approach provides a bridge between the microscopic landscape and the macroscopic observable. Thus, the necessity for

such approaches conserve the necessary accuracy at each step: PES construction, quasi-classical simulations, and state-to-distribution modeling over a wide range of temperatures.

The validity of such an approach has been demonstrated with the consistency with the experiment and T-dependent equilibrium constants such as the one reported by JANAF and CEA. This while providing refined details such as the characterization of regions in the potential energy surfaces where particular processes such as vibrational relaxation is most susceptible (as shown in Figs. 3.8 in Chapter 3 and 4.8 in Chapter 4). This "probing" effect on the surface can give an immediate realization of the underlying process, just by examining which areas of the PES were probed. Effects such as "gatting" which is well defined in Chapter 3 can only be studied with a detailed approach such as this one. Other topography characterizations such as crossings or conical intersections give insights that can determine if further implementation is necessary such as the inclusion of non-adiabatic effects into the construction of the surface.

In addition to QCT-generated observables the effective prediction of product state distributions of the rotational, vibrational, and translational degrees of freedom from our developed state-to-distribution model has given us a rapid chemical-physics model which is within the accuracy of QCT simulations ($R^2 \sim 0.98$), and in certain cases outperformed commonly used phenomenological models such as Larsen-Borgnakke (as shown in Fig. 5.8 in Chapter 5). The STD model can additionally be useful in reducing the computational cost of averaged observables such as reaction rate (as shown in Fig. 5.7 in Chapter 5) which are currently being calculated by QCT simulations. Further, implementation has been addressed with the blending of accurate spectroscopic information into the model (MH), which shows a difference in the population of v' in comparison to the assignment from semiclassical theory (SC). This leads to a difference in the fraction of final

states that are above the product molecular dissociation energy (as shown in Fig. 6.8 in Chapter 6). This wide range of observables at different scales can serve as input to coarse-grain simulations at different stages of the simulation. Although, this highly accurate predictability framework comes at a cost for future application into the polyatomic systems (pentatomic and higher). Further, development needs to be made in the construction and representation of potential energy surfaces for larger systems in addition to QCT or other simulation methods that can support the increased simulation cost while preserving the same levels of accuracy.

Bibliography

[1] E. Herbst and E. F. Van Dishoeck, *Annu. Rev. Astron. Astrophys.*, 2009, **47**, 427–480.

[2] V. Wakelam, I. Smith, E. Herbst, J. Troe, W. Geppert, H. Linnartz, K. Öberg, E. Roueff, M. Agúndez, P. Pernot *et al.*, *Space Sci. Rev.*, 2010, **156**, 13–72.

[3] V. Wakelam, E. Herbst, J.-C. Loison, I. Smith, V. Chandrasekaran, B. Pavone, N. Adams, M.-C. Bacchus-Montabonel, A. Bergeat, K. Béroff *et al.*, *Astrophys. J. Suppl. Ser.*, 2012, **199**, 21.

[4] S. Stankovich, D. A. Dikin, G. H. Dommett, K. M. Kohlhaas, E. J. Zimney, E. A. Stach, R. D. Piner, S. T. Nguyen and R. S. Ruoff, *nature*, 2006, **442**, 282–286.

[5] P. J. Hajduk and J. Greer, *Nat. Rev. Drug Discov.*, 2007, **6**, 211–219.

[6] T. E. Schwartzentruber, L. C. Scalabrin and I. D. Boyd, *J. Comput. Phys.*, 2007, **225**, 1159–1174.

[7] I. D. Boyd and T. E. Schwartzentruber, *Nonequilibrium Gas Dynamics and Molecular Simulation*, 2017, vol. 42.

[8] J. D. Anderson, *Hypersonic and high temperature gas dynamics*, Aiaa, 2000.

[9] D. Koner, R. J. Bemish and M. Meuwly, *J. Phys. Chem. A*, 2020, **124**, 6255–6269.

[10] G. Sarma, *Progr. Aerospace Sci.*, 2000, **36**, 281–349.

[11] P. V. Marrone and C. E. Treanor, *Phys. Fluids*, 1963, **6**, 1215–1221.

[12] J. Appleton, M. Steinberg and D. Liquornik, *J. Chem. Phys.*, 1968, **48**, 599–608.

[13] S. Byron, *J. Chem. Phys.*, 1966, **44**, 1378–1388.

[14] R. K. Hanson and D. Baganoff, *AIAA Journal*, 1972, **10**, 211–215.

[15] H. Hornung, *J. Fluid Mech.*, 1972, **53**, 149–176.

[16] R. C. Millikan and D. R. White, *J. Chem. Phys.*, 1963, **39**, 3209–3213.

[17] C. Park, R. L. Jaffe and H. Partridge, *J. Thermophys. Heat Transfer.*, 2001, **15**, 76–90.

[18] C. Park, *J. Thermophys. Heat Transfer.*, 1993, **7**, 385–398.

[19] P. Valentini, T. E. Schwartzentruber, J. D. Bender and G. V. Candler, *Phys. Rev. Fluids*, 2016, **1**, 043402.

[20] M. Panesi, R. L. Jaffe, D. W. Schwenke and T. E. Magin, *J. Chem. Phys.*, 2013, **138**, 044312.

[21] O. Denis-Alpizar, R. J. Bemish and M. Meuwly, *J. Chem. Phys.*, 2017, **146**, 111102.

[22] G. A. Bird, *NASA STI/Recon Technical Report A*, 1976, **76**, 40225.

[23] W. Wagner, *J. Stat. Phys.*, 1992, **66**, 1011–1044.

[24] C. Borgnakke and P. S. Larsen, *J. Comput. Phys.*, 1975, **18**, 405–420.

[25] M. Hankel, S. C. Smith, S. K. Gray and G. G. Balint-Kurti, *Computer Physics Communications*, 2008, **179**, 569–578.

[26] D. G. Truhlar and J. T. Muckerman, in *Atom - Molecule Collision Theory*, ed. R. B. Bernstein, Springer US, 1979, pp. 505–566.

[27] S. Goswami, J. C. San Vicente Veliz, M. Upadhyay, R. J. Bemish and M. Meuwly, *Phys. Chem. Chem. Phys.*, 2022, **24**, 23309–23322.

[28] B. Liu, *J. Chem. Phys.*, 1973, **58**, 1925–1937.

[29] J. Olsen, *Int. J. Quantum Chem.*, 2011, **111**, 3267–3272.

[30] P. J. Knowles and H.-J. Werner, *Chemical physics letters*, 1988, **145**, 514–522.

[31] R. Franke and G. Nielson, *International journal for numerical methods in engineering*, 1980, **15**, 1691–1704.

[32] P. Lancaster and K. Salkauskas, *Mathematics of computation*, 1981, **37**, 141–158.

[33] B. J. Braams and J. M. Bowman, *International Reviews in Physical Chemistry*, 2009, **28**, 577–606.

[34] B. G. Sumpter and D. W. Noid, *Chemical physics letters*, 1992, **192**, 455–462.

[35] O. T. Unke and M. Meuwly, *J. Chem. Theory Comput.*, 2019, **15**, 3678–3693.

[36] S. Käser, O. T. Unke and M. Meuwly, *New J. Phys.*, 2020, **22**, 055002.

[37] S. Kaser, E. D. Boittier, M. Upadhyay and M. Meuwly, *J. Chem. Theory Comput.*, 2021, **17**, 3687–3699.

[38] D. Koner, J. C. San Vicente Veliz, A. van der Avoird and M. Meuwly, *Phys. Chem. Chem. Phys.*, 2019, **21**, 24976–24983.

[39] J. C. San Vicente Veliz, D. Koner, M. Schwilk, R. J. Bemish and M. Meuwly, *Phys. Chem. Chem. Phys.*, 2020, **22**, 3927–3939.

[40] D. Koner, J. C. S. V. Veliz, R. J. Bemish and M. Meuwly, *Physical Chemistry Chemical Physics*, 2020, **22**, 18488–18498.

[41] D. Koner, R. J. Bemish and M. Meuwly, *J. Chem. Phys.*, 2018, **149**, 094305.

[42] J. C. S. V. Veliz, D. Koner, M. Schwilk, R. J. Bemish and M. Meuwly, *Physical Chemistry Chemical Physics*, 2021, **23**, 11251–11263.

[43] H. Pan, K. Liu, A. Caracciolo and P. Casavecchia, *Chem. Soc. Rev.*, 2017, **46**, 7517–7547.

[44] A. Caracciolo, J. Zhang, S. A. Lahankar and T. K. Minton, *J. Phys. Chem. A*, 2022, **126**, 2091–2102.

[45] T. E. Schwartzentruber, M. S. Grover and P. Valentini, *J. Thermophys. Heat Transfer.*, 2018, **32**, 892–903.

[46] D. Koner, O. T. Unke, K. Boe, R. J. Bemish and M. Meuwly, *J. Chem. Phys.*, 2019, **150**, 211101.

[47] P. Lykos and G. Pratt, *Reviews of Modern Physics*, 1963, **35**, 496.

[48] H. F. Schaefer, *Methods of electronic structure theory*, Springer Science & Business Media, 2013, vol. 3.

[49] T. J. Lee and P. R. Taylor, *Int. J. Quantum Chem.*, 1989, **36**, 199–207.

[50] K. Hirao, *Recent Advances in Multireference Methods*, WORLD SCIENTIFIC, 1999.

[51] A. Balková and R. J. Bartlett, *J. Chem. Phys.*, 1994, **101**, 8972–8987.

[52] H. Lischka, R. Shepard, R. M. Pitzer, I. Shavitt, M. Dallos, T. Müller, P. G. Szalay, M. Seth, G. S. Kedziora, S. Yabushita *et al.*, *Physical Chemistry Chemical Physics*, 2001, **3**, 664–673.

[53] P. G. Szalay, T. Müller, G. Gidofalvi, H. Lischka and R. Shepard, *Chemical Reviews*, 2012, **112**, 108–181.

[54] P. J. Knowles and H.-J. Werner, *Theoretica chimica acta*, 1992, **84**, 95–103.

[55] R. Lindh and L. González, *Quantum Chemistry and Dynamics of Excited States: Methods and Applications*, John Wiley & Sons, 2020.

[56] T. Hollebeek, T.-S. Ho and H. Rabitz, *J. Chem. Phys.*, 1997, **106**, 7223–7227.

[57] O. T. Unke and M. Meuwly, *J. Chem. Theory. Comput.*, 2017, **57**, 1923–1931.

[58] J. C. San Vicente Veliz, D. Koner, M. Schwilk, R. J. Bemish and M. Meuwly, *Phys. Chem. Chem. Phys.*, 2020, **22**, 3927–3939.

[59] J. C. San Vicente Veliz, D. Koner, M. Schwilk, R. J. Bemish and M. Meuwly, *Phys. Chem. Chem. Phys.*, 2021, **23**, 11251–11263.

[60] O. T. Unke, J. C. Castro-Palacio, R. J. Bemish and M. Meuwly, *J. Chem. Phys.*, 2016, **144**, 224307.

[61] B. Schölkopf, R. Herbrich and A. J. Smola, International conference on computational learning theory, 2001, pp. 416–426.

[62] G. H. Golub and C. F. Van Loan, *Matrix computations*, JHU press, 2013.

[63] R. A. Willoughby, *SIAM Review*, 1979, **21**, 266–267.

[64] P. Soldán and J. M. Hutson, *J. Chem. Phys.*, 2000, **112**, 4415–4416.

[65] T. Hollebeek, T.-S. Ho and H. Rabitz, *Annual review of physical chemistry*, 1999, **50**, 537–570.

[66] N. E. Henriksen and F. Y. Hansen, *Theories of molecular reaction dynamics: the microscopic foundation of chemical kinetics*, Oxford University Press, 2018.

[67] Y. Zeldovich, *Acta Physicochimica U.S.S.R.*, 1946, **21**, 577–628.

[68] D. Bose and G. V. Candler, *J. Chem. Phys.*, 1997, **107**, 6136–6145.

[69] J. A. Dodd, R. B. Lockwood, E. S. Hwang, S. M. Miller and S. J. Lipson, *J. Chem. Phys.*, 1999, **111**, 3498–3507.

[70] R. Gupta, J. Yos, R. Thompson and K. Lee, *Acta Physicochimica U.S.S.R.*, 1946, **21**, 577–628.

[71] C. Park, *J. Thermophys. Heat Transfer*, 1993, **7**, 385–398.

[72] K. Venkataramani, J. D. Yonker and S. M. Bailey, *J. Geophys. Res. - Space Phys.*, 2016, **121**, 2450–2461.

[73] G. Caledonia, R. Krech, D. Oakes, S. Lipson and W. Blumberg, *J. Geophys. Res. - Space Phys.*, 2000, **105**, 12833–12837.

[74] I. Winkler, R. A. Stachnik, J. I. Steinfeld and S. M. Miller, *J. Chem. Phys.*, 1986, **85**, 890–899.

[75] P. J. B. S. Caridade and A. J. C. Varandas, *J. Phys. Chem. A*, 2004, **108**, 3556–3564.

[76] J. W. Duff, F. Bien and D. E. Paulsen, *Geophys. Res. Lett.*, 1994, **21**, 2043–2046.

[77] B. Ramachandran, N. Balakrishnan and A. Dalgarno, *Chem. Phys. Lett.*, 2000, **332**, 562–568.

[78] S. Walch and R. Jaffe, *J. Chem. Phys.*, 1987, **86**, 6946–6956.

[79] R. Sayós, C. Oliva and M. González, *J. Chem. Phys.*, 2002, **117**, 670–679.

[80] M. González, I. Miquel and R. Sayós, *J. Chem. Phys.*, 2001, **115**, 8838–8851.

[81] A. Varandas, *J. Chem. Phys.*, 2003, **119**, 2596–2613.

[82] M. V. Ivanov, H. Zhu and R. Schinke, *J. Chem. Phys.*, 2007, **126**, 054304.

[83] V. C. Mota, P. J. S. B. Caridade and A. J. C. Varandas, *J. Phys. Chem. A*, 2012, **116**, 3023–3034.

[84] J. C. Castro-Palacio, T. Nagy, R. J. Bemish and M. Meuwly, *J. Chem. Phys.*, 2014, **141**, 164319.

[85] P. J. S. B. Caridade, V. C. Mota, J. R. Mohallem and A. J. C. Varandas, *J. Phys. Chem. A*, 2008, **112**, 960–965.

[86] E. S. Hwang, K. J. Castle and J. A. Dodd, *J. Geophys. Res.*, 2003, **108**, 1109.

[87] P. J. S. B. Caridade, J. Li, V. C. Mota and A. J. C. Varandas, *J. Phys. Chem. A*, 2018, **122**, 5299–5310.

[88] Gordon and J. McBride, 1996, **19**, 1311.

[89] M. W. Chase, J. L. Curnutt, J. R. Downey, R. A. McDonald, A. N. Syverud and E. A. Valenzuela, 1982, **11**, 695–940.

[90] H. Werner and P. J. Knowles, *J. Chem. Phys.*, 1985, **82**, 5053–5063.

[91] P. J. Knowles and H.-J. Werner, *Chem. Phys. Lett.*, 1985, **115**, 259 – 267.

[92] H. Werner and W. Meyer, *J. Chem. Phys.*, 1980, **73**, 2342–2356.

[93] H.-J. Werner and P. J. Knowles, *J. Chem. Phys.*, 1988, **89**, 5803–5814.

[94] P. J. Knowles and H.-J. Werner, *Chem. Phys. Lett.*, 1988, **145**, 514 – 522.

[95] T. H. Dunning, *J. Chem. Phys.*, 1989, **90**, 1007–1023.

[96] H.-J. Werner, P. J. Knowles, G. Knizia, F. R. Manby and M. S. et al., *MOLPRO, version 2019.1, A package of ab initio programs*, 2019.

[97] O. T. Unke and M. Meuwly, *J. Chem. Inf. Model*, 2017, **57**, 1923–1931.

[98] G. Henkelman, B. Uberuaga and H. Jonsson, *J. Chem. Phys.*, 2000, **113**, 9901–9904.

[99] A. H. Larsen and J. J. Mortensen, *J. Phys. Condens. Matter*, 2017, **29**, 273002.

[100] N. E. Henriksen and F. Y. Hansen, *Theories of Molecular Reaction Dynamics*, Oxford, 2011.

[101] D. Koner, T. Barrios, Lizandra andGonzález-Lezana and A. N. Panda, *J. Phys. Chem. A*, 2016, **120**, 4731–4741.

[102] D. Koner, R. J. Bemish and M. Meuwly, *J. Chem. Phys.*, 2018, **149**, 094305.

[103] L. Bonnet and J.-C. Rayez, *Chem. Phys. Lett.*, 1997, **277**, 183–190.

[104] L. Bonnet and J.-C. Rayez, *Chem. Phys. Lett.*, 2004, **397**, 106–109.

[105] J. D. Bender, P. Valentini, I. Nompelis, Y. Paukku, Z. Varga, D. G. Truhlar, T. Schwartzentruber and G. V. Candler, *J. Chem. Phys.*, 2015, **143**, 054304.

[106] E. L. Kolsbjerg, M. N. Groves and B. Hammer, *J. Chem. Phys.*, 2016, **145**, 094107.

[107] R. A. Sultanov and N. Balakrishnan, *J. Chem. Phys.*, 2006, **124**, 124321.

[108] F. Kaufman and L. J. Decker, *7th Symp. (Int.) Combustion*, 1959, 57.

[109] J. B. Livesey, A. L. Roberts and A. Williams, *Combust. Sci. Technol.*, 1971, **4**, 9–15.

[110] K. L. Wray and J. D. Teare, *J. Chem. Phys.*, 1962, **36**, 2582–2596.

[111] T. C. Clark, S. H. Garnett and G. B. Kistiakowsky, *J. Chem. Phys.*, 1969, **51**, 2885–2891.

[112] R. K. Hanson, W. L. Flower and C. H. Kruger, *Combust. Sci. Technol.*, 1974, **9**, 79–86.

[113] A. Fernandez, A. Goumri and A. Fontijn, *J. Phys. Chem. A*, 1998, **102**, 168–172.

[114] R. K. Hanson and S. Salimian, *Combustion Chemistry*, Springer, New York, NY, 1984.

[115] I. D. Boyd and T. E. Schwartzentruber, in *Nonequilibrium Gas Dynamics and Molecular Simulation*, Cambridge University Press, 2017.

[116] J. C. Castro-Palacio, R. J. Bemish and M. Meuwly, *J. Chem. Phys.*, 2015, **142**, 091104.

[117] A. Rahbee and J. J. Gibson, *J. Chem. Phys.*, 1981, **74**, 5143–5148.

[118] R. R. Herm, B. J. Sullivan and M. E. Whitson, *J. Chem. Phys.*, 1983, **79**, 2221–2230.

[119] G. E. Caledonia, R. H. Krech, D. B. Oakes, S. J. Lipson and W. A. M. Blumberg, *J. Geophys. Res.*, 2000, **105**, 12833–12837.

[120] R. P. Fernando and I. W. Smith, *Chem. Phys. Lett.*, 1979, **66**, 218 – 222.

[121] R. D. Sharma and R. G. Roble, *J. Geophys. Res. - Space Phys.*, 2001, **106**, 21343–21350.

[122] M. Quack and J. Troe, *Ber. Bunsenges. Phys. Chem.*, 1975, **79**, 170–183.

[123] M. V. Ivanov, R. Schinke and G. C. Mcbane, 2007, **105**, 1183–1191.

[124] K. Glänzer and J. Troe, *J. Chem. Phys.*, 1975, **63**, 4352–4357.

[125] H. V. Lilenfeld, *Phillips Laboratory, Hanscom Air Force Base, Mass*, 1994, **PL-TR-94–2180**, 24pp.

[126] S. M. Anderson, F. S. Klein and F. Kaufman, *J. Chem. Phys.*, 1985, **83**, 1648–1656.

[127] M. Meuwly and J. Hutson, *J. Chem. Phys.*, 1999, **110**, 8338–8347.

[128] M. Sharma, A. B. Swantek, W. Flaherty, J. M. Austin, S. Doraiswamy and G. V. Candler, *J. Thermophys. Heat Transfer.*, 2010, **24**, 673–683.

[129] M. E. Lewittes, C. C. Davis and R. A. McFarlane, *J. Chem. Phys.*, 1978, **69**, 1952–1957.

[130] D. Husain and A. N. Young, *J. Chem. Soc., Faraday Trans. 2*, 1975, **71**, 525–531.

[131] A. Bergeat, T. Calvo, G. Dorthe and J. Loison, *Chem. Phys. Lett.*, 1999, **308**, 7–12.

[132] W. D. Geppert, D. Reignier, T. Stoecklin, C. Naulin, M. Costes, D. Chastaing, S. D. Le Picard, I. R. Sims and I. W. M. Smith, *Phys. Chem. Chem. Phys.*, 2000, **2**, 2873–2881.

[133] K. H. Becker, K. J. Brockmann and P. Weisen, *J. Chem. Soc., Faraday Trans. 2*, 1988, **84**, 455–461.

[134] G. Dorthe, P. Caubet, T. Vias, B. Barrere and J. Marchais, *J. Phys. Chem.*, 1991, **95**, 5109–5116.

[135] D. Chastaing, P. L. James, I. R. Sims and I. W. M. Smith, *Phys. Chem. Chem. Phys.*, 1999, **1**, 2247–2256.

[136] D. Chastaing, S. D. Le Picard and I. R. Sims, *J. Chem. Phys.*, 2000, **112**, 8466–8469.

[137] A. J. Dean, D. F. Davidson and R. K. Hanson, *J. Phys. Chem.*, 1991, **95**, 183–191.

[138] E. Ogryzlo, J. Reilly and B. Thrush, *Chem. Phys. Lett.*, 1973, **23**, 37–39.

[139] J. Dubrin, C. MacKay, M. Pandow and R. Wolfgang, *J. Inorg. Nuc. Chem.*, 1964, **26**, 2113–2122.

[140] S. S. Xantheas and K. Ruedenberg, *Int. J. Quantum Chem.*, 1994, **49**, 409–427.

[141] R. F. Heidner, D. Husain and J. R. Wiesenfeld, 1973, **69**, 927–938.

[142] R. Heidner and D. Husain, *Nat. Phys. Sci.*, 1973, **241**, 10–11.

[143] A. W. Jasper and R. Dawes, *J. Chem. Phys.*, 2013, **139**, 154313.

[144] J. Troe, *Fifth Symp. (Int.) Combust.*, 1975, **15**, 667–679.

[145] M. Braunstein and J. W. Duff, *J. Chem. Phys.*, 2000, **112**, 2736–2745.

[146] P. Kozlov, V. Makarov, V. Pavlov and O. Shatalov, *Shock Waves*, 2000, **10**, 191–195.

[147] R. E. Center, *J. Chem. Phys.*, 1973, **58**, 5230–5236.

[148] J. D. Kelley and R. L. Thommarson, *J. Chem. Phys.*, 1977, **66**, 1953–1959.

[149] J. A. Davidson, H. I. Schiff, T. J. Brown and C. J. Howard, *J. Chem. Phys.*, 1978, **69**, 1216–1217.

[150] J. C. Tully, *J. Chem. Phys.*, 1975, **62**, 1893–1898.

[151] N. W. Winter, C. F. Bender and W. A. Goddard III, *Chemical Physics Letters*, 1973, **20**, 489–492.

[152] S. Y. Grebenshchikov and R. Borrelli, 2012, **3**, 3223–3227.

[153] S. Y. Grebenshchikov, *J. Chem. Phys.*, 2013, **138**, 224107.

[154] S. Y. Grebenshchikov, *J. Chem. Phys.*, 2013, **138**, 224106.

[155] J. A. Schmidt, M. S. Johnson and R. Schinke, *Proc. Nat. Acad. Sci. USA*, 2013, **110**, 17691–17696.

[156] B. Zhou, C. Zhu, Z. Wen, Z. Jiang, J. Yu, Y.-P. Lee and S. H. Lin, *The Journal of Chemical Physics*, 2013, **139**, 154302.

[157] R. N. Dixon and G. Porter, *Proc. R. Soc. Lond. A.*, 1963, **275**, 431–446.

[158] S. Kinnersly and J. Murrell, 1977, **33**, 1479–1494.

[159] A. L. Brunsvold, H. P. Upadhyaya, J. Zhang, R. Cooper, T. K. Minton, M. Braunstein and J. W. Duff, *J. Phys. Chem. A*, 2008, **112**, 2192–2205.

[160] D. W. Schwenke, R. L. Jaffe and G. M. Chaban, *"unpublished"*, 2016, 1–56.

[161] M. Costes and C. Naulin, *Comptes Rendus de l'Académie des Sciences-Series IIC-Chemistry*, 1998, **1**, 771–775.

[162] A. J. Dean, D. F. Davidson and R. K. Hanson, *J. Phys. Chem.*, 1991, **95**, 183–191.

[163] T.-S. Ho and H. Rabitz, *J. Chem. Phys.*, 1996, **104**, 2584.

[164] S. Langhoff and E. Davidson, *Int. J. Quant. Chem.*, 1974, **8**, 61–72.

[165] D. A. Kreplin, P. J. Knowles and H.-J. Werner, *J. Chem. Phys.*, 2019, **150**, 194106.

[166] T.-S. Ho and H. Rabitz, *J. Chem. Phys.*, 2000, **113**, 3960–3968.

[167] V. K. Shen, D. W. Siderius, W. P. Krekelberg, , H. W. Hatch and Eds., *NIST Chemistry WebBook, NIST Standard Reference Database Number 69*.

[168] D.-Y. Hwang and A. M. Mebel, *cp*, 2000, **256**, 169 – 176.

[169] M. Braunstein and J. W. Duff, *J. Phys. Chem. A*, 2009, **113**, 10795–10802.

[170] A. R. Fairbairn and A. G. Gaydon, *Proc. Royal Soc. Lond. A.*, 1969, **312**, 207–227.

[171] A. Bergeat, T. Calvo, G. Dorthe and J. Loison, *Chem. Phys. Lett.*, 1999, **308**, 7–12.

[172] D. Husain and A. N. Young, *J. Chem. Soc., Faraday Trans. 2*, 1975, **71**, 525–531.

[173] I. R. Sims, *Nat. Chem.*, 2013, **5**, 734–736.

[174] J. Malcolm W. Chase, *NIST-JANAF thermochemical tables*, Fourth edition. Washington, DC: American Chemical Society ; New York : American Institute of Physics for the National Institute of Standards and Technology, 1998.

[175] S. Jaffe and F. S. Klein, *Trans. Faraday Soc.*, 1966, **62**, 3135–3141.

[176] S. H. Garnett, G. B. Kistiakowsky and B. V. O Grady, *J. Chem. Phys.*, 1969, **51**, 84–91.

[177] D. Koner, *Scattering studies of proton transfer reactions between rare gas atoms*, Indian Institute of Technology Guwahati, 2016.

[178] E. Parzen, *The Annals of Mathematical Statistics*, 1962, **33**, 1065–1076.

[179] R. C. Team, *R: A Language and Environment for Statistical Computing*, R Foundation for Statistical Computing, Vienna, Austria, 2017.

[180] M. Meuwly and M. Karplus, *J. Chem. Phys.*, 2002, **116**, 2572–2585.

[181] S. Chandra, V. Maheshwari and A. Sharma, *AAS*, 1996, **117**, 557–559.

[182] W. Braun, R. L. Brown, D. Garvin, J. T. Herron, R. E. Huie, M. J. Kurylo, A. H. Laufer, J. D. McKinley, H. Okabe, M. D. Scheer, W. Tsang and D. H. Stedman, *J. Phys. Chem. Ref. Data*, 1973, **2**, 267–312.

[183] M. Meuwly and J. Hutson, *J. Chem. Phys.*, 1999, **110**, 8338–8347.

[184] J. M. Bowman and B. Gazdy, *J. Chem. Phys.*, 1991, **94**, 816–817.

[185] S. Venturi, R. L. Jaffe and M. Panesi, *J. Phys. Chem. A*, 2020, **124**, 5129–5146.

[186] M. Meuwly, *Chem. Rev.*, 2021, **121**, 10218–10239.

[187] M. S. Grover, E. Torres and T. E. Schwartzentruber, *Phys. Fluids*, 2019, **31**, 076107.

[188] D. Koner, O. T. Unke, K. Boe, R. J. Bemish and M. Meuwly, *J. Chem. Phys.*, 2019, **150**, 211101.

[189] T. E. Schwartzentruber, M. S. Grover and P. Valentini, *J. Thermophys. Heat Transfer.*, 2018, **32**, 892–903.

[190] I. Goodfellow, Y. Bengio and A. Courville, *Deep Learning*, MIT Press, 2016.

[191] J. Arnold, D. Koner, S. Käser, N. Singh, R. J. Bemish and M. Meuwly, *J. Phys. Chem. A*, 2020, **124**, 7177–7190.

[192] I. D. Boyd and T. E. Schwartzntruber, *Nonequilibrium Gas Dynamics and Molecular Simulation*, Cambridge University Press, New York, 2017.

[193] D. Knight, J. Longo, D. Drikakis, D. Gaitonde, A. Lani, I. Nompelis, B. Reimann and L. Walpot, *Progr. Aerospace Sci.*, 2012, **48-49**, 8–26.

[194] M. Karplus, R. N. Porter and R. D. Sharma, *J. Chem. Phys.*, 1965, **43**, 3259–3287.

[195] J. D. Bender, P. Valentini, I. Nompelis, Y. Paukku, Z. Varga, D. G. Truhlar, T. Schwartzentruber and G. V. Candler, *J. Chem. Phys.*, 2015, **143**, 054304.

[196] Y.-R. Luo and J. Kerr, *CRC handb. chem. phys.*, 2012, **89**, 89.

[197] K. He, X. Zhang, S. Ren and J. Sun, Proceedings of the IEEE conference on computer vision and pattern recognition, 2016, pp. 770–778.

[198] C. Dugas, Y. Bengio, F. Bélisle, C. Nadeau and R. Garcia, Advances in neural information processing systems, 2001, pp. 472–478.

[199] D.-A. Clevert, T. Unterthiner and S. Hochreiter, *arXiv preprint arXiv:1511.07289*, 2015.

[200] Y. A. LeCun, L. Bottou, G. B. Orr and K.-R. Müller, in *Neural networks: Tricks of the trade*, Springer, 2012, pp. 9–48.

[201] X. Glorot and Y. Bengio, Proceedings of the 13th International Conference on Artificial Intelligence and Statistics, 2010, pp. 249–256.

[202] D. Kingma and J. Ba, *arXiv preprint arXiv:1412.6980*, 2014.

[203] M. Abadi, A. Agarwal, P. Barham, E. Brevdo, Z. Chen, C. Citro, G. S. Corrado, A. Davis, J. Dean, M. Devin *et al.*, *arXiv preprint arXiv:1603.04467*, 2016.

[204] N. Singh and T. Schwartzentruber, *Proc. Nat. Acad. Sci. USA*, 2018, **115**, 47–52.

[205] A. Piel, *Plasma physics: an introduction to laboratory, space, and fusion plasmas*, Springer, 2017.

[206] I. D. Boyd, *J. Spacecr. Rockets*, 2015, **52**, 38–53.

[207] G. A. Bird, *Molecular Gas Dynamics and the Direct Simulation of Gas Flows*, 1994.

[208] I. Boyd, D. Bose and G. Candler, *Phys. Fluids*, 1997, **9**, 1162–1170.

[209] C. Park, R. Jaffe and H. Partridge, *J. Thermophys. Heat Transfer.*, 2001, **15**, 76–90.

[210] R. C. Millikan and D. R. White, *J. Chem. Phys.*, 1963, **39**, 3209–3213.

[211] C. Park, J. T. Howe, R. L. Jaffe and G. V. Candler, *J. Thermophys. Heat Transfer.*, 1994, **8**, 9–23.

[212] L. Landau, *Phys. Z. Sowjetunion*, 1936, **10**, 34–43.

[213] E. Nikitin and J. Troe, *Phys. Chem. Chem. Phys.*, 2008, **10**, 1483–1501.

[214] N. Singh and T. Schwartzentruber, *J. Chem. Phys.*, 2020, **152**, 224301.

[215] N. Singh and T. Schwartzentruber, *J. Chem. Phys.*, 2020, **152**, 224302.

[216] P. V. Marrone and C. E. Treanor, *The Physics of Fluids*, 1963, **6**, 1215–1221.

[217] P. Valentini, T. E. Schwartzentruber, J. D. Bender and G. V. Candler, *Phys. Rev. Fluids*, 2016, **1**, 043402.

[218] D. Koner, O. T. Unke, K. Boe, R. J. Bemish and M. Meuwly, *J. Chem. Phys.*, 2019, **150**, 211101.

[219] J. Arnold, J. C. San Vicente Veliz, D. Koner, N. Singh, R. J. Bemish and M. Meuwly, *J. Chem. Phys.*, 2022, **156**, 034301.

[220] G. Herzberg, *Molecular spectra and molecular structure: Spectra of diatomic molecule s*, Van Nostrand Reinhold, New York, 1950.

[221] J. Dunham, *Phys. Rev.*, 1932, **41**, 713.

[222] J. K. Watson, *Mol. Phys.*, 1968, **15**, 479–490.

[223] W. Wilson, *J. Chem. Phys.*, 1967, **46**, 2017–2018.

[224] D. Andrienko and I. D. Boyd, 46th AIAA Thermophysics Conference, Washington, D.C., 2016, p. 4021.

[225] A. Martin and I. Boyd, 49th AIAA Aerospace Sciences Meeting including the New Horizons Forum and Aerospace Exposition, 2011, p. 18 pp.

[226] T. E. Schwartzentruber, L. C. Scalabrin and I. D. Boyd, *J. Spacecraft Rockets*, 2008, **45**, 1196–1206.

[227] O. Denis-Alpizar, R. J. Bemish and M. Meuwly, *Phys. Chem. Chem. Phys.*, 2017, **19**, 2392–2401.

[228] D. Koner, J. C. S. V. Veliz, R. J. Bemish and M. Meuwly, *Phys. Chem. Chem. Phys.*, 2020, **22**, 18488–18498.

[229] J. Castro-Palacio, T. Nagy, R. Bemish and M. Meuwly, *J. Chem. Phys.*, 2014, **141**, 164319.

[230] J. Castro-Palacio, R. Bemish and M. Meuwly, *J. Chem. Phys.*, 2015, **142**, 091104.

[231] D. Koner, R. J. Bemish and M. Meuwly, *J. Chem. Phys.*, 2018, **149**, 094305.

[232] O. T. Unke and M. Meuwly, *J. Chem. Inf. Model*, 2017, **57**, 1923–1931.

[233] D. Koner, O. T. Unke, K. Boe, R. J. Bemish and M. Meuwly, *J. Chem. Phys.*, 2019, **150**, 211101.

[234] J. Arnold, D. Koner, S. Käser, N. Singh, R. J. Bemish and M. Meuwly, *J. Phys. Chem. A*, 2020, **124**, 7177–7190.

[235] J. Arnold, J. C. San Vicente Veliz, D. Koner, N. Singh, R. J. Bemish and M. Meuwly, *J. Chem. Phys.*, 2022.

[236] N. Singh and T. Schwartzentruber, *J. Chem. Phys.*, 2020, **152**, 224303.

Appendix A

CO_2 Temperature dependent rates

T (K)	N_r	$k_1^f(^1A')$	$k_2^f((2)^1A')$	$k_3^f(^1A'')$	$k_1^f(^1A') + k_2^f((2)^1A') + k_3^f(^1A'')$
15	93057	1.718×10^{-10}	0.000	0.000	1.718×10^{-10}
27	90583	1.245×10^{-10}	0.000	0.000	1.245×10^{-10}
54	85791	8.778×10^{-11}	0.000	0.000	8.778×10^{-11}
63	84463	8.261×10^{-11}	0.000	0.000	8.261×10^{-11}
83	81512	7.501×10^{-11}	0.000	0.000	7.501×10^{-11}
112	77896	6.868×10^{-11}	2.617×10^{-17}	0.000	6.868×10^{-11}
207	68861	5.925×10^{-11}	1.186×10^{-14}	0.000	5.926×10^{-11}
295	66814	5.551×10^{-11}	7.371×10^{-14}	2.095×10^{-16}	5.558×10^{-11}
300	66493	5.532×10^{-11}	7.785×10^{-14}	2.108×10^{-16}	5.540×10^{-11}
500	58788	5.152×10^{-11}	5.265×10^{-13}	6.183×10^{-15}	5.205×10^{-11}
600	56358	5.104×10^{-11}	8.512×10^{-13}	2.394×10^{-14}	5.191×10^{-11}
1000	53536	5.057×10^{-11}	2.643×10^{-12}	4.761×10^{-13}	5.369×10^{-11}
1500	49748	5.217×10^{-11}	5.368×10^{-12}	2.070×10^{-12}	5.961×10^{-11}
2000	50708	5.421×10^{-11}	8.266×10^{-12}	4.592×10^{-12}	6.707×10^{-11}
2500	49341	5.686×10^{-11}	1.132×10^{-11}	7.810×10^{-12}	7.599×10^{-11}
3000	48425	5.955×10^{-11}	1.434×10^{-11}	1.159×10^{-11}	8.549×10^{-11}
4000	46964	6.442×10^{-11}	2.102×10^{-11}	1.942×10^{-11}	1.049×10^{-10}
5000	46270	6.939×10^{-11}	2.752×10^{-11}	2.757×10^{-11}	1.245×10^{-10}
8000	52737	8.250×10^{-11}	4.748×10^{-11}	5.138×10^{-11}	1.814×10^{-10}
10000	52363	9.090×10^{-11}	6.025×10^{-11}	6.469×10^{-11}	2.158×10^{-10}
12000	51930	9.818×10^{-11}	7.120×10^{-11}	7.585×10^{-11}	2.452×10^{-10}
15000	50987	1.066×10^{-10}	8.462×10^{-11}	9.010×10^{-11}	2.813×10^{-10}
20000	49054	1.164×10^{-10}	1.013×10^{-10}	1.054×10^{-10}	3.232×10^{-10}

Table A.1: Rates for the $C(^3P) + O_2(^3\Sigma_g^-) \rightarrow CO(^1\Sigma^+) + O(^1D_2)$ from 15 to 20000 K calculated using QCT on the $^1A'$, $(2)^1A'$, $^1A''$ PESs. Units for rates are in $cm^3s^{-1}molecule^{-1}$. N_r is the number of reacting trajectories.

T (K)	N_r	$k_1^f(^3A')$	$k_2^f(^3A'')$	$k_1^f(^3A') + k_2^f(^3A'')$
15	49736	8.414×10^{-11}	0.000	8.414×10^{-11}
27	47390	5.682×10^{-11}	0.000	5.682×10^{-11}
54	44900	3.632×10^{-11}	0.000	3.632×10^{-11}
63	44406	3.337×10^{-11}	0.000	3.337×10^{-11}
83	43644	2.949×10^{-11}	0.000	2.949×10^{-11}
112	43489	2.671×10^{-11}	0.000	2.671×10^{-11}
207	43238	2.460×10^{-11}	0.000	2.460×10^{-11}
295	46131	2.486×10^{-11}	1.467×10^{-15}	2.487×10^{-11}
300	46187	2.506×10^{-11}	1.476×10^{-15}	2.506×10^{-11}
500	46573	2.742×10^{-11}	8.043×10^{-14}	2.750×10^{-11}
600	46856	2.906×10^{-11}	1.818×10^{-13}	2.924×10^{-11}
1000	50249	3.498×10^{-11}	1.321×10^{-12}	3.630×10^{-11}
1500	50968	4.156×10^{-11}	4.213×10^{-12}	4.578×10^{-11}
2000	54396	4.706×10^{-11}	8.086×10^{-12}	5.514×10^{-11}
3000	54474	5.717×10^{-11}	1.729×10^{-11}	7.446×10^{-11}
4000	54387	6.554×10^{-11}	2.710×10^{-11}	9.264×10^{-11}
5000	54311	7.304×10^{-11}	3.655×10^{-11}	1.096×10^{-10}
8000	62916	9.208×10^{-11}	6.297×10^{-11}	1.551×10^{-10}
10000	62254	1.025×10^{-10}	7.745×10^{-11}	1.799×10^{-10}
12000	61260	1.113×10^{-10}	8.944×10^{-11}	2.007×10^{-10}
15000	59333	1.205×10^{-10}	1.027×10^{-10}	2.232×10^{-10}
20000	55854	1.306×10^{-10}	1.166×10^{-10}	2.472×10^{-10}

Table A.2: Rate coefficients for the $C(^3P) + O_2(^3\Sigma_g^-) \rightarrow CO(^1\Sigma^+) + O(^3P)$ from 15 to 20000 K calculated using QCT on the $^3A'$ and $^3A''$ PESs. Units are in $cm^3s^{-1}molecule^{-1}$. N_r is the number of reacting trajectories.

T (K)	N_r	$k_1^r(^1A')$	$k_2^r((2)^1A')$	$k_3^r(^1A'')$	$k_1^r(^1A') + k_2^r((2)^1A') + k_3^r(^1A'')$
3000	0	0.000	0.000	0.000	0.000
4000	3	6.226×10^{-16}	3.738×10^{-16}	0.000	9.964×10^{-16}
5000	16	6.236×10^{-15}	3.239×10^{-15}	4.351×10^{-15}	1.383×10^{-14}
8000	383	2.902×10^{-13}	1.588×10^{-13}	1.651×10^{-13}	6.141×10^{-13}
10000	1037	9.278×10^{-13}	5.759×10^{-13}	6.744×10^{-13}	2.178×10^{-12}
12000	1897	1.928×10^{-12}	1.533×10^{-12}	1.653×10^{-12}	5.114×10^{-12}
15000	3711	4.616×10^{-12}	3.796×10^{-12}	4.239×10^{-12}	1.265×10^{-11}
20000	6655	1.008×10^{-11}	8.983×10^{-12}	9.373×10^{-12}	2.844×10^{-11}

Table A.3: Rate coefficients for the $CO(^1\Sigma^+) + O(^1D) \rightarrow C(^3P) + O_2(^3\Sigma_g^-)$ from 3000 to 20000 K calculated using QCT on the $^1A'$, $(2)^1A'$, $^1A''$ PESs. Units are in $cm^3s^{-1}molecule^{-1}$. N_r is the number of reacting trajectories.

T (K)	N_r	$k_1^r(^3A')$	$k_2^r(^3A'')$	$k_1^r(^3A') + k_2^r(^3A'')$
3000	0	0.000	0.000	0.000
4000	0	0.000	0.000	0.000
5000	2	9.055×10^{-17}	2.175×10^{-17}	1.123×10^{-16}
8000	223	1.429×10^{-14}	7.940×10^{-15}	2.223×10^{-14}
10000	1332	9.277×10^{-14}	6.892×10^{-14}	1.617×10^{-13}
12000	4339	3.340×10^{-13}	2.609×10^{-13}	5.948×10^{-13}
15000	11796	1.098×10^{-12}	9.348×10^{-13}	2.033×10^{-12}
20000	28176	3.449×10^{-12}	3.087×10^{-12}	6.535×10^{-12}

Table A.4: Rate coefficients for the $CO(^1\Sigma^+) + O(^3P) \rightarrow C(^3P) + O_2(^3\Sigma_g^-)$ from 3000 to 20000 K calculated using QCT on the $^3A'$ and $^3A''$ PESs. Units are in $cm^3s^{-1}molecule^{-1}$. N_r is the number of reacting trajectories.

T (K)	N	$k_1^f(^3A')$	$k_1^f(^3A'')$	$k_1^f(^3A' + ^3A'')$	$\Delta k_1^f(^3A' + ^3A'')$
500	57	3.859×10^{-16}	1.053×10^{-16}	4.912×10^{-16}	3.052×10^{-16}
1000	425	3.511×10^{-14}	1.242×10^{-14}	4.754×10^{-14}	1.972×10^{-15}
2000	4734	5.570×10^{-13}	2.812×10^{-13}	8.382×10^{-13}	1.746×10^{-14}
3000	11621	1.503×10^{-12}	9.694×10^{-13}	2.472×10^{-12}	3.340×10^{-14}
4000	20393	2.649×10^{-12}	2.012×10^{-12}	4.661×10^{-12}	3.969×10^{-14}
5000	28143	3.808×10^{-12}	3.233×10^{-12}	7.041×10^{-12}	5.890×10^{-14}
8000	52280	7.947×10^{-12}	7.777×10^{-12}	1.572×10^{-11}	7.493×10^{-14}
10000	78807	1.116×10^{-11}	1.099×10^{-11}	2.215×10^{-11}	1.088×10^{-13}
12000	93891	1.459×10^{-11}	1.468×10^{-11}	2.927×10^{-11}	1.606×10^{-13}
15000	127016	2.008×10^{-11}	2.043×10^{-11}	4.051×10^{-11}	3.037×10^{-13}
20000	182669	2.932×10^{-11}	3.001×10^{-11}	5.933×10^{-11}	1.990×10^{-13}

Table A.5: Temperature dependent rates for the $CO_A(^1\Sigma^+) + O_B(^3P) \rightarrow CO_B(^1\Sigma^+) + O_A(^3P)$ exchange reaction from 500 to 20000 K calculated using QCT on the $^3A'$ PESs. Units are in $cm^3s^{-1}molecule^{-1}$. N_r is the number of reacting trajectories.

T (K)	N_r	$k_1^f(^3A')$	$k_1^f(^3A'')$	$k_1^f(^3A') + k_1^f(^3A'')$
300	0	0.000	0.000	0.000
500	5	1.086×10^{-15}	9.675×10^{-16}	3.021×10^{-15}
1000	301	1.235×10^{-13}	1.081×10^{-13}	3.396×10^{-13}
2000	1713	1.329×10^{-12}	1.490×10^{-12}	4.309×10^{-12}
3000	2956	3.043×10^{-12}	3.966×10^{-12}	1.097×10^{-11}
4000	3950	4.780×10^{-12}	6.701×10^{-12}	1.818×10^{-11}
5000	4524	6.237×10^{-12}	9.933×10^{-12}	2.610×10^{-11}

Table A.6: Rate coefficients for the $CO(^1\Sigma^+) + O(^3P) \rightarrow CO(^1\Sigma^+) + O(^3P)$ vibrational relaxation $\nu = 1 \rightarrow 0$ from 300 to 5000 K calculated using QCT on the $^3A'$ and $^3A''$ PESs. Units for rates are in $cm^3s^{-1}molecule^{-1}$ and N_r is the number of reacting trajectories.

Appendix B

List of publications

Debasish Koner, Juan Carlos San Vicente Veliz, Ad van der Avoird and Markus Meuwly, "Near dissociation states for H_2+–He on MRCI and FCI potential energy surfaces." *Physical Chemistry Chemical Physics* **21**, 24976=24983 (2019)

Debasish Koner, Juan Carlos San Vicente Veliz, Raymond J Bemish and Markus Meuwly, "Accurate reproducing kernel-based potential energy surfaces for the triplet ground states of N_2O and dynamics for the N + NO $\leftrightarrow$ O+ N_2 and N_2 + O $\rightarrow$ 2N + O reactions." *Physical Chemistry Chemical Physics* **22**, 18488-18498 (2020)

Juan Carlos San Vicente Veliz, Debasish Koner, Max Schwilk, Raymond J Bemish and Markus Meuwly, "The $N(^4S) + O_2(X^3\Sigma_g^-) \leftrightarrow O(^3P) + NO(X^2\Pi)$ reaction: thermal and vibrational relaxation rates for the $^2A^{'}$, $^4A'$ and $^2A^{''}$ states." *Physical Chemistry Chemical Physics* **22**, 3927-3939 (2020)

Juan Carlos San Vicente Veliz, Debasish Koner, Max Schwilk, Raymond J Bemish and Markus Meuwly, "The $C(^3P) + O_2(^3\Sigma_g^-) \leftrightarrow CO_2 \leftrightarrow CO(^1\Sigma^+) + O(^1D)/O(^3P)$ reaction: thermal and vibrational relaxation rates from 15 K to 20000 K" *Physical Chemistry Chemical Physics* **23**, 11251-11263 (2021)

Sarbani Patra, Juan Carlos San Vicente Veliz, Debasish Koner, Evan J. Bieske and Markus Meuwly, "Photodissociation dynamics of N_3^+" *The Journal of Chemical Physics* **156**, 124307 (2022)

Julian Arnold, Juan Carlos San Vicente Veliz, Debasish Koner, Narendra Singh, Raymond J. Bemish and Markus Meuwly, "Machine learning product state distributions from initial reactant states for a reactive atom–diatom collision system." *The Journal of Chemical Physics* **156**, 034301 (2022)

Sugata Goswami, Juan Carlos San Vicente Veliz, Meenu Upadhyay, Raymond J. Bemish and Markus Meuwly, "Quantum and Quasi-classical Dynamics of the $C(^3P) + O_2(^3\Sigma_g^-) \rightarrow CO(^1\Sigma^+) + O(^1D)$ Reaction on Its Electronic Ground State." *Physical Chemistry Chemical Physics* **24**, 23309 (2022)

Juan Carlos San Vicente Veliz, Julian Arnold, Raymond J. Bemish and Markus Meuwly,."Combining Machine Learning and Spectroscopy to Model Reactive Atom + Diatom Collisions." *The Journal of Physical Chemistry A* **126**, 7971-7980 (2022)

Kevin Hickson, Juan Carlos San Vicente Veliz, Debasish Koner and Markus Meuwly, "Low-temperature kinetics for the N + NO reaction: experiment guides

the way." *Physical Chemistry Chemical Physics* **25**, 13854 (2023)

Adriana Caracciolo, Juan Carlos San Vicente Veliz, Dandan Lu, Hua Guo, Markus Meuwly and Timothy K. Minton,. "Experimental and Theoretical Studies of Hyperthermal N + O_2 Collisions." *(ChemRxiv)* (2023)

JUAN CARLOS SAN VICENTE

(+41) 76-828-4758 ◇ j.sanvicente@unibas.ch ◇ https://orcid.org/0000-0002-5939-0571

EDUCATION

University of Basel *Jan 2023*
PhD in Computational Chemistry
Thesis: Small Molecules Atomistic Simulations: From QCT to Machine Learned Models
Supervisor: Prof. Markus Meuwly
Grade: Magna Cumlaude

Venezuelan Institute for Scientific Research *Jun 2016*
MSc Physics

University Simon Bolivar, Venezuela *Jan 2012*
BSc Physics

PROFESSIONAL EXPERIENCE

University of Basel **July 2023 - Present**
Postdoctoral Researcher ***Basel, Switzerland***

· **Development and application of machine-learned state-to-state reaction networks**

University of Basel **Nov 2017 - June 2023**
Research Assistant ***Basel, Switzerland***

· **Development and application of high fidelity potential energy surfaces for research at high and low temperatures**
· **Model computational fluid dynamics at intense temperatures where non-equilibrium physical chemistry is prevalent**
· **Part of a large intercontinental research collaboration (USA & Switzerland)**

University of Basel **Nov 2017 - May 2023**
Teaching Assistant ***Basel, Switzerland***

· **General Computational Chemistry Lab**
· **Organization, supervision, and grading**
· **Design and implementation of new modules and exercises**
· **Development and implementation of a new teaching platform using Jupyterhub**

TECHNICAL SKILLS

Computer Languages	**BASH, Fortran, Python, ML (TensorFlow), R**
Developer Tools	**Vim, Emacs, LaTeX, VS Code, Visual Studio, PyCharm**
Other Programs	**Inkscape, Orca, Molpro, VMD**
Libraries	**pandas, NumPy, Matplotlib**

LANGUAGE SKILLS

Spanish	**Native**
English	**Fluent**
French	**Advance**
German	**Basic**

PEER REVIEWED JOURNAL PUBLICATIONS

1. A. Caracciolo, J. C. San Vicente, D. Lu, H. Guo, M. Meuwly, and T. Minton. "Experimental and Theoretical Studies of Hyperthermal N + O_2 Collisions" *Chemrxiv* (2023).

2. K. M. Hickson, D. Koner, J. C. San Vicente, and M. Meuwly. "Low-Temperature Kinetics for the N + NO reaction: Experiment Guides the Way" *Physical Chemistry Chemical Physics* **25**, 20, 13854–13863 (2023).

3. J.C. San Vicente, J. Arnold, R. J. Bemish, and M. Meuwly. "Combining Machine Learning and Spectroscopy to Model Reactive Atom + Diatom Collisions." *The Journal of Physical Chemistry A* **126**, 43, 7971–7980 (2022).

4. S. Goswami, J. C. San Vicente, M. Updadhyay, R. J. Bemish, and M. Meuwly. "Quantum and quasi-classical dynamics of the C(^{3}P) + O_2($^3\Sigma_g^-$) → CO($^1\Sigma^+$) + O(^{1}D) reaction on its electronic ground state." *Physical Chemistry Chemical Physics* **24**, 38, 23309–23322 (2022).

5. S. Patra, J. C. San Vicente, D. Koner, E. J. Bieske, and M. Meuwly. "Photodissociation dynamics of N_3^+" *The Journal of Chemical Physics* **156**, 12, 124307 (2022).

6. J. Arnold, J. C. San Vicente, D. Koner, N. Singh, R. J. Bemish, and M. Meuwly. "Machine learning product state distributions from initial reactant states for a reactive atom–diatom collision system" *The Journal of Chemical Physics* **156**, 3, 034301 (2022).

7. J. C. San Vicente, D. Koner, M. Schwilk, R. J. Bemish, and M. Meuwly. "The C (^{3}P) + O_2 ($^3\Sigma_g^-$) → CO_2 ↔ CO($^1\Sigma^+$)+ O(1 D)/O(^{3}P) reaction: thermal and vibrational relaxation rates from 15 K to 20000 K." *Physical Chemistry Chemical Physics* **23**, 19, 11251–11263 (2021).

8. J. C. San Vicente, D. Koner, M. Schwilk, R. J. Bemish, and M. Meuwly. "The N(^{4}S)+ O_2($X^3\Sigma$) O(^{3}P)+ NO($X^2\Pi$) reaction: thermal and vibrational relaxation rates for the ^{2}A′, ^{4}A′ and ^{2}A″ states." *Physical Chemistry Chemical Physics* **22**, 7, 3927-3939 (2020).

9. D. Koner, J. C. San Vicente, R. J. Bemish, and M. Meuwly. "Accurate reproducing kernel-based potential energy surfaces for the triplet ground states of N_2O and dynamics for the N + NO ↔ O + N_2 and N_2 + O → 2N + O reactions" *Physical Chemistry Chemical Physics* **22**, 33, 18488–18498 (2020).

10. D. Koner, J. C. San Vicente, A. van der Avoird, and M. Meuwly. "Near dissociation states for H_2^+–He on MRCI and FCI potential energy surfaces" *Physical Chemistry Chemical Physics* **21**, 45, 24976–24983 (2019).